Search for pair-produced first and second generation scalar leptoquarks in *pp* collisions at $\sqrt{s} = 13$ TeV & work with the liquid argon purity monitoring system in the ATLAS experiment

DISSERTATION

ZUR ERLANGUNG DES GRADES

DOKTOR DER NATURWISSENSCHAFTEN

AM FACHBEREICH PHYSIK, MATHEMATIK UND INFORMATIK

DER JOHANNES GUTENBERG-UNIVERSITÄT

IN MAINZ

ANTON WOLF

geboren in Nowosibirsk

Mainz, den 6. Mai 2020

1. Berichterstatter:
2. Berichterstatter:

Datum der mündlichen Prüfung: 5. März 2021

KURZFASSUNG

Der Large Hadron Collider (LHC) am CERN hat bisher Daten von den Proton-Proton (pp) Kollisionen mit der Schwerpunktsenergie bis zu 13 TeV geliefert. In der Zukunft ist geplant die Energie noch weiter zu erhöhen. Die gesammelten Daten erlauben es noch präzisere Aussagen über das Standardmodell zu liefern und sind zudem Teil der Suche nach Neuer Physik. Es ist wichtig sich zu vergewissern, dass diese Daten unter besten Konditionen des ATLAS Detektors gesammelt wurden. In dieser Arbeit wurden zwei verschiedene Themen behandelt: zum einen die Suche nach paar-produzierten skalaren Leptoquarks der ersten und zweiten Generation in pp Kollisionen bei $\sqrt{s} = 13\,\text{TeV}$ mit dem ATLAS Detektor, zum anderen die Arbeit an dem System zur Reinheitsbestimmung des flüssigen Argons im ATLAS Detektor.

Die Suche nach paar-produzierten skalaren Leptoquarks der ersten und zweiten Generation in pp Kollisionen bei $\sqrt{s} = 13\,\text{TeV}$ wurde ausgeführt unter Verwendung der Daten mit der integrierten Luminosität von $36.1\,\text{fb}^{-1}$. Die Leptoquarks sind in mehreren Erweiterungen des Standardmodells vorgestellt und könnten eine Erklärung für die Ähnlichkeiten im Quark- und Leptonensektor des Standardmodells bieten. Sie erscheinen auch in einigen Modellen, die sich mit kürzlich entdeckten b-Anomalien befassen. Es werden Ereignisse mit mindestens zwei Jets selektiert und zwei geladenen Leptonen von dem gleichen Flavour. Die erwartete Anzahl an Untergrundereignissen von den Prozessen im Standardmodell wurde aus den Monte Carlo Simulationen und den datenbasierten Methoden gewonnen. Sie wurde mit den Daten verglichen, und die Resultate wurden mithilfe der Profile-Likelihood-Methode interpretiert. Kein signifikanter Überschuss in jedem Kanal oberhalb des Untergrunds von dem Standardmodell wurde beobachtet und die Ausschlussgrenzen wurden gesetzt. Innerhalb des minimalen Buchmüller-Rückl-Wyler Modells und vorausgesetzt, dass das Verzweigungsverhältnis für den Zerfall zu einem geladenen Lepton und Quark 50% beträgt, können Leptoquarks mit den Massen bis zu 1.20 TeV mit 95% Konfidenzniveau ausgeschlossen werden.

Das Überwachungssystem von der Reinheit des flüssigen Argons besteht aus 30 im ATLAS Detektor installierten Monitoren, der Softwarekette außerhalb des Detektors und vielen Hardware Komponenten dazwischen. Die meisten Monitoren enthalten Am und Bi Ionizationskammern. Um einen schnelleren Weg zur Visualisierung des Spektrumverhaltens von diesen Ionisationskammern zu finden, wurde ein „Expertpanel“ von Grund auf neu entworfen und sofort gebrauchsfertig, direkt an der Produktionsmaschine implementiert. Aufgrund von Hinweisen auf Unstimmigkeiten in den Spektren, wurde die Kartierung von der Hochspannung untersucht. Dabei kam es zu unerwarteten Ergebnissen, die durch die Nichtübereinstimmung der Kartierung erklärt werden können. Um das Spektrumverhalten besser zu verstehen, wurden die sogenannten Rauschenspektren unter reduzierten Detektorbedingungen aufgezeichnet und ihre Eigenschaften studiert. Im Zuge des Upgrades von dem ATLAS Detektor, damit dieser für die zukünftigen Runs vom LHC bereit sein kann, müssen die Subsysteme, zu denen auch das Reinheitsüberwachungssystem von flüssigem Argon zählt, ebenfalls auf den neuesten Stand gebracht werden. Die ersten Gedanken über die mögliche Upgradeschritte sind in dieser Arbeit zusammengefasst.

ABSTRACT

The Large Hadron Collider (LHC) at CERN delivered data from proton-proton (*pp*) collisions up to the 13 TeV center of mass energy so far. In the future the energy is even planned to grow. The collected data allows to make more precise assumptions on the Standard Model (SM) and the search of new physics. It is essential to make sure that this data was collected under the best conditions of the ATLAS detector. In this thesis two different topics are covered. On the one hand the search for pair-produced first and second generation scalar leptoquarks in *pp* collisions at $\sqrt{s} = 13\,\text{TeV}$ with the ATLAS detector is described. On the other hand the work with the liquid argon purity monitoring system of the ATLAS detector is summarized.

The search for pair-produced first and second generation scalar leptoquarks in *pp* collisions at $\sqrt{s} = 13\,\text{TeV}$ has been carried out using data with an integrated luminosity of $36.1\,\text{fb}^{-1}$. Leptoquarks are featured in a number of extensions of the Standard Model and may provide an explanation for the similarities of the quark and lepton sectors in the Standard Model. They also appear in models adressing some of the recent *b*-flavours anomalies. The presented search used events with at least two jets and two charged same-flavour leptons. The expected amount of background from Standard Model processes has been estimated using Monte Carlo simulations and methods based on already recorded data. It has been compared to recorded data and the results were interpreted using the profile likelihood method. No significant excess above the SM background expectation is observed in any channel and exclusion limits have been evaluated. Within the minimal Buchmüller-Rückl-Wyler model and assuming a branching ratio for the decay into a charged lepton and a quark of 50%, leptoquarks with masses up to 1.20 TeV are excluded with a confidence level of 95%.

The liquid argon purity monitoring system consists of 30 monitors installed in the ATLAS detector, the software chain outside of the detector and several hardware components in between. In the most monitors Am and Bi ionization chambers are available. In order to fasten the visualization of the behaviour of the spectra from these ionization chambers the „expert panel“ was designed from scratch and implemented to be ready to use instantly and directly on the production machine. Following by some indications seen on these spectra, the investigation on the high voltage mapping was performed with unexpected results which could be explained by the mismatching on the mapping. In order to better understand the behaviour seen on the spectra the so-called noise spectra were recorded under reduced detector conditions and their properties were studied. In the course of the ATLAS detector upgrade to be ready for the future Runs of LHC every subsystem including the LAr purity monitoring system has to be prepared for this. The first thoughts about the possible upgrade steps are summarized in this thesis.

For everyone who really believed that I could go that far...

...Especially for my parents and all beloved ones.

Contents

Introduction

> *I'm just a simple man trying to make my way in the universe.*
>
> Jango Fett from Star Wars: Episode II - Attack of the Clones

Since several thousands of years people around the globe want to understand what their whole world including themself is made of. These thoughts are the basis of the science known by today as particle physics. However, it was Democritus, a greek philosopher, who around 400 BC raised an idea, that all matter is made of invisible particles. His teacher Leucippus evolved this idea further by calling these particles atomes. At that time point it became the general name for all fundamental particles. The research was continued only about 2000 years later, as John Dalton proposed that each element should consist of indivisible atoms of many different types. These atoms can not be destroyed, but however, they can be at least reordered in chemical processes [1]. Nevertheless, it was J.J. Thompson, who showed in his experiments from 1897, that the hydrogen, the least massive known atom so far, was not the lightest element. In his experiments he showed, that cathode rays were made up out of even lighter particles [2]. These particles became to what we know today as electrons, the first particles without any substructure (at least judging by the human knowledge of today). Few years later, in 1911, the atomic nucleus was discovered. Shortly after that, in 1932, the proton was discovered by Ernest Rutherford [3]. Finally, in 1932, the neutron entered the scene by James Chadwick [4] which made it possible together with previous knowledge to explain the formation of matter as the atoms made out of the fundamental particles. Up to that point, there were known only two fundamental forces: the electromagnetic interaction and gravity. The electromagnetic interaction could be used to explain atoms and their isotopes. Later, the nuclear force, a foundation stone to the discovery of the strong force, was uncovered by studying the interactions within the atomic nuclei. After that, the exploration of isotopes and radioactivity gave another boost to the research.

A big progress was made in the 1950s since it was possible to perform inelastic scattering experiments on protons and atomic nuclei as a consequence of the particle accelerator development. Even if the highest collision energies were about a few hundred MeV during that time period, it was enough to discover several unstable particles with short lifetimes and to strive for more knowledge. Further development on particle accelerators was improved leading to higher collision energies. In parallel the particle detectors were improved as well leading to the discovery of more unstable particles. During that time the term „particle zoo“ was born since the amount of uncovered particles was already huge. Theorists began to develop models in order to better describe this „particle zoo“. So, the quark model was born [5, 6], which describes the structure of particles as bound states of quarks. Later, in 1969, as a result of the deep inelastic scattering of electrons on protons, the substructure of the proton was discovered at SLAC (Stanford Linear Accelerator Center) [7, 8]. This milestone was a proof for the quark model and simultaneously the foundation stone to the Standard Model of particle physics. According to this model, the substructure of all hadrons (proton is a hadron as well) was made up out of fundamental particles - quarks. At that time, the up, down and strange quarks were discovered at SLAC. The interactions of particles were studied by theorists as well leading to the predictions of mediators of these interactions. So, in 1979, the mediator of the strong force, the gluon, was discovered at the electron-positron collider PETRA (Positron-Elektron Tandem Ring Anlage) at DESY (Deutsches Elektronen-Synchrotron) [9–12]. The discovery of the mediators of the weak force, the Z^0 and $W^{\pm}$ bosons, followed four years later at CERNs (Conseil Européen pour la Recherche Nucleaire) Super-Proton-Antiproton Synchrotron (SppS) collider [13–16]. The last discovery in the particle physics field of the past century was the top quark, the heaviest particle of the Standard Model. It was found in 1995 at the Fermi National Accelerator Laboratory [17–20]. However, the Standard Model was still not complete yet. In 2012, the Higgs boson, a particle theorized in 1964, filled the gap in the Standard Model since experiments at the LHC (Large Hadron Collider) at CERN [21, 22] finally found this boson.

Many experiments proved and even verified up to the highest precision that the Standard Model is a very powerful theory. However, there are observations, which it still can not explain, like dark matter or the matter-antimatter asymmetry to name a few. So, the extensions of the Standard Model are proposed. Some of them predict the existence of new particles, like leptoquarks, with masses in the TeV range, which could be found directly or indirectly using particle detectors. Judging by the past observations, it is very likely to find these particles by operating particle colliders at high energies and making the measurements [23–26]. The precision of these measurements at ATLAS, a multi-purpose detector located at the LHC particle-accelerator at the European Organization for Nuclear Physics (CERN), depends among other things on the precision of the energy determination by the calorimeters and therefore on their energy resolution and temporal constancy, which in turn depends at some point on the purity of the liquid argon (LAr) regarding electronegative substance. It is important to monitor and maintain the state of LAr purity on the experiment in order to make sure that the energy resolution is still in trustable range.

This introduction gives an overview of the Chapters in this thesis which describe the leptoquark search as well as the work with the liquid argon (LAr) purity monitoring system. Since science inspires humankind to explore Nature more deeply or to develop great fiction art, the thesis describes my work behind the exploration of Nature and the quotes at the beginning of each Chapter are responsible for the fiction part, taken from the Science-Fiction works, so all inspiration aspects are covered.

Part I describes the theoretical foundations for the data analysis presented in this thesis. Chapter 1 briefly describe the SM of the particle physics, followed by a discussion on proton-proton collisions in Chapter 2. The open questions in the current state of the SM and a leptoquark phenomenology as a possible answer to these questions are discussed in Chapter 3.

Part II describes the experimental apparatus behind the search performed at ATLAS of leptoquarks and work with LAr purity monitoring system presented in this thesis. Chapter 4 gives more information about LHC and their experiments, and Chapter 5 describes the ATLAS experiment and its detector which makes this scientific endeavor possible. During all the time, different groups of thousands of physicists and engineers have different tasks in order to develop, maintain and operate this massive detector.

The first main component of this thesis describes a search for new physics in Part III. Chapter 6 gives a motivation for this search. In order to make the search possible, a preselected sample is defined which mimics the topology of the leptoquarks. This sample has a very low signal-to-background ratio since it is dominated by the backgrounds to the analysis. The contributions of these backgrounds are estimated using simulations. After that, the two control regions are defined from the preselected sample in order to validate the background modeling in signal regions. The first steps of the analysis are discussed in Chapter 7. Having properly collected and modeled the data, the method used to assess the sensitivity of the results is described in Chapter 8. The final results, conclusions and an outlook are given in Chapter 9.

The second main component of this thesis describes the work performed on the LAr purity monitoring system in Part IV. Chapter 10 gives a motivation behind the usage of this system and the importance of its maintenance. Chapter 11 gives a theoretical insight and an overview of the current monitoring system. Several maintenance steps performed during my PhD time are summarized and discussed in Chapter 12. In Chapter 13 the challenges for the LAr purity monitoring system due to increased goals for the ATLAS experiment in future LHC runs are summarized, and first thoughts about needed steps for the improvement of the current LAr purity monitoring system are discussed. Chapter 14 gives a conclusion and an outlook since the work described in this thesis is just a beginning of the improvement.

There will be a short summary of the presented leptoquark search and work with LAr purity monitoring system at the end of the thesis.

Part I

Theory overview

CHAPTER

1 THE STANDARD MODEL

> “*The Force is strong with this one.*”
> DARTH VADER FROM STAR WARS: EPISODE IV - A NEW HOPE

THE Standard Model (SM) of particle physics is one of the most successful theoretical models that describes the electromagnetic, weak and strong interactions of elementary particles which are divided into three generations of spin-1/2 particles - fermions, and twelve spin-1 particles - gauge bosons. Within this thesis the convention $\hbar = c = 1$ is used.

A short explanation of the SM concept will be introduced in Section 1.1 and a more detailed discussion of the mathematical formalism of the SM will be discussed in Section 1.2, all mostly based on References [25, 27].

1.1 Introduction to the Standard Model

1.1.1 Quarks and leptons

The idea behind the SM is that the visible matter has to be made up of a few particles called fermions. Furthermore, they consist of no further substructure, which means that they are fundamental. These fermions have a half-integer spin (angular momentum) and therefore obey Fermi-Dirac statistics [28, 29] by having unique quantum states. This means that there are no two fermions with the same quantum numbers existing in the same quantum state. The fermions are divided into three generations and two categories: leptons and quarks. However, the SM describes anti-particles as well. For every fermion exists an anti-particle with opposite quantum numbers.

There are two types of leptons: charged ones and neutral ones. The electron (e) might be the most familiar charged lepton. It is also the lightest one. Its heavier „brothers“ are the muon (μ) and the tau lepton (τ). Neutrinos belong to the other category of leptons. They are neutral and have an interesting nomenclature. Neutrinos are denoted with the symbol ν_x, where the subscript x is replaced with e, μ or τ depending on the flavour of the neutrino which corresponds to the name of the charged lepton. For example, the electron neutrino (ν_e) is the first generation neutrino partner to the electron. The definition of generation is that the leptons of the higher generation are also the heavier leptons. So, the leptons from a higher generation can decay into any leptons of a generation below. Neutrinos are the exception here since they are to be expected massless in the SM. However, after performing neutrino oscillation experiments, it was shown that neutrinos have a very small mass [30]. So far only the upper limits on the neutrino masses could be given since it is not possible at the moment to measure the mass directly.

Next category of fermions are the quarks. There are many differences between leptons and quarks. One of them is that quarks exist only in bound states while leptons can exist alone. These bound states are generally called hadrons. The quarks form either quark-antiquark pairs (mesons) or triplets (baryons) due to the laws of the strong force (see Section 1.2.3). However, combined states with four and even five quarks, called tetra- and pentaquarks respectively, also could be observed recently [31–33]. Protons and neutrons are the most familiar bound states of quarks. Protons are the triplets of two up (u) and one down (d) quarks (both from the first generation) leading to a particle with a charge of $+1e$. Neutrons are made of the same quark types, but in different combination: one u und two d quarks, leading to a neutrally charged particle. Since protons and neutrons are made up of three quarks, they are baryons. Another two generations of up-type quarks are the charm (c) and the top (t) quarks. The top quark is also the heaviest one. The strange (s) and the bottom (b) quarks are the analogous down-type quarks.

The quantum numbers of the quarks and leptons are summarized in Table 1.1.

Fermion	Charge/e	1st Generation		2nd Generation		3rd Generation	
			Mass		Mass		Mass
Quarks	+2/3	u	2.2 MeV	c	1.3 GeV	t	173.0 GeV
	-1/3	d	4.7 MeV	s	95 MeV	b	4.2 GeV
Leptons	-1	e	0.51 MeV	μ	105.7 MeV	τ	1776.9 MeV
	0	ν_e	<2 eV	ν_μ	<0.19 MeV	ν_τ	<18.2 MeV

Table 1.1: *Quarks and Leptons. Three generations of fermions (anti-particles not shown). Each family has identical gauge interactions, and differ only by mass and flavour quantum number [34].*

1.1.2 Force mediators

The achievement of the SM is not only that it describes the fundamental particles, but also that it describes their interactions. These interactions are performed via the exchange of bosons which have commonly an integer spin and therefore obey Bose-Einstein statistics [35]. Unlike Fermi-Dirac statistics, this means that multiple bosons with the same quantum numbers can exist in the same quantum state. The bosons which mediate the forces are summarized in Table 1.2. The gravitational force is not included here, since gravity is not a part of the SM.

Boson	Force	Mass [GeV]	Relative strength	Range
gluon (g)	Strong	0	1	10^{-15} m
photon (γ)	Electromagnetic	0	10^{-2}	∞
Z^0	Weak	≈91.2	10^{-7}	10^{-18} m
$W^\pm$	Weak	≈80.4	10^{-7}	10^{-18} m
Higgs (H)	-	≈125.2	-	-

Table 1.2: *Force mediators. These are the forces that are described by the SM. They are mediated by bosons listed in the first column along with their mass and relative strength compared to the strong force between two protons when just in contact, and their range [34, 36].*

The electromagnetic force, first described by Maxwell in 1873 [37], is for example responsible for the interactions between electrons with nuclei. The mediators of the electromagnetic force are photons (γ), which couple to particles containing electric charge. Because photons have no mass, the range of the electromagnetic force is infinite and obeys the inverse square law. It means that the force decreases as the squared inverse of the separation of two charged particles. However, even if this force is the second one by strength, it is still the best understood one.

The weak force, first described by Fermi in 1934 [38], is for example responsible for the nuclear β-decay of a neutron. In this decay a proton, electron and anti-neutrino are produced ($n \to p+e^-+\bar{\nu}_e$). The weak force also allows the reverse process ($p \to n+e^++\nu_e$)[1], which is responsible for the deuterium formation and causes the sun to burn. The mediators of the weak interaction in general are three different gauge bosons: the electric positively and negatively charged $W^\pm$ bosons and the neutral Z^0 boson[2]. The $W^\pm$ bosons are the mediators of the charged current, while the Z boson is the mediator of the neutral current. The weak force allows to change the flavour between quarks and the flavour between leptons (with the help of $W^\pm$ bosons) making this force distinctive upon all other forces. Finally, it is the only force in which all leptons and quarks can participate.

The strong force, first described by Fritsch and Gell-Mann in 1973 [39], is responsible for binding the nucleus of atoms together. The mediators of this force are eight different massless and electrically neutral gluons (g). They can act on different scales: on one level they bind quarks together in a proton and a neutron, on another level they bind protons and neutrons together in an atomic nucleus. Furthermore, they can also act on other gluons. The range of the strong force increases with distance leading to the fact, that quarks unlike leptons can not exist alone. This effect is generally referred to as confinement.

1.2 Formalism of the Standard Model

The theory behind the SM is called Quantum Field Theory, where the particles represent the fields with different values for a position in space and time [40]. The SM makes use of the mathematical constructs called Lagrangians in order to describe the possible changes in a physical system. However, the key usage of the Lagrangians is the possibility to construct them to be gauge invariant. This permits to describe observations in form of several local continuous symmetries. It means that the Lagrangian is invariant under a group of transformations and that the field is invariant under the local phase transformation: $\psi(x) \to e^{i\alpha(x)}\psi(x)$ [41].

The gauge invariance, which is the invariance under local group transformations, is one of the key features of the SM, because it leads to symmetries which are the building blocks for the formulation of conservation laws. This invariance could be established by adding gauge fields into Lagrangian. The complete Lagrangian of the SM is invariant under local gauge transformations of the $SU(2) \times U(1) \times SU(3)$ group. Invariance under transformations under the first part, $SU(2) \times U(1)$, generate the four gauge bosons - mediators of the interactions of the SM - corresponding to the weak and electromagnetic interactions. Invariance under transformations under the last part, $SU(3)$, generate the eight gluons.

1.2.1 Electromagnetic force and Quantum Electrodynamics

The theoretical model for the electromagnetic force called Quantum Electrodynamics (QED), and the symmetry group $U(1)$ is responsible for its description. In order to describe the electromagnetic force, the following free electromagnetic Lagrangian is needed:

$$\mathcal{L}_0 = \bar{\psi}\left(i\gamma^\mu\partial_\mu - m\right)\psi, \tag{1.1}$$

where γ^μ are the gamma matrices and $\bar{\psi} = \psi^\dagger\gamma^0$. This Lagrangian has to be gauge invariant under symmetry transformation. This can be achieved by the following fermion field transformation (in case of a $U(1)$ symmetry):

$$\psi \to e^{i\theta(x)}\psi. \tag{1.2}$$

---

[1] However, this decay can not occur in an isolated proton because it requires energy, due to the mass of the neutron being greater than the mass of the proton. The decay can only happen inside nuclei when the daughter nucleus has a greater binding energy (and therefore a lower total energy) than the mother nucleus.

[2] The Z^0 boson is also referred to as Z boson in the further appearances.

The transformation is called local if the real phase $\theta(x)$ is dependent on the space coordinate x and global if it is not. The Lagrangian takes the following form after inserting the transformed fermion field into it:

$$\delta\mathcal{L} = -\bar{\psi}(x)\gamma^{\mu}\partial_{\mu}\theta(x)\psi(x). \tag{1.3}$$

According to the previously mentioned definition this Lagrangian is not invariant under local gauge transformations. In order to make it invariant, a modified derivative D_μ has to be considered first, which transforms covariantly under phase transformations:

$$D_\mu \equiv \partial_\mu - ieA_\mu, \tag{1.4}$$

where e can be identified as a conserved charge of the particle described by ψ, following Noether's theorem [42], and a vector field A_μ is the gauge field corresponding to the photon. It transforms as defined in the following Equation:

$$A_\mu \to A_\mu + \frac{1}{e}\partial_\mu\alpha_\mu. \tag{1.5}$$

If A_μ corresponds to a physical photon field, then there has to be a term representing the kinetic energy of the field. Furthermore, it has to be invariant when transformed as the gauge field, so the gauge invariant field strength tensor has to be introduced given by the following Equation:

$$F_{\mu\nu} = \partial_\mu A_\nu - \partial_\nu A_\mu. \tag{1.6}$$

Substituting these into $\mathcal{L}_0$ results the QED Lagrangian given in the following Equation:

$$\mathcal{L}_{\text{QED}} = \bar{\psi}(i\gamma^{\mu}\partial_{\mu} - m)\psi + e\bar{\psi}\gamma^{\mu}A_{\mu}\psi - \frac{1}{4}F_{\mu\nu}F^{\mu\nu}. \tag{1.7}$$

The first term of this Lagrangian shows the dynamics of a fermionic field. The second term shows the interaction of the fermions with the photon field (represented by the gauge field A_μ). The third term is added to the Equation in order to show that photons can also exist as free particles, not as part of an interaction. Lastly, it should be mentioned, that additional fourth term representing the mass would violate local gauge invariance. Therefore, this term is not added and as a conclusion, the photon has to be massless.

1.2.2 Feynman formalism

The Feynman formalism is not only a nice method to visualize processes of particle interaction, but also a useful guideline for the amplitude calculation of a process by using the so-called Feynman rules [43]. These rules settle that straight lines with arrows represent fermions, where the arrow points in time direction for particles and other way around for anti-particles. If these lines intersect, the points of intersection are called vertices which in turn are connected with other lines called propagators.

As an example the process of e^+e^- scattering (also known as Bhabha-scaterring) is shown via two different diagrams in Figure 1.1. Since it is a QED process, the propagator is here a (virtual[3]) photon. The left side of the Figure shows the annihilation of the electron and positron to a virtual photon which in turn decays again into e^+ and e^- (this procedure is also called s-channel). The right side of the Figure shows a scattering process of e^+ and e^- via the photon exchange (this procedure is also called t-channel). Each vertex delivers a factor of the square root of the coupling constant (here, in case of QED: $\sqrt{\alpha_{\text{em}}} = \sqrt{e^2/4\pi}$, where e is the electron charge) to which the amplitude is proportional. The coupling constant is a measure of

---

[3] A particle called virtual if its invariant mass do not match with the real (experimentally observable) mass. Alternatively, these particles are also called as off-shell particles.

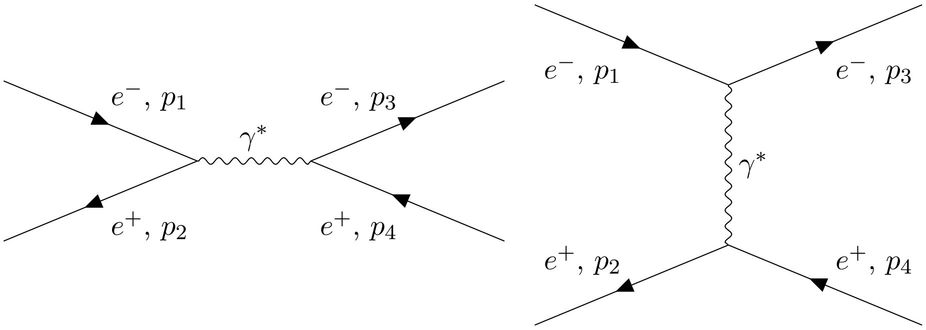

(a) s-channel.

(b) t-channel.

Figure 1.1: *Different leading order Feynman graphs for Bhabha-scattering. The time axis is horizontally adjusted.*

the interaction strength. Using this information the overall amplitude for both shown diagrams is proportional to $\sqrt{\alpha_{\text{em}}} \times \sqrt{\alpha_{\text{em}}} = \alpha_{\text{em}}$.

The connection between the amplitude and a cross section is established by usage of Fermi's Golden rule [44]. For this the squared, absolute value of the amplitude has to be integrated over the available phase space. This amplitude can be obtained using Feynman rules as described previously. The phase space, however, follows from the kinematics of the process. Using this information, the cross section for Bhabha-scattering is given by:

$$\sigma = \frac{1}{4\sqrt{(p_1 \cdot p_2)^2 - (m_1 m_2)^2}} \int |\mathcal{M}|^2 (2\pi)^4 \delta^4 (p_1 + p_2 - p_3 - p_4) \times \prod_{j=3}^{4} 2\pi\delta\left(p_j^2 - m_j^2\right) \Theta\left(p_j^0\right) \frac{d^4 p_j}{(2\pi)^4}, \tag{1.8}$$

where p_i and m_i are the four momenta and corresponding masses of the incoming and outcoming leptons labeled in Figure 1.1. The energy and momentum conservation is established with the factor $\delta^4 (p_1 + p_2 - p_3 - p_4)$, while the delta function $\delta\left(p_j^2 - m_j^2\right)$ ensures that the particles are on their mass shells. The Heaviside function $\Theta\left(p_j^0\right)$ forces the outgoing energy to be positive. The matrix amplitude $\mathcal{M}$ leaves the possibility for interference terms since it is squared. Alternatively, the cross section can be derived as a series expansion of the coupling constant:

$$\sigma = \sum_{i=1} \alpha^i \sigma^{(i)}, \tag{1.9}$$

where $\sigma^{(i)}$ stays for all contributing graphs to the order of $\mathcal{O}\left(\alpha^i\right)$. The graphs to the order of $\mathcal{O}\left(\alpha^i\right)$ have their own description, like leading order (LO) for a graph to the lowest order, next-to-leading order (NLO) for the second lowest order and so on. Figure 1.2 shows some examples of NLO diagrams, which contribute to the NLO correction of the Bhabha-scattering.

The diagram 1.2(a) is an example of a correction to the decay vertex of the photon (also known as vertex correction). The diagram 1.2(b) shows final state photon radiation (FSR) and the diagram 1.2(c) initial state radiation (ISR). The diagram 1.2(d) is an example of (fermion) loop correction.

Ideally all orders (see Equation 1.9) have to be considered for the cross section calculation. However, this task is just too big for theoretical calculations, so in practice there is a need to make a cut after a few orders[4]. For the calculation of higher order loop corrections the

---

[4] The number of orders is different for different interactions. The model and resources used for cross section calculation in practice are two main points which have to be considered for the choice of number of orders. However, NNLO calculations are often good enough for strong interaction processes. It is also the best possible theory prediction at the moment.

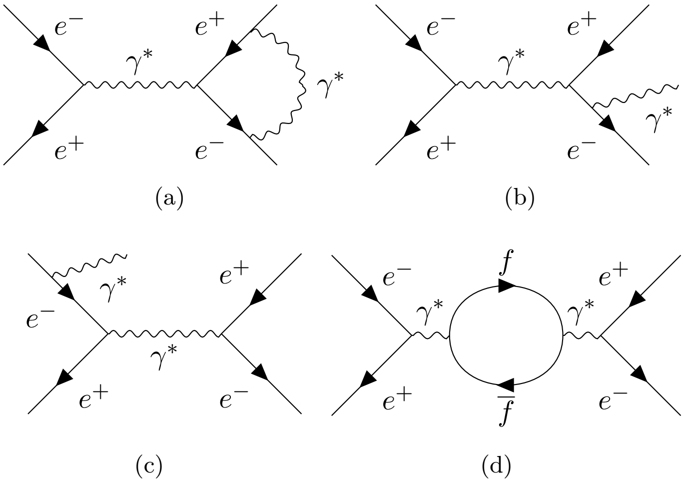

(a) (b) (c) (d)

Figure 1.2: *Some of the Feynman graphs contributing to the NLO correction of the process* $e^+e^- \to \gamma^* \to e^+e^-$*. Graph (a) shows a vertex correction, (b) is an example of final state radiation (FSR), (c) is an example of initial state radiation (ISR) and (d) is a fermion loop correction.*

integration over the particle momenta in loops has to be performed. However, this can lead to so-called ultra violet divergences. In order to regularize the integrals a cutoff scale Λ_{cutoff} can be used. If the integral is solved, two parts remain from the regularization, where one part is dependent on Λ_{cutoff} and the other is not. This dependence can be expressed as follows:

$$\alpha_{\text{em, physical}} = \alpha_{\text{em}} + \delta\alpha_{\text{em}}, \tag{1.10}$$

where it can be seen as modification of the coupling. If Λ_{cutoff} goes to infinity, then $\delta\alpha_{\text{em}} \to \infty$, which means that α_{em} must contain some compensating infinities. The idea of an infinite charge shielded by charges originating from vacuum polarizations can serve as a vivid example. This leads then to a finite measured charge. As a next step, the regularized integrals have to be renormalized. This procedure allows to do predictions of physical quantities since the dependency of the cutoff scale will be removed. However, a new renormalization scale dependency of couplings appears instead, which leads to the so-called „running couplings“. In case of QED α_{em} increases for higher scales.

1.2.3 Strong force and Quantum Chromodynamics

The strong force deserves its name very well since it is indeed the strongest fundamental force. The theoretical model for the strong force called Quantum Chromodynamics (QCD), and the $SU(3)$ gauge theory of color charged[5] fermions is responsible for its description. This theory was postulated in order to add one more degree of freedom (color) for quarks, so that some baryons could not violate the Pauli exclusion principle[6]. $SU(3)$ desribes three different colors (red (r), blue (b) and green (g)) and eight different gluons, which have the following color combinations:

- $\left(r\bar{b} + b\bar{r}\right)/\sqrt{2}$, $-i\left(r\bar{b} - b\bar{r}\right)/\sqrt{2}$
- $\left(r\bar{g} + g\bar{r}\right)/\sqrt{2}$, $-i\left(r\bar{g} - g\bar{r}\right)/\sqrt{2}$
- $\left(b\bar{g} + g\bar{b}\right)/\sqrt{2}$, $-i\left(b\bar{g} - g\bar{b}\right)/\sqrt{2}$

---

[5] The quarks and gluons carry the charge of the strong interaction, the so-called color.

[6] The quantum mechanical principle which states that two or more identical fermions can not occupy the same quantum state within a quantum system simultaneously.

- $\left(r\bar{r}-b\bar{b}\right)/\sqrt{2}$, $\left(r\bar{r}+b\bar{b}-2g\bar{g}\right)/\sqrt{6}$

The two unique features of QCD are confinement and asymptotic freedom. Confinement is the reason why no free quarks exist. A process in order to separate two quarks from each other would take an infinite amount of energy since the force between quarks does not get smaller during this separation. For example at colliders, if the production of a very high energetic parton (quark or gluon) is initiated, this parton begins to radiate additional gluons. This process goes further until the energy scale gets to be small and the hadrons are formed due to confinement. The resulting bundles of particles are called jets. Asymptotic freedom is the property that describes the fact, that at higher energies the interactions between quarks and gluons become so small as if the interacting partons are free.

The free Lagrangian for the $SU(3)$ group for the quark color fields can be expressed with the following Equation:

$$\mathcal{L}_0 = \bar{q}_j \left(i\gamma^\mu \partial_\mu - m\right) q_j, \tag{1.11}$$

where $j = 1, 2, 3$ represent the three color fields.

In order to force $SU(3)$ local gauge invariance on $\mathcal{L}_0$, the covariant derivative as shown in Equation 1.4 has to be applied. However, instead of the single gauge field A_μ and charge $-e$, the quantities G^a_μ and charge gT_a have to be used, where G^a_μ is a 3×3 matrix. The eight color gauge fields corresponding to the eight gluons build this matrix, which transforms in the following way:

$$G^a_\mu \rightarrow G^a_\mu - \frac{1}{g}\partial_\mu \alpha_a - f_{a,b,c}\alpha_b G^c_\mu, \tag{1.12}$$

where $f_{a,b,c}$ are structure constants [45], $T_a = \frac{\lambda_a}{2}$, and λ_a are the Gell-Mann matrices [46], the generators of the $SU(3)$ quark triplets. Finally, ∂_μ has to be replaced with D_μ, which leads to the final gauge invariant QCD Lagrangian:

$$\mathcal{L}_{\mathrm{QCD}} = \bar{q}_j \left(i\gamma^\mu \partial_\mu - m\right) q_j - g\left(\bar{q}\gamma^\mu T_a q\right) G^a_\mu - \frac{1}{4} G^a_{\mu\nu} G^{\mu\nu}_a, \tag{1.13}$$

where $G^a_{\mu\nu}$ (the gluon field strength tensor) is defined by the following Equation:

$$G^a_{\mu\nu} = \partial_\mu G^a_\nu - \partial_\nu G^a_\mu - g f_{a,b,c} G^b_\mu G^c_\nu. \tag{1.14}$$

The last term of Equation 1.14 corresponds to the self-coupling between the gluons. After expanding these two Equations many different terms will emerge to light. They describe the free propagation of quarks (terms containing $q\bar{q}$), of gluons (G^2) and of the quark-gluon interaction ($gq\bar{q}G$). Lastly, gluon-gluon interactions can be expressed as well which are represented by three and four gluon vertices (shown in terms with cubic and quartic powers of G).

1.2.4 Weak force and electroweak symmetry

The weak processes are separated into two types: charged and neutral. The charged processes are mediated by the $W^\pm$ bosons, while the neutral ones by the Z boson. Only in the charged processes the flavour of quarks and leptons changes by the weak force. This force is also the weakest fundamental force (except gravity) due to the fact that all mediators are massive and therefore with increasing distance the force decreases very fast.

The unification of the electromagnetic and weak forces appeared in 1967 by Glashow, Salam and Weinberg [47] on the order of 100 GeV (unification theory), even if these forces may look very different at the first moment. The $SU(2) \times U(1)$ gauge group is responsible for the description of this unification [48]. The corresponding gauge bosons are the three W bosons and the B^0 boson. The W bosons have a weak isospin coming from $SU(2)$ symmetry (W^1, W^2 and W^3), while the B^0 boson has a weak hypercharge coming from $U(1)$ symmetry. All these bosons are massless [49, 50].

In order to create a formalism for electromagnetic and weak interactions several constraints have to be considered (similar procedure like it was for strong interactions with QCD). The observations showed that only left-handed fermions or right-handed anti-fermions interact weakly by changing the flavour. Furthermore, it was observed that leptons like to appear in doublets (pairs) containing two components: a charged and a neutral one. However, the right-handed contribution from neutrinos was not observed. These constraints pushed forward the development of the electroweak symmetry formalism.

For the expression of the electroweak Lagrangian a similiar method as seen for the QCD and electromagnetic case can be applied: the usage of a modified derivative to the free Lagrangian. On this way the electroweak Lagrangian can be separated into two parts:

$$\mathcal{L}_{\text{EWK}} = \mathcal{L}_{\text{gauge}} + \mathcal{L}_{\text{fermion}}. \tag{1.15}$$

$\mathcal{L}_{\text{gauge}}$ describes the gauge interactions between the W and B particles, and its form is similar to the kinetic energy term for the gauge field which is present in the QED Lagrangian:

$$\mathcal{L}_{\text{gauge}} = -\frac{1}{4} W^i_{\mu\nu} W^{\mu\nu i} - \frac{1}{4} B_{\mu\nu} B^{\mu\nu}, \tag{1.16}$$

where

$$W^i_{\mu\nu} = \partial_\nu W^i_\mu - \partial_\mu W^i_\nu + g\epsilon^{ijk} W^j_\mu W^k_\nu, \tag{1.17}$$

$$B_{\mu\nu} = \partial_\nu B_\mu - \partial_\mu B_\nu. \tag{1.18}$$

$\mathcal{L}_{\text{fermion}}$ has also a form which is similar to a part in the QED Lagrangian and $i = 1, 2, 3$. This term stays for the gauge bosons interactions with the fermions through the modified covariant derivatives, and is expressed in the following Equation:

$$\mathcal{L}_{\text{fermion}} = \bar{\psi}_L i\gamma^\mu (D_\mu) \psi_L + \bar{\psi}_R i\gamma^\mu (D_{\mu,R}) \psi_R. \tag{1.19}$$

Here, the ψ_L term represents the left-handed isospin doublet of the fermion $\begin{pmatrix} \nu_i \\ l_i \end{pmatrix}_L$. However, it exists only the isospin singlet $(l_i)_R$ because neutrinos seem to not possess a right-handed component as described previously. Furthermore, it is worth to mention, that the right-handed covariant derivative $(D_{\mu,R})$ has one term less. This results from the fact that the right-handed fermions are not coupling to isospin. These covariant derivates can be written as:

$$D_\mu = \partial_\mu + i\frac{g'}{2} B_\mu Y + i\frac{g}{2} \vec{\tau} \cdot \vec{W}_\mu, \tag{1.20}$$

$$D_{\mu,R} = \partial_\mu + i\frac{g'}{2} B_\mu Y, \tag{1.21}$$

where $\vec{\tau}$ represents the Pauli matrices, and g and g' are coupling constants [50]. The two Lagrangians ($\mathcal{L}_{\text{gauge}}$ and $\mathcal{L}_{\text{fermion}}$) build the system which sustains a gauge theory of the weak isospin and weak hypercharge. But there is a conflict which appears in the real world. According to the experimental observations of W and Z bosons, discovered at the SppS collider at CERN [13–16] in 1983, these bosons are not massless. This is against the requirement of local gauge invariance, which needs the field to be massless. In order to claim the consistency back, the electroweak gauge symmetry has to be broken.

1.2.5 Spontaneous symmetry breaking

In order to solve the problem with the masses of the gauge bosons described previously, these masses have to be generated with break of the vacuum state symmetry. However, the full Lagrangian gauge symmetry has to be kept. The solution is called spontaneous symmetry breaking. Electroweak symmetry breaking (for electroweak theory) is also known as the Higgs mechanism. In order to make this type of symmetry breaking possible, $\mathcal{L}_{\text{EWK}}$ needs to be appended by an additional term ($\mathcal{L}_{\text{Higgs}}$) and to become to the following Equation:

$$\mathcal{L}_{\text{EWK}} = \mathcal{L}_{\text{gauge}} + \mathcal{L}_{\text{fermion}} + \mathcal{L}_{\text{Higgs}}. \tag{1.22}$$

The spontaneous symmetry breaking mechanism allows the W and Z bosons to be massive while the photon is kept massless. For this a single complex scalar doublet field (also called as Higgs field [51]) is used:

$$\Phi = \begin{pmatrix} \phi^{+}(x) \\ \phi^{0}(x) \end{pmatrix} \tag{1.23}$$

with its Lagrangian

$$\mathcal{L}_{\text{Higgs}} = \left(D_{\mu}\Phi\right)^{\dagger}\left(D^{\mu}\Phi\right) - V(\Phi). \tag{1.24}$$

Here, $V(\Phi)$ represents the self-interaction of the Higgs field. The description of $V(\Phi)$ is expressed in the following Equation:

$$V(\Phi) = -\mu^{2}\Phi^{\dagger}\Phi + \lambda\left(\Phi^{\dagger}\Phi\right)^{2}. \tag{1.25}$$

This potential is invariant under the local gauge transformations of $SU(2)_{L} \times U(1)_{Y}$. The construction of $V(\Phi)$ requires a degenerate ground state $\Phi^{\dagger}\Phi = -\frac{4\mu^{2}}{\lambda} = v^{2}$ for $\mu^{2} > 0$ and $\lambda > 0$, where v is a vacuum expectation value which can not disappear. Now the ground state $\langle\Phi\rangle = \frac{1}{\sqrt{2}}\begin{pmatrix} 0 \\ v \end{pmatrix}$ has to be set suitable in order to brake the $SU(2)_{L} \times U(1)_{Y}$-symmetry to $U(1)_{\text{EM}}$. Φ takes then the form

$$\Phi(x) \approx \frac{1}{\sqrt{2}}\begin{pmatrix} 0 \\ v + H(x) \end{pmatrix}, \tag{1.26}$$

if it is expanded around the vacuum expectation value [48]. Here, the field $H(x)$ represents a so-called Higgs boson, a physical neutral scalar, which has a mass of $m_{H} = \mu\sqrt{2}$. Recently, in 2012 according to the observations from ATLAS [52] and CMS [53] experiments at the LHC, a new boson was found, which has the properties that also the Higgs boson was expected to have. The latest mass measurement of this boson delivers the mass of 124.98 ± 0.28 GeV [54].

Finally, while the photon still remains massless, the following constraints on the mass terms of the electroweak gauge bosons are established:

$$m_{W} = \frac{1}{2}vg \quad \text{and} \quad m_{Z} = \frac{1}{2}v\sqrt{g^{2} + g'^{2}}, \tag{1.27}$$

which result from the fact that the Higgs doublet has three additional degrees of freedom. It should be mentioned, that $\mathcal{L}_{\text{Higgs}}$ does not break electroweak Lagrangian gauge symmetry since $\mathcal{L}_{\text{Higgs}}$ is invariant under the local gauge transformations of the electroweak symmetry group, but, however, the W and Z bosons became massive with the presented solution. In order to express the ratio of the weak force mediators masses the electroweak mixing angle θ_{W} can be introduced as

$$\cos(\theta_{W}) = \frac{m_{W}}{m_{Z}}, \tag{1.28}$$

and the relation of the coupling constants which are testable within the SM, can be written as

$$g\sin\left(\theta_W\right) = g'\cos\left(\theta_W\right) = e. \tag{1.29}$$

Furthermore, a Yukawa coupling to the scalar Higgs field [55] is helpful to set the positive fermion masses, which were otherwise required to be zero. The corresponding Lagrangian has the following form in the unitary gauge:

$$\mathcal{L}_{\text{Yukawa}} = -\sum_f m_f \bar{\psi}_f \psi_f - \sum_f \frac{m_f}{v} \bar{\psi}_f \psi_f H. \tag{1.30}$$

As a conclusion, the fermions couple to the Higgs field using a coupling constant which is set to their mass. But more precise measurements are needed in order to study this and other properties of the Higgs mechanism more closely. However, already performed measurements agree with the theoretical predictions resulting from the electroweak theory and the Higgs mechanism in particular [24].

Chapter

2 Proton-proton collisions

> “*Power! Unlimited power!*”
> Darth Sidious from Star Wars: Episode III - Revenge of the Sith

Due to the confinement it is impossible to build a pure parton collider. Instead for example *pp* colliders are used. Protons consist of three valence quarks (uud) and gluons, while the gluons prevent the protons from decaying freely. However, the gluons can split into other gluons, which recombine after a short period of time, or into quark pairs, which also are known as sea quarks. If the protons collide with enough energy to being split into their inner structure, then all quarks (valence and sea) and/or gluons from these protons collide as well and scatter.

This Chapter is based on Reference [56]. Section 2.1 introduces the hard scattering process, while Section 2.2 outlines the way how parton density functions are obtained needed for making the predictions in this process. The last Section 2.3 describes effects like multiparton interactions, parton shower and hadronization which make the *pp* collision to be a complex process.

2.1 Hard scattering process

Figure 2.1 shows a picture representing the basics of a *pp* collision. The challenge is that experiments can not provide the momentum or the type of colliding particles directly. Therefore, probability functions of the momentum distribution of the partons coming from protons can be used for this purpose. At least the predictions about proton-proton collisions can be stated. The parton-distribution function (PDF) $f_{a/p}(x, \mu_F)$ provides the probability of a parton a with momentum fraction x of the proton ($p_{\text{parton}} = xp_{\text{proton}}$), where x is the Bjorken-x variable[1]. μ_F is the factorization scale which is generally set to be equivalently to the renormalization scale μ_R. The PDF provides parton emissions up to the threshold defined by μ_F. However, above μ_F the partonic cross section is responsible for the information about the splitting. In 1971 it was shown by Drell and Yan in their factorization theorem [57] that PDFs are not dependent on the hard scatter and therefore are universal. In order to determine the probability for a process in *pp* colliders two folded components are needed: the probability for the random selection of two partons from the proton with a fixed momentum fraction x and the scatter probability of two partons into the needed final state $\hat{\sigma}_{ab}$. Finally, the integrated cross section can be determined by the sum over all possible parton types and integration over the parton momentum fractions. This procedure can be expressed via the following Equation:

$$\sigma = \sum_{a,b} \int_0^1 dx_a \int_0^1 dx_b \hat{\sigma}_{ab} \left(x_a, x_b, s, \mu_R^2, \mu_F^2\right) f_{a/p}(x_a, \mu_F) f_{b/p}(x_b, \mu_F), \tag{2.1}$$

where $\sqrt{s}$ is the center-of-mass energy of the two protons.

---

[1] The Bjorken-x variable is also known from deep inelastic scattering.

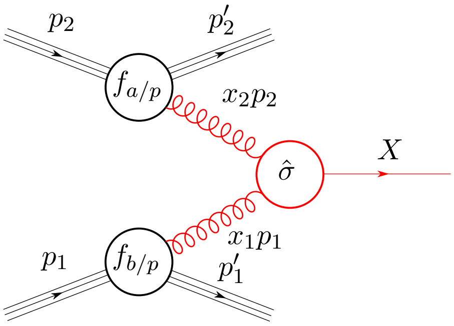

Figure 2.1: *Hard scattering in a proton-proton collision. The lines by p_1 and p_2 indicate the incoming protons, built of many partons. The momentum fraction carried by the colliding partons is given by the PDFs $f_{a/p}$ and $f_{b/p}$. The hard scattering itself is indicated in red, where the outgoing arrow X is not necessarily a single particle, but could also represent a system of many particles.*

2.2 Parton density function

In order to obtain a PDF (introduced in Section 2.1), the inner structure of the proton has to be studied more deeply. The probabilities of the splittings caused by partons inside of the proton are given by the Altarelli-Parisi splitting functions [58].

The x-dependency of the PDFs is not predicted, so measurements are needed for gaining this information. The pionier measurements of PDFs at high x and low scale of momentum transfer Q^2 were performed in deep inelastic scattering (fixed target end *ep* collisions at HERA [59, 60]). In order to apply this information for the other regions of Q^2 a need for PDF fits is born, which use data from several different experiments over a large x and Q^2 range. H1 [59] and ZEUS [60] Collaborations contributed to the precise measurements (especially in the low x region). While the evolution in x has to be determined using the measurements, the expansion in Q^2 is performed using the DGLAP formalism [58, 61–63]. First, a parametrization in x at a starting scale Q_0 is selected using given factorization scale, which is chosen randomly, and order of $\alpha_S(\mu_R)$. Then, these PDFs are expanded to the momentum scales of the provided measurements by usage of the DGLAP formalism, and consequently are folded with partonic cross sections. Finally, a result comparison with the measurements is performed. All free parameters are provided using the minimization of a global χ^2 fit to all measurements which are used in the global fit. Since the gluon momentum goes to zero the gluon emission probability diverges. Furthermore, the possibility for the splitting resolution is proportional to the collision momentum scale. Therefore, as long as the momentum scale is finite, divergences disappear. However, with rising momentum scale the contribution from sea quarks rises as well. The MSTW PDF group provides the PDF as a function of the momentum fraction x, which can be seen in Figure 2.2.

There are two observations noticeable. First, 50% of the proton momentum is coming not from the valence quarks but from gluons. Second, the contribution from sea quarks rises at higher momentum scales and low x because of a higher resolution. For example at $x = 10^{-3}$, when going from $Q^2 = 10\,\text{GeV}^2$ to $Q^2 = 10\,000\,\text{GeV}^2$ a rise by almost an order of magnitude is visible for the sea quarks PDF. The colored bands stay for the different PDF uncertainties. There is uncertainty on the data which is used for the PDF fits, that is propagated to the PDFs. However, since there might be a correlation between the contributing uncertainties, the propagation can be hard. The Hessian method [65] is used in order to establish a set of uncorrelated parameters, which in turn are used for the error propagation since the chosen parametrization can be varied[2]. The variations are taken as uncertainties. Last but not least the input parameters contribute to PDF uncertainties as well. For example there are parameters which are not fixed: heavy quark

---

[2] However, this type of uncertainty was not considered in the analysis presented in this thesis.

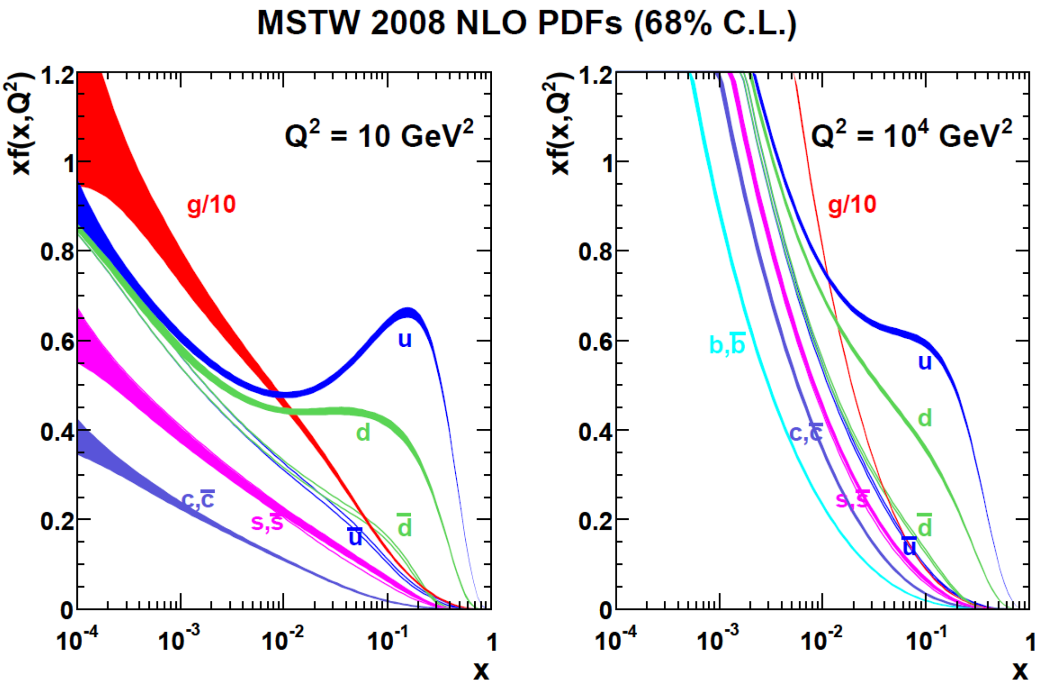

Figure 2.2: *MSTW 2008 NLO parton density functions at* $Q^2 = 10\,\mathrm{GeV}^2$ *and* $Q^2 = 10\,000\,\mathrm{GeV}^2$, *including the associated one-sigma (68%) confidence level uncertainty bands. The gluon contribution is scaled by 0.1 [64].*

masses and the strong coupling constant. However, they can be chosen to be fixed within some uncertainties, or they are used as additional parametrization fit parameters. In both cases the additional uncertainties appear. Furthermore, using the same input data by two different PDF groups can still lead to two different PDF predictions due to different choices of parametrization and the way of handling with input parameters.

2.3 Multiparton interactions, parton shower and hadronization

Figure 2.3 shows a full picture of a *pp* collision, where also the underlying event and hadronization (the transition from partons to hadrons, which are observed in the detector) are presented. The before mentioned hard scattering is marked in red color.

The picture is complex since it is not always sure if only one parton pair scatters. The possible additional scatterings (mainly soft 2 → 2 QCD scatterings) are also known as the underlying event, which are marked in purple color. They are pushed into the the non-perturbative regime due to the low momentum transfer, and are described using phenomenological models. The basic idea behind these models is that the number of parton interactions can be expressed as the cross section ratio $\langle N_{\mathrm{int}} \rangle = \sigma_{\mathrm{soft}}/\sigma_{pp}$. In order to make sure that this number is finite, σ_{soft} is only used above a certain threshold, called minimum transverse momentum $p_{\mathrm{T}}^{\mathrm{min}}$. However, this cut-off is only one of many free parameters which are used in the phenomenological models for the modeling of the underlying event via Monte Carlo generators[3]. So, the underlying event has to be well described since it is responsible for additional energy depositions in the detector to the hard scaterring processes, which are important for the analysis.

The complete picture includes also initial and final state radiation/parton shower. This extended

---

[3] Monte Carlo generators are programs which perform random generation processes. The set of generated events using such a Monte Carlo generator is often called as Monte Carlo sample.

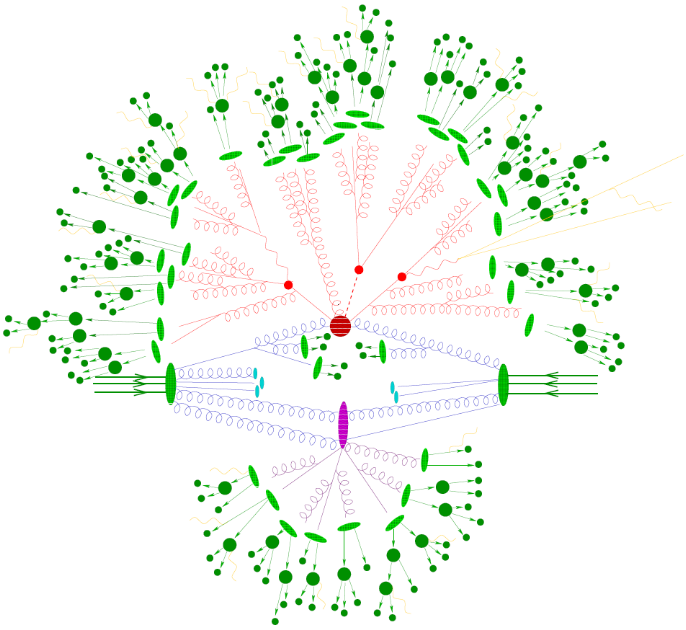

Figure 2.3: *Schematic view of the inelastic scattering between two protons. The incoming partons are drawn in blue, the hard scattering is colored in red and contributions of the underlying event in purple. Primary and secondary vertices are shown as red circles. The hadronization is indicated by green lines [66].*

shower in form of quark anti-quark pairs or two gluons originates from the gluons, which are radiated from the color charged in- and outgoing partons of the hard interaction. The parton showering is based on the so-called Sudakov form factors, $\Delta\left(Q_0, Q_1\right)$, which represents the parton probability, where a parton does not decay into two new partons between the scale Q_0 and Q_1. Sudakov form factors are applied for a $2 \rightarrow 2$ scattering first. They are used recursively to each in- and outgoing parton down to Q_0, which is a minimum scale. The final state parton shower is time-like and therefore progresses in time by decreasing the virtuality Q. The initial state radiation is space-like, which progresses in the opposite direction of time flow. It begins at the hard scattering and decreases the scale Q until the agreement with the PDFs is achieved. In order to avoid divergences, the minimum scale Q_0^2 is set to be the energy at which it would be not possible anymore to reach emission resolution. Monte Carlo simulations use values of few GeV in common. The choices of the radiated gluon transverse momentum or the angle between the radiated gluon and the parton are usual choices for Monte Carlo simulations, while the scale Q is chosen randomly. A collinear approximation yields the Sudakov form factors, leading to the good description of the soft radiation by the parton shower, while the description of the harder/non collinear radiations is bad. Combinations of next-to-leading order (NLO) predictions and parton shower are further complicated due to double counting (calculation contributions coming from parton shower and NLO matrix elements). In order to avoid this a scale barrier has to be added, which ensures that the parton shower does not go further and the NLO matrix elements predict the radiation. Finally, a matching needs to be performed.

The process of hadronization is drawn in green which stands for all previously described partons since they carry a color charge that is non-neutral. The original *pp* collision model from Figure 2.1 is simple and represents only a small part. However, the behaviour of parton shower, the underlying event and hadronization has to be deeply studied since they can help to understand the complete picture by giving a closer look into non-perturbative QCD.

Chapter

3 BEYOND THE STANDARD MODEL

> *They continually speak to us, telling us the will of the Force. When you learn to quiet your mind, you'll hear them speaking to you.*
> QUI-GON JINN FROM STAR WARS: EPISODE I - THE PHANTOM MENACE

Even if the SM is successful in describing the observed elementary particles and their interactions there is evidence that the SM is not a complete description. Some phenomena remain unexplained by the SM which hints to physics beyond the SM (BSM).

This Chapter is mostly based on Reference [27]. Section 3.1 gives a short overview of the open questions beyond the explanations of the SM and the possible answers to them, while Section 3.2 describe the leptoquark phenomenology from the general point of view up to the one used in this thesis.

3.1 Open questions and possible answers

Particle physicists have still a few challenges left to describe Nature. They can be summarized in the following two categories:

- **Experimental observations not modeled**: there exists no theoretical framework compatible with the SM for example for gravity, dark energy (unknown form of energy which is hypothesized to permeate all of space, tending to accelerate the expansion of the universe), dark matter (an invisible form of matter that is thought to account for approximately 27% of the matter in the universe), matter-antimatter asymmetry and for the explanation why neutrino masses are not exactly zero.

- **Theoretical oddities**: the theoretical framework itself contains some odd features even though the search of physics beyond the SM is not successful yet. Some of these features are:

  - the larger number of numerical parameters - the SM depends on 19 (determined from experiments),
  - the need for three generations of leptons and quarks.

These open questions which the SM has left unanswered inspire scientists to search for new physics. The solutions to these questions can be described by the following two categories of theoretical frameworks: weakly coupled and strongly coupled.

Weakly coupled solutions use additional symmetries. With this approach the quadratic divergences cancelation could be explained. The prevalent theory in this category is called Supersymmetry (SUSY). Main idea of this theory is that each elementary particle has a „super-partner“ whose spin is slightly different. More precisely, all fermions have a superpartner of integer spin and all bosons have a superpartner of half integer spin, where the spin difference is 1/2.

Strongly coupled solutions add a new asymptotically free gauge group to the SM. The most developed theory in this category is Technicolor. However, strongly coupled solutions are very difficult to calculate due to some struggles which they have and which are not related to the SM. Furthermore, there exist some trials to develop the theories which unify all fundamental forces (electromagnetic, weak and strong forces) on the similar way like the electroweak symmetry unify the electromagnetic and weak forces. These attempts are called Grand Unified Theories (GUTs). In the following Sections some meanings of these theories and different predictions are presented.

3.2 Leptoquark Phenomenology

Leptons and quarks have similar and even symmetrical properties within the SM. So it is likely that they have even more interactions between each other within some more fundamental theory. In such a theory, the mentioned interactions between leptons and quarks are mediated by a leptoquark (LQ), which represents a completely new type of particle. LQs have already a huge phenomenology, appearing in many extensions to the SM. However, they have some general features in common. LQs stay for color-triplet bosons carrying both lepton and baryon number. They can be either scalar particles with a spin 0 or vector particles with a spin 1. Scalar LQs have one undetermined coupling at the LQ $- l - q$ vertex which is given by a Yukawa coupling (λ). On the other side, the vector LQs have even one more undetermined coupling. In general, LQs have a non integer electric charge which can be determined using the sum of the charges of one lepton and one quark [67, 68].

This Section describes a few theories behind the LQ pair production mechanisms and presents the experimental signatures for these particles.

3.2.1 Leptoquarks in BSM physics

An effective Lagrangian, a start for the LQs discussion, is given by the following Equation [69]:

$$\mathcal{L}_{\mathrm{LQ}} = \mathcal{L}^{f}_{|F|=0} + \mathcal{L}^{f}_{|F|=2} + \mathcal{L}^{g}_{S} + \mathcal{L}^{g}_{V}, \tag{3.1}$$

where F is the fermion number defined by $F = L + 3B$, which is composed of the lepton number L and the baryon number B (for quarks is $B = +1/3$). S and V stay for scalar and vector LQs respectively. Each Lagrangian can be expressed via the following Equations:

$$\begin{aligned}\mathcal{L}^{f}_{|F|=0} = {} & (h_{2L}\bar{u}_R l_L + h_{2R}\bar{q}_L i\tau_2 e_R)\, S_{1/2} + \tilde{h}_{2L}\bar{d}_R l_L \tilde{V}^{L}_{1/2} \\ & + \left(h_{1L}\bar{q}_L\gamma^{\mu} l_L + h_{1R}\bar{d}_R\gamma^{\mu} e_R\right) V_0 \\ & + \tilde{h}_{1R}\bar{u}_R\gamma^{\mu} e_R \tilde{V}^{R}_{0} + h_{3L}\bar{q}_L \boldsymbol{\tau}\gamma^{\mu} l_L V^{L}_{1} + h.c.,\end{aligned} \tag{3.2}$$

$$\begin{aligned}\mathcal{L}^{f}_{|F|=2} = {} & (g_{1L}\bar{q}^{c}_{L} i\tau_2 l_L + g_{1R}\bar{u}^{c}_{R} e_R)\, S_0 \\ & + \tilde{g}_{1R}\bar{d}^{c}_{R} e_R \tilde{S}^{R}_{0} + g_{3L}\bar{q}^{c}_{L} u\tau_2 \boldsymbol{\tau} l_L S^{L}_{1} \\ & + \left(g_{2L}\bar{d}^{c}_{R}\gamma^{\mu} l_L + g_{2R}\bar{q}^{c}_{L}\gamma^{\mu} e_R\right) V_{1/2} \\ & + \tilde{g}_{2L}\bar{u}^{c}_{R}\gamma^{\mu} l_L \tilde{V}^{L}_{1/2} + h.c.,\end{aligned} \tag{3.3}$$

$$\mathcal{L}_S^g = \sum_{scalars} \left[\left(D_{ij}^{\mu} \Phi^j \right)^{\dagger} \left(D_{\mu}^{ik} \Phi_k \right) - M_S^2 \Phi^{i\dagger} \Phi_i \right], \tag{3.4}$$

$$\mathcal{L}_V^g = \sum_{vectors} \left\{ -\frac{1}{2} V_{\mu\nu}^{i\dagger} V_i^{\mu\nu} + M_V^2 \Phi_{\mu}^{i\dagger} \Phi_i^{\mu} - i g_s \left[\left(1 - \kappa_G\right) \Phi_{\mu}^{i\dagger} t_{ij}^a \Phi_{\nu}^j \mathcal{G}_a^{\mu\nu} + \frac{\lambda_G}{M_V^2} V_{\sigma\mu}^{i\dagger} t_{ij}^a V_{\nu}^{j\mu} \mathcal{G}_a^{\nu\sigma} \right] \right\}, \tag{3.5}$$

where, g_s denotes the strong coupling constant, t_a are the generators of $SU\left(3\right)_c$, and M_S $\left(M_V\right)$ is the scalar (vector) LQ mass. Table 3.1 lists a summary of the possible quantum numbers for LQs. It includes the different possibilities for charge Q (given in units of proton charge), the lepton-quark Yukawa coupling λ, the decay branching fraction to a charged lepton β and the fermion number F. The notation refers to first generation LQs, the equivalent can be defined for the second and third generation. The generation of LQ defines to which quark and lepton generation LQ is coupled.

Type	Q	Coupling	β	F
S_0^L	$-1/3$	$\lambda_L\left(e_L u\right)$, $-\lambda_L\left(\nu_e d\right)$	1/2	2
S_0^R	$-1/3$	$\lambda_R\left(e_R u\right)$	1	2
$\tilde{S}_0^R$	$-4/3$	$\lambda_R\left(e_R d\right)$	1	2
S_1^L	$-4/3$	$-\sqrt{2}\lambda_L\left(e_L d\right)$	1	2
	$-1/3$	$-\lambda_L\left(e_L u\right)$, $-\lambda_L\left(\nu_e d\right)$	1/2	2
	$+2/3$	$\sqrt{2}\lambda_L\left(\nu_e u\right)$	0	2
$V_{1/2}^L$	$-4/3$	$\lambda_L\left(e_L d\right)$	1	2
	$-1/3$	$\lambda_L\left(\nu_e d\right)$	0	2
$V_{1/2}^R$	$-4/3$	$\lambda_R\left(e_R d\right)$	1	2
	$-1/3$	$\lambda_R\left(e_R u\right)$	1	2
$\tilde{V}_{1/2}^L$	$-1/3$	$\lambda_L\left(e_L u\right)$	1	2
	$+2/3$	$\lambda_L\left(\nu_e u\right)$	0	2
$S_{1/2}^L$	$-5/3$	$\lambda_L\left(e_L \bar{u}\right)$	1	0
	$-2/3$	$\lambda_L\left(\nu_e \bar{u}\right)$	0	0
$S_{1/2}^R$	$-5/3$	$\lambda_R\left(e_R \bar{u}\right)$	1	0
	$-2/3$	$-\lambda_R\left(e_R \bar{d}\right)$	1	0
$\tilde{S}_{1/2}^L$	$-2/3$	$\lambda_L\left(e_L \bar{d}\right)$	1	0
	$+1/3$	$\lambda_L\left(\nu_e \bar{d}\right)$	0	0
V_0^L	$-2/3$	$\lambda_L\left(e_L \bar{d}\right)$, $\lambda_L\left(\nu_e \bar{u}\right)$	1/2	0
V_0^R	$-2/3$	$\lambda_R\left(e_R \bar{d}\right)$	1	0
$\tilde{V}_0^R$	$-5/3$	$\lambda_R\left(e_R \bar{u}\right)$	1	0
V_1^L	$-5/3$	$\sqrt{2}\lambda_L\left(e_L \bar{u}\right)$	1	0
	$-2/3$	$-\lambda_L\left(e_L \bar{d}\right)$, $\lambda_L\left(\nu_e \bar{u}\right)$	1/2	0
	$+1/3$	$\sqrt{2}\lambda_L\left(\nu_e \bar{d}\right)$	0	0

Table 3.1: *LQ quantum numbers [70]: Charge is given by Q (in units of proton charge), the lepton-quark Yukawa coupling is given by λ, the decay branching fraction to a charged lepton by β and the fermion number by F. The notation here refers to first generation LQs, the equivalent can be defined for the second and third generation.*

The parameters κ_G and λ_G, which appear in Equation 3.5, stay for the anomalous couplings. They are related to some moments of the vector LQs, namely the anomalous magnetic moment μ_V and electric quadrupole moment q_V as defined in the following Equations:

$$\mu_{V,G} = \frac{g_s}{2M_V}\left(2 - \kappa_G + \lambda_G\right), \tag{3.6}$$

$$q_{V,G} = \frac{-g_s}{M_V^2}\left(1 - \kappa_G - \lambda_G\right). \tag{3.7}$$

Furthermore, $\mathcal{G}$ and V are the field strength tensors and D is the covariant derivative, which appear in Equations 3.4 and 3.5 and are defined in the following way:

$$\mathcal{G}^a_{\mu\nu} = \partial_\mu G^a_\nu - \partial_\nu G^a_\mu + g_s f^{abc} G_{\mu b} G_{\nu c}, \tag{3.8}$$

$$V^i_{\mu\nu} = D^{ik}_\mu \Phi_{\nu k} - D^{ik}_\nu \Phi_{\mu k}, \tag{3.9}$$

$$D^{ij}_\mu = \partial_\mu \delta^{ij} - i g_s t^{ij}_a G^a_\mu. \tag{3.10}$$

In the following the different extensions to the SM which include LQs are discussed.

Grand Unified Theories (GUTs)

The very first model, where LQs appeared, is the Pati-Salam $SU(4)$ color symmetry model, which assumes, that the lepton number can be used as a fourth color [67, 71]. This follows to the spontaneously brake of $SU(4)$ leading to the massless gluons and the massive LQs. Even if LQs violate lepton family number in this model, the mixing between the generations is suppressed.

Next model, which includes LQs, is the $SU(5)$ model, which assumes that vector LQs have unification scale masses leading to the fact, that they are not reachible by accelerators. Some scalar LQs, however, can also couple to two quarks (as another coupling possibility to the already known coupling to a lepton and a quark). If this coupling is set to zero, scalar $SU(5)$ LQs can be light (in the order of 100 GeV) and therefore accessable by accelerators. However, in case that the $LQ - q - q'$ coupling is left unconstrained, the LQ mass remains unreachable by accelerators since it has to be large [72].

Finally, LQs also occur in superstring E_6 models [73, 74], which allow the addition of extra $U(1)$ symmetries. In this case the LQs can be found in the low energy limit on the way like as in other GUTs.

Supersymmetry

LQ-like objects at the TeV mass scale are also allowed within SUSY. However, the requirements are R-parity violation and addition of Yukawa terms to the superpotential. R-parity denotes a $+1$ for particles and -1 for supersymmetric partners. It is not conserved if particles and sypersymmetric particles are produced in non equal amounts. The newly added Yukawa term takes care of lepton number violation and leads to the production of single scalar quarks, which are identified as LQ-like objects [75].

Technicolor

In Section 1.2.5 the Higgs was introduced as a solution to electroweak symmetry breaking. Additional options are given by modeling chiral symmetry breaking in QCD, leading to the mass delivery for the W and Z bosons (even if these masses are few orders of magnitudes too small). One of these options is technicolor, a strongly interacting theory. It represents a solution to electroweak symmetry breaking which appears to be different and dynamic. The original idea which inspired the technicolor force is a QCD-like strongly-interacting gauge theory [76].

The W and Z boson masses are generated by technicolor using new gauge interactions. The theory predicts technifermions (new technicolor fermions) which form technimesons (lowest bound states of fermions). On the experimental side, the experiments on flavour changing neutral currents strongly constrained the initial technicolor models. However, the extensions to technicolor are more or less unconstrained.

One extended technicolor model, which increases the group number symmetry, has a property allowing existence of large numbers of Goldstone bosons - bosons that appear necessarily in models exhibiting spontaneous breakdown of continuous symmetries. An example for this would be the brake of $SU(8)$ symmetry leading to the production of 63 Goldstone bosons. Three of them will be „eaten“ by the electroweak gauge bosons. In the remaining 60, a composition of a techniquark and an anti-technilepton bound together by the technicolor force, will be found (so-called „leptoquark mesons“). Such bosons will appear also outside of the technicolor sector, because there are analogous mesons to quarks and leptons, which would have as a requirement a mediator to quark and anti-lepton with the same SM quantum numbers.

3.2.2 Leptoquarks at LHC

Figure 3.1 shows the pair production of LQs via gg fusion and $q\bar{q}$ annihilation. gg fusion is the dominant process for pair production at the Large Hadron Collider (LHC) for LQ masses below ~ 1 TeV due to the nature of pp colliders in general. However, with increasing LQ mass the $q\bar{q}$ annihilation production process gains inreased importance. So, at $\sqrt{s} = 14$ TeV, the $q\bar{q}$-contribution increases up to 30% at LQ masses of 2 TeV [68].

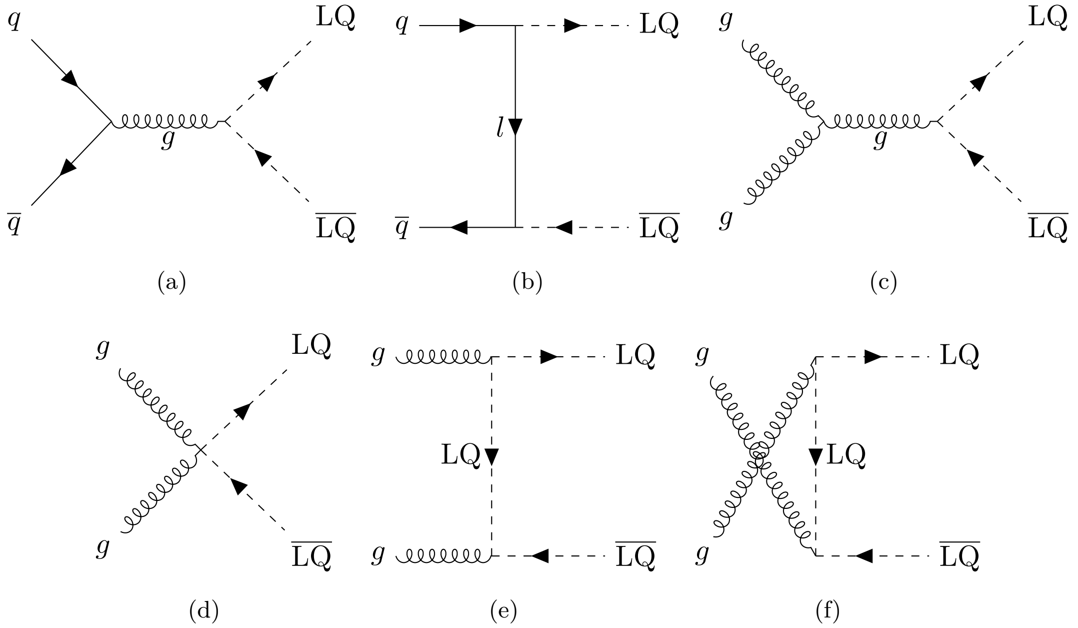

Figure 3.1: *Leading order Feynman diagrams for LQ pair production. Up to $\sim$ 1 TeV is gg fusion the dominant production mechanism at the LHC, while the $q\bar{q}$ annihilation production process becomes more important for higher LQ masses.*

The two important parameters which characterize the production and decay of scalar LQs are the mass of the LQ (m_{LQ}) and the Yukawa coupling ($\lambda_{\mathrm{LQ}\to lq}$). The coupling to a charged lepton and a quark can be parametrized as $\lambda_{\mathrm{LQ}\to lq} = \sqrt{\beta}\lambda$ (similarly the coupling to a neutrino and a quark can be parametrized as $\lambda_{\mathrm{LQ}\to \nu_l q} = \sqrt{1-\beta}\lambda$), where β represents the LQ decay branching ratio into a charged lepton and a quark. This parametrization can be used only if a model allows exactly two types of a LQ decay and in a limit of equal masses of the neutrino and the charged lepton. However, in contrast to the single LQ production, the pair production of LQs is largely insensitive to the value of the coupling. An illustration of a LQ−charged lepton−quark vertex is shown in Figure 3.2.

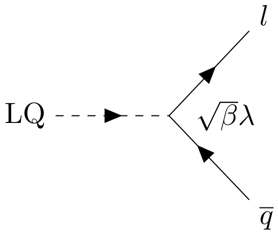

Figure 3.2: *Feynman diagram showing the Yukawa coupling* $\lambda_{LQ\to lq}$ *between a LQ, a lepton and a quark.* λ *is the coupling parameter of the model,* β *the branching fraction for the decay involving a charged lepton.*

The search for scalar LQs performed in this thesis relies on the minimal Buchmüller-Rückl-Wyler (mBRW) model [77]. This model defines that the interactions of the LQs with SM bosons rely only on SM interactions in the case of scalar LQs. The coupling between vector LQs and SM bosons is however more complicated, as it depends on trilinear and quartic couplings, which might require the introduction of anomalous couplings. The mBRW model postulates additional constraints on the LQ properties: the couplings have to be purely chiral and LQs have to be divided into three families (first, second and third generation), such that LQs couple to leptons and quarks only within the same generation. On this way the flavour-changing neutral currents (FCNC) [78] would be not possible, which are not have been observed anyway.

The mBRW model requires that the branching fraction $\beta = \mathrm{BR}\left(\mathrm{LQ} \to l^{\pm}\overset{(-)}{q}\right)$ can have one of the following values: 0, 1/2, 1. However, in most experimental searches, and also in this thesis, β is handled as a free parameter, for which the following Equation assumed to be true: $\mathrm{BR}\,(\mathrm{LQ} \to lq) + \mathrm{BR}\,(\mathrm{LQ} \to \nu_l q) = 1$ [79].

Previous searches for pair-produced LQs have been performed at LHC by the ATLAS Collaboration using $3.2\,\mathrm{fb}^{-1}$ of data collected at 13 TeV and the CMS Collaboration using $2.7\,\mathrm{fb}^{-1}$ of data collected at 13 TeV. The corresponding results will be mentioned in Chapter 6 as a motivation for the performed search, the discussion will be described in the Chapters thereafter.

Part II

Experimental apparatus

CHAPTER

4

THE LARGE HADRON COLLIDER

> “*That’s no moon. It’s a space station.*”
> OBI-WAN KENOBI FROM STAR WARS: EPISODE IV - A NEW HOPE

THE Large Hadron Collider (LHC) [80] is a particle accelerator which is located at CERN[1], the European Organization for Nuclear Research. Geographically it is located near Geneva in Switzerland. The main design goals for this accelerator are the search for and discovery of new physics beyond the Standard Model as well as precise measurement of the Standard Model parameters (including the discovery of the Higgs boson). This goals can be achieved by reaching high center of mass energies which make it possible to get an access to new phase space regions.

There are two types of beams the LHC can operate with: proton beams and heavy ion beams[2]. However, the majority of planned physics program is based on proton-proton collisions. Initially, it was foreseen that the energies can go up to 7 TeV per proton beam reaching luminosities up to $10^{34}\,\mathrm{cm}^{-2}\,\mathrm{s}^{-1}$. Today, the LHC counts as the particle collider, which can reach highest center of mass energy up to date.

This Chapter is mostly based on Reference [24]. Section 4.1 describes a short overview about the CERN accelerator complex. The key accelerator parameters during the 2015 and 2016 operation are discussed in Section 4.2. Finally, the experiments at the LHC are introduced in Section 4.3.

4.1 Accelerator complex

Before the protons are filled into the LHC, they have to be accelerated first. This is done by a chain of preaccelerators, which together with the LHC itself, is schematically shown in Figure 4.1. However, this Figure does not contain accelerators which are not count as a preaccelerator to the LHC. For every accelerator its maximum energy per beam, its circumference and the year of its initial-startup are shown. The production of protons is performed by ionizing hydrogen. After the production the protons are moved to a linear accelerator LINAC2, which marks the beginning of the accelerator chain and accelerates the protons in bunches. These proton bunches have a a length of 33 m and are accelerated to an energy of 50 MeV. Next destination of these bunches is a chain of circular accelerators: the Booster, the Proton Synchrotron (PS) and the Super Proton Synchrotron (SPS). In the end the proton bunches are filled with an energy of 450 GeV per proton into the LHC[3], where they are accelerated to energies up to 6.5 TeV[4].

---

[1] The acronym is derived from the name **C**onseil **e**uropéen pour la **r**echerche **n**ucléaire.

[2] Typically lead ions.

[3] The filling is performed in both directions: clockwise and counterclockwise.

[4] Energies up to 7 TeV have not been reached until December 2018, but they are planned for Run 3 of the LHC starting in year 2021.

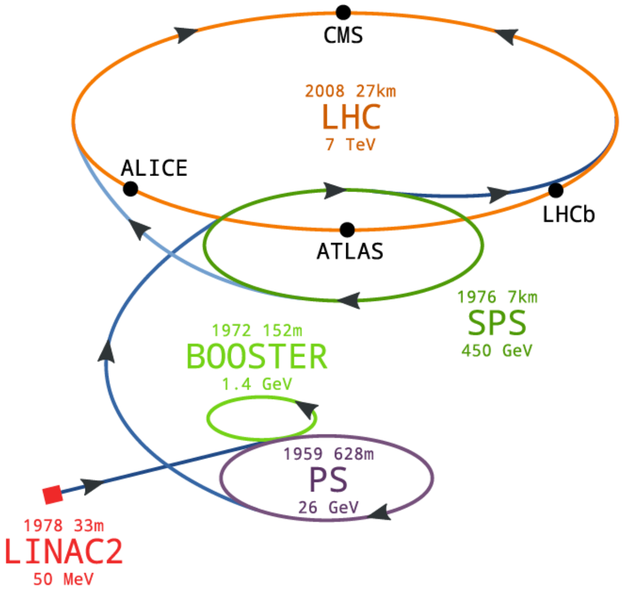

Figure 4.1: *Schematic view of accelerators and locations of experiments at LHC. Date of construction, circumference of rings or length of linear accelerator and maximum energy per beam are given [81].*

The LHC is located in an underground tunnel (up to 175 m under the surface), which is 27 km long. To be precise, the LHC utilizes the tunnel, which was initially build for the Large Electron Positron (LEP) collider. Each proton bunch is accelerated by eight superconduction radiofrequency cavities. In order to make sure that the proton bunches do not leave their circular trajectory 1232 superconducting dipole magnets are installed. These dipoles use niobium-titanium (NbTi) cables and are cooled down to a temperature of 1.9 K. The dipole magnets establish a strong magnetic field up to 8.3 T, which is pointing in opposite directions in the two beam pipes. This is essential for the proton movement, because they are accelerated in the two beam pipes in opposite directions as well. In order to focus the proton beams, a total of 392 quadrupole magnets are used. These proton beams keep moving in the two beam pipes until they are forced to collide at four interaction points.

4.2 LHC performance

One of the main collider parameters is its luminosity. From the instantaneous luminosity $\mathscr{L}$ and the cross section σ of the physics process its event rate R can be determined: $R = \mathscr{L} \cdot \sigma$. The instantaneous luminosity is described by following Equation:

$$\mathscr{L} = \frac{N_p^2 n_b f_r \gamma}{4\pi \epsilon_n \beta^*} F, \tag{4.1}$$

where N_p is the number of protons per bunch, n_b is the number of bunches per proton beam, f_r is the revolution frequency[5], γ is relativistic γ-factor, ϵ_n is the normalized transverse emittance, β^* is the value of the beta function at the interaction point and F is a luminosity reduction factor. The parameters ϵ_n and β^* are used in order to describe the brightness of the beam. F describes the effect of a finite crossing angle of the two beams, which appears at the interaction point. Since the amount of stored bunched is large and the bunch distance is small the beams have to be crossed resulting in an angle ϕ between the two beams. Otherwise the frontal collision would lead to many unwanted secondary collisions at the interaction point (both upstream and downstream of it), which in turn would have negative effects on the beam stability and the data

---

[5] It is about 11.2 kHz for the LHC.

quality. The dependencies of the parameter F are the finite crossing angle, the bunch length σ_s and the transverse beam sizes in the plane of crossing [26]. The parameter design values and their values obtained during the LHC operation in 2015 and 2016 are summarized in Table 4.1. The LHC was operated with the nominal bunch spacing of 25 ns on the regular basis for the first time during its operation in 2015. This makes it possible to fill up to 2244 proton bunches into the machine. The peak luminosities at the start of the fill[6] reached up to $5.0 \times 10^{33}\,\mathrm{cm}^{-2}\,\mathrm{s}^{-1}$ during 2015, which is about 50% of the design goal of the LHC, and about $1.4 \times 10^{34}\,\mathrm{cm}^{-2}\,\mathrm{s}^{-1}$ during 2016, a bit more than the designed value. In 2015 an emittance of $\epsilon_n = 3.5\,\mu\mathrm{m}$ and $\beta^* = 80\,\mathrm{cm}$ were achieved while these parameters decreased in 2016 to $\epsilon_n = 2.5\,\mu\mathrm{m}$ and $\beta^* = 40\,\mathrm{cm}$.

Year	E_{beam} [TeV]	N_p	n_b	ϵ_n [μm]	β^* [cm]	Bunch spacing [ns]	Peak luminosity [cm^{-2}s^{-1}]
2015	6.5	1.15×10^{11}	2244	3.5	80	25	5.0×10^{33}
2016	6.5	1.15×10^{11}	2220	2.0	40	25	1.4×10^{34}
Design	7	1.15×10^{11}	2808	3.75	55	25	1.0×10^{34}

Table 4.1: *LHC parameters during the 2015 [82] and 2016 [83] operation and their design values.*

For the experiments also the (time-) integrated luminosity $\mathcal{L} = \int \mathscr{L} dt$ is interesting to determine, as it represents a measure for the amount of data produced in a certain period of time. This luminosity is measured in inverse cross section units, for example in fb^{-1} [23]. Further details on luminosity measurement are given in Section 5.5.

4.3 Experiments at the LHC

Around the LHC ring four main experiments, also called detectors, are located in caverns. Two of them are the ATLAS[7] experiment [84] and the CMS[8] experiment [85], which have similar general goals: to be involved in a bright spectrum of the physics program available at the LHC. Two other detectors are the LHCb experiment [86] and the ALICE[9] experiment [87]. The LHCb experiment focusses on physical phenomena involving bottom quarks. The experiment was designed for lower luminosities of $2 \times 10^{32}\,\mathrm{cm}^{-2}\,\mathrm{s}^{-1}$ and therefore the proton beams are less focused at their interaction point for the experiment. The purpose of the ALICE experiment is to study heavy-ion collisions.

However, LHC has also other, smaller experiments to offer. The TOTEM[10] experiment [88] is located near to the CMS experiment, because its goal is to measure protons from elastic collisions which escape the CMS experiment. Another purpose of the TOTEM experiment is the LHC luminosity monitoring. There is also a detector which is located near to the ATLAS experiment (140 m away, to be precisely). Its name is the LHCf[11] experiment [89], and it was designed for a study of neutral pions in order to test air-shower Monte Carlo models, which are used for the simulation of cosmic rays interactions in the Earth atmosphere. Finally, there is the MoEDAL[12] experiment [90], which represents an extension of the LHCb experiment. Its usage covers for example the magnetic monopoles search.

---

[6] With progressing time the instantaneous luminosity is decreasing since the beam width is getting larger and the number of protons is decreasing due to the inelastic collisions.

[7] **A T**oroidal **L**HC **A**pparatu**S**

[8] **C**ompact **M**uon **S**olenoid

[9] **A L**arge **I**on **C**olliding **E**xperiment

[10] **TOT**al **E**lastic and Diffractive Cross Section **M**easurement

[11] **LHC f**orward

[12] **Mo**nopole and **E**xotics **D**etector **A**t the **L**HC

Chapter

5

The ATLAS experiment

> *There's always a bigger fish.*
> Qui-Gon Jinn from Star Wars: Episode I - The Phantom Menace

The ATLAS experiment [84] is one of the four large experiments at the LHC, which is built at one of the four interaction points. ATLAS is a multi-purpose detector since it was constructed in order to accomplish several tasks: precise measurements of many particles (electrons, photons, muons, and jets in large kinematic regions), searches for new particles and tests of the Standard Model. Different detector systems, which surround the beam axis, represent several layers of ATLAS detector. A visual overview of the ATLAS experiment is shown in Figure 5.1.

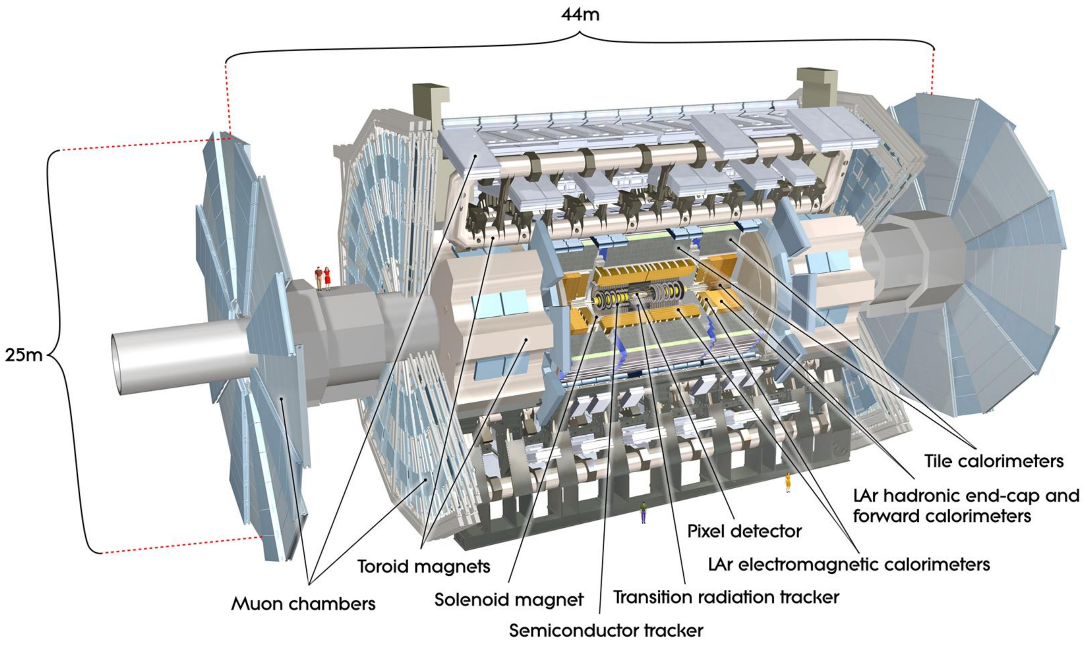

Figure 5.1: *A detailed computer-generated image of the ATLAS detector and its subsystems [91].*

This Chapter is based on References [24, 26]. The physical goals and required performance of the ATLAS experiment are summarized in Section 5.1. The coordinate system used in ATLAS and some commonly used kinematic variables are described in Section 5.2. A brief overview about the ATLAS experiment and its detector systems is given in Section 5.3. The multi-level trigger system and data acquisition system are addressed in Section 5.4. The luminosity estimation is described in Section 5.5. Detector simulation and description of the pile-up are addressed in

Sections 5.7 and 5.8, respectively. Finally, the particle identification of selected physical objects is described in Section 5.9.

5.1 Physical goals and required performance

ATLAS is built as a multi-purpose detector in order to answer as many physical questions as possible. To support this the design of the experiment takes into account several requirements with emphasis on some physical objectives [92]:

- **The Higgs sector**: the Higgs boson has many different decay channels leading to a large amount of different final states. However, due to the huge hadronic activity at the LHC, the most promising final states are the $H \to \gamma\gamma$ and $H \to ZZ^* \to 4l$ with small branching fraction but clear signature. The study of the diphoton channel presumes a very good photon identification, in particular a good particle rejection which fake photons such as π^0 (decaying to two collimated photons) in jets. Channels like $H \to b\bar{b}$ would be studied using VH associated production, where V means vector boson $W^\pm$ or Z. So, one of the desired requirements is a reliable b-tagging, which is correlated to a high precision secondary vertex reconstruction.

- **Supersymmetry**: in the most common models of Supersymmetry (SUSY) the events involving SUSY particles would contain a heavy weakly interacting particle which would leave behind some missing transverse energy in the event (similar signature in the event would have also a neutrino). In order to achieve a good resolution on missing transverse energy, good determination of the energy of all other objects is the next desired requirement.

- ***B* physics**: the B sector[1] is an important place in order to find matter-antimatter asymmetries, which could explain why matter appears to be more dominant as antimatter in the current state of the universe. In terms of desired requirements, a good vertex resolution is needed in order to identify displaced vertex due to the long B lifetime in B meson studies.

- **Other processes**: for example, exotic processes such as mini black hole and new heavy boson production or leptoquarks are expected to involve particles with energies up to the TeV scale. So, the desired requirements on the detector performance especially at the high energy range are high precision of the energy, momentum and position reconstruction.

From these desired requirements, some constraints on the detector design and required performances can be expressed:

- An efficient displaced vertex finding, like a precise track detector which is placed as close as possible to the interaction area;

- A good calorimeter system which should have the following specifications: a high granularity, which ensures the good separation between photons and jets, and a good energy resolution and optimal hermiticity, which ensure that no particle is missing that would create fake missing energy;

- An effective muon detector with precise track measurement in a large momentum range;

- The usage of radiation resistant materials, which is important due to the high luminosity.

These main requirements, combined with overall detector performance, lead to the final design of the ATLAS detector.

---

[1] The sector of particle physics involving among other things the study of the properties of B mesons, which consist of b quark and s quark.

5.2 Coordinate system and common kinematic variables

Before describing the details of the detector, an overview of its coordinate system is given and most common kinematic variables are introduced.

5.2.1 Coordinate system

The origin of the coordinate system is represented by the interaction point. The x axis points from the interaction point to the center of the LHC ring while the y axis points upwards and the z axis points along the beam line. The x-y plane, which is referred to as the „transverse plane“ in the following, is perpendicular to the beam line. However, it is more useful to introduce cylindrical coordinates since the ATLAS detector has a cylindrical design. The transverse plane is described in terms of r-ϕ coordinates where r measures the distance from the beam line and ϕ denotes the azimuthal angle measured from the x axis around the beam line. The polar angle θ, which is usually given in terms of the pseudo-rapidity η, is defined from the positive z axis. The pseudo-rapidity is based on the rapidity y which is defined for a particle with energy E and longitudinal momentum $p_z = |\boldsymbol{p}|\sin(\theta)$ along the beam as

$$y = \frac{1}{2}\ln\left(\frac{E + p_z}{E - p_z}\right). \tag{5.1}$$

The energy-momentum relation reduces for massless particles to $E = |\boldsymbol{p}|c = |\boldsymbol{p}|$ with $c = 1$. If the energies of particles produced in the collisions at the LHC are much larger than their rest energies, determined by their rest masses, the following relation can be used to approximate the pseudo-rapidity:

$$y \approx \eta = \frac{1}{2}\ln\left(\frac{|\boldsymbol{p}| + p_z}{|\boldsymbol{p}| - p_z}\right) = -\ln\left(\tan\left(\frac{\theta}{2}\right)\right). \tag{5.2}$$

The motivation for the usage of rapidity as well as the pseudo-rapidity at hadron colliders is driven by the fact that rapidity intervals Δy and differential cross sections $\frac{\mathrm{d}\sigma}{\mathrm{d}y}$ are Lorentz invariant under a boost along the beam direction. In addition, the particle density in inelastic proton-proton collisions is approximately constant when measured in equal rapidity intervals. The components of the ATLAS detector are typically segmented in such intervals for this reason. Figure 5.2 shows the coordinate system of the ATLAS detector with few values of the pseudo-rapidity η as an example.

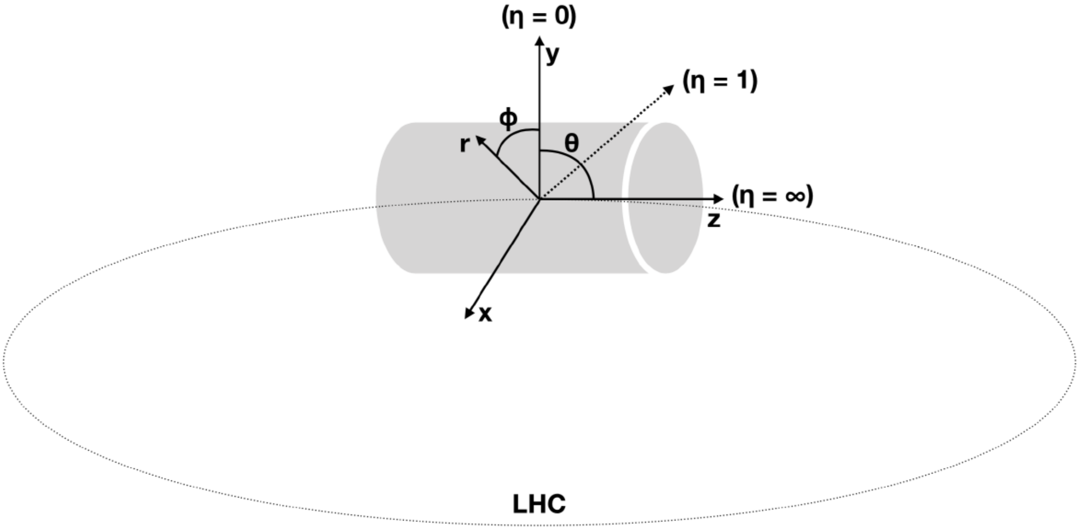

Figure 5.2: *Coordinate system of the ATLAS detector [26].*

5.2.2 Common kinematic variables

The rapidity y of a massive particle described in Equation 5.1 is already one of the common kinematic variables used in ATLAS analyses. Other common kinematic variables are the transverse momentum p_{T}, transverse energy E_{T} and the missing transverse energy $E_{\mathrm{T}}^{\mathrm{miss}}$. They are measured in the x-y plane. Transverse momentum is defined by

$$p_{\mathrm{T}} = \sqrt{p_x^2 + p_y^2}, \tag{5.3}$$

and transverse energy is defined by

$$E_{\mathrm{T}} = \sqrt{p_{\mathrm{T}}^2 + m^2}, \tag{5.4}$$

where m is the mass of the particle. Therefore p_{T} and E_{T} are equal for massless particles. The incoming partons within a proton have to first approximation only a momentum parallel to the beam axis. This leads to the fact that the vectorial sum of all momenta in the transverse plane has to be zero due to momentum conservation. The usage of this fact allows to indirectly measure particles, which leave the detector unseen (for example neutrinos). On this way the missing transverse momentum is defined as the negative vector sum of all reconstructed transverse momenta:

$$\vec{p}_{\mathrm{T}}^{\,\mathrm{miss}} = -\sum_i \vec{p}_{\mathrm{T},\,i}^{\,\mathrm{rec}}. \tag{5.5}$$

The missing transverse energy is then defined as $E_{\mathrm{T}}^{\mathrm{miss}} = |\vec{p}_{\mathrm{T}}^{\,\mathrm{miss}}|$. Another commonly used variable is the distance ΔR in the η-ϕ plane:

$$\Delta R = \sqrt{\Delta\eta^2 + \Delta\phi^2}. \tag{5.6}$$

5.3 The detector

5.3.1 The tracking system

The tracking system of ATLAS is the Inner Detector (ID) [93], which is the closest detector to the beam axis. It consists of three subsystems: the Pixel Detector, the Semiconductor Tracker (SCT) and the Transition Radiation Tracker (TRT), and has a coverage up to $|\eta| = 2.5$. The transverse momentum of charged particles could be measured thanks to a solenoidal magnetic field of 2 T. Further designed purposes of the ID are measurements of vertices and identification of the electrons. The superconducting solenoid [94] has a length of 5.3 m and a diameter of 2.5 m. A momentum resolution of $\Delta p_{\mathrm{T}}/p_{\mathrm{T}} = 0.05\%\ p_{\mathrm{T}}[\mathrm{GeV}] \oplus 1\%$ can be reached with the mentioned solenoidal magnetic field and the components of ID. Figure 5.3 shows the ID with its three parts which will be discussed in the following in more detail.

The Pixel Detector

The Pixel Detector [97] is the innermost part of the ID, which has a coverage of $|\eta| < 2.5$. Furthermore, it is one of the two precision tracker detectors. Three layers of silicon pixel modules are cylindrically mounted around the beam axis in the central region. However, in the endcap region three discs are mounted differently: perpendicularly to the beam axis. The Pixel Detector has several purposes: to measure particle tracks with a very high resolution and to reconstruct the interaction point (primary vertex[2]) and secondary vertices from the decay of long-lived particles. Before 2012 b-layer was the innermost layer of the Pixel Detector. This

---

[2] The vertex with the highest $\sum p_{\mathrm{T}}^2$.

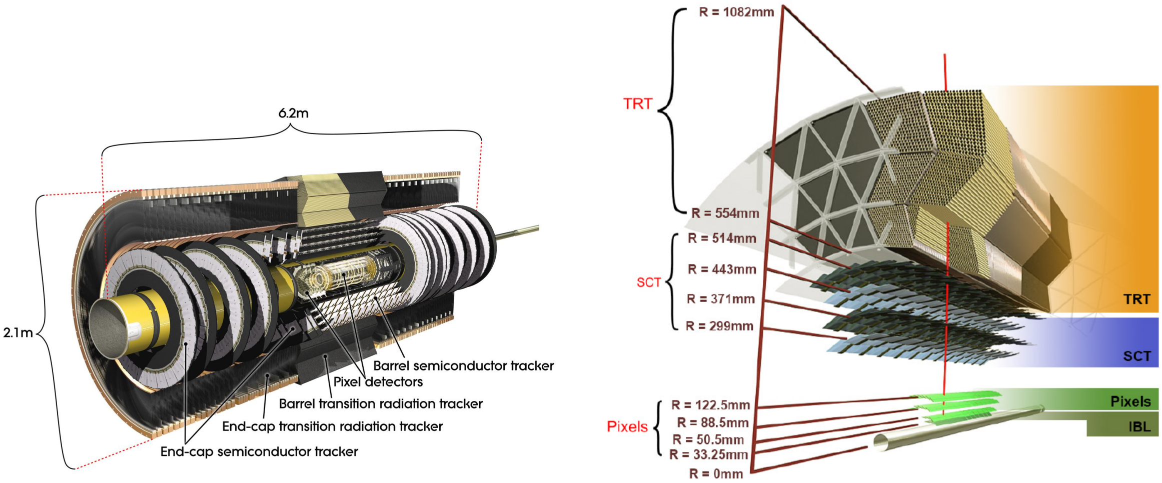

(a) (b)

Figure 5.3: *Schematic view of (a) the ATLAS Inner Detector [95], with (b) a detailed layout of the Inner Detector including the new Insertable b-layer (IBL) [96].*

layer was important due to its role for the reconstruction of the secondary vertices of decaying B-hadrons. The dimensions of the pixel modules are $50 \times 400\,\mu\text{m}^2$. The position resolution is $10\,\mu\text{m}$ in the R-ϕ plane and $115\,\mu\text{m}$ in z (R) for the central (endcap) region. In total there are around 80.4 million readout channels needed in order to keep fine granularity.

After the 2012 data taking a fourth pixel layer, the so-called Insertable b-layer (IBL) [98] was installed between the beam pipe and the Pixel Detector during the two year long LHC shutdown (LS1) in order to improve the reconstruction of secondary vertices. The more precisely position of IBL is 33.25 mm away from the beam axis. The pixel modules of the IBL have a size of $50 \times 250\,\mu\text{m}^2$, which is smaller than the size of the other layers.

The SCT-Detector

The SCT-Detector is the middle part of the ID, which like the Pixel Detector has a coverage of $|\eta| < 2.5$. It is a silicon microstrip detector and is installed in a distance of 299 mm to 514 mm from the beam axis. Eight strip layers are installed in the central region. They are connected to four layers of 40 mrad stereo strips in order to allow the measurement of the R-ϕ coordinate. Nine discs on each side are installed in the endcap region. Each of them uses two radial layers of strips. The idea behind the design of the SCT is that each particle within the coverage of the SCT travels through all four double layers. The spatial resolution of the SCT is $17\,\mu\text{m}$ in the R-ϕ plane and $580\,\mu\text{m}$ in the z (R) for the central (endcap) region. The total number of readout channels in the SCT is approximately 6.3 million.

The TRT-Detector

The TRT-Detector is the outer part of the ID, which has a coverage up to $|\eta| = 2.0$. It consists of straw tubes with a diameter of 4 mm. In the central region these straw tubes are 144 cm long and located parallel to the beam axis. However, in the endcap region they are 37 cm long and located radially in wheels. The TRT allows to get R-ϕ information in order to determine the transverse momentum with an accuracy of $130\,\mu\text{m}$. The straw tubes are filled with a xenon based gas mixture. The transition radiation material, which is located between the tubes, is different for different regions: polypropylene fibres in barrel region and polypropylene foils in endcap region. If charged particles traverse this medium, transition radiation is emitted then by this material.

The intensity of the transition radiation is proportional to the Lorentz factor $\gamma = E/m$. For the electrons, which have $m \approx 0$, the transition radiation at high energies is located above a characteristic threshold. However, for heavy objects like hadrons the transition intensity is much lower. Therefore the transition radiation can be used for the electron identification. The TRT has approximately 351000 readout channels in total.

The TRT is an important component for the momentum measurement because compared to the silicon detectors the larger track length and the high number of hits compensate for the lower precision per point.

5.3.2 The calorimeter system

The calorimeter system provides the measurement of the particle energy based on its shower. There are two basic types of showers: the shower that develops in the electromagnetic calorimeter and the hadronic shower. Incoming electrons or photons are responsible for the electromagnetic shower formation. They start to evolve in the passive material and divide their energy between daughter-particles. These daughter particles are different for different incoming particles: a radiated photon (Bremsstrahlung) and an electron for an incoming electron, and an electron and a positron due to pair production for an incoming photon. The electromagnetic shower keeps evolving up to the point where the daughter-particles are stopped through ionization. The decrease of the initial energy E_0 of an incoming electron with distance x is given by $E(x) = E_0 e^{-x/X_0}$, where X_0 is the material dependent radiation length. The evolution of hadronic shower is different. Hadronic showers are produced by hadrons and are dominated by subsequently inelastic hadronic interactions via the strong force. The length of a hadronic shower is expressed via a characteristic quantity λ, which is the absorption length.

The calorimeter system consists of two different parts: the electromagnetic (EM) calorimeter and the hadronic calorimeter. Hadronic showers are typically longer and broader, and need more time to develop compared to the EM shower detected with an EM calorimeter. For this reason the hadronic calorimeter is installed behind the EM calorimeter. As EM calorimeter a liquid argon (LAr) sampling-calorimeter is used covering the range up to $|\eta| < 3.2$. As hadronic calorimeter a scintillator tile calorimeter is used, which has a coverage of $|\eta| < 1.7$. The hadronic endcap calorimeters, which use LAr technology as well, have a coverage of $1.5 < |\eta| < 3.2$. Finally, there is the LAr forward calorimeter, which has a coverage of $3.1 < |\eta| < 4.9$ and is used for measuring both, EM and hadronic objects. Figure 5.4 shows the whole calorimeter system with its ingredients which will be discussed in the following in more detail.

The electromagnetic calorimeter

For the ATLAS EM calorimeter [100], lead (Pb) is used in the region $|\eta| < 3.2$ as an absorber medium and LAr as an active medium. The accordion geometry is used for the installment of the electrodes, which measure the energy deposited in the Pb absorbers and the LAr. This geometry allows to establish the complete and uniform coverage in ϕ. In order to select the optimal energy resolution, the absorber plates are differently thick for different η [101]. The EM calorimeter consists of four different regions. First, there is barrel calorimeter, which is the central part covering the range up to $|\eta| = 1.475$. Its thickness amounts to at least 22 X_0. Each half-barrel consists of 16 modules, each covering an angle of $\Delta\phi = 22.5°$. Then, there is the endcap calorimeter, which covers the range of $1.375 < |\eta| < 3.2$. It subsequently consists of 16 modules for two wheels: the „outer wheel“ $1.375 < |\eta| < 2.5$ and the „inner wheel“ $2.5 < |\eta| < 3.2$. Finally, there is the forward calorimeter, which is also used for the measurement of hadrons. It covers the range of $3.1 < |\eta| < 4.9$.

In the range where it is intended to perform precision measurements in the calorimeter ($|\eta| < 2.5$) the latter is divided into three layers. In front of the first layer, there is a so-called presampler

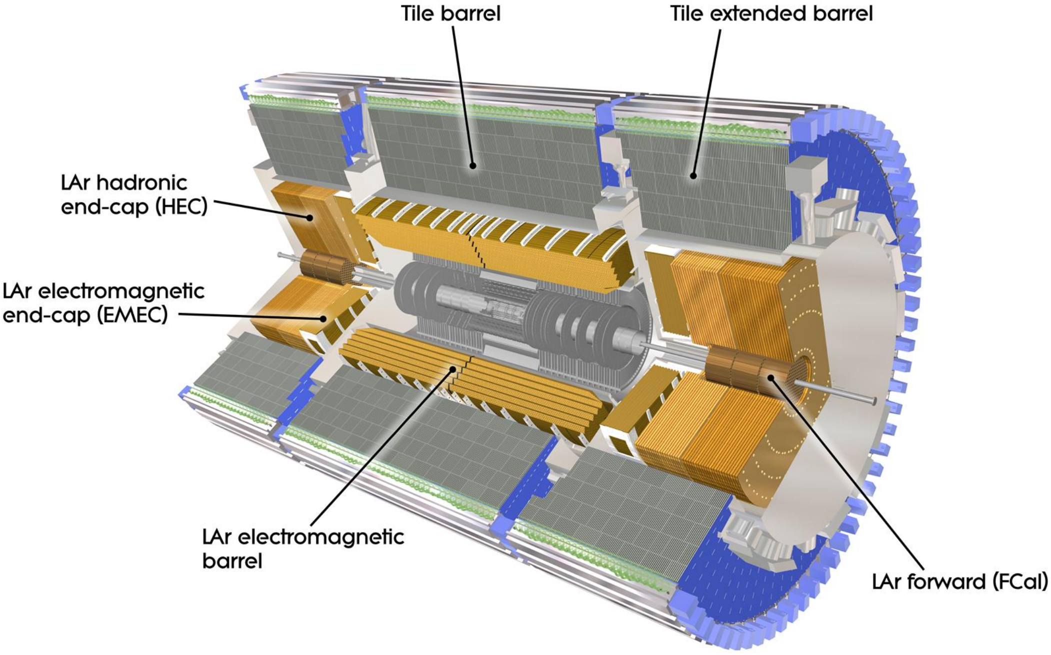

Figure 5.4: *A computer generated image of the full calorimenter [99].*

which is a 11 mm thick layer of LAr in the range $|\eta| < 1.8$. Its main purpose is the estimation of the energy loss in front of the calorimeter. The first layer has a granularity of 0.0031×0.0982 in $\eta \times \phi$. Since the cells have fine segmentation in η they are also called „strips“. They establish better differentiation of particles which enter the calorimeter, for example two photons from a π_0 decay. The second layer has a more coarse granularity of 0.025×0.0245 in $\eta \times \phi$. Due to its thickness of 16 X_0 this layer is supposed to measure the main part of the energy. The third layer has again a much coarser granularity. Its purpose is the correction for the overlap of the energy deposition in the following hadronic calorimeter. Overall, a barrel module consists of 3424 readout cells and a module in the endcap of roughly 4000 readout cells, including the presampler cells. The total number of EM calorimeter channels is around 160000.

The relative energy resolution in the EM calorimeter can be parametrized as followed [102]:

$$\frac{\Delta E}{E} = \frac{a}{\sqrt{E}} \oplus \frac{b}{E} \oplus c, \tag{5.7}$$

where a is the sampling term, b is the noise term and c is the constant term. These three terms are η-dependent parameters. At low $|\eta|$ the sampling term is set to its design value which is about $10\%/\sqrt{E\,[\mathrm{GeV}]}$. At large $|\eta|$ it is expected to worsen due to increase of the amount of material in front of the calorimeter. Assuming the mean number of interactions per bunch crossing of $\langle\mu\rangle = 20$, the noise term for a typical cluster in the barrel calorimeter is about $350 \times \cosh(\eta)$ MeV. However, it is dominated by the pile-up noise at high $|\eta|$. Going further to the higher energies the sampling term and the noise term become not much significant. In this case the relative energy resolution tends asymptotically to the constant term c, which has a design value of 0.7%. The origin of this term is coming from the calibration of the calorimeter.

The hadronic calorimeter

Three different hadronic calorimeters are included in ATLAS detector depending on the respective detector region.

In the central region the tile calorimeter [103] is installed, which consists of a central barrel covering the range up to $|\eta| = 1.0$ and the extended barrel covering the range $0.8 < |\eta| < 1.7$. The tile calorimeter is also a sampling calorimeter like the EM calorimeter. However, iron is used as an absorber (instead of lead) and scintillating tiles as active material. The barrel and extended barrels are separated azimuthally into 64 modules. The tile calorimeter is divided into several layers with some interaction lenghts λ: in the barrel region there are three layers with approximately 1.5, 4.1 and 1.8 λ, and in the extended barrel region layers with 1.5, 2.6 and 3.3 λ. The readout is performed by photomultipliers which are mounted on wavelength shifting fibers. The latter are build on both sides of the detector.

In the endcaps a LAr calorimeter is used as hadronic calorimeter, which has a coverage of $1.5 < |\eta| < 3.2$. It is located behind the EM endcap calorimeter and uses the same cryostats in order to keep LAr to be cool. The relative energy resolution of the hadronic tile and endcap calorimeter can be expressed as:

$$\frac{\Delta E}{E} = \frac{50\%}{\sqrt{E\,[\mathrm{GeV}]}} \oplus 3\%. \tag{5.8}$$

At the end of the hadronic calorimeter the forward calorimeter [104] is installed, which has a coverage of $3.1 < |\eta| < 4.9$. The forward calorimeter is integrated in the endcap cryostats, consists of three modules in each endcap and is approximately 10 interaction lengths deep. The first module, which is optimized for EM measurements, is made of copper. However, the other two are made of tungsten and predominantly measure the energy of hadronic interactions. The relative energy resolution of the forward calorimeter can be expressed as:

$$\frac{\Delta E}{E} = \frac{100\%}{\sqrt{E\,[\mathrm{GeV}]}} \oplus 10\%. \tag{5.9}$$

5.3.3 The muon system

Muons are special particles since only they can travel through the calorimeters unstopped but still detected. During their journey through the calorimeters they only deposit a small amount of energy (typically about 3 GeV). In order to measure and identify the muons a system of trigger and high-precision tracking chambers [105] is developed. The location of this system is given outside of the calorimeters. For the measurement of the muon momentum the magnetic deflection of the muon tracks is used in the large superconducting air-core toroid magnets [106]. In the region $|\eta| < 1.4$, magnetic bending is provided by the large barrel toroid [107]. It can achieve a bending power of 1.5 Tm (Tesla meter) to 5.5 Tm. In the region $1.6 < |\eta| < 2.7$, the tracks are bent by two smaller endcap magnets [108] which are inserted into both ends of the barrel toroid. The bending power of approximately 1.0 Tm to 7.5 Tm can be achieved here. All three magnets consists of eight coils each. In the transition region $1.4 < |\eta| < 1.6$, a combination of barrel and endcap fields is responsible for magnetic deflection. However, the bending power is reduced in this region. The magnetic field is orthogonal to the muon trajectories in most cases.

Figure 5.5 shows the whole muon system with its components, which are a toroid system, divided into a long barrel and two inserted endcap magnets, and tracking chambers. The toroid system, which has an air-core, generates a strong magnetic field with strong bending power in a large volume within a light and open structure. There exist three layers of tracking chambers, which cover the range up to $|\eta| = 2.7$. Furthermore, they also define the overall dimension of the ATLAS experiment. Trigger chambers, which cover a range up to $|\eta| = 2.4$, are also a part of the muon system.

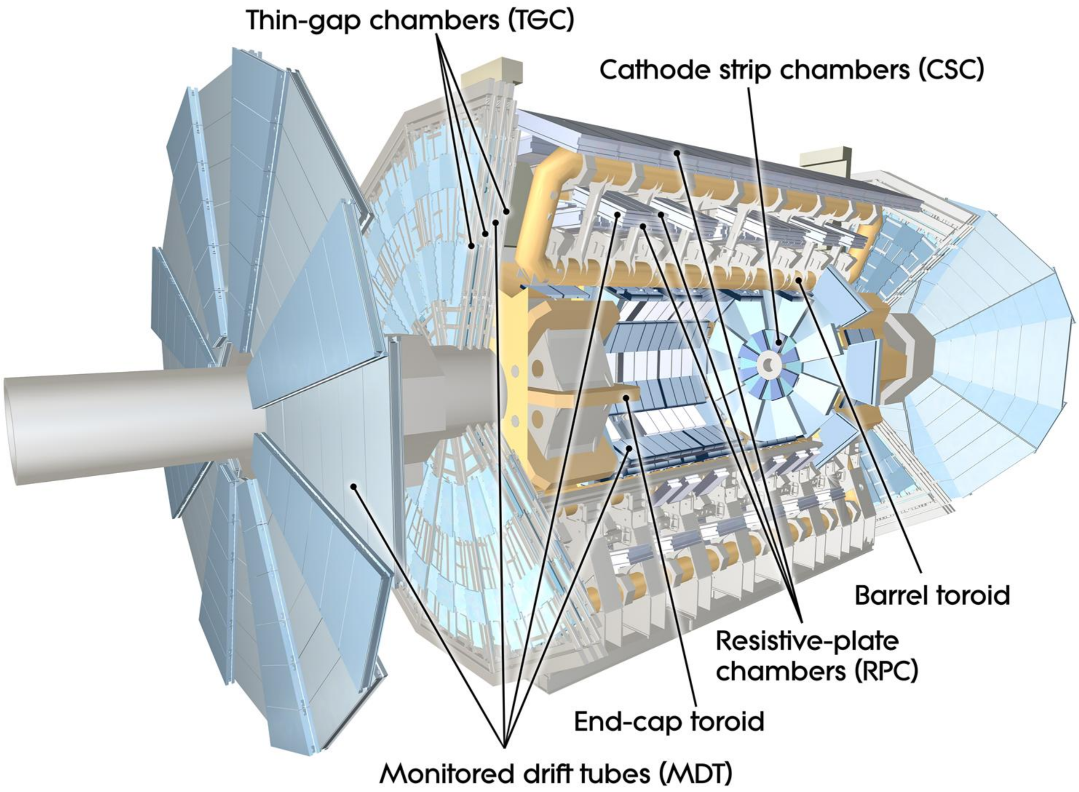

Figure 5.5: *Overview of the ATLAS muon spectrometer components [109].*

MDT and CSC

The goal of the precision-tracking chambers is the precise determination of the muon track in the bending plane. The Monitored Drift Tube (MDT) chambers are responsible for the precise measurement of the η position which make it possible to precisely determine the muon momentum. These chambers are placed in three layers between and on the eight coils of the superconduction barrel toroid magnet. The first layer has a coverage of $|\eta| < 2.0$, while the second and the third layer cover the range $|\eta| < 2.7$. However, there has been left a gap in the center of the detector ($|\eta| \approx 0$) in order to make the services possible to the solenoid magnet, the calorimeters and the ID. The MDT chambers consist of three to eight layers of drift tubes that reach an average resolution of 80 µm per tube and about 35 µm per chamber.

Cathode-Strip Chambers (CSC) are placed in the innermost layer covering the range $2.0 < |\eta| < 2.7$. The CSC are multiware proportional chambers where cathode planes are divided into strips in orthogonal directions. They have a higher rate capability and a time resolution of 7 ns, where the latter makes it possible to measure both coordinates. The measurement of the ϕ coordinate is done from the time which the induced charges need to drift to the cathode. In the bending plane the resolution of a CSC is 40 µm, while in the transverse plane it is about 5 mm.

A muon transverse momentum resolution of $\Delta p_{\mathrm{T}}/p_{\mathrm{T}} = 10\%$ at $p_{\mathrm{T}} = 1$ TeV can be reached using the precision tracking chambers. Further benefit for the momentum resolution is coming from the open structure of the air-core toroid magnet which reduces multiple-scattering effects.

RPC and TGC

In order to trigger on muons special fast muon chambers are built in, which can sent signals about 15 ns − 25 ns after the passage of a particle and therefore make it possible to tag the beam-crossing. These chambers measure both coordinates of the track, one in the bending plane (η)

and one in the non-bending plane (ϕ). On this way the trigger chambers give additional ϕ information on the muon tracks. In the barrel region ($|\eta| < 1.05$) Resistive Plate Chambers (RPC) are installed, which have a resolution of about 10 mm in both the bending and the non-bending plane. In the endcap region ($1.05 < |\eta| < 2.4$) Thin Gap Chambers (TGC) are installed, which give muon track information with a precision of $2\,\text{mm} - 7\,\text{mm}$ in the η coordinate and $3\,\text{mm} - 7\,\text{mm}$ in the ϕ coordinate.

5.4 Triggers and data acquisition

The LHC delivers a bunch-crossing rate of about 40 MHz, which results in the fact, that the raw data stream of the ATLAS detector become huge. This makes it impossible to store the entire raw data. Furthermore, cross sections of the most of the interesting physical processes are several orders of magnitude smaller than the inelastic proton-proton cross section. As a result, the design of a trigger system was proposed and fulfilled in order to filter out events with these interesting processes. Many physical objects like electrons, photons, muons, hadronically decaying τ leptons, jets and missing transverse momentum represent a base for the ATLAS trigger system. An interesting process is indicated as soon as these mentioned objects pass a certain threshold in transverse momentum p_{T}. However, weakly interacting particles, like neutrinos, can be triggered via missing transverse momentum. There are two stages of the trigger system of the ATLAS detector: the Level-1 trigger (L1) [110] and the High Level Trigger (HLT) [111]. Furthermore, there is the data acquisition (DAQ) system, which purpose is to manage the data streams from the trigger system up to the data storage of the accepted events. A schematic connection of the L1 trigger, the HLT and the DAQ system can be seen in Figure 5.6 and will be discussed in the following.

5.4.1 The trigger system

Level-1 trigger

The L1 trigger is a hardware-based system, which uses custom electronics in order to process the signals recorded in the ATLAS detector. This system consists of the three components: L1 Calo, L1 Muon and Central Trigger.

The L1 Calo has a cluster processor which identifies the following physical objects: electron, photon, hadron and tau candidates. The transverse momenta of these candidates can be discriminated against different thresholds. The transverse momenta of jet candidates, which are identified by a jet/energy processor, can be similarly discriminated by this processor against different thresholds as well. An additional task of the jet/energy processor is the evaluation of global energy sums like the missing transverse energy. The information about the identified candidates is sent to the Central Trigger.

One of the tasks of the L1 Muon is to check if there are hit coincidences within a track in different stations of the muon spectrometer and to identify muon candidates. Furthermore, the transverse momenta of the muon candidates can be discriminated by L1 Calo against different thresholds. Finally, L1 Calo is also responsible for sending the information to the Central Trigger.

The Central Trigger includes a trigger menu which is a set of triggers with different requirements on the events. It collects the information from L1 Calo and L1 Muon and based on this information it creates an L1 Accept signal which is a logical „or“ of all triggers from this trigger menu. The decision time, which L1 trigger has for the L1 Accept signal, amounts to 2.5 µs. This is the time duration for which the Front-End Electronics (FE) of the sub-detectors are keeping all the event data in their memory. The data is transferred then to the Read Out System (ROS), but only if the L1 trigger accepts the event. Furthermore, the L1 trigger also builds a Region

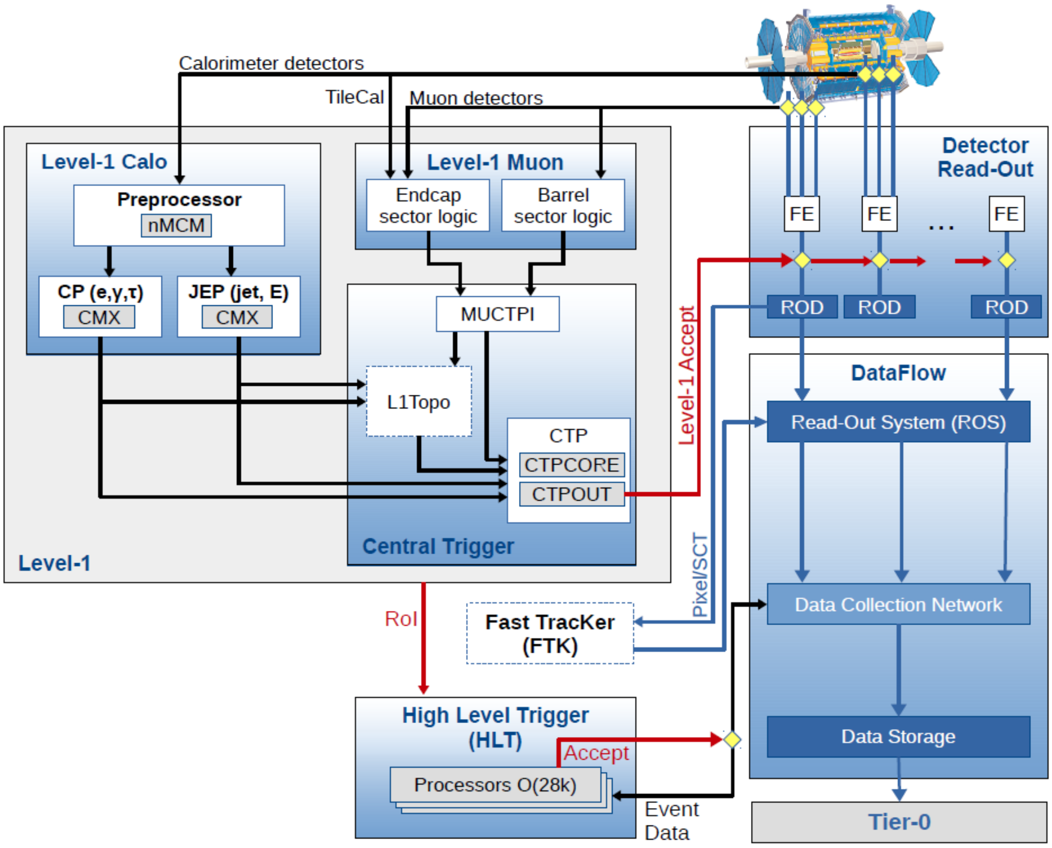

Figure 5.6: *Schematic view of the ATLAS trigger system [112]. L1Topo and FTK are not included for the data used in the analysis presented in this thesis since they were being commissioned.*

Of Interest (ROI). ROI is based on the η and ϕ coordinates of the objects which caused the L1 Accept signal and on the trigger. At the end the LHC bunch-crossing rate is reduced by the L1 trigger from about 40 MHz to about 75 kHz. ROIs defined by L1 trigger are sent to the HLT.

During the LS1, the L1 Topo as an additional system was installed. It is located between the L1 Calo and L1 Muon systems and the Central Trigger. L1 Topo can combine information from the L1 Calo and L1 Muon systems and compute more complex quantities like angular variables and invariant masses. The additional information, which is based on these complex quantities, is used for the trigger decision as well after sending it to the Central Trigger.

High Level Trigger

The HLT is a software-based system, which uses sophisticated selection algorithms. These software algorithms are able to reject the event at any stage in the decision process. If this happens, the event data, which was previously stored in the Data Collection Network, is deleted. There are two stages of the event data procession with the HLT. At a first stage the HLT makes a request about event data from the Data Collection Network identified from the ROI. Compared to the L1 trigger, the HLT uses the full granularity detector information in the ROI and reach therefore the highest precision. Additionally the gained information from the tracking detectors is used. If the signal is accepted at this stage, a second stage occurs, which reconstructs the full event with all gained detector information. Finally, after the full reconstruction of the event, it reaches a mean size of around 1.6 MB and is sent to the Data Storage. Overall, the HLT has a processing time of about 200 ms for its decision. The L1 rate is reduced further to about 200 Hz by the HLT.

5.4.2 Data acquisition and processing

Data acquisition

While the trigger is busy with making its decisions all information of the detector has to be stored for that time. Since it is still possible that the triggers decision will be positive all signals of the detector components are digitized, buffered and ready for possibly further procession. Each detector component has an on-detector buffer pipeline, which makes it possible to buffer the data during the L1 trigger decision. In case of acceptance of the event by the L1 trigger, the data from the pipelines are transferred off the detector via 1574 readout links. The signals are digitized and transferred to the DAQ system. The readout system is the first stage of the DAQ system and stores the data temporarily in local buffers where it can be read by the HLT in order to build further decisions and reconstruct the event. The complete event is stored, after a positive HLT decision, in a so-called RAW format on magnetic tapes in the CERN computer center.

The ATLAS data taking is steered by the RunControl (RC) system [113], which communicates with all the different detector components described before. The requirements for the start of data taking are the readiness of all parts of the ATLAS detector and declaration of stable beams by LHC. Each run receives its own unique run number. One data taking run usually correlates with a single fill of the LHC. Therefore one data taking run can last a couple of hours up to a day. However, these runs are separated further into luminosity blocks, which correspond to a data taking time of approximately a minute. The instantaneous luminosity is approximately constant in these luminosity blocks, which can be flagged at a later time point indicating if a problem with one of the subsystems occured. If there is no problem and all detector parts of the ATLAS experiment that are important for physical analyses are normal running, then the luminosity blocks are listed in the so-called Good Run Lists. The runs in which the LHC delivered stable conditions are grouped in periods, which are labeled alphabetically and typically have a length of days up to weeks.

Data processing

The further processing and reprocessing of the data occurs in the LHC Computing Grid [114, 115], which is a network of many worldwide computer clusters organized in several levels, so-called Tiers. The first Tier, Tier-0, is responsible for the application of reconstruction algorithms and calibrations to the data. A data format called Event Summary Data (ESD) was developed in order to store the information which results from the transformation of the whole information on detector level into information on object level. Further step for these ESD is their distribution to the Tier-1 centers, which are placed around the globe. These centers are responsible for several tasks. They provide storage space for the data, offer additional processing power, like for recalibration of the data, and distribute a copy of the new data among the Tier-1 centers. However, ESD contain to much information since some of them is not important for the physics analysis. Therefore, the Analysis Object Data (AOD) are derived from the ESD, which only contain information about specific physical objects which are necessary for the analysis, like electrons, photons, muons or jets. The usage of the Tier-2 clusters is mainly limited to Monte-Carlo production, but they also offer processing power for physics analysis.

Most particle physicists prefer to use the program ROOT [116] for the final analysis step[3]. Therefore, the AOD were modified in order to be readable by ROOT. On this way the new format was developed, called xAOD. In order to reduce the physical size of data even further,

---

[3] ROOT is a statistical analysis framework which is also used in this analysis. It offer the possibility of data analysis and has various possibilities to visualize data in histograms. All shown histograms in this thesis were produced using ROOT.

each analysis defines an analysis specific preselection which is applied to the xAOD. Furthermore, the information for an event itself is reduced to the information necessary for the analysis. The resulting preselected data format is called derived xAOD (DAOD)[4]. These DAOD are usually stored at the Tier-3 clusters, such as the *mainzgrid*[5] which is part of the computing cluster *mogon* [117], where the physics analyses are locally performed.

5.5 Luminosity measurement

The luminosity can be determined for a pp collider by

$$\mathscr{L} = \frac{R_{\text{inel}}}{\sigma_{\text{inel}}}, \tag{5.10}$$

where R_{inel} is the rate of inelastic collisions and σ_{inel} is the pp inelastic cross section. The luminosity can be further rewritten for a storage ring operating at a revolution frequency f_r and with n_b bunch pairs colliding per revolution:

$$\mathscr{L} = \frac{\mu n_b f_r}{\sigma_{\text{inel}}}, \tag{5.11}$$

where μ is the number of average inelastic interactions per bunch crossing. In order to measure the luminosity within ATLAS and as well as special detectors like LUCID [118] or ALFA [119] there exist several methods and algorithms, which are based on the measurement of σ_{inel}. However, when using different detectors and algorithms, a correction with the efficiency and acceptance of the detector and algorithm has to be applied for the measured μ_{meas} in order to obtain $\mu = \mu_{\text{meas}}/\epsilon$. Using similar consideration σ_{meas} is corrected to $\sigma = \sigma_{\text{meas}}/\epsilon$.

Equation 4.1 can be rewritten as

$$\mathscr{L} = \frac{n_b f_r N_1 N_2}{2\pi \sum_x \sum_y}, \tag{5.12}$$

where N_1 (N_2) is the number of protons in beam one (two) and $\sum_x$ and $\sum_y$ characterizes the horizontal and vertical convolved beam width. The combination of Equations 5.11 and 5.12 leads to:

$$\sigma_{\text{meas}} = \mu_{\text{meas}} \frac{2\pi \sum_x \sum_y}{N_1 N_2}. \tag{5.13}$$

Since μ is an experimentally observable quantity, the calibration of the luminosity scale for a particular detector and algorithm is equivalent to determining the cross section σ_{meas}. The beam-separation scans, also known as van der Meer (vdM) scans [120] are used for the calibration of the luminosity detectors to the inelastic cross section σ_{inel}. In such a scan, the beams are divided in steps of known distances. The measurement of μ_{meas} during a vdM scan as a function of the beam separation in x or y results in a Gaussian distribution with a width of $\sum_x$ or $\sum_y$. Then, the extraction of the parameters by a fit can be performed. The product $N_1 N_2$ is provided by the LHC group, which determines this product by beam current measurements. A more detailed description of the algorithms and sub-detectors used for luminosity determination can be found in Reference [118].

The systematic uncertainty for the determination, which is obtained by comparing the results from the different sub-detectors and methods, is for the used 2015-2016 combined data set 2.1% [121].

---

[4] For the leptoquark search different DAOD formats were used:
DAOD_EXOT19 for fake electron background,
DAOD_EXOT9 for analysis in $t\bar{t}$ control region,
DAOD_EXOT12 for everything else.

[5] In 2018 *mainzgrid* was replaced with *mainz*.

5.6 Detector performance during Run 2

Although the data taking conditions are hard, ATLAS still managed to record a large fraction of the delivered luminosity. Some of the recorded events have to be dropped for physics analysis for example due to temporarily defects in sub-detector. At the end, 87.1% (93%-95%) of the events recorded in 2015 (2016) are used for physics analyses. The losses broken down by sub-system are summarized in Reference [122]. The lowest (93.5%) luminosity weighted relative detector uptime and good data quality efficiency in 2015 is assigned to the pixel detector, while the detector performance in 2016 was better, leading to the efficiency of 97.2% by toroid magnets as the lowest one compared to the other sub-systems.

5.7 Detector simulation

In Section 2.3 the simulation of *pp* collisions has been described. However, the simulation of the detector and the response of the detector to the physical event have to be simulated separately in order to compare the simulation with data. For this purpose a software is needed which can simulate the response of the detector components when the final state particles of the *pp* collisions enter the detector. The ATLAS detector is simulated using the toolkit GEANT4 [123]. This simulation represent a detailed model of the whole detector including materials, geometry and the magnetic fields. Furthermore, the interaction of the particles with the detector (for example Bremsstrahlung or particles in an EM or hadronic shower) is included in this simulation as well. The simulation includes also the response of the detector components (also containing the electronics of the readout system) to the energy depositions. Lastly, there are several details taken into account as well, like pile-up effects, or known problems with some readout modules or defective components of the detector, which correspond to the state of the detector during data taking. The combination of the event simulation and the detector simulation is a full simulation of the expectation of the physical process from the collision of two protons provided by the LHC up to the electronical signals read out by the ATLAS detector. The information of each such a full simulation is divided into two levels: the *truth level* which represents the state of the simulation when the final state particles have been produced and the *reconstruction level* which represents the state when the particles have been reconstructed by the ATLAS detector. Since the simulation of one event can take up to several minutes it is not a surprise, that such a detailed simulation of an event in the detector can be a very time and power consuming task. Therefore, in order to provide simulation samples with sufficient statistics several fast simulation programs have been developed. They use a simplified detector geometry either in the ID or the calorimeter or both and reduce on this way a lot of computing time [23].

5.8 Pile-up

The LHC provides the *pp* collisions in intervals of 25 ns. However, since many detector components have sensitivity windows larger than 25 ns the correct detection of all *pp* collisions serves as a big challenge for the ATLAS detector. Furthermore, each collision of two proton bunches provides several *pp* collisions in one crossing of two proton bunches. These two facts are the reasons for the effects of pile-up. The categorization of these effects can be performed based on Reference [124] as following:

- **In-time pile-up**
  In-time pile-up are additional *pp* collisions which appear in the same crossing of two proton bunches. This effect represent a significant background for all physical objects in the detector. In the data taking period from 2015 (2016) an average of around 14 (25) *pp* collisions took place in each crossing of two proton bunches [125]. The numbers are different

for different years because the LHC operated at higher instantaneous luminosity in the 2016 data taking period.

- **Out-of-time pile-up**
  Out-of-time pile-up are additional *pp* collisions which appear in the crossings of two proton bunches before or after the bunch crossing with the *pp* collision of interest. However, the detector technology plays also a non-significant role here. For example, the LAr calorimeter is sensitive to around 250 ns after the collision of interest and many bunch crossings before which can result in reduced total pulse heights.

For the simulation of both pile-up effects it is important to be as close as possible to reality. For this reason, at the beginning, the event simulation and detector simulation is run for single *pp* interactions. Each component of the pile-up can be simulated individually. Hence, the simulation of future detector layouts is possible, which has not been used for any data taking, as well as the direct simulation of high-luminosity scenarios, which has not yet been realized at the LHC. Furthermore, this allows to trace particles through the simulation in order to provide an easy route to understanding background origins. This step is also called digitization step of the simulations, where multiple simulated *pp* interactions are combined. A simple overlay of the particle hits in the detector takes place as well. The advantage of the inclusion of the pile-up effects in the digitization step is that it is not necessary to perform the whole simulation again in order to adapt the pile-up conditions.

5.9 Particle identification

There are many physical objects reconstructed with the ATLAS detector, like photons, electrons, muons, τ leptons, individual hadrons, jets, total energy and missing transvers energy. For the analysis presented in Part III electrons, muons, jets and missing transverse energy are relevant and will be discussed in the following Sections in more detail based on References [24–26].

5.9.1 Track reconstruction

The main goal of the track reconstruction is the determination of the path of charged particles from hits in dedicated detector elements, which are located in the Inner Detector. The reconstruction is based on several different tracking algorithms, which are explained in Reference [126] in more detail. Further track properties, which can be measured using the muon system, are described in Section 5.9.3.

Firstly, three dimensional space points are formed in the Pixel and SCT Detectors. The TRT is missing here because there is no information about the coordinate along the straw direction. Then, the formation of the track segments is performed using a projection to the r-ϕ plane for the barrel region and to the r-z plane for the endcap region. Furthermore, additional timing information is used in order to run two different track-finding approaches.

The first approach makes use of an inside-out track finding algorithm, which has combinations of space points of the Pixel Detector as an input. One combination of three space points is called a seed. Then, the extrapolation of these seeds to the TRT is performed using a Kalman-filter [127]. Finally, the fits of the track candidates to the actual hits in the Pixel Detector, SCT and TRT are performed. The main purpose of this inside-out approach is the reconstruction of tracks from particles, which are directly produced in the *pp* collision or from decaying particles, whose lifetime is less than 3×10^{-11} s.

A second algorithm uses the track segments from the TRT as an input. It extends the segments inwards by including the hits in the Pixel Detector. The main purpose of this outside-in approach is the reconstruction of tracks from decays of converted photons or long-lived particles, which might not produce hits in the inner-most layers of the detector.

After complete track reconstruction, the tracks are used as an input for vertex finding algorithms, which are responsible for assignment of the vertices to the tracks. In common, a vertex is defined to have at least two associated tracks. Thereby the vertex, which has the highest $\sum p_{\mathrm{T}}^2$, is defined as the primary vertex. More information about the track reconstruction and its performance using $\sqrt{s} = 13\,\mathrm{TeV}$ data from 2015 can be found in Reference [128] and about the vertex performance in Reference [129].

The transverse impact parameter d_0 is an important quality criterion of tracks. It is defined as the distance between the reconstructed primary vertex or the beam spot and the (extrapolated) track in the transverse plane. In order to get the beam spot, the measurement of the primary vertex position over several collisions in combination of the usage of the mean of their (Gaussian) distribution is needed. Furthermore, there are frequently placed cuts in the d_0 significance. The latter is defined as the nominal value divided by its uncertainty. Another important variable is the longitudinal impact parameter z_0. It is commonly defined with respect to the primary vertex as the distance of the track from the vertex along the beam axis. Restricting these variables reduces the contributions from particles, which come from secondary particle decays, like muons coming from τ-lepton decays.

5.9.2 Electrons

The detection of an electron in the ATLAS detector is based on the following: an energy deposition in the EM calorimeter, which is matched to a track recorded in the tracking detectors. However, an actual identification of an electron is performed in several steps. First, the signature of an energy deposition and a matching track gets reconstructed as an electron candidate. Second, identification and isolation criteria are defined for the electron candidate to be used in analyses in order to further constrain the candidate to a real electron. The following explanations are based on Reference [130].

Reconstruction

There are several steps, which have to be performed, in order to reconstruct an electron in the central region of the ATLAS detector ($|\eta| < 2.47$). First, the reconstruction of the clusters in the EM calorimeter is performed. Second, the reconstruction of the tracks in the tracking detectors is done followed by a procedure fitting electron-specific tracks. Finally, the resulted clusters and tracks are combined in order to reconstruct the electrons. The detailed procedure is described in the following:

1. *Seed-cluster reconstruction*: A seed-cluster is an energy deposition in the EM calorimeter, which has a total cluster transverse energy above 2.5 GeV. A sliding window algorithm scans over the $\eta \times \phi$ space of the calorimeter with smallest units of 0.025×0.025. For the search of seed-clusters a window size of 3×5 (measured in the smallest calorimeter units) is used. If a seed-cluster was found, a cluster algorithm [131] removes the duplicates and builds the full cluster.

2. *Track reconstruction*: The reconstruction of tracks is performed in two steps: the recognition of the track pattern and subsequent fit of the track. Due to interactions with the detector material, the standard algorithm, which performs the mentioned steps, uses a pion hypothesis for energy loss. However, this is complemented by an algorithm, which takes possible bremsstrahlung into account by allowing up to 30% energy loss. If a track-seed of three hits in different layers of the tracking detectors with a transverse momentum larger than 1 GeV can not be extended to a full track with at least seven hits but fails within

one of the seed-clusters in the EM calorimeter another try is initiated, but this time using an electron hypothesis, which make it possible to have a larger energy loss. The fits are performed with the ATLAS Global χ^2 Track Fitter [132].

3. *Electron specific track fit*: A loose matching of the obtained tracks to the EM clusters is performed by usage of the distance in η and ϕ between the position of the track in the middle layer of the calorimeter and the barycenter of the cluster. This matching also take into account the energy loss due to bremsstrahlung and the number of hits in the tracking system. For the tracks with ≥ 4 hits and loosely associated EM clusters a refit is performed with the help of an optimized Gaussian Sum Filter [133], which consider the non-linear effects due to bremsstrahlung for the fit.

4. *Electron candidate reconstruction*: The last step is the electron candidate reconstruction. Here, the refitted track of the previous step is matched to the EM cluster with stricter conditions for the η and ϕ distances. In case that several tracks fulfill the matching conditions a decision for the most optimal track is made by an algorithm, which uses the cluster-track distance $R = \sqrt{\Delta\eta^2 + \Delta\phi^2}$. Finally, the reformation of the EM cluster takes place using windows of size 3×7 (5×5) in units of the smallest calorimeter segments in the barrel (end-caps) of the EM calorimeter.

The properties of an electron candidate are computed as followed. Its four-momentum is calculated from the information from the track and from the EM cluster. Further on, its energy is gained by the EM cluster. Finally, its η and ϕ coordinates are computed from the track with respect to the primary vertex.

Identification

For the electron identification there exist some algorithms, which determine whether the reconstructed electron candidates are signal-like objects or background-like objects, like hadronic jets or converted photons. Converted photons are electrons that are the result of pair production by a photon. In order to distinguish signal from background these algorithms rely on quantities, which are related to the electron cluster and track measurements including the shape of the calorimeter shower, track properties, information from the TRT and variables measuring effects due to bremsstrahlung. However, there is a probability that a hadronic jet could be misidentified as an electron candidate since this jet could leave clusters and tracks that are similar to the ones of electrons. The identification algorithms use likelihoods, which are based on the discriminating quantities. Some examples are described in the following:

- *Hadronic leakage*: Electrons deposit most of their energy in the EM calorimeter before they reach the hadronic calorimeter. This means that if energy is deposited in the first layer of the hadronic calorimeter, then this is an indication of a hadronic jet rather than an electron.

- *Shower width*: The EM shower caused by hadronic jets or converted photons is usually wider than the shower of electrons, which can be used as an advantage by several discriminating quantities. One variable is constructed as the ratio of the energies measured in 3×7 and 7×7 calorimeter cells in $\eta \times \phi$ space such that the 3×7 window is centered in the 7×7 window. For electrons most of the energy is contained in the 3×7 cells. However, hadronic jets and converted photons can deposit energy outside of this small window.

- *Hits in Pixel and SCT Detector*: The number of Pixel and SCT Detector hits can be used to distinguish between prompt electrons and converted photons. The difference is that a photon does not leave hits in the detector before it converts, while prompt electrons still can leave hits from their origin. This means, that prompt electrons supposed to have more hits in the tracking detectors than converted photons.

- *Track to cluster η*: The matching of the tracks and clusters requires the comparison of the η variable, which is measured with the tracking detectors and the EM calorimeter. A distribution $\Delta\eta$ can be formed. Additional produced particles in hadronic jets can bias the cluster position with respect to the matching track leading to a wider $\Delta\eta$ distribution. However, this distribution is narrower for the electrons.
- $\frac{E}{p}$: $\frac{E}{p}$ is defined as the ratio of the energy measured in the EM calorimeter to the momentum determined by the tracking detectors. This ratio peaks at one for electrons and has a long tail for larger ratios. The tail visually represents the energy loss due to bremsstrahlung in the tracking detectors. However, the radiated photons in the EM calorimeter contribute to the EM cluster. $\frac{E}{p}$ has lower values for hadronic jets because they deposit a significant fraction of their energy also in the hadronic calorimeter.

In order to make a decision for a signal-like or a background-like object a multivariate analysis technique has been developed, which simultaneously evaluates the different quantities of the reconstructed electron candidates. So, probability density functions, which can be obtained from MC simulations, of the discriminating quantities for signal and for background objects are used by the algorithm. At the end, the information on the signal and background probability density functions is combined into a discriminant $d_{\mathcal{L}}$:

$$d_{\mathcal{L}} = \frac{\mathcal{L}_{\mathrm{S}}}{\mathcal{L}_{\mathrm{S}} + \mathcal{L}_{\mathrm{B}}} \quad \text{with} \quad \mathcal{L}_{\mathrm{S(B)}}\left(\vec{x}\right) = \prod_{i=1}^{n} P_{\mathrm{S(B)},i}\left(x_i\right), \tag{5.14}$$

where the vector $\vec{x}$ denotes the discriminating variables, and $P_{\mathrm{S(B)},i}\left(x_i\right)$ is the value of the signal (background) probability density function of the i^{th} discriminant variable. Therefore, $\mathcal{L}_{\mathrm{S(B)}}$ represents the entire likelihood, which describes the probability of the reconstructed object being signal-like (backround-like). Furthermore, $d_{\mathcal{L}}$ is used to define the degree of identification, for which the three levels Loose, Medium and Tight have been defined. Depending on the operating point, the signal (background) efficiencies for electron candidates with missing transverse energy of 25 GeV are in the range from 78% to 90% (0.3% to 0.8%) and increase (decrease) with the missing transverse energy. However, these criteria are already applied at some HLT triggers in a slightly softened version in order to get efficient data.

Isolation

The electron isolation is another quantity used for the discrimination of the signal-like reconstructed electron candidate from the background-like one. The isolation variable describes the energy around the reconstructed electron candidate and can be used in order to distinguish between prompt electrons from signal decays, like commonly isolated $Z \rightarrow e^{+}e^{-}$, and other non-isolated objects. The latter can be for example electrons originating from converted photons, which are produced in hadron decays, electrons from heavy flavour hadron decays and light hadrons, which are misidentified as electrons. In order to reach this goal two discriminating variables have been designed:

- *Calorimeter isolation*: The calorimeter isolation value $E_{\mathrm{T}}^{cone0.2}$ is the transverse energy contained in the cells around the reconstructed electron candidate cluster with a cone of $\Delta R = 0.2$ subtracted by the transverse energy in the cells defined by $\Delta\eta \times \Delta\phi = 0.125 \times 0.175$ around the barycenter of the cluster of the reconstructed electron candidate.
- *Track isolation*: The track isolation value $p_{\mathrm{T}}^{varcone0.2}$ is the sum of the transverse momenta of all tracks within a cone of $\Delta R = \min\left(0.2, 10\frac{\mathrm{GeV}}{E_{\mathrm{T}}}\right)$ around the reconstructed

electron candidate track, which is excluded together with additional tracks from converted bremsstrahlung photons. The tracks included in the $p_{\mathrm{T}}^{varcone0.2}$ value have to be originated from the primary vertex of the hard scattering and meet the following criteria:

- $E_{\mathrm{T}} > 1\,\mathrm{GeV}$.
- A combined seven hits in the Pixel and the SCT Detector with no more than two missing hits in total and one missing hit in the Pixel Detector. Furthermore, there has to be no more than one hit assigned to more than one track.
- $|\Delta z_0 \sin(\theta)| < 3\,\mathrm{mm}$, where z_0 is the closest distance between the primary vertex and the lepton candidates track component along the beam line.

From the values $E_{\mathrm{T}}^{cone0.2}$ and $p_{\mathrm{T}}^{varcone0.2}$ the levels LooseTrackOnly, Loose and Tight have been designed. LooseTrackOnly represents the weakest background rejection followed by Loose and Tight, which reflects the strongest background rejection. Depending on the level, the total isolation efficiency for electron candidates is in the range from $\sim 95\%$ (Tight level) over $\sim 98\%$ (Loose Level) to 99% (LooseTrackOnly level).

Electron energy calibration

The energy of electrons, which is built from the energy of the clusters in the EM calorimeter, is calibrated using multivariate techniques based on simulations. More details about this first calibration procedure can be found in Reference [134]. After this initial calibration procedure preliminary cuts on the energy are performed in order to reduce the data size. A second calibration of data follows later after the completion of a detailed analysis. In order to do this, the energy is recalibrated by using η-dependent corrections. Finally, the correction values are computed by comparing invariant mass spectra around selected Z- and J/Ψ-candidates between data and simulation. At the end, this corrections are below one percent and provided in a tool[6] by the ATLAS electron performance group [134].

5.9.3 Muons

A muon can be detected in the ATLAS detector by the following hints: a track recorded in the tracking detectors and a track recorded in the muon spectrometer. In order to identify a muon, several steps have to be run through in order to reconstruct a signature as a muon candidate, using the information from the tracking detectors and the muon spectrometer. In order to further constrain the muon candidate to a real muon several identification and isolation criteria are defined for the muon candidate which are commonly used in analyses. The following explanations are based on Reference [135].

Reconstruction

The reconstruction of muons rely on the information coming from the tracking system and the muon spectrometer. However, it is performed independently first. Then the gained information from the individual subdetectors is combined in order to form the muon tracks used in further analyses. The reconstruction procedure of muons in the tracking system is similar to the one of electrons and is run in the same way, but without using the hypothesis of bremsstrahlung. In the muon spectrometer there is a different story. Hit patterns are searched there in each muon chamber. More precisely, a Hough transform [136] is used in each MDT chamber and close enough trigger chamber in order to search for hits aligned on a trajectory in the bending plane of the detector. If there are some hits found, a straight line is fitted to them in order to

---

[6] In the analysis presented in this thesis the version of the tool is: *ElectronPhotonFourMomentumCorrection-02-03-00*.

reconstruct the hit segments of the MDT chamber. The RPC and TGC measure the coordinate in the transverse plane, which is orthogonal to the bending plane. The reconstruction of the segments in the CSC is performed using a combinatorial search in the η and ϕ planes of the detector.

The formation of muon track candidates is done by fitting hits from segments in different layers. The track reconstruction uses the algorithm, which is based on a combinatorial search. First, the segments found in the middle layers of the detector (with large availability of trigger hits) are used as seeds. Then the segments from the outer and inner layers are used as seeds by this algorithm. The selection of the segments is based on hit-multiplicity and fit quality. The subsequent matching is done by the usage of their relative positions and angles. In order to build a track at least two matching segments are needed. However, only one single high-quality segment with η and ϕ information is already enough in the transition region from the barrel to the end-cap. A segment is not limited to the formation of one track candidate and can be used for the formation of several track candidates. However, an overlap removal algorithm is used in order to decide if there is the best assignment to a single track or the segment can be shared between two tracks. A global χ^2 fit is used for the hits associated to a track candidate. This fit takes into account the energy loss of the muons in the calorimeters. At the end, there are four types of muons defined in the following using a combined information about the muon track coming from the tracking system, the muon spectrometer and the calorimeter:

- *Combined muons*: At the beginning, a track is independently reconstructed in the tracking system and in the muon spectrometer. The hits from the tracking system and the muon spectrometer are used for a global fit which forms a combined track. Depending on which information is used first, there are two different strategies defined. An outside-in strategy is used for the muon reconstruction in the muon spectrometer first with subsequent extrapolation inwards in order to match the track in the tracking system. An inside-out strategy is used for the muon reconstruction in the tracking system first with subsequent extrapolation outwards in order to match the track in the muon spectrometer.

- *Segment-tagged muons*: A track, which is reconstructed in the tracking system, is identified as a muon if it is associated with at least one local track segment in the MDT chamber or CSC. A segment-tagged muon is a muon, which has a low transverse momentum, or falls in a reduced acceptance region, meaning that only one layer of the muon spectrometer is crossed.

- *Calorimeter-tagged muons*: A track, which is reconstructed in the tracking system, is identified as a muon when a minimum-ionizing calorimeter signature can be matched to the muon track. This muon type has advantages in the region $|\eta| < 0.1$, since there is the muon spectrometer not fully equipped because of cabling and services for the tracking system and calorimeters.

- *Extrapolated muons*: A track in the muon spectrometer, which is extrapolated to the interaction point. This muon type is used in order to extend the acceptance of muons into the region $2.5 < |\eta| < 2.7$, since there is no tracking information available from the tracking system.

If a track is shared between some muons of different types an overlap algorithm is used, which gives the preference to the combined muons. The reconstruction efficiency is measured to be close to 99%.

Identification

For the identification of the muons some quality requirements are used in order to suppress background muons, which are mainly coming from pion and kaon decays. Muon candidates, which have their origin from in-flight decays of charged hadrons in the tracking system are commonly identified by a „kink“ topology. This means, that the expectation of the fit quality of the combined muon track is poor. Furthermore, it can be, that the the independently measured momentum in the tracking system and in the muon spectrometer are incompatible to each other. A good discrimination between prompt muons and background muons can be achieved using the following variables:

- *q/p significance*: It is defined as the absolute value of the difference between the ratio of the charge q and momentum p of the muons measured in the tracking system and the muon spectrometer divided by the sum in quadrature of the corresponding uncertainties.
- p': It is defined as the absolute value of the difference between the transverse momentum measured in the tracking system and the muon spectrometer divided by the p_{T} of the combined track.
- *Fit quality*: It is characterized by the normalized χ^2 of the combined track fit.

Several requirements on the number of hits in the tracking system and in muon spectrometer have to be accomplished in order to measure a robust muon momentum. In the tracking system at least one hit in the Pixel Detector, at least five hits in the SCT Detector and fewer than three missing hits in all layers of the SCT and Pixel Detectors are required. At least 10% of the TRT hits in the region $0.1 < |\eta| < 1.9$, which were assigned to the track first, have to be used in the final fit. There are several identification levels defined for a muon:

- *Medium*: The Medium level is the default selection for muons in ATLAS. This identification level minimizes the systematic uncertainties regarding to the muon reconstruction and calibration. Only combined muons and extrapolated muons are used for this level. Generally, combined muons should have at least three hits in at least two MDT layers. However, it is allowed to have hits in at least one MDT layer in the region $|\eta| < 0.1$, but in this case there has to be no more than one missing hit in an MDT layer. Extrapolated muons are used only in the region $2.5 < |\eta| < 2.7$ in order to extend the acceptance outside of the tracking system. The requirements for this muon type is to have at least three hits in the MDT chamber or CSC. Furthermore, the q/p significance has to be less than seven. About 0.5% of the Medium muons in the region $|\eta| < 2.5$ are reconstructed using the inside-out strategy.
- *Loose*: The Loose level is defined in order to maximize the reconstruction efficiency during the availability of good-quality muon tracks. In particular, this identification level is optimized for the reconstruction of Higgs boson candidates in the four-lepton final state [137]. All combined and extrapolated muons, which pass the Medium requirements, are also included in the Loose definition. Calorimeter-tagged and segment-tagged muons are used for this identification level only in the region $|\eta| < 0.1$. For the region $|\eta| < 2.5$ the following muons are used for Loose identification level: around 97.5% are combined muons, around 1.5% are calorimeter-tagged muons and the remaining ones are segment-tagged muons.
- *Tight*: The Tight level is defined in order to maximize the purity of muons, which costs some of the efficiency. Only combined muons with hits in at least two stations of the muon spectrometer, which also pass the Medium selection, are required for this identification level. The normalized χ^2 of the global fit has to be smaller than eight. A 2D criterion describing the variables p' and q/p significance as a function of the muon p_{T} is used in order to make sure, that a stronger background rejection occurs. In particular, this is important for muons with momenta smaller than 20 GeV since there is higher probability, that a muon can be misidentified.

- *High-p_T*: The High-p_{T} level is defined in order to maximize the momentum resolution for tracks with transverse momenta above 100 GeV. In particular, this identification level is optimized for searches for high mass resonances [138, 139]. For this level the combined muons passing at least three hits in three muon spectrometer stations are used. In case specific regions of the muon spectrometer have a sub-optimal alignment, they are vetoed in order to be sure. The reconstruction efficiency of High-p_{T} muons is reduced by about 20%. However, the p_{T} resolution of muons above 1.5 TeV is improved by about 30%.

Isolation

The muon isolation, similar to electrons, is another quantity used for the discrimination of the signal-like reconstructed muon candidate from background-like one. The energy around the muon candidate can be used in order to decide if the muon is produced through a decay of a heavy boson or through a semi-leptonic decay. In latter case the muon is produced around other particles. The following two variables have been declared in order to ensure this discrimination:

- *Calorimeter isolation*: The calorimeter isolation value $E_{\mathrm{T}}^{\mathrm{topocone20}}$ is defined as the sum of the transverse energy of the topological clusters [140] in a cone with size $\Delta R = 0.2$ around the muon candidate after subtracting the energy deposit from the muon candidate itself.

- *Track isolation*: The track isolation value $p_{\mathrm{T}}^{\mathrm{varcone30}}$ is defined as the scalar sum of the transverse momenta of the tracks in a cone of size $\Delta R = \min\left(\frac{10\,\mathrm{GeV}}{p_{\mathrm{T}}}, 0.3\right)$ around the muon of transverse momentum p_{T}, excluding the muon track itself. The transverse momentum of a track entering the sum has to be at least 1 GeV.

Using $E_{\mathrm{T}}^{\mathrm{topocone20}}$ and $p_{\mathrm{T}}^{\mathrm{varcone30}}$ the isolation levels LooseTrackOnly, Loose and Tight have been designed, like for the electrons. LooseTrackOnly represents the weakest background rejection followed by Loose and Tight, which reflects the strongest background rejection. The isolation efficiency varies between 93% and 100% depending on the level applied and on the momentum of the muon.

Muon momentum scale and resolution corrections

Differences of the muon momentum scale and resolution are corrected between data and simulation, similar like the electrons are corrected. However, compared to the electrons, no corrections are applied to data. In order to derive the corrections the position and width of the Z- and J/Ψ-resonance are determined in data and Monte Carlo simulation. Since only the simulation was corrected, the position of the Z- and J/Ψ-resonance in the data may not match with the PDG value, which was used in the simulation. The binning for the corrections is performed in muon η. At the end, the corrections are usually in the per mille range for the momentum scale (with an accuracy on the order of 0.1%) and in the low percent range for the resolution. The corrections are provided in a tool[7] by the ATLAS muon performance group [135].

5.9.4 Jets

Jets are defined as the clusters of final state hadrons after the hadronization process. The here presented description of the reconstruction of jets follows Reference [141]. The reconstruction of the dominant majority of jets is performed in ATLAS with the anti-k_{T} algorithm [142]. This jet finding algorithm is based on $\Delta_{ij}^2 = (y_i - y_j)^2 + (\phi_i - \phi_j)^2$ between the objects i and j, where y_i and ϕ_i are rapidity and azimuth angle of object i, respectively, as well as the transverse momenta $k_{t,i}$ and $k_{t,j}$. d_{ij} is the distance in a η-ϕ space between two objects i and j, and d_{iB} is the distance between the object i and the beam. At the beginning, it is identified which distance

---

[7] In the analysis presented in this thesis the version of the tool is: *MuonMomentumCorrections-01-00-60.*

is the smallest one. If it is d_{ij} the two objects are recombined, if it is d_{iB} the object i is declared as a jet and removed from the list of objects. The distances are recalculated and this procedure is repeated until no objects are left. The definition of the distances is

$$d_{ij} = \min\left(k_{t,i}^{-2}, k_{t,j}^{-2}\right) \frac{\Delta_{ij}^2}{R^2}, \tag{5.15}$$

$$d_{iB} = k_{t,i}^{-2}, \tag{5.16}$$

where R is the radius parameter[8]. Different values of the exponent for the transverse momentum $k_{t,i}$ change the behaviour of the clustering algorithm fundamentally. For the exponent of +2 the algorithm accumulates at the beginning particles with small transverse momentum. This results in jets of irregular shape and subsequently the contributions from additional interactions become hard to subtract. If the exponent is zero, then the accumulation takes only the geometrical distance into account, since it is become independent from kinematical properties of the particles. However, this leads to an irregular shape as well, which is dependent on soft radiation. Finally, usage of the exponent of -2, as it was chosen for the anti-k_{T} algorithm, leads to non-irregular shape of the jets as wanted [81]. The jet finding algorithm has as an input either ID tracks, or energy deposits in the calorimeter, or a combination of both [143, 144]. Jets, which are reconstructed from tracks, are low dependent on pile-up because the jet finding algorithm uses only tracks from the primary vertex. However, since the ATLAS ID tracking is limited to region $|\eta| < 2.5$ a jet reconstruction is mostly used, which involves the energy deposits in the calorimeter. These calorimeter jets are reconstructed from „topologically“ clustered calorimeter cells which are known as topo-clusters [145]. This procedure is based on a topological noise suppression involving removal of specific cells as explained in the following. Topological cell clusters with shape and location information, which can be used for the jet reconstruction, represent the results. The assumption is made, that σ is the total noise of the cell. The latter represents the quadratic sum of the measured electronics and pile-up noise. At the beginning, the clustering algorithm defines topo-clusters from seed cells with energy deposits larger than 4σ. The neighbouring cells of the seed cells are accumulated to the top-cluster, if they have an energy deposit larger than 2σ. Finally, all adjacent cells of the topo-cluster are added. The overlaps are avoided by a cluster splitting algorithm, which separates topo-clusters based on local energy maxima. In the end, a topo-cluster must have a positive energy to be considered for the reconstruction of a jet.

The determination of the jet energy resolution appears in in-situ measurements and in simulated events. For the measurement of the energy resolution the transverse momentum balance between two jets is used. [146]. The fractional jet energy resolution depends on the η region and the transverse momentum of the jet. It also decreases with p_{T}, for example the resolution varies from $\sim 18\%$ for $p_{\mathrm{T}} = 30\,\mathrm{GeV}$ down to $\sim 4\%$ for $p_{\mathrm{T}} = 1000\,\mathrm{GeV}$ [147].

The calibration of the jet energy scale is done in several steps. At the beginning an offset correction of the energy due to pile-up interactions is performed. Next step is the correction of the origin, which have to point to the vertex instead of the nominal interaction point. In the end, a residual correction is performed with the help of in-situ techniques. These techniques are based on measurements of transverse momentum in balancing processes like $pp \to Z\left(e^+e^-\right) + \mathrm{jets} + X$, where the jets must compensate the transverse momentum of the reconstructed Z boson. All these corrections are provided by the ATLAS jet performance group [148] and implemented in a tool[9].

---

[8] $R = 0.4$ is used for the jets in the presented leptoquark search.

[9] In the analysis presented in this thesis the version of the tool is: *JetCalibTools-00-04-76*.

5.9.5 Missing transverse momentum

The missing transverse momentum is a quantity, which describes the transverse momentum of particles, that have left the detector unregistered. Neutrinos can serve as an example of particles in the SM, which only interact weekly and therefore can leave the detector with some „unseen“ particle momentum and energy. Other examples are unknown particles that either rarely or never interact with the detector. All these particles can contribute to the missing transverse momentum. For the determination of the missing transverse momentum a sum of all calorimeter cells and tracks is needed. However, an object based reconstruction can benefit from the object based calibrations. This leads to a better resolution of the missing transverse momentum. According to Reference [149] the missing transverse momentum can be defined as the negative vector sum of transverse momenta $\vec{p}_{\mathrm{T}}$ of reconstructed objects, which can be electrons, photons, muons, τ leptons and jets. All these contributions represent hard terms while the soft term consists of any contribution, which is not included to any of the hard terms. The missing transverse momentum can be expressed as:

$$E_{x(y)}^{\text{miss}} = E_{x(y)}^{\text{miss, } e} + E_{x(y)}^{\text{miss, } \gamma} + E_{x(y)}^{\text{miss, } \tau} + E_{x(y)}^{\text{miss, jets}} + E_{x(y)}^{\text{miss, } \mu} + E_{x(y)}^{\text{miss, soft}}, \tag{5.17}$$

where each term is calculated separately along the x and y axes. The magnitude of the missing transverse momentum is calculated using the following Equation:

$$E_{\mathrm{T}}^{\text{miss}} = \sqrt{(E_x^{\text{miss}})^2 + \left(E_y^{\text{miss}}\right)^2}. \tag{5.18}$$

The main algorithm for the soft term reconstruction used by ATLAS at Run 2 is the so-called Track Soft Term, which fully relies on tracks. The algorithm is very robust against varying pile-up condition, but it misses the contribution from neutral particles. The removal of pile-up jets is important for $E_{\mathrm{T}}^{\text{miss}}$ resolution and is performed with the jet-vertex-tagger technique, which extracts the pile-up jets using track-to-vertex association method [150]. In addition, a novel forward pile-up tagging technique that exploits the correlation between central and forward jets originating from pile-up interactions is developed [151]. This technique improves the $E_{\mathrm{T}}^{\text{miss}}$ resolution in high pile-up conditions (from $\sim 10\,\text{GeV}$ to $\sim 27\,\text{GeV}$ with increasing number of reconstructed vertices) [141].

Part III

Leptoquark search

Chapter

6

Motivation

> *Much to learn, you still have.*
>
> Yoda from Star Wars: Episode II - Attack of the Clones

The search for new physics is motivated by several reasons. First, there exist some conceptual problems of the Standard Model (SM). Second, there are still open questions left, like the nature of dark matter. The solutions for these problems or explanations for these open questions deliver new physics models, which often represent an extension of the SM. In most cases the extension of the SM offers an opportunity for the search of new particles, which are predicted by these new models. Furthermore, due to the hierarchy problem it is very likely that new physics appears at the TeV scale. Some theories are already very sophisticated (for example, Supersymmetry) since they often provide explicit predictions about expected particles. However, there are also a lot of theories, which are still in the early stages of concept development [24].

Leptoquarks (LQs) are introduced in a number of extensions of the SM [71, 72, 152–157] and may explain the similarities of the lepton and quark sectors in the SM. Furthermore, they also appear in models which deal with some of the b-flavour anomalies observed recently [158–160]. LQs are colour-triplet bosons with fractional electric charge and have non-zero baryon and lepton numbers [161]. There were two types of LQs proposed: scalar and vector LQs. Both of them are expected to decay directly to lepton-quark pairs, where the lepton can be either electrically charged or neutral.

A single Yukawa coupling, $\lambda_{\text{LQ}\to lq}$, defines the coupling strength between scalar LQs and the lepton-quark pair [162]. For vector LQs two additional coupling constants are required due to magnetic moment and electric quadrupole moment interactions [75]. The production cross section of vector LQs is expected to be enhanced relative to the contribution of scalar LQs, however, the kinematic of their experimental signature is similar for both types of LQ.

The production of LQs in proton-proton (pp) interactions can appear singly or in pairs. Figure 6.1 shows the Feynman diagrams of the representative single- and pair-production processes. The single LQ production cross section depends on the single Yukawa coupling. However, the pair-production cross section is largely insensitive to this coupling. For pp interactions with a centre-of-mass energy $\sqrt{s} = 13\,\text{TeV}$, the dominant pair-production mechanism for LQ masses below around $1\,\text{TeV}$ is gluon fusion. However, with rising LQ mass the contribution of the $q\bar{q}$-annihilation process becomes more significant. In this thesis only the pair-production of scalar LQs is considered. However, the results can be used as conservative estimates of limits on vector LQ pair-production [157]. More theoretical details about LQs are given in Section 3.2.

The benchmark signal model used in the analysis presented in this thesis is the minimal Buchmüller-Rückl-Wyler model [77]. This model sets a number of constraints on the LQs properties. Couplings are purely chiral and LQs are grouped into three families, which correspond to three

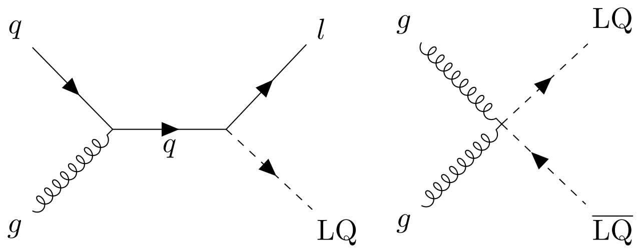

(a) (b)

Figure 6.1: *Feynman diagrams for representative (a) single and (b) pair production of LQs.*

SM generations. Generations, such that only interactions between leptons and quarks within a given generation are allowed. The requirement of same-generation interactions excludes flavour-changing neutral currents (FCNC) [78]. The branching ratio (BR) of a LQ into different states is considered to be a free parameter. In this analysis the BR is denoted as β, and is defined with respect to a LQ decaying to a charged lepton and quark: $\beta = BR\left(\mathrm{LQ} \rightarrow l^{\pm}\overset{(-)}{q}\right)$ [163].

The ATLAS Collaboration has already performed searches for pair-produced LQs at the Large Hadron Collider (LHC) in the past [164–168]. Using $3.2\,\mathrm{fb}^{-1}$ of data collected at 13 TeV, the existence of scalar LQs with masses below 1100 GeV (900 GeV) for first-generation LQs at $\beta = 1\,(0.5)$ and, for second-generation LQs, 1050 GeV (830 GeV) at $\beta = 1\,(0.5)$ is excluded at 95% confidence level (CL) [168]. The CMS Collaboration has also made similar searches [169–175]. Their results deliver that scalar LQs with masses below 1130 GeV (920 GeV) for first-generation LQs at $\beta = 1\,(0.5)$ and that 1165 GeV (960 GeV) for second-generation LQs at $\beta = 1\,(0.5)$ are excluded at 95% CL using a data sample of $2.7\,\mathrm{fb}^{-1}$ collected at $\sqrt{s} = 13$ TeV [174, 175]. An overview of limits on LQ production and masses can be found in Reference [34].

Chapter

7 Analysis

> *Your weapons, you will not need them.*
> Yoda from Star Wars: Episode V - The Empire Strikes Back

This Chapter presents a search for pair production of scalar leptoquarks (LQ) which decay into two electron-quark pairs or two muon-quark pairs. A possible decay into an electron-quark pair and a muon-quark pair is not considered in this analysis. The presented search is a cross-check analysis to the one published in Reference [163] using a cut-based approach from the previous round of ATLAS leptoquark search [168], therefore many relevant aspects, like Monte Carlo samples, object selection, region definitions, background determination and uncertainty descriptions are directly taken from Reference [163].

Section 7.2 describes the used data and Monte Carlo samples for the analysis. The event selection is discussed in Section 7.3, followed by the object selection in Section 7.4. Section 7.5 briefly describes the definitions of the control and signal regions. The background determination is explained in Section 7.6, followed by the discussion of the systematic uncertainties in Section 7.7. Finally, Sections 7.8 and 7.10 show the comparison of background with data and signal, respectively. In between placed Section 7.9 explains performed Z+jets reweighting after discovering the problems which have the provided Monte Carlo samples as the origin.

7.1 Analysis strategy

This analysis takes into account events with at least two jets and two charged same-flavour leptons, where the latter can be either electrons or muons[1]. Here and during this analysis electrons and positrons are summarized as electrons, and muons and antimuons are summarized as muons. The process describing this scenario at leading order can be expressed in a Feynman diagram (see Figure 7.1) and is called signal process.

In order to search for such a signal process all other processes resulting in the same final state as well as processes faking this final state need to be considered. These processes are called background processes. The approach is to compare the data with simulations of all these background processes. The background consists of the following processes: Z/γ^*+jets, $t\bar{t}$, single top and diboson and fake electron background.

- Z/γ^*+jets is one of the main background processes since Z boson can decay leptonically. Including jets, the picture is complete for the final state similar to the LQ pair production final state.

---

[1] An exception here is the $t\bar{t}$ control region, defined in Section 7.5, which uses events with at least two jets and one lepton, and $E_{\mathrm{T}}^{\mathrm{miss}}$.

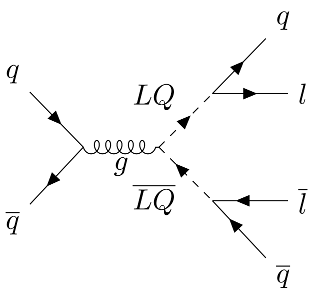

Figure 7.1: *An example of a Feynman diagram of the leading order LQ pair production.*

- $t\bar{t}$ is another main background process, where a top quark can decay into b-jet and a W boson decaying to the required lepton. The anti-top quark delivers the anti-particles accordingly.

- Diboson, or boson-pair production, also contributes considerably to the SM background, mostly through the decay of one (W or Z) boson into two quarks while another Z-boson decays into two charged leptons. Diboson production with less or more than two charged leptons in the final state yields only a small contribution to the overall background.

- Single top production gives a small, but non-negligible contribution to the background because the needed objects which would come from $\bar{t}$ in $t\bar{t}$ process are found to be generated from gluons or fake identifications.

- Fake electron background contributes only in the channel, where the electrons are involved, and its determination is described in Section 7.6 in more detail.

A major difference between LQ signal and background events is the presence of jet-lepton pairs coming from the decay of the parent LQ, giving a peak in the reconstructed jet-lepton mass spectrum for the signal. The reconstruction of these masses provides a very important variable used to distinguish between signal and background events.

7.2 Data and Monte Carlo samples

7.2.1 Data

The data for this analysis was delivered by the LHC at 13 TeV with 25 ns bunch spacing and recorded by the ATLAS experiment. In 2015, data was recorded in periods D3-J6 (16th August - 3rd November), runs 276262-284484. In 2016, data was recorded in periods A3-L11 (28th April - 26th October), runs 297730-311481. The delivered luminosity of the 2015 (2016) data is $4.2\,\text{fb}^{-1}$ ($38.5\,\text{fb}^{-1}$). The ATLAS experiment could record $3.9\,\text{fb}^{-1}$ ($35.6\,\text{fb}^{-1}$) of data as shown in Figure 7.2. The uncertainty in the combined 2015+2016 integrated luminosity is 2.1% [121]. It is derived, following a methodology similar to that detailed in [176], and using the LUCID-2 detector for the baseline luminosity measurements [177], from calibration of the luminosity scale using x-y beam-separation scans.

The difference in luminosity between 2015 and 2016 is explainable due to the rise of the instantaneous luminosity and is also related to the differences in the number of collisions per bunch crossing in the data periods. Figure 7.3 shows the increase over these two periods from $\langle\mu\rangle = 13.7$ in 2015 to $\langle\mu\rangle = 24.9$ in 2016.

An increased number of collisions per bunch crossing results in a larger number of particles created at multiple primary vertices. This can lead to observable effects in the analysis and

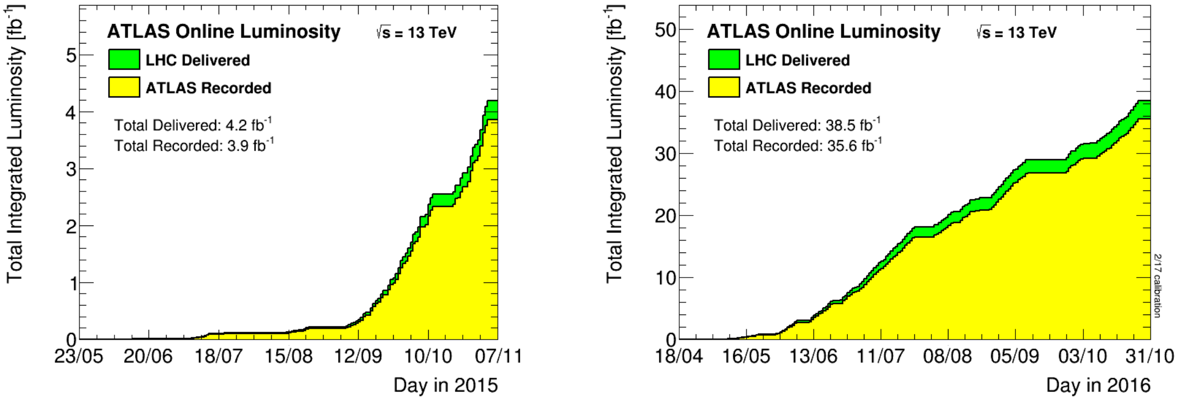

(a) Integrated luminosity in 2015.

(b) Integrated luminosity in 2016.

Figure 7.2: *Luminosity delivered and recorded in ATLAS in (a): 2015 and (b): 2016 year [125].*

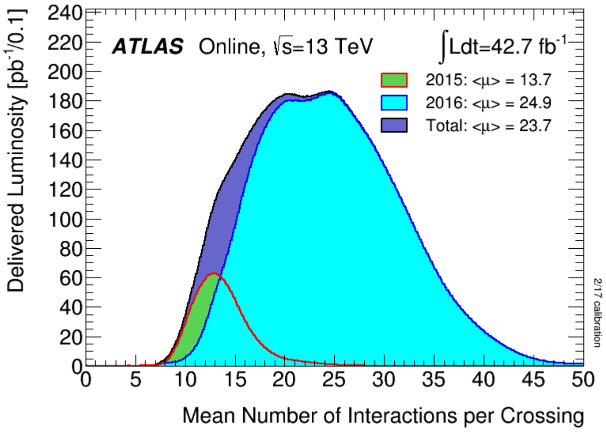

Figure 7.3: *Comparison of number of collisions per bunch crossing between data taking periods [125].*

is complemented by other changes in the experimental setup such as different trigger names. Thus, a differentiation between the data taking periods will be presented, otherwise the data is considered as a single dataset.

7.2.2 Monte Carlo

The physical processes were modeled by Monte Carlo (MC) simulations produced using a combination of generators each with specific strengths for a LQ signal or a particular background. For this analysis MC samples for the leptoquark signal and the following processes are used: Z/γ^*+jets, $t\bar{t}$, single top and diboson. The descriptions of the MC samples are derived from Reference [163].

The production of the samples of simulated pair-produced scalar LQ events was performed at next-to-leading order (NLO) in QCD with the MadGraph 2.4.3 [178, 179] program using MadSpin [180] for the decay of LQs. These samples were generated with LQ masses between 200 GeV and 1800 GeV, in intervals of 50 GeV up to 1500 GeV and thereafter 100 GeV. The generated partons were interfaced with Pythia 8.212 [181] using A14 tune [182] for parton showering and hadronization. Used parton distribution function (PDF) was the NNPDF3.0 NLO [183] set. The coupling $\lambda_{\mathrm{LQ}\to lq}$ was set to $\sqrt{4\pi\alpha}$, where α corresponds to the fine-structure constant. This coupling defines the LQ width and lifetime [162]. The value of this coupling represents a LQ full width of about 0.2% of its mass. This allows to consider, that LQs can decay promptly. Samples were generated for $\beta = 0.5$.

The simulations of events, which contain Z bosons and associated jets [184], were performed with the Sherpa 2.2.1 generator [185]. The calculation of matrix elements was done in perturbative QCD for up to two partons at NLO and four partons at leading order (LO) using the Comix [186] and OpenLoops [187] matrix element generators. Merging with the Sherpa parton shower was performed with the ME+PS@NLO method [188]. Used PDF at next-to-next-to-leading order (NNLO) was the NNPDF3.0 PDF set [189].

The production of $t\bar{t}$ and single top-quark in the Wt and s channel was simulated using the Powheg-Box v2 [190–193] generator. Used PDF in the matrix element calculations for the $t\bar{t}$ samples was NNPDF3.0 PDF set. For the single-top samples it was CT10. The production of electroweak t-channel single top-quark events was performed with the Powheg-Box v1 generator. The parton shower, fragmentation process, and the underlying event for the generation of single-top samples were simulated using Pythia 6.428 [194] with the CTEQ6L1 [195] PDF sets and Perugia 2012 [196] tune. The value of the top mass (m_t) was set to 172.5 GeV. For properties of the bottom and charm hadron decays the EvtGen v1.2.0 [197] program was used. For the $t\bar{t}$ samples, Pythia 8.210 was used instead of Pythia 6, with the A14 tune and the NNPDF2.3 LO [198] PDF set. The simulation of diboson processes with four charged leptons, three charged leptons and one neutrino, or two charged leptons and two neutrinos were performed using the Sherpa 2.1.1 generator. All diagrams with four electroweak vertices were considered. These diagrams were determined for up to one parton at NLO and up to three partons at LO with the usage of the Comix and OpenLoops matrix element generators and merged with the Sherpa parton shower using the ME+PS@NLO prescription. The CT10 PDF set was used for these processes. Additionaly, the dedicated parton shower tuning was performed which is developed by the Sherpa authors. The generator cross sections were used, which were calculated up to NLO.

In order to model the pile-up effect, simulated inclusive proton-proton events were overlaid on each generated background and signal event. The multiple interactions were calculated with Pythia 8.186 using tune A2 [199] and the MSTW2008LO PDF set [64]. The correction of simulated events using weights available for each event was performed in order to describe the distribution of the average number of interactions per proton bunch-crossing as observed in data. Additionaly, scale factors were applied as event weights in order to correct the simulation description of lepton trigger, reconstruction, identification, isolation and impact-parameter as well as b-tagging efficiencies.

The evaluation of the detector response to the SM background samples was done with the detector simulation which is based on GEANT4 [123, 200]. However, for the signal samples a fast simulation including a parameterization of calorimeter response [201] and GEANT4 for the other components of the detector was used. For simulated and pp data the standard ATLAS reconstruction software was utilized. Detailed information about the samples can be found in Appendix A.

7.3 Event selection

7.3.1 General idea

The whole analysis is split into two channels: the electron ($eejj$) and the muon ($\mu\mu jj$) channel. For the electron (muon) channel at least two jets and exactly two isolated electrons (muons) are required in the final state. In order to reach the orthogonal event selection between the channels a common baseline object selection, called *baseline* selection in the following, is defined. The object and event selection chain can be described schematically in the following manner [79]:

- Apply the event cleaning, described in Section 7.3.2.
- Check the trigger decision, described in Section 7.3.3.
- Select electrons, muons and jets according to the *baseline* selection, described in Section 7.4.
- Determine $E_{\mathrm{T}}^{\mathrm{miss}}$ with the *baseline* selection of electrons, muons and jets (overlap removal is applied internally in the corresponding MET tool).
- Remove *baseline* objects that appear in two different object containers (for example in both the electron and the jet container). In this case remove the object only from one container.
- Impose requirements on the exact numbers of *baseline* electrons and muons in the event.
- Apply the jet cleaning (event) selection.
- Select events with at least two jets according to the *final* selection criteria.
- Select electrons and muons according to the *final* selection criteria.
- Impose requirements on the exact numbers of *final* electrons and muons in the event.

This analysis uses the NTuples[2] readable by ROOT and produced by ATLAS member V. Pleskot, where all above steps were already processed. All further analysis steps are covered by myself if it is not otherwise stated.

7.3.2 Event cleaning

The luminosity blocks in the collected data should be a part of the Good Run List (GRL) as mentioned in Section 5.4.2. These lists contain the events only for one year of data taking, so GRL of 2015[3] and of 2016[4] are two different lists.

If an ionizing particle runs through electronic modules with high energy, corruption of the information coming from the SCT might occur. Events containing corrupted tracking information are rejected. Further events with corrupted data are rejected, where LAr or Tile calorimeters experienced a coherent noise during data taking. They can be caused by unshielded high-voltage cables. Events with LAr noise bursts observed in the electromagnetic or hadronic calorimeter are rejected as well, because a noise burst could falsify energy depositions leading to the non-accurate measurement of the energy. Finally, it might be necessary during data taking to perform a TTC restart, which is needed in order to restart the trigger system. This can lead to the incomplete events in the luminosity blocks. These incomplete events are rejected as well.

There are many vertices in an event, which have the origin from the pp collisions. For the analysis only primary vertex is taken which should satisfy the following criteria:

- The vertex has the largest $\sum p_{\mathrm{T}}^2$ of associated tracks among all vertices.
- The vertex has at least two associated tracks with $p_{\mathrm{T}} > 400\,\mathrm{MeV}$.

---

[2] Containers filled with all needed information extracted from the MC samples and data.

[3] `data15__13TeV.periodAllYear__DetStatus-v79-repro20-02__DQDefects-00-02-02__PHYS__StandardGRL__All__Good__25ns.xml`

[4] `data16__13TeV.periodAllYear__DetStatus-v88-pro20-21__DQDefects-00-02-04__PHYS__StandardGRL__All__Good__25ns.xml`

Due to preselection requirement the integrated luminosity of the 2015 (2016) data considered as useful for physics analysis is $3.2\,\text{fb}^{-1}$ ($32.9\,\text{fb}^{-1}$) [202].

The samples have been preselected, in order to reduce the amount of data to analyze and the required amount of disk space. Only events which contain at least two electron candidates, two muon candidates or one electron candidate and one muon candidate with $p_{\text{T}} > 20\,\text{GeV}$ are used.

7.3.3 Triggers

For the electron channel a trigger requiring at least two electrons with a p_{T} of at least 17 GeV and an identification criterion of at least Loose is applied. „nod0“ in the name of the trigger for 2016 indicates that no d_0 impact parameter cuts are required in the trigger. The electron trigger efficiency for 2015 data is around of 93% [112] which is improved a bit for 2016 data.

For the muon channel a combination of two triggers is used. The first trigger requires at least one muon with a p_{T} of at least 26 GeV and the muon to be isolated with Medium criterion. The isolation criterion of this trigger is a bit different for the data from 2015 compared to the trigger used for the 2016 data. Nevertheless, both first triggers have a high efficiency at low values of p_{T}. However, the efficiency starts to fall at very high p_{T} values [26]. For this reason a second trigger is used for both 2015 and 2016 data, which do not have an isolation criterion, but requires at least one muon with a p_{T} of at least 50 GeV. The event is rejected only if none of the two combined triggers decides to keep it. The muon trigger efficiency for 2015 data is close to 70% in the barrel and 90% in the end-cap regions [112] which is again improved a bit for 2016 data.

The triggers used in this analysis are summarized in Table 7.1 sorted by the different channels and different years of data taking. They are all unprescaled[5] and written using common ATLAS notations.

	2015	2016
$eejj$	HLT_2e17_lhloose	HLT_2e17_lhvloose_nod0
$\mu\mu jj$	HLT_mu26_imedium || HLT_mu50	HLT_mu26_ivarmedium || HLT_mu50

Table 7.1: *Triggers used in the LQ search for different final states.*

7.4 Object selection

The goal is to select the events with two electrons (muons) for electron (muon) channel and at least two jets in the final state. However, these objects should satisfy the requirements discussed in the further Sections of this thesis. In case a selected event has more than two jets, the first two jets with largest p_{T} are further considered for the analysis.

7.4.1 Kinematic variable definitions

Table 7.2 summarizes all important kinematic variables used for this analysis. The common kinematic variables described in Section 5.2.2 are not mentioned here for the simplicity. Single

---

[5] In the prescaled system, after the trigger decides that the event is interesting, a random number is used to decide whether the event has to be considered or not. This is controlled by the prescale factor f_{prescale}, where $f_{\text{prescale}} = 100$ means that 1 in 100 events marked as interesting is recorded, and $f_{\text{prescale}} = 1$ is the special case of an unprescaled trigger. The majority of ATLAS analyses uses unprescaled triggers for simplicity, since they are purely interested in the high p_{T} region and therefore are willing to discard data from lower thresholds, where more work is required to perform combinations of prescaled triggers [203].

objects are labeled by letters (l, e, μ for lepton, electron, muon, respectively) and a number (1(2) for the (sub)leading object, where a leading object has greater p_{T} than a subleading one). The quantity $m_{\mathrm{LQ}}^{\mathrm{min}}$ ($m_{\mathrm{LQ}}^{\mathrm{max}}$) is defined as the lower (higher) of the two invariant masses which can be reconstructed using the two lepton-jet pairs and therefore corresponding to the LQ and anti-LQ. For the lepton-jet pairing pairs are chosen, which minimize the absolute difference between $m_{\mathrm{LQ}}^{\mathrm{min}}$ and $m_{\mathrm{LQ}}^{\mathrm{max}}$. The variable m_{T} appears only in $t\bar{t}$ control region described in Section 7.5 which has by construction only one lepton.

Variable	Description
$m_{\mathrm{LQ}}^{\mathrm{min}}$	Smaller of the two lepton-jet pair masses
$m_{\mathrm{LQ}}^{\mathrm{max}}$	Larger of the two lepton-jet pair masses
S_{T}	$p_{\mathrm{T}}^{l,\text{ leading}} + p_{\mathrm{T}}^{l,\text{ subleading}} + p_{\mathrm{T}}^{\text{jet, leading}} + p_{\mathrm{T}}^{\text{jet, subleading}}$
H_{T}	$p_{\mathrm{T}}^{\text{jet, leading}} + p_{\mathrm{T}}^{\text{jet, subleading}}$
L_{T}	$p_{\mathrm{T}}^{l,\text{ leading}} + p_{\mathrm{T}}^{l,\text{ subleading}}$
m_{ll}	Invariant mass of the two leading leptons
m_{jj}	Invariant mass of the two leading jets
m_{lljj}	Invariant mass of the two leading leptons and two leading jets
m_{T}	$\sqrt{2 \cdot p_{\mathrm{T}}^{l} \cdot E_{\mathrm{T}}^{\mathrm{miss}} \cdot (1 - \cos(\Delta\phi(l, E_{\mathrm{T}}^{\mathrm{miss}})))}$
p_{T}^{ll}	p_{T} of the pair of the two leading leptons
N_{jet}	Number of jets in an event after all cuts

Table 7.2: *Important kinematic variables and their meaning.*

7.4.2 Electrons

The reconstruction and identification of electrons is made by imposing requirements on the shape of the cluster of energy deposits, information from the transition radiation tracker, the quality of the associated track and of the track-to-cluster matching [130] as mentioned in Section 5.9.2. The transverse energy of the electron candidates in the electron channel is required to be higher than 40 GeV. Only electron candidates in the pseudo-rapidity region $|\eta| < 2.47$ and excluding the transition region between the central and forward regions of the calorimeters ($1.37 < |\eta| < 1.52$) are used. The Medium identification working point is used, which has an efficiency above 90% for the candidates considered in this analysis. Loose isolation working point is used with both calorimeter- and track-based criteria. The isolation efficiency is 98%. Lastly, the electron candidates must have an origin from the primary vertex.

Estimation of the fake background, described in more detail in Section 7.6.1, requires a looser electron definition for the selection of a sample, which is enriched in fake electrons. This loosened definition involves the usage of the Loose identification working point. No isolation requirement is set for the selection of a fake-enriched sample of the fake background estimation [79].

7.4.3 Muons

The reconstruction of muon tracks is done independently in the ID and the muon spectrometer [135]. Tracks should reach a certain minimum number of hits in each system, and must match within the momentum measurement and geometry of the system. The measurement of the momentum of each muon is refined using information from both the ID and muon spectrometer in a combined fit [204]. For this analysis the Medium identification working point is used, yielding an efficiency for reconstructing muons of 98%. Muon candidates are required to have $p_{\mathrm{T}} > 40\,\mathrm{GeV}$ in order to be symmetric to the electron channel, and $|\eta| < 2.5$. (The acceptance in $|\eta|$ of muon triggers is $|\eta| < 1.05$ in barrel region and $1.05 < |\eta| < 2.4$ in end-cap region [205].) Furthermore, they must have an origin from the primary vertex as in Reference [135]. A track-based LooseTrackOnly isolation working point is applied to the muons, resulting to a selection efficiency of 99%.

7.4.4 Jets

Reconstruction of the jets is performed using the anti-k_t algorithm [142] with a radius parameter $R = 0.4$ from topological clusters of calorimeter cells which are noise-suppressed and calibrated to the electromagnetic scale. The calibration uses energy- and η-dependent correction factors, which are derived from simulation, and is done with residual corrections from in-situ measurements [206]. The jets are required to have $p_{\mathrm{T}} > 60\,\mathrm{GeV}$ and $|\eta| < 2.5$. Furthermore, in order to remove fake jets, which are caused by different detector effects, jet quality criteria are applied as well [207].

The identification of the b-jets (jets, which contain B-hadrons) is performed using an algorithm, which is based on multivariate techniques. This algorithm combines information coming from the impact parameters of displaced tracks and from topological properties of secondary and tertiary decay vertices, which are reconstructed within the jet. A b-tagging efficiency for a chosen working point amounts to around 77% for jets with the origin from a b-quark. This information is gained with a MC simulation of $t\bar{t}$ processes [208, 209].

7.4.5 Overlap removal

The object identification might be inconclusive during reconstruction (when a reconstructed object can match multiple object hypotheses (electron, muon, jet)). However, these ambiguities are resolved in several steps. At the beginning, electrons are removed if they share a track with a muon. In removing jet-lepton ambiguities a variable $\Delta R_{\mathrm{slide}}$ is used, given by $\Delta R_{\mathrm{slide}} = \min(0.4, 0.04 + 10/p_{\mathrm{T}})$, where the p_{T} is that of the lepton, measured in GeV. Ambiguities between electrons and jets are resolved in two steps. First, jets within $\Delta R < 0.2$ of an electron are removed. Then, electrons are removed if they are within $\Delta R_{\mathrm{slide}}$ of one of the remaining jets. For the solution of muon-jet ambiguities the following procedure is used: if a muon and a jet are closer than $\Delta R_{\mathrm{slide}}$, the jet is rejected if it has less than three tracks, otherwise the muon is rejected.

7.5 Region definitions

A set of background enhanced regions has been defined, where the signal is mostly removed, in order to make sure, that the background is modeled properly. There are two regions defined by the dominant backgrounds to the signal: Z/γ^*+jets control region (Z CR) and $t\bar{t}$ CR. The Z CR is defined by restricting m_{ll} to a window around the Z-peak. For $t\bar{t}$ CR the events with one electron in electron (one muon in muon) channel and $E_{\mathrm{T}}^{\mathrm{miss}} > 40\,\mathrm{GeV}$ are preselected exceptionally since this region was adapted from the so-called neutrino channels studied in Reference [163], which have at least two jets, one electron (muon) and missing transverse energy in the final state. On the further analysis level the $t\bar{t}$ CR is defined by restricting m_{T} to a window around the W-peak and requiring at least two b-tagged jets. The signal region is the region above m_{ll} of 130 GeV requiring S_{T} (sum of the transverse momenta of the four objects in the final state) to be at least 600 GeV.

All regions of phasespace used in the LQ search with their clear definitions are summarized in Table 7.3.

Region	Requirements
Z CR	$70 < m_{ll} < 110$
$t\bar{t}$ CR	$40 < m_{\mathrm{T}} < 130$, ≥ 2 b-jets
SR	$m_{ll} > 130$, $S_{\mathrm{T}} > 600$

Table 7.3: *Regions of phasespace. All numbers except amount of b-jets are in GeV.*

7.6 Background determination

The major SM background processes to the LQ signal correspond to the production of Z/γ^*+jets and $t\bar{t}$ events in which at least one top quark decays leptonically. They are determined using data in selected control regions, as described in Section 7.3. Subdominant contributions arise from diboson and single-top production and are estimated entirely from simulations. Possible contribution from Z/γ^*+jets, where Z decays into two τ leptons, is negligible and therefore is not considered for this analysis. In the electron channel, there are also background contributions due to jets being misidentified as electrons or non-prompt electrons that are produced in the decay of hadrons inside jets. These backgrounds are collectively referred to as fake (electron) background and are estimated in a data driven way using matrix method [210]. For this analysis the fake background determination and the corresponding uncertainties were completely taken from Reference [163].

7.6.1 Matrix method

The matrix method is used in order to estimate the contribution of events containing fake electrons to a sample of selected events, which are based on the nominal electron object definition. For this purpose, a looser object definition is considered, which softens isolation and identification requirements for the suppression of the fake contributions in the nominal selection. Based on this definition an object passing the nominal selection will always also pass the loose selection. This modified looser selection is already described in Section 7.4.2: no isolation requirements are imposed and looser identification working points are used than for the nominal selection. It would be better to have as loose criteria as possible in order to increase the fake purity. However, some criteria are applied already at the trigger level (see Section 7.3.3) and can therefore not be softened.

In the following the nominal definition will be denoted as *tight*, while the modified definition will be marked as *loose*. There are four types of objects considered in the matrix method:

- tight object: a physical object that passes the tight selection
- loose object: a physical object that passes the loose but fails the tight selection
- real electron: an object that is an electron and passes the loose selection
- fake: an object that is not an electron but passes the loose selection

At the analysis level the only gained information about an object is whether this object is loose or tight, but not whether it is real or fake. However, the number of events with a certain number of loose and/or tight objects can be related to the desired quantity, like the number of events with different combinations of multiplicities of real electrons and fakes. For this, the estimation of the probabilities is determined, where real electrons and fakes pass the tight selection if they already pass the loose selection. These probabilities are called real rate r, which is estimated from simulation, and fake rate f, which is estimated from data. The determination of the rates is described in Sections 7.6.2 and 7.6.3.

There are four different event classes at the analysis level: events with two tight electrons (N_{TT}), two loose electrons (N_{LL}) or one loose and one tight electron, where either the leading (N_{TL}) or the sub-leading (N_{LT}) electron can be the tight one. Analogically, the events could be classified into the events with two real electrons (N_{RR}), two fakes (N_{FF}) or one real electron and one fake (N_{RF} or N_{FR}, respectively), if it would be known whether the object is a real electron or a fake one. The relation between these categories is given in terms of real and fake rates, this time one for each object, like r_1, r_2, f_1, f_2:

$$\begin{pmatrix} N_{\mathrm{TT}} \\ N_{\mathrm{TL}} \\ N_{\mathrm{LT}} \\ N_{\mathrm{LL}} \end{pmatrix} = \begin{pmatrix} r_1 r_2 & r_1 f_2 & f_1 r_2 & f_1 f_2 \\ r_1(1-r_2) & r_1(1-f_2) & f_1(1-r_2) & f_1(1-f_2) \\ (1-r_1)r_2 & (1-r_1)f_2 & (1-f_1)r_2 & (1-f_1)f_2 \\ (1-r_1)(1-r_2) & (1-r_1)(1-f_2) & (1-f_1)(1-r_2) & (1-f_1)(1-f_2) \end{pmatrix} \begin{pmatrix} N_{\mathrm{RR}} \\ N_{\mathrm{RF}} \\ N_{\mathrm{FR}} \\ N_{\mathrm{FF}} \end{pmatrix} \tag{7.1}$$

The fake background contamination is defined as the sum of the fractions of N_{FF}, N_{RF} and N_{FR}, which contribute to N_{TT}:

$$N_{\mathrm{TT}}^{\mathrm{fake}} = r_1 f_2 N_{\mathrm{RF}} + f_1 r_2 N_{\mathrm{FR}} + f_1 f_2 N_{\mathrm{FF}}. \tag{7.2}$$

Equation 7.1 can be inverted and used for the definition of the expressions for the unknown numbers N_{FF}, N_{RF} and N_{FR}. The fake background contribution to N_{TT} can be determined via the following Equation once the real and fake rates are known:

$$\begin{aligned} N_{\mathrm{TT}}^{\mathrm{fake}} &= \alpha r_1 f_2 \left[(f_1-1)(1-r_2)N_{\mathrm{TT}} + (1-f_1)r_2 N_{\mathrm{TL}} + f_1(1-r_2)N_{\mathrm{LT}} - f_1 r_2 N_{\mathrm{LL}}\right] \\ &\quad + \alpha f_1 r_2 \left[(r_1-1)(1-f_2)N_{\mathrm{TT}} + (1-r_1)f_2 N_{\mathrm{TL}} + r_1(1-f_2)N_{\mathrm{LT}} - r_1 f_2 N_{\mathrm{LL}}\right] \\ &\quad + \alpha f_1 f_1 \left[(1-r_1)(1-r_2)N_{\mathrm{TT}} + -(r_1-1)r_2 N_{\mathrm{TL}} + r_1(r_2-1)N_{\mathrm{LT}} + r_1 r_2 N_{\mathrm{LL}}\right] \end{aligned} \tag{7.3}$$

with

$$\alpha = \frac{1}{(r_1-f_1)(r_2-f_2)}. \tag{7.4}$$

7.6.2 Real rate

The real rate r is given by the ratio of the number of real electrons that pass the tight selection (N_{tight}) over the number of real electrons that pass the loose selection (N_{loose}):

$$r = \left.\frac{N_{\mathrm{tight}}}{N_{\mathrm{loose}}}\right|_{\text{real electrons}}. \tag{7.5}$$

The Powheg simulation of $Z \rightarrow ee$ events is used for its estimation.

The real rate is estimated as a function of the electron p_{T} for different η regions. The rate is higher in more central regions, varying from about 94% to 99%, while for more forward regions it increases from about 91% to 96%. This is expected since the detector is more suitable for object identification in central regions due to finer granularity of LAr in the barrel region.

7.6.3 Fake rate

The fake rate is given by the ratio of number of objects that pass the tight electron selection (N_{tight}) over number of objects that pass the loose electron selection (N_{loose}), after the contribution of real electrons has been subtracted from the loose sample:

$$f = \left.\frac{N_{\mathrm{tight}}}{N_{\mathrm{loose}}}\right|_{\text{fake electrons}}. \tag{7.6}$$

It is studied as a function of p_{T}, η, $E_{\mathrm{T}}^{\mathrm{miss}}$ and b-jet activity. For the selection of the loose sample, the same triggers as for the nominal analysis described in Table 7.1 are used and the same requirements on data quality and for the primary vertex are imposed. Events are selected if they contain a loose electron candidate with a p_{T} above 65 GeV, $|\eta| < 2.47$ and are not in the crack region, fulfilling the standard impact parameter cuts and the Medium (Loose) identification criteria for $p_{\mathrm{T}} < 145$ GeV ($p_{\mathrm{T}} > 145$ GeV). These objects have no isolation requirement. In order to reduce contributions coming from Drell-Yan events to the fake-enriched sample, events are vetoed if they contain two or more objects, which fulfil this loose selection and the Medium ID requirement. Furthermore, the overlap removal between different objects is applied as described in Section 7.4.4. In order to subtract the remaining real dilution, the MC simulated POWHEG V+jets samples are used. Several different single electron triggers are used for the selection of a fake-enriched sample. The usage of these triggers, few of which are prescaled, depends on the p_{T} region. Table 7.4 lists the triggers used and the luminosities collected by each of them. Events collected by a given trigger are weighted with the ratio of the total luminosity to the luminosity collected by this trigger.

Trigger name	p_{T} range [GeV]	Luminosity [pb^{-1}]
HLT_e24_lhvloose_nod0_L1EM20VH	29–31	172.1
HLT_e26_lhvloose_nod0_L1EM20VH	31–65	298.8
HLT_e60_lhvloose_nod0	65–125	1153.3
HLT_e120_lhloose_nod0	125–145	2280.8
HLT_e140_lhloose_nod0	>145	32861.2

Table 7.4: *The trigger scheme used to build the fake-enriched sample in the study of the electron fake rate in the electron channel [79].*

The same requirements on data quality and primary vertex are used as in the nominal analysis. However, the electron object selection is loosened compared to the selection decribed in Section 7.4.2: events are selected if they contain an electron candidate with $p_{\mathrm{T}} > 40$ GeV, $|\eta| < 2.47$ and are not in the crack region, fulfilling the standard impact parameter cuts and the Loose ID requirements. The objects have no isolation requirement.

In order to reduce the contribution coming from $Z \to ee$ events, events that contain a pair of loose objects with an invariant mass in a window of ±20 GeV around the Z-mass (91.2 GeV) are vetoed. Furthermore, if events contain two or more loose objects that also pass the Medium ID requirement, they are rejected.

The fake rate is estimated as a function of the object p_{T} in different η regions. It varies from less than 20% at low p_{T} up to about 25% at higher values of p_{T}. It is also estimated as a function of η for different p_{T} regions. Here is the behaviour similar for different p_{T} bins and the fake rate is typically larger in the more central bins and decreases for more forward regions.

The fake rate is applied as a function of objects p_{T}, η and b-jet activity since in this case the best modelling is obtained.

7.6.4 Uncertainties

The estimation of an uncertainty on the fake background is performed by varying the real dilution by 30% up and down and re-deriving the fake rate. For example, the uncertainties are almost 100% at low values of $m_{\mathrm{LQ}}^{\mathrm{min}}$ in the signal region and decrease to about 20% above 1 TeV. The uncertainty coming from the statistical uncertainty in the fake rate (treated correlated bin-by-bin) is found to be of the order of a few % [79].

7.6.5 Summary

Table 7.5 provides an amount of events for each background process just before applying the selection of the Z CR cuts summarized in Table 7.3 and after implementing them. Analogously, Table 7.6 provides the numbers for $t\bar{t}$ CR. The luminosity scale factor is applied on the background MC samples such that number of events, which is rounded to be an integer, corresponds to an integrated luminosity of 36.1 fb^{-1}. The difference between the numbers for preselection is due to different DAOD format of the MC samples mentioned in Section 5.4.2.

Process	Electron channel		Muon channel	
	Preselection	Z CR	Preselection	Z CR
$Z \to ee$	86965	79688 (91.6%)	-	-
$Z \to \mu\mu$	-	-	111053	101523 (91.4%)
$t\bar{t}$	21529	3844 (17.9%)	25222	4647 (18.4%)
Diboson	2549	1979 (77.6%)	2996	2348 (78.4%)
Single top	1057	166 (15.7%)	1222	194 (15.9%)
Fake electron	2372	1269 (53.5%)	-	-
Data	117048	88441 (75.6%)	150966	115520 (76.5%)

Table 7.5: *Amount of events after the preselection and after the complete selection in the Z CR. The numbers in brackets give the percentage with respect to the preselection numbers.*

Process	Electron channel		Muon channel	
	Preselection	$t\bar{t}$ CR	Preselection	$t\bar{t}$ CR
$Z \to ee$	61174	777 (01.3%)	-	-
$Z \to \mu\mu$	-	-	54030	777 (01.4%)
$t\bar{t}$	465446	135794 (29.2%)	391200	113933 (29.1%)
Diboson	18940	344 (01.8%)	16213	306 (01.9%)
Single top	47563	9197 (19.3%)	39578	7715 (19.5%)
Fake electron	265635	6610 (02.5%)	-	-
Data	1277792	151721 (11.9%)	1044008	128722 (12.3%)

Table 7.6: *Amount of events after the preselection and after the complete selection in the $t\bar{t}$ CR. The numbers in brackets give the percentage with respect to the preselection numbers.*

It can be seen, that as expected, there are more events originating from the process $Z \to ll$ in the Z CR than other background and the $t\bar{t}$ process is the dominant one in the $t\bar{t}$ CR. The comparison of numbers between electron and muon channel leads to similar fractions of the final selected events to the preselected events for every background and for data.

7.7 Systematic uncertainties

This Section lists and discusses all systematic uncertainties which affect this analysis. The systematic uncertainties can be subdivided into the experimental uncertainties for the selected electrons, muons, jets, pile-up und luminosity, and uncertainties from theoretical predictions [79]. First, all experimental sources are discussed in Section 7.7.1. Thereafter follows a discussion of the sources for the theoretical uncertainties in Section 7.7.2.

7.7.1 Experimental uncertainties

Luminosity uncertainty

The uncertainty on the luminosity is estimated to be 2.1% [121] following a methodology similar to that detailed in Reference [176], from a calibration of the luminosity scale using x-y beam-separation scans performed in August 2015 and May 2016.

Pile-up reweighting uncertainty

An additional uncertainty is estimated regarding the reweighting of the vertex multiplicity. This uncertainty is needed for pile-up description, which is made by scaling the number of average interactions per bunch-crossing in data by different factors. The effect on the event yields in this analysis can vary by several per cent in the signal regions, but is less than 1% in the control regions.

Electron related uncertainties

Six sources of uncertainty in the electron reconstruction are considered of which the two major uncertainties correspond to the electron energy scale and resolution. The analysis also considers uncertainties due to the modelling of the efficiencies of the four electron selection criteria: trigger, reconstruction, identification and isolation. Electron related systematic uncertainties on the total background yield in the SR for the electron channel are in the range 2-18%.

The ATLAS ElectronGamma working group provides uncertainties related to the calibration of electron energies. The full uncertainty set contains more than 60 components in total [211]. However, a simplified uncertainty set, which includes only two components, is also provided by this working group. One component covers the uncertainty on the electron energy scale, while the other is responsible for the uncertainty on the electron energy resolution. In order to receive them, a quadrature sum of all the different uncertainty sources is calculated, while these sources are assumed to be fully correlated in η. In this analysis, this simplified set is used.

Muon related uncertainties

Experimental uncertainties related to muon reconstruction and calibration are taken from the following sources: uncertainties in the determination of the muon spectrometer (MS) momentum scale, MS momentum resolution, ID momentum resolution and additional charge dependent corrections. Uncertainties in the determination of the four efficiency scale factors (trigger, identification, isolation and track-to-vertex association) are considered as well. Muon related systematic uncertainties on the total background yield in the SR for the muon channel vary between 2% and 24%. All uncertainties are provided by the ATLAS Muon Combined Performance working group [135].

Jet related uncertainties

Uncertainty related to the jet reconstruction stems mainly from the following two sources: jet energy scale (JES) and jet energy resolution (JER). Both are provided by the ATLAS JetEtMiss working group [212]. Another source of jet-related uncertainty corresponds to corrections, which are made for the b-tagging efficiency. It is taken into account in $t\bar{t}$ CR.

The JES uncertainty is largely derived from various in-situ techniques. It is commonly split into ~ 70 components since many correlations among various effects, which affect the JES, have to be considered. All the components are intended to be propagated through the analysis separately in order to achieve the best treatment of their correlations that is available. However, it might become too complicated to handle all these components. For this reason, the ATLAS JetEtMiss working group provides reduced sets of the JES uncertainty components. Besides others, there are four sets with each four components only. Different jet-jet correlation assumptions are used for the formation of these sets in order to probe the sensitivity of an analysis to jet correlations. The jet-jet correlation scheme is found to have no impact on the uncertainty and therefore the first reduced set is used in the analysis. JES uncertainties on the total background yield in the SR for the electron (muon) channel vary between 1% and 6% (1% and 12%).

The JER uncertainty is split into about ten components. However, the ATLAS JetEtMiss working group also provides a set, which contain just one component of the JER uncertainty. This set exists in parallel to the full set and represents a quadrature sum of the uncertainty components contained in the full set. It should be applied in just one direction (up). This one-component set is used in this analysis. The JER uncertainty on the total background yields in the SR for the electron (muon) channel vary between 1% and 13% (1% and 5%).

7.7.2 Theoretical uncertainties

Modelling of Z+jets production

The used Z+jets samples[6] include event weights in order to reflect variations of the nominal PDF set and the usage of two other different PDF sets: MMHT2014NNLO68CL [213] and CT14NNLO [214]. The estimation of the NNPDF intra-PDF uncertainty is performed as the standard deviation of the set of 101 NNPDF3.0 sets. An additional uncertainty is used, which is calculated by the envelope of the differences between the nominal NNPDF set and the other two PDF sets (in the further analysis denoted as „interPDF“ uncertainty).

An uncertainty, which considers the effect of varying α_s by ±0.001 around its nominal value of 0.119, is gained from weights calculated using the same nominal PDF.

The weights for a „7 point“ variation of the renormalisation (μ_R) and factorisation (μ_F) scale are included into the samples. The scales are varied for these weights either together or independently by a factor of 2 up and down. For the estimation of the scale uncertainty the envelope of all these variations is taken. In Figures 7.4(a) and 7.4(c) the different sources of uncertainties together with the total uncertainty, which is obtained as the quadratic sum of the separate components of Z+jets, are shown in different regions of phase space. It can be seen that the scale uncertainty is the dominant uncertainty in all cases. As can be seen from Figures 7.4(b) and 7.4(d) the scale uncertainty is in turn driven by the renormalisation scale uncertainty.

There is one more uncertainty taken into account, namely an uncertainty from the reweighting of the Z+jets simulations in m_{jj}. This uncertainty is estimated by considering the full difference between the reweighted and the unweighted distributions. The need for this reweighting (and therefore the usage of its uncertainty) is explained in Section 7.8.

Modelling of $t\bar{t}$ production

The uncertainties in the modelling of the production of $t\bar{t}$ are calculated using a number of alternative simulation samples, which are listed in Table 7.7. The up- and down-variation of different sources of uncertainty (radiation parameters, hdamp parameter[7] and scales) is represented by its own sample. All these sources of uncertainty are correlated. Furthermore, there is a sample, which is produced with a different generator (aMC@NLO) in order to take into account differences in the modeling of the hard-scattering. Another two samples were produced

---

[6] Only Z+jets samples, where a Z boson decays into two electrons contain event weights for different PDF variations. The samples, where Z boson decays into two muons do not have this information. Therefore the same size of theoretical uncertainty as for electron channel is applied in muon channel.

[7] Resummation damping parameter, which is one of the parameter controlling the NLO matrix element / Parton Shower matching in Powheg and effectively regulates the high-p_{T} radiation [215].

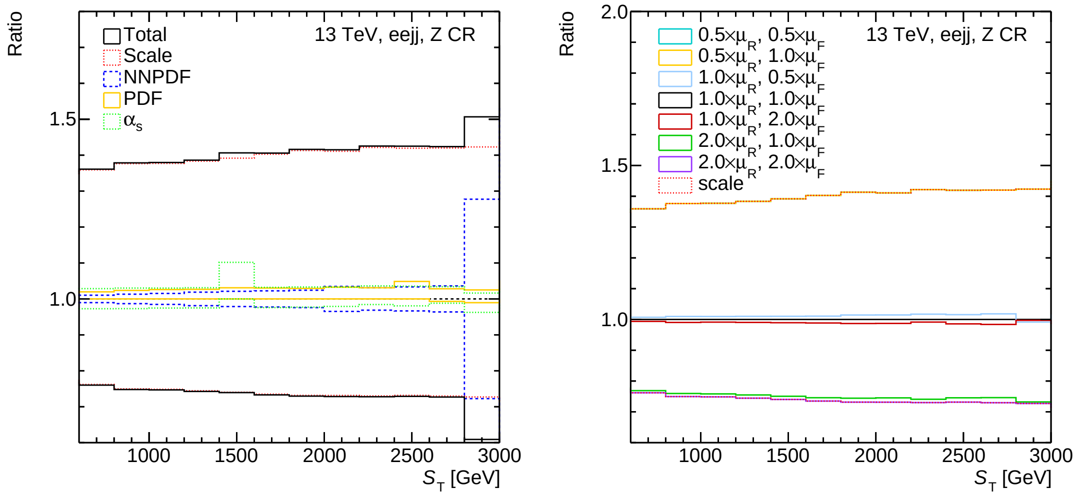

(a) Z+jets, Z CR. (b) Z+jets, Z CR.

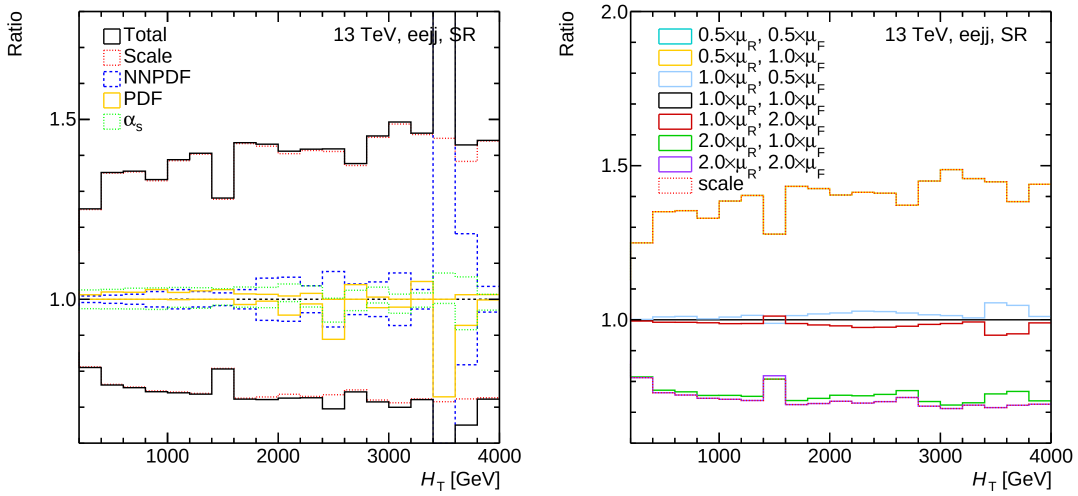

(c) Z+jets, SR. (d) Z+jets, SR.

Figure 7.4: *Theoretical uncertainties for Z+jets in the control and signal regions as a function of S_T and H_T.*

with a different showering program (HERWIG7 instead of PYTHIA8), where one sample represents the dilepton-filtered version of the other one. The nominal sample contains weights for the PDF sets MMHT, CT14 and PDF4LHC as well as replicas and error sets for NNPDF3.0 and PDF4LHC, respectively [216]. The default PDF is NNPDF3.0 and the estimation of the uncertainty is performed using the PDF4LHC15 error sets, following the ATLAS top group recommendations [217].

In Figure 7.5 the different sources of uncertainties together with the total uncertainty obtained as the quadratic sum of the separate components of $t\bar{t}$ MC samples in both electron and muon channels are shown. It can be seen that the Hard Scatter Generator uncertainty is the dominant one in all bins. Moreover, in some bins 100% is exceeded. Since this large uncertainty is not reasonable in terms of physics, it was scaled down for the further analysis (see Section 8.2 for more details).

Table 7.7: *Alternative $t\bar{t}$ Monte Carlo samples used to assess the $t\bar{t}$ modelling uncertainties. The first column gives the internal ATLAS dataset number (DSID), the second a brief description of the difference with respect to the nominal sample, the third gives the generator.*

DSID	comment	generator
410511	variations (hdamp, scale, ISR/FSR)	PowhegPythia8
410512	variations (hdamp, scale, ISR/FSR)	PowhegPythia8
410225	Hard Scatter Generator	aMC@NLO+Pythia8
410525	Fragmentation/Hadronisation Model	Powheg+Herwig7
410527	Fragmentation/Hadronisation Model, dilepton filtered	Powheg+Herwig7
410248	colour reconnection	PowhegPythia8

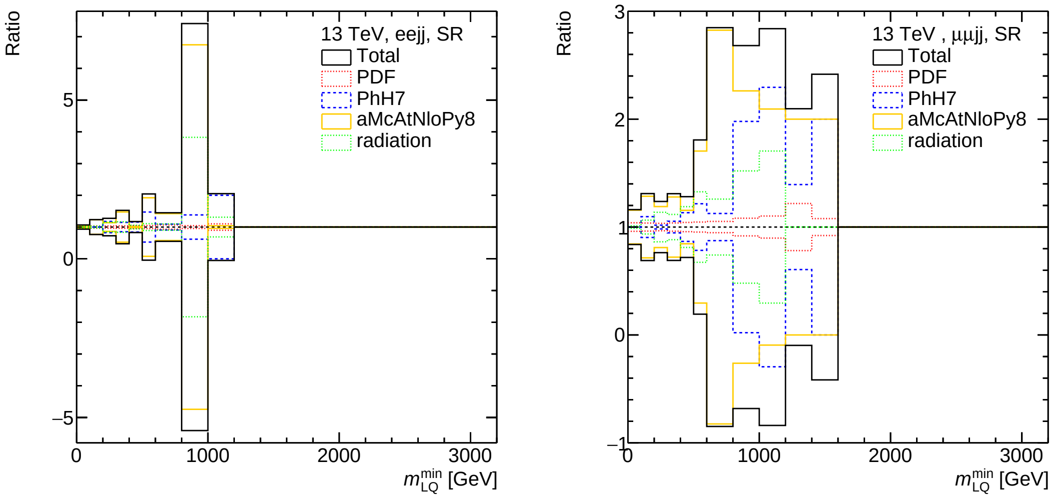

(a) $t\bar{t}$, electron channel.

(b) $t\bar{t}$, muon channel.

Figure 7.5: *Theoretical uncertainties for $t\bar{t}$ MC samples in the signal region as a function of m_{LQ}^{min} in electron (left) and muon (right) channel. PhH7 denotes an uncertainty on fragmentation and hadronization and aMcAtNloPy8 - on Hard Scatter Generator.*

Uncertainties on the signal

The signal samples contain the same set of weights for PDFs, α_s, and scale variations as the Z+jets samples and the uncertainties are estimated as described at the beginning of Section 7.7.2. Figure 7.6 shows the uncertainty in the selected number of events for a signal with LQ mass of 1 TeV, as a function of different variables in the signal region. It can be seen that again the scale uncertainty is the dominant one. The PDF uncertainty has another large contribution to the overall uncertainty.

7.8 Comparison of background with data in control regions

All distributions shown in this Section are based on the full (2015-2016) 13 TeV dataset corresponding to 36.1 fb^{-1}. Comparisons are done for the Z CRs and $t\bar{t}$ CRs defined in Section 7.5. The displayed contributions to the MC simulated background processes are drawn stacked. In each Figure, the grey band represents the total (experimental and theoretical) systematic uncertainty, which is calculated by a quadrature sum of all its components. The statistical uncertainty of MC simulated background processes is displayed by the hatched orange band. The statistical uncertainty of data is shown by the black error bars.

Figures 7.7, 7.8 and 7.9 show various distributions in the Z CR for the electron channel. Figure 7.7 shows some common distributions (p_{T}, η, ϕ) for the leading and subleading electrons. Figure 7.8 lists the same distributions for the leading and subleading jets, and Figure 7.9 summarizes the distributions of more complex variables.

It can be seen that $Z \to ee$ MC process is dominating over all background sources in Z CR as expected. Furthermore there are no subleading electrons above 500 GeV. Otherwise both p_{T} spectra for the electrons are steeply falling towards higher values of p_{T}. The η distributions show symmetric behaviour around the zero value with dips around $|\eta| \approx 1.4$, which corresponds to the transition region between central and endcap calorimeter and therefore matches very well with the expectations. The expectations for the ϕ distributions have a symmetry around zero and a flat behaviour since the leptons from the LQ event should be produced statistically evenly over the ϕ values. The dips around $|\phi| \approx 3.2$ are there due to the corresponding bins having a size up to $|\phi| = 3.2$, but contain the content up to $|\phi| = \pi < 3.2$. The described observation holds also for the jet distributions shown in Figure 7.8 except there are a few subleading jets above 500 GeV and no dips are seen around $|\eta| \approx 1.4$. All distributions for electron channel shown in Figure 7.9 are steeply falling as well. However, there is one exception in the first bin of the m_{lljj} distribution, which is expected due to high p_{T} thresholds used in the analysis.

Figures 7.10, 7.11 and 7.12 show various distributions in Z CR for muon channel. Figure 7.10 shows the distributions of p_{T}, η and ϕ for the leading and subleading muons. Figure 7.11 lists the same distributions for the leading and subleading jets, and Figure 7.12 again summarizes the distributions of more complex variables.

It can be seen that $Z \to \mu\mu$ MC process is dominant in Z CR. Both p_{T} spectra for the muons are steeply falling towards higher values of p_{T}. The η and ϕ distributions show symmetric behaviour around zero. The η distributions have a dip in the central region which corresponds to a worse trigger efficiency in the barrel region than in the end-cap regions for muons. The dips around $|\eta| \approx 3.2$ (and especially $|\phi| \approx 3.2$ since otherwise the ϕ distribution is flat) exist due to the content up to π value. The jet distributions shown in Figure 7.11 look as expected as well. Compared to the distributions from electron channel it can be seen that data in muon channel has significantly less events than in electron channel (seen for example in Figure 7.11(c)). However the deviations lie well inside the total systematic uncertainty. All distributions for muon channel shown in Figure 7.12 are steeply falling as well with a dip in the first bin of m_{lljj} distribution like in the electron channel distribution for the same reasons as described above for muon channel distribution.

It can be seen that the systematic uncertainties are large, typically of the order 20%-50% depending on the distribution and region of the spectrum. This is driven by the large renormalisation scale uncertainty on the Z+jets background as described in Section 7.7.2. Most of the deviations of the simulation from the data are covered by these large uncertainties. However, there are some clear trends in the data-to-MC ratios in some variables. In some cases the discrepancies are on the edge of the uncertainty band or even beyond it like for the distribution of H_{T}, m_{jj} and m_{lljj} in Figure 7.9. More precisely, the discrepancies occur for variables related to the jet activity, whereas lepton or dilepton variables are generally well described. In particular, the dilepton p_{T} (Figures 7.12(e) and 7.9(e)) is modelled very well, but the H_{T} distribution is much harder in the simulation than in data. This is compensated by additional jets in the simulation as can be seen from the jet multiplicity distribution in Figure 7.9(f). This mis-modeling is known to the Physics Modelling Group (PMG) and understood to be related to the choice of the renormalisation scale in the Z+jets samples. A reweighting is derived to achieve a good description of the data (see Section 7.9).

Figures 7.13 and 7.14 show various distributions in $t\bar{t}$ CR for electron channel. Figure 7.13 shows the distributions of p_{T}, η and ϕ for the leading and subleading jets. Figure 7.14 lists the distributions of more complex variables.

It can be seen that $t\bar{t}$ MC process is dominating in $t\bar{t}$ CR. The p_{T} distributions and all distributions shown in Figure 7.14 are steeply falling. The η and ϕ distributions show an expected behaviour similar to the ones from Z CR.

Figures 7.15 and 7.16 show various distributions in $t\bar{t}$ CR for muon channel. Figure 7.15 shows the distributions of p_{T}, η and ϕ for the leading and subleading jets. Figure 7.16 lists the distributions of more complex variables.

The distributions in $t\bar{t}$ CR for muon channel look overall as expected. The behaviour is quite similar to the distributions from electron channel.

Overall it can be stated that the data is well described by the MC simulations except the jet related distributions in Z+jets samples and most of the deviations are covered by the total systematic uncertainty. As mentioned previously, in order to take into account the mis-modeling in Z+jets samples, a reweighting is derived.

7.9 Reweighting of Z+jets sample

The Sherpa Z+jets samples have poor modelling of the jet related variables due to the choice, which was made for the renormalisation scale, as mentioned in Section 7.7.2. In order to improve the description of data a reweighting was derived in the Z+jets control regions. This reweighting will also be used in order to correct the simulation before performing the fit described in Section 8.1. It was chosen to use m_{jj} as the variable to use for deriving the weights [79]. In order to be independent of the binning, a fit of the ratio of data to simulation is performed. The turn-on at low values of m_{jj} and the tail are fitted separately. For the low-mass turn-on a second order polynomial is chosen for the determination of the weights. The same decision is made for the fit at higher masses since the second order polynomial provides the smoothest transition to the low-mass region. The stitching point is at 450 GeV. The resulting function for the weight w is taken from the analysis described in Reference [79] and has the following definition:

$$w = \begin{cases} 0.999 + 0.0009 \cdot m_{jj} - 1.7 \cdot 10^{-6} \cdot (m_{jj})^2 \,, & m_{jj} < 450\,\mathrm{GeV} \\ 1.24 - 0.00043 \cdot m_{jj} + 6.3 \cdot 10^{-8} \cdot (m_{jj})^2 \,, & m_{jj} \geq 450\,\mathrm{GeV} \end{cases} . \tag{7.7}$$

The weights derived in this way for the muon channel are also applied in the electron channel.

Figure 7.17 show the direct comparison of the m_{jj} distribution from Z+jets sample before and after applying the reweighting in Z CR. The description of data is significantly improved in Figure 7.17(b) compared to the original situation shown for reference in Figure 7.17(a). The small deviations in low mass region are expected since the fit is different from a bin-by-bin reweighting.

Figures 7.18 and 7.19 show the distributions of some jet related variables in the muon Z CR before and after applying the reweighting. Figure 7.18 illustrates the improvement in jet related variables. From Figure 7.19, on the other hand, it can be seen that lepton related variables are not affected and are described well before and after the reweighting.

7.10 Comparison of background with signal and data

Figure 7.20 shows the distribution of $m_{\mathrm{LQ}}^{\mathrm{min}}$ variable in SR both for electron and muon channels. For these distributions the Z+jets reweighting, mentioned in Section 7.9, is applied. As an example the distribution for a LQ signal with the mass of 1.4 TeV and $\beta = 1$ is shown there as well. No significant excess could be seen and therefore the statistical interpretation of the results is done which will be discussed in the next Chapter.

The comparison of the amount of events in background, signal and data just before applying the selection of the signal region cuts summarized in Table 7.3 and after implementing them can be found in Table 7.8.

It is interesting that the fraction of the final selected events to the preselected events is rising with increased LQ mass. This can be explained by the fact that a higher LQ mass leads to a higher invariant mass of two leptons in the final state in an average event. So more events will pass the m_{ll} requirement of the SR cut.

Process / LQ mass	Electron channel		Muon channel	
	Preselection	SR	Preselection	SR
$Z \to ee$	86965	829 (001.0%)	-	-
$Z \to \mu\mu$	-	-	111053	931 (000.8%)
$t\bar{t}$	21529	1980 (009.2%)	25222	2338 (009.3%)
Diboson	2549	121 (004.7%)	2996	137 (004.6%)
Single top	1057	189 (017.9%)	1222	203 (016.6%)
Fake electron	2372	216 (009.1%)	-	-
200	612635	109339 (017.8%)	648771	97499 (015.0%)
250	284496	79562 (028.0%)	307399	76434 (024.9%)
300	136152	63438 (046.6%)	146359	62355 (042.6%)
350	68867	47631 (069.2%)	69867	44784 (064.1%)
400	33909	27457 (080.1%)	35298	28140 (079.7%)
450	18641	16634 (089.2%)	19515	16930 (086.8%)
500	11024	10253 (093.0%)	10889	9923 (091.1%)
550	6389	6005 (094.0%)	6333	5933 (093.7%)
600	3910	3728 (095.3%)	3923	3697 (094.2%)
650	2410	2332 (096.8%)	2263	2173 (096.0%)
700	1491	1449 (097.2%)	1442	1400 (097.1%)
750	929	907 (097.6%)	909	886 (097.5%)
800	627	615 (098.1%)	595	579 (097.3%)
850	421	415 (098.6%)	395	385 (097.5%)
900	279	275 (098.9%)	267	262 (098.1%)
950	196	193 (098.5%)	183	180 (098.3%)
1000	133	131 (098.5%)	124	122 (098.4%)
1050	93	92 (098.9%)	88	87 (098.9%)
1100	66	65 (098.5%)	62	62 (100.0%)
1150	46	46 (100.0%)	43	42 (097.7%)
1200	34	34 (100.0%)	31	31 (100.0%)
1250	24	24 (100.0%)	22	21 (095.5%)
1300	17	17 (100.0%)	16	16 (100.0%)
1350	13	13 (100.0%)	12	12 (100.0%)
1400	9	9 (100.0%)	8	8 (100.0%)
1450	7	7 (100.0%)	6	6 (100.0%)
1500	5	5 (100.0%)	5	5 (100.0%)
1600	3	3 (100.0%)	2	2 (100.0%)
1700	2	2 (100.0%)	1	1 (100.0%)
1800	1	1 (100.0%)	1	1 (100.0%)
Data	117048	3242 (002.8%)	150966	3518 (002.3%)

Table 7.8: *Amount of events after the preselection and after the complete selection in SR. The LQ mass for the signal samples is given in GeV. The numbers in brackets give the percentage with respect to the preselection numbers.*

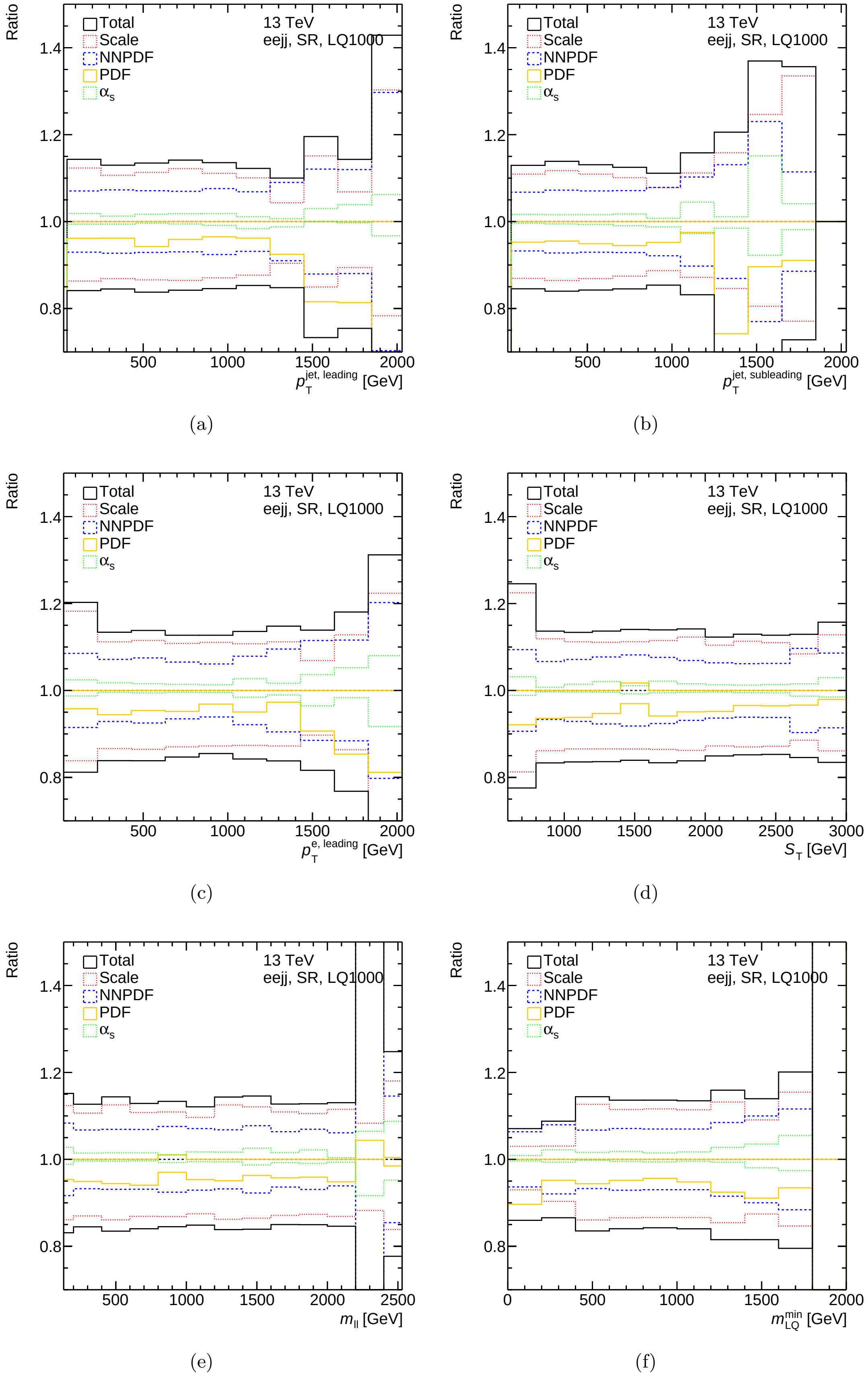

Figure 7.6: *Theoretical uncertainties for a signal with an LQ mass of 1 TeV in the signal region as a function of a number of variables.*

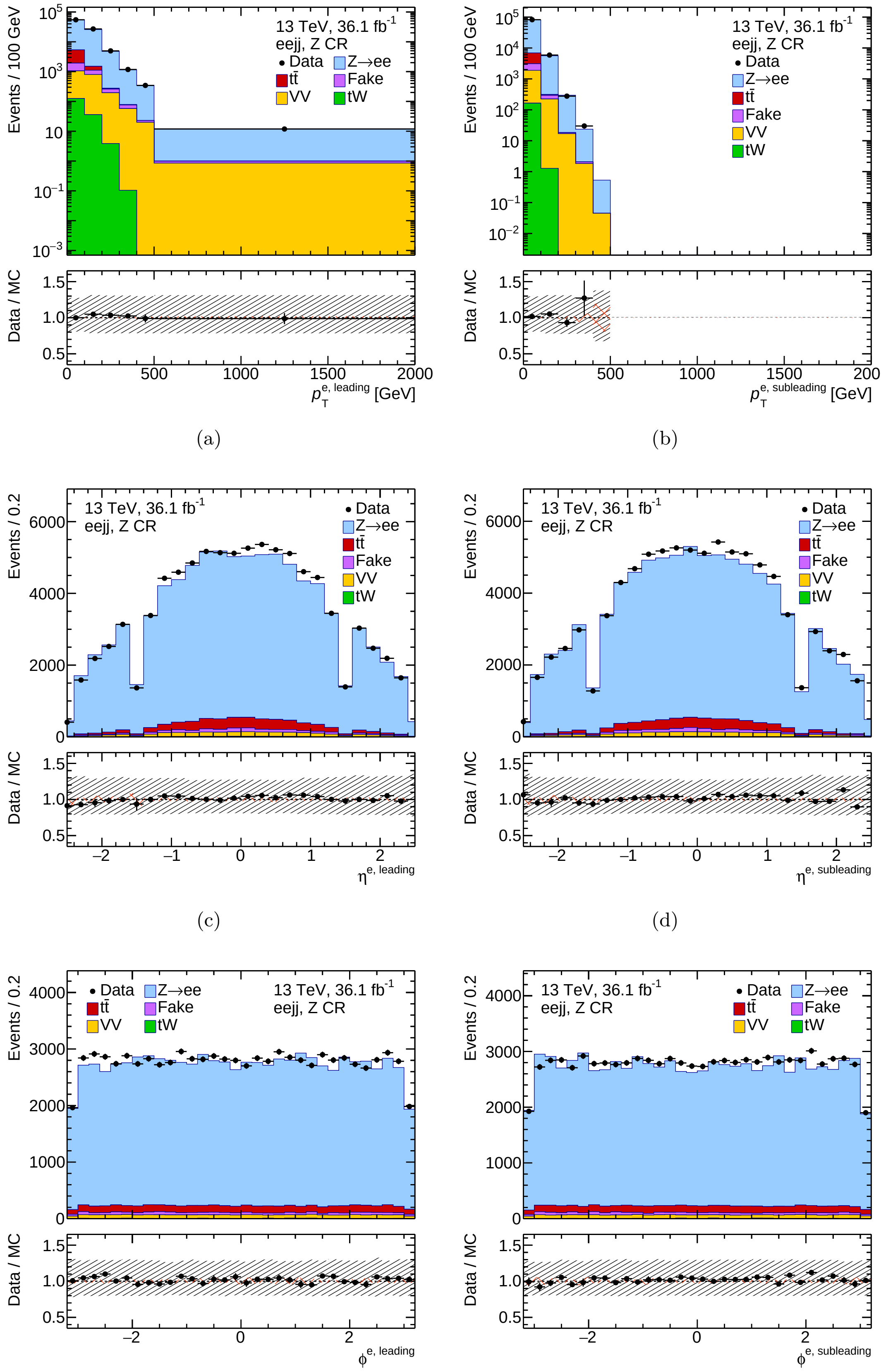

(a) (b)

(c) (d)

(e) (f)

Figure 7.7: *Kinematic distributions of p_T, η and ϕ of the leading electron (left) and the subleading electron (right) in the Z CR for the electron channel. The gray band displays the total systematic uncertainty. The hatched orange band shows the statistical uncertainty in the simulation.*

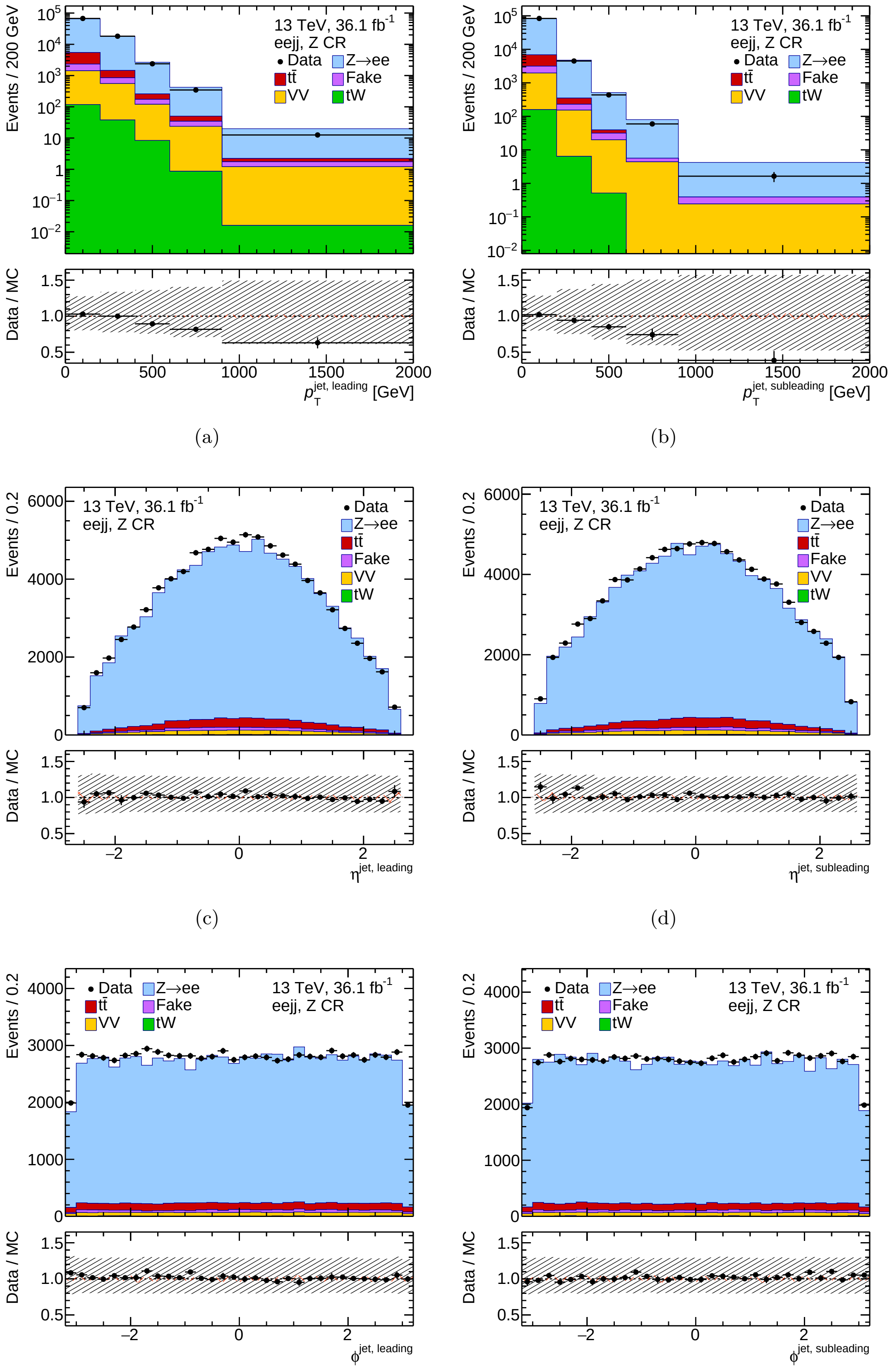

(a) (b)

(c) (d)

(e) (f)

Figure 7.8: *Kinematic distributions of* p_T*,* η *and* ϕ *of the leading jet (left) and the subleading jet (right) in the Z CR for the electron channel. The gray band displays the total systematic uncertainty. The hatched orange band shows the statistical uncertainty in the simulation.*

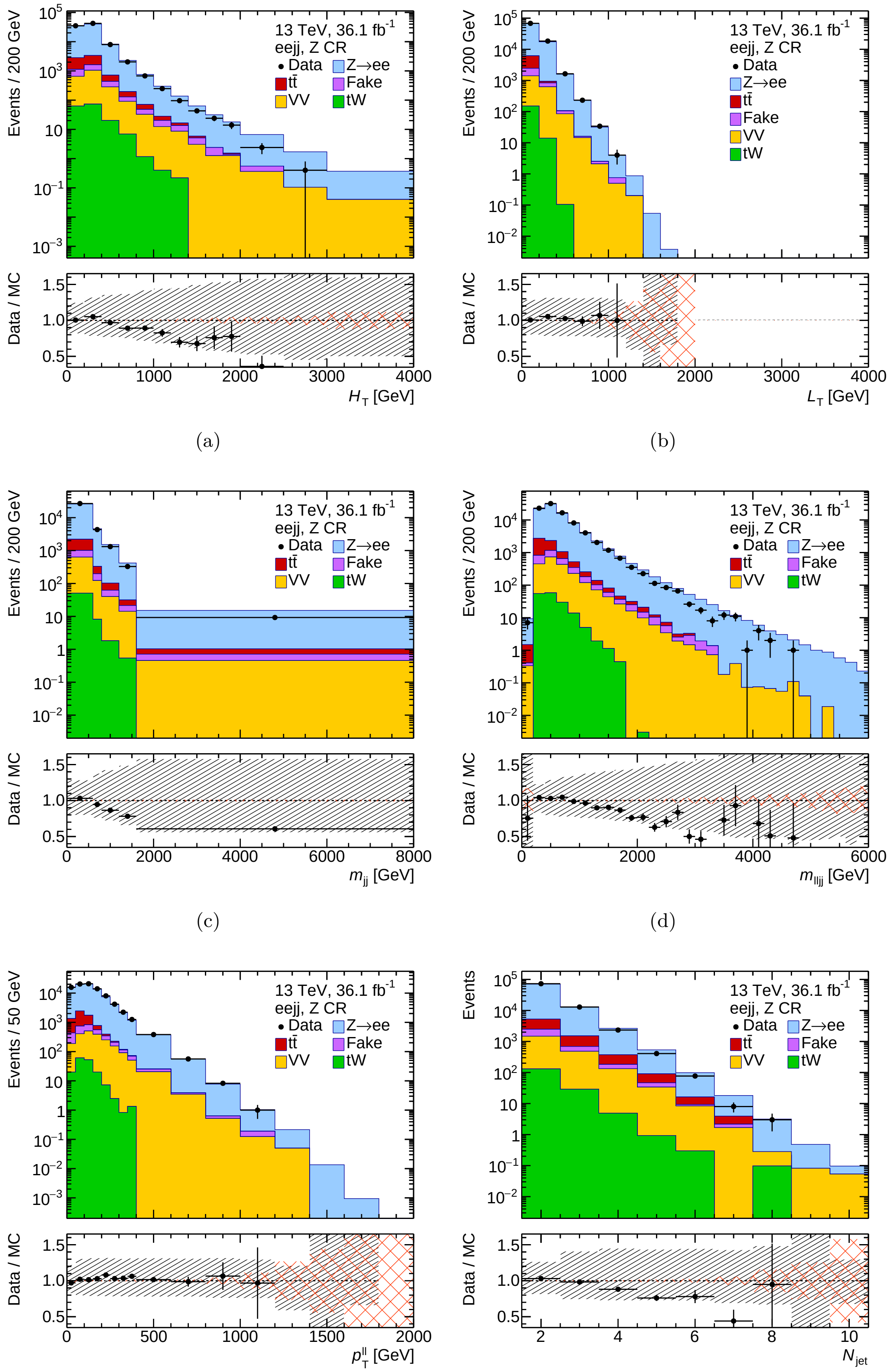

(a)

(b)

(c)

(d)

(e)

(f)

Figure 7.9: *Kinematic distributions of H_T, L_T, m_{jj}, m_{lljj}, p_T^{ll} and N_{jet} (see Table 7.2 for the variable descriptions) in the Z CR for the electron channel. The gray band displays the total systematic uncertainty. The hatched orange band shows the statistical uncertainty in the simulation.*

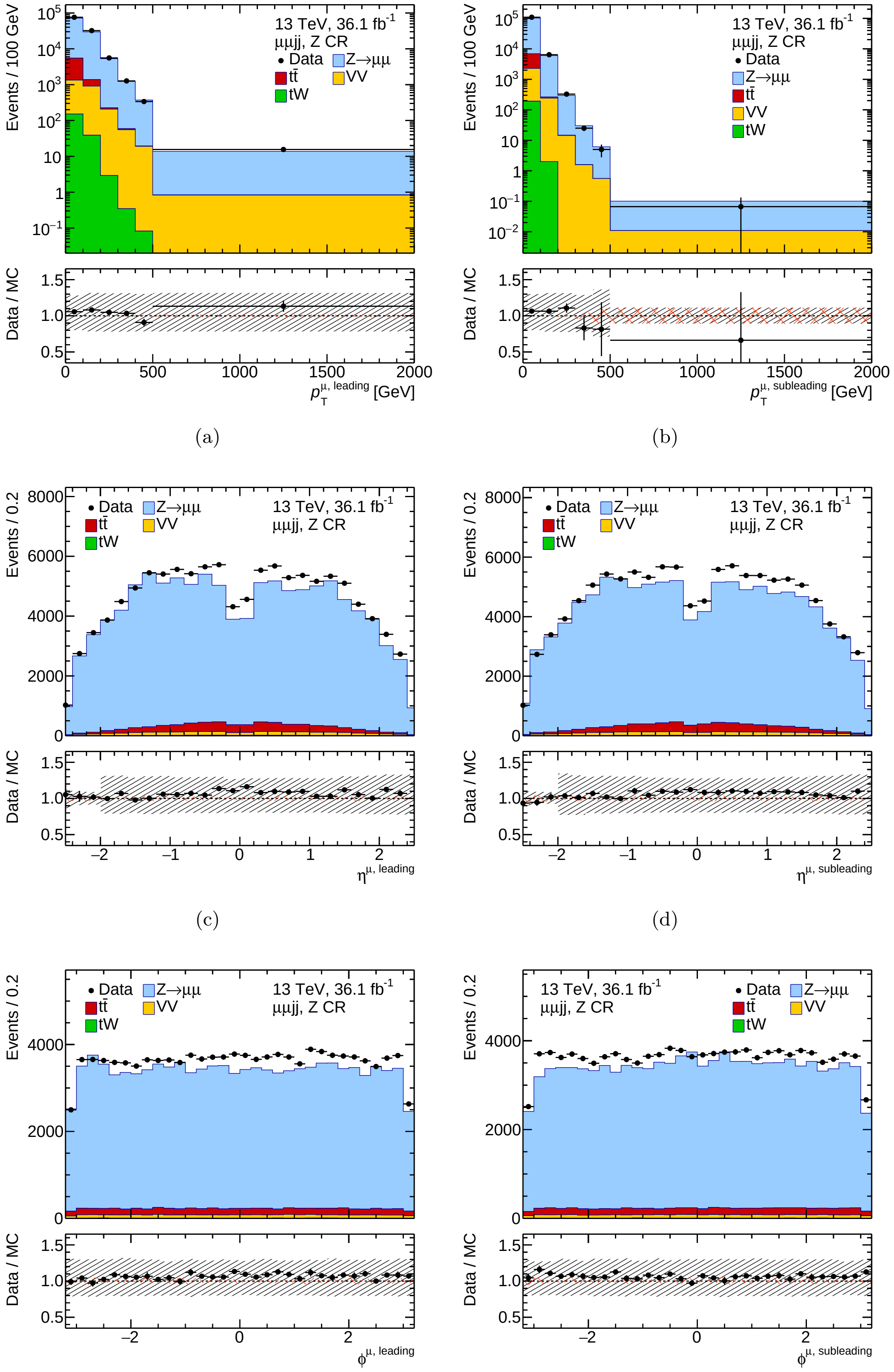

(a) (b)

(c) (d)

(e) (f)

Figure 7.10: *Kinematic distributions of p_T, η and ϕ of the leading muon (left) and the subleading muon (right) in the Z CR for the muon channel. The gray band displays the total systematic uncertainty. The hatched orange band shows the statistical uncertainty in the simulation.*

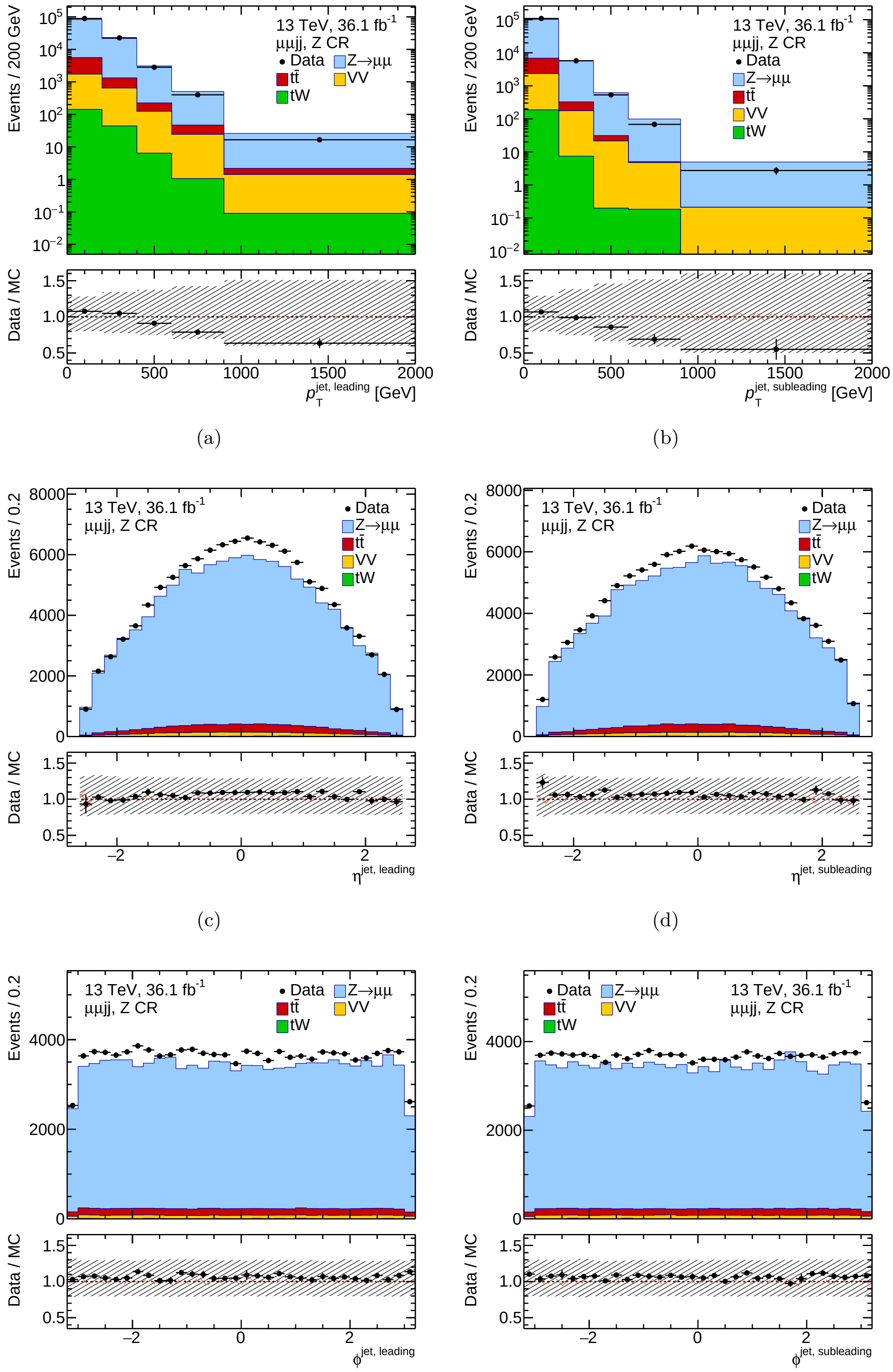

(a) (b)

(c) (d)

(e) (f)

Figure 7.11: *Kinematic distributions of p_T, η and ϕ of the leading jet (left) and the subleading jet (right) in the Z CR for the muon channel. The gray band displays the total systematic uncertainty. The hatched orange band shows the statistical uncertainty in the simulation.*

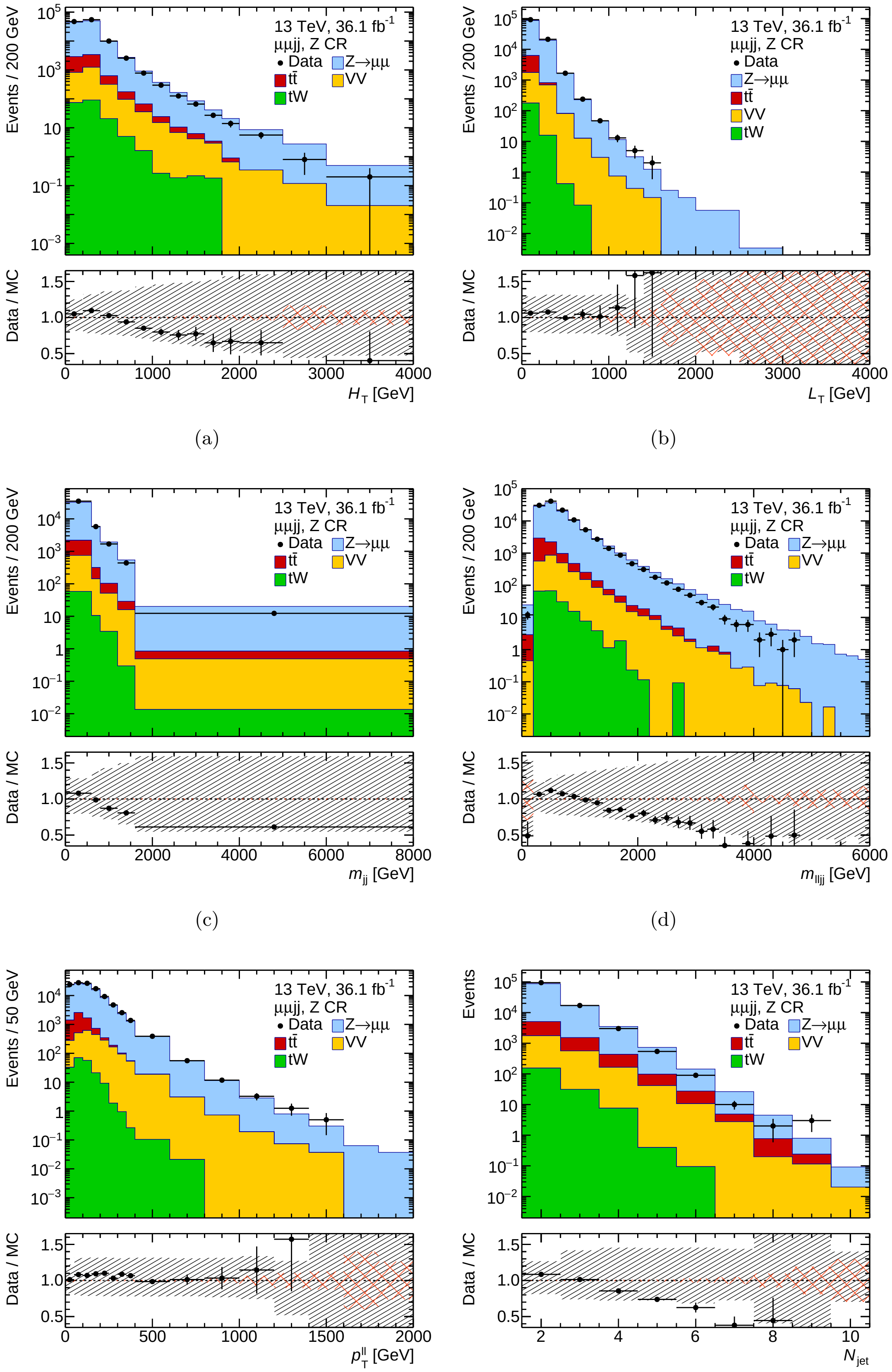

(a) (b)

(c) (d)

(e) (f)

Figure 7.12: *Kinematic distributions of H_T, L_T, m_{jj}, m_{lljj}, p_T^{ll} and N_{jet} (see Table 7.2 for the variable descriptions) in the Z CR for the muon channel. The gray band displays the total systematic uncertainty. The hatched orange band shows the statistical uncertainty in the simulation.*

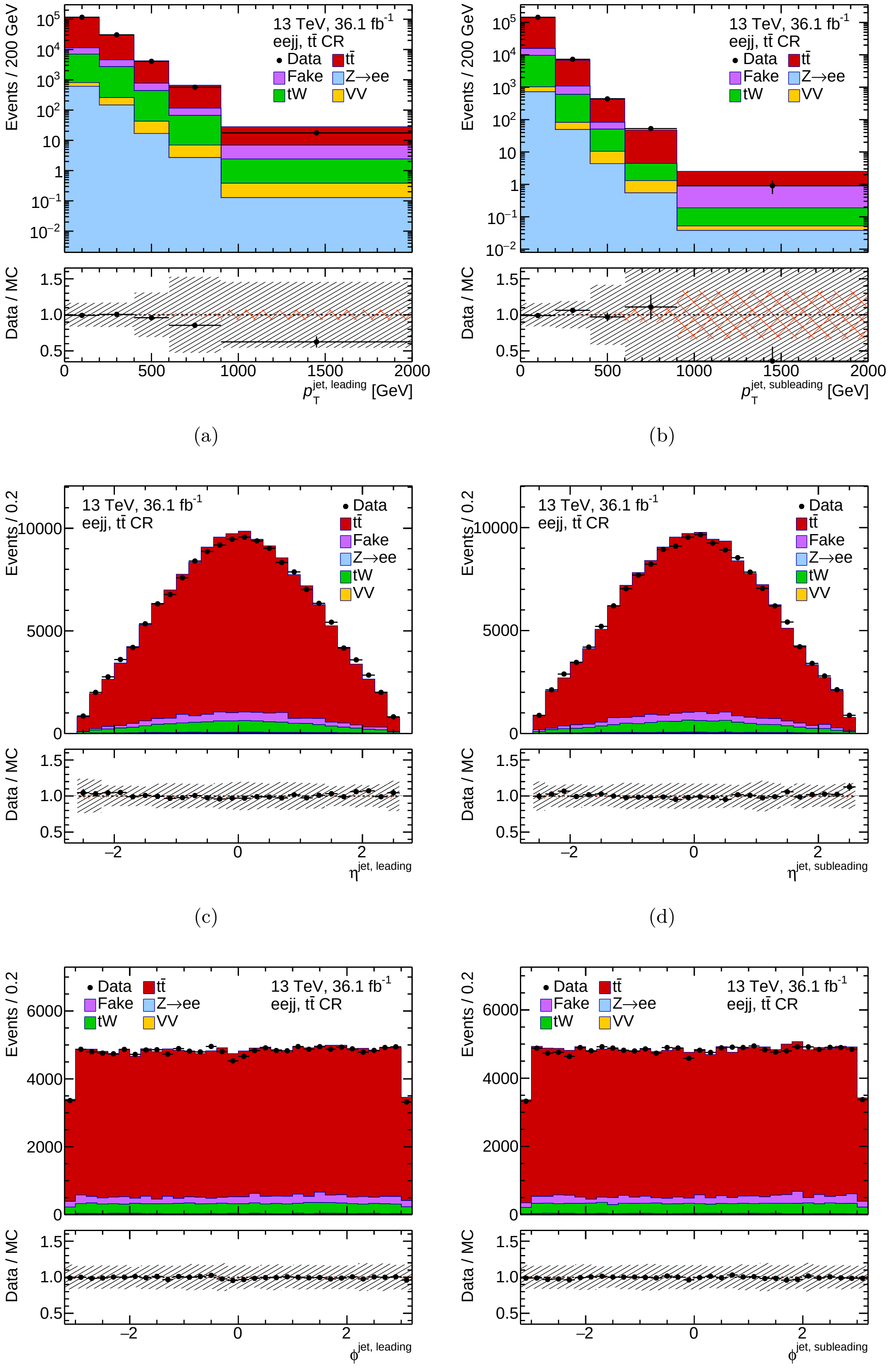

(a) (b)

(c) (d)

(e) (f)

Figure 7.13: *Kinematic distributions of p_T, η and ϕ of the leading jet (left) and the subleading jet (right) in the $t\bar{t}$ CR for the electron channel. The gray band displays the total systematic uncertainty. The hatched orange band shows the statistical uncertainty in the simulation.*

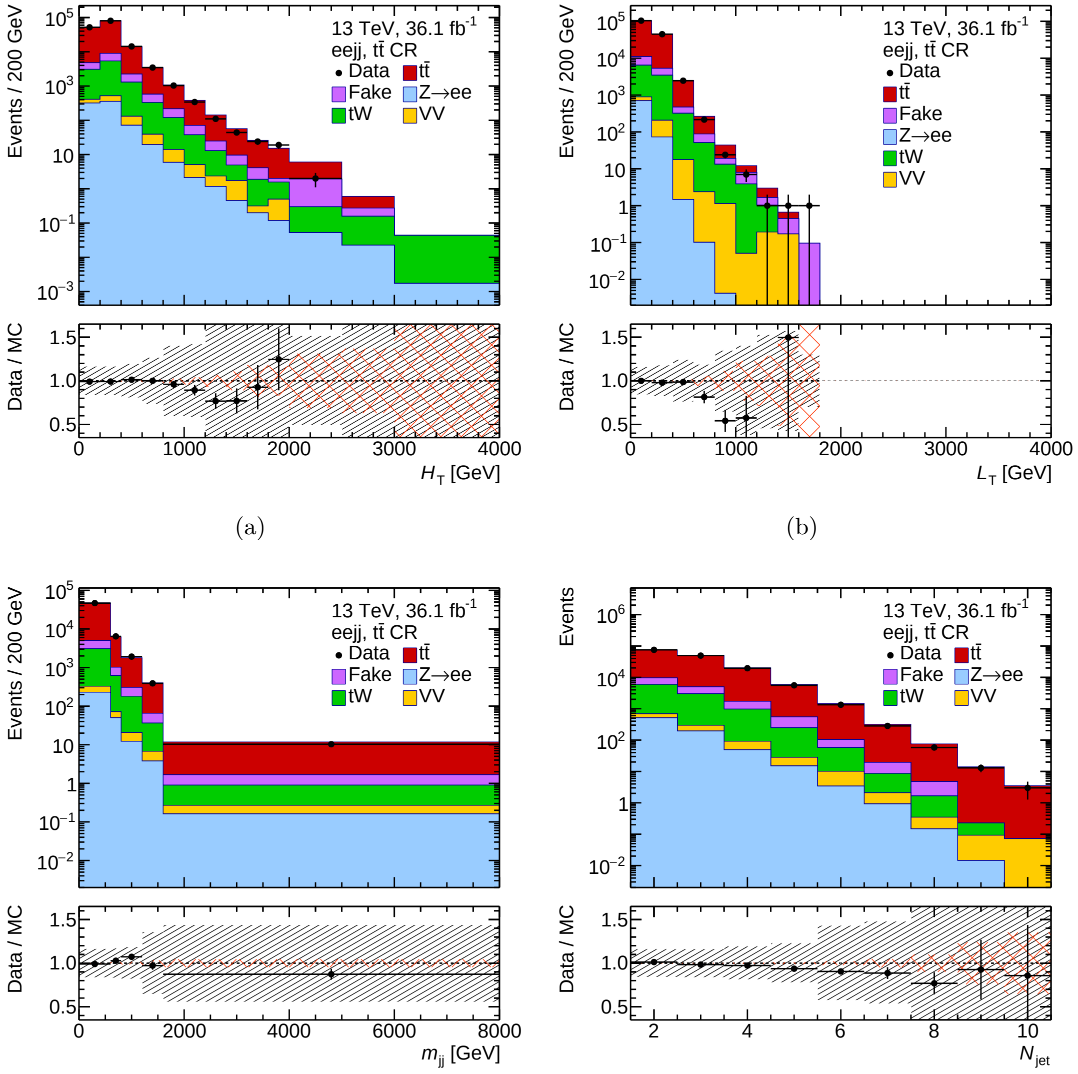

(a)

(b)

(c)

(d)

Figure 7.14: *Kinematic distributions of H_T, L_T, m_{jj} and N_{jet} in the $t\bar{t}$ CR for the electron channel. The gray band displays the total systematic uncertainty. The hatched orange band shows the statistical uncertainty in the simulation.*

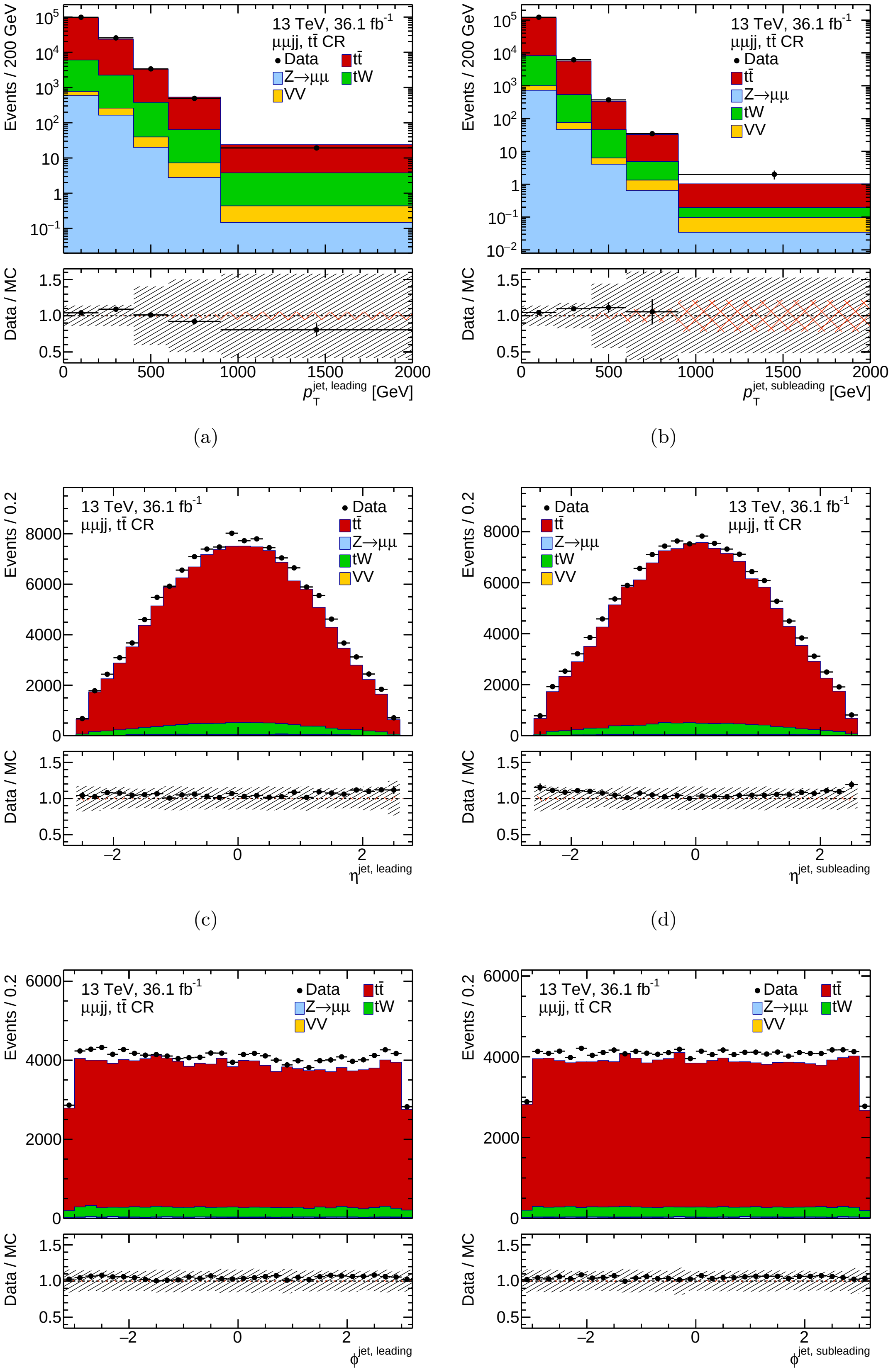

(a) (b)

(c) (d)

(e) (f)

Figure 7.15: *Kinematic distributions of p_T, η and ϕ of the leading jet (left) and the subleading jet (right) in the $t\bar{t}$ CR for the muon channel. The gray band displays the total systematic uncertainty. The hatched orange band shows the statistical uncertainty in the simulation.*

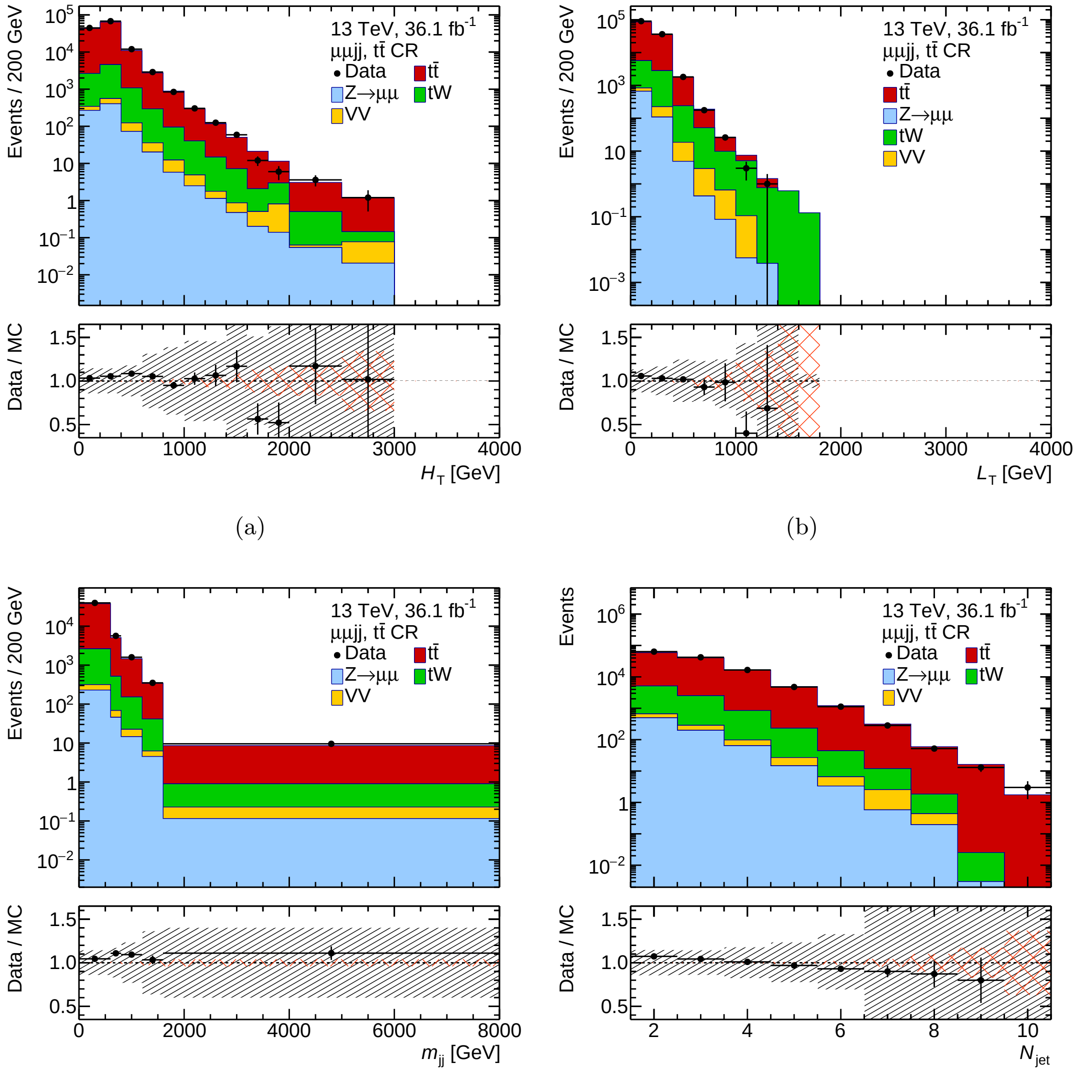

(a)

(b)

(c)

(d)

Figure 7.16: *Kinematic distributions of H_T, L_T, m_{jj} and N_{jet} in the $t\bar{t}$ CR for the muon channel. The gray band displays the total systematic uncertainty. The hatched orange band shows the statistical uncertainty in the simulation.*

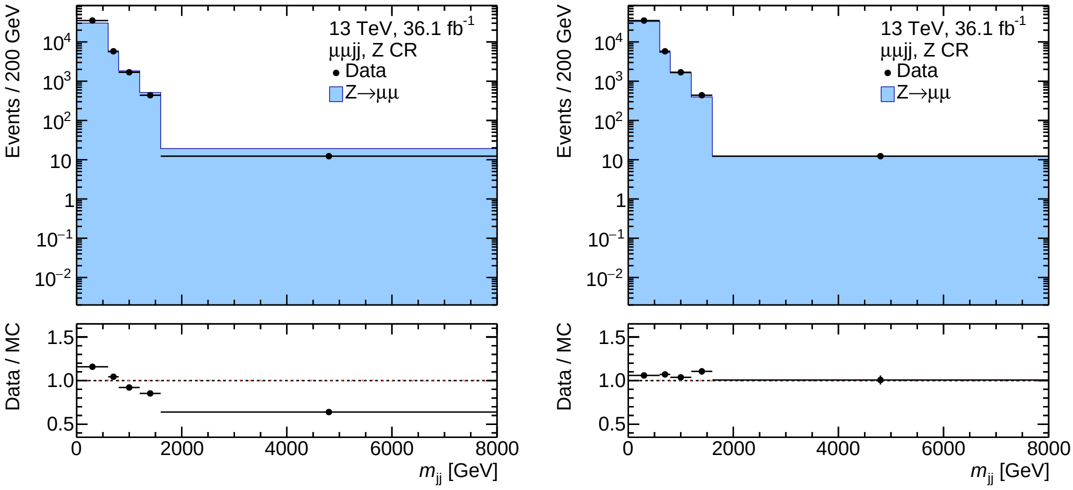

(a)

(b)

Figure 7.17: *Distribution of m_{jj} before (left) and after (right) the reweighting for the Z CR.*

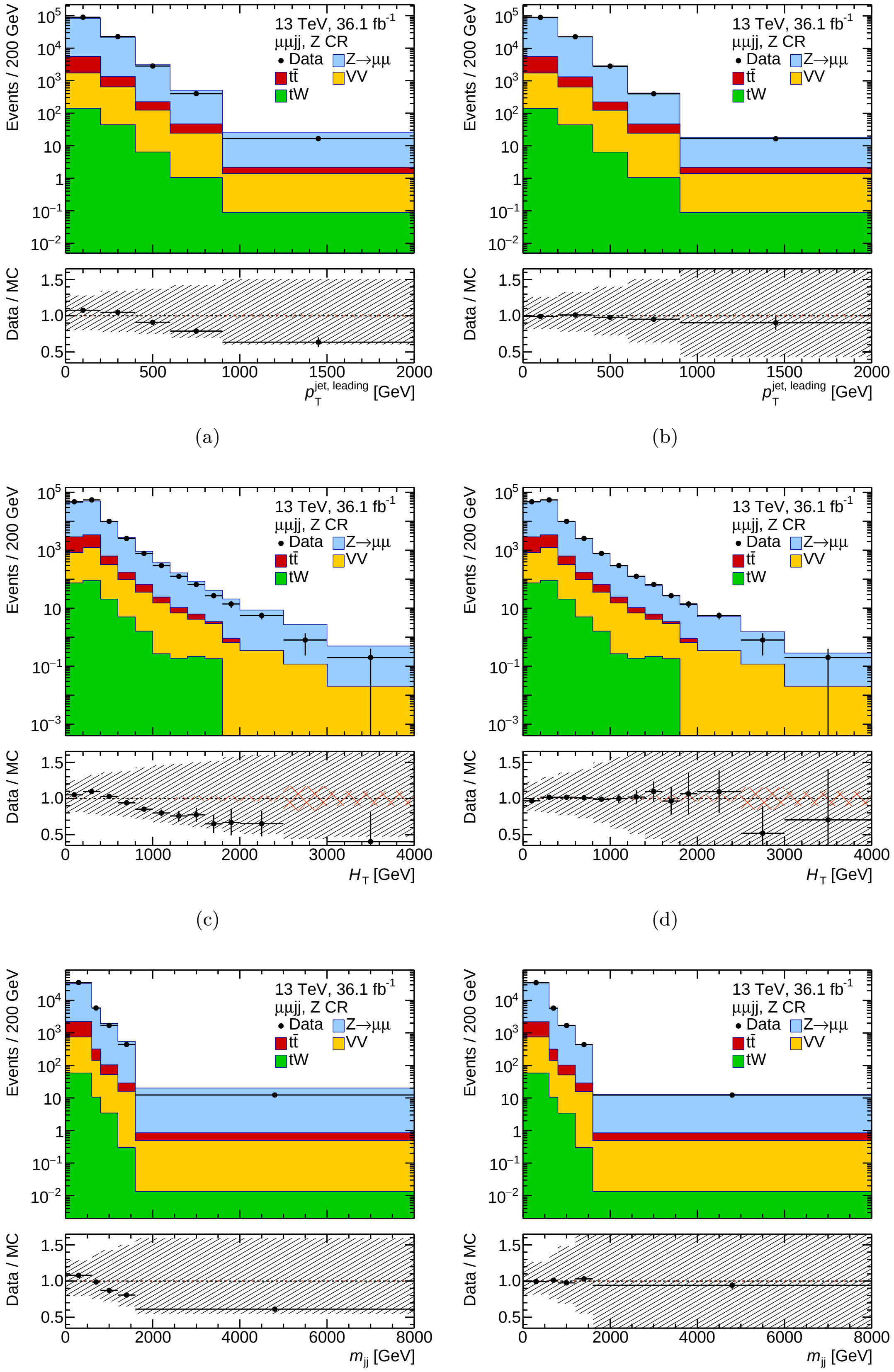

(a) (b)

(c) (d)

(e) (f)

Figure 7.18: *Distributions of* $p_T^{jet,\ leading}$, H_T *and* m_{jj} *in the* Z *CR for the muon channel before (left) and after (right) reweighting in* m_{jj}. *The gray band displays the total systematic uncertainty. The hatched orange band shows the statistical uncertainty in the simulation.*

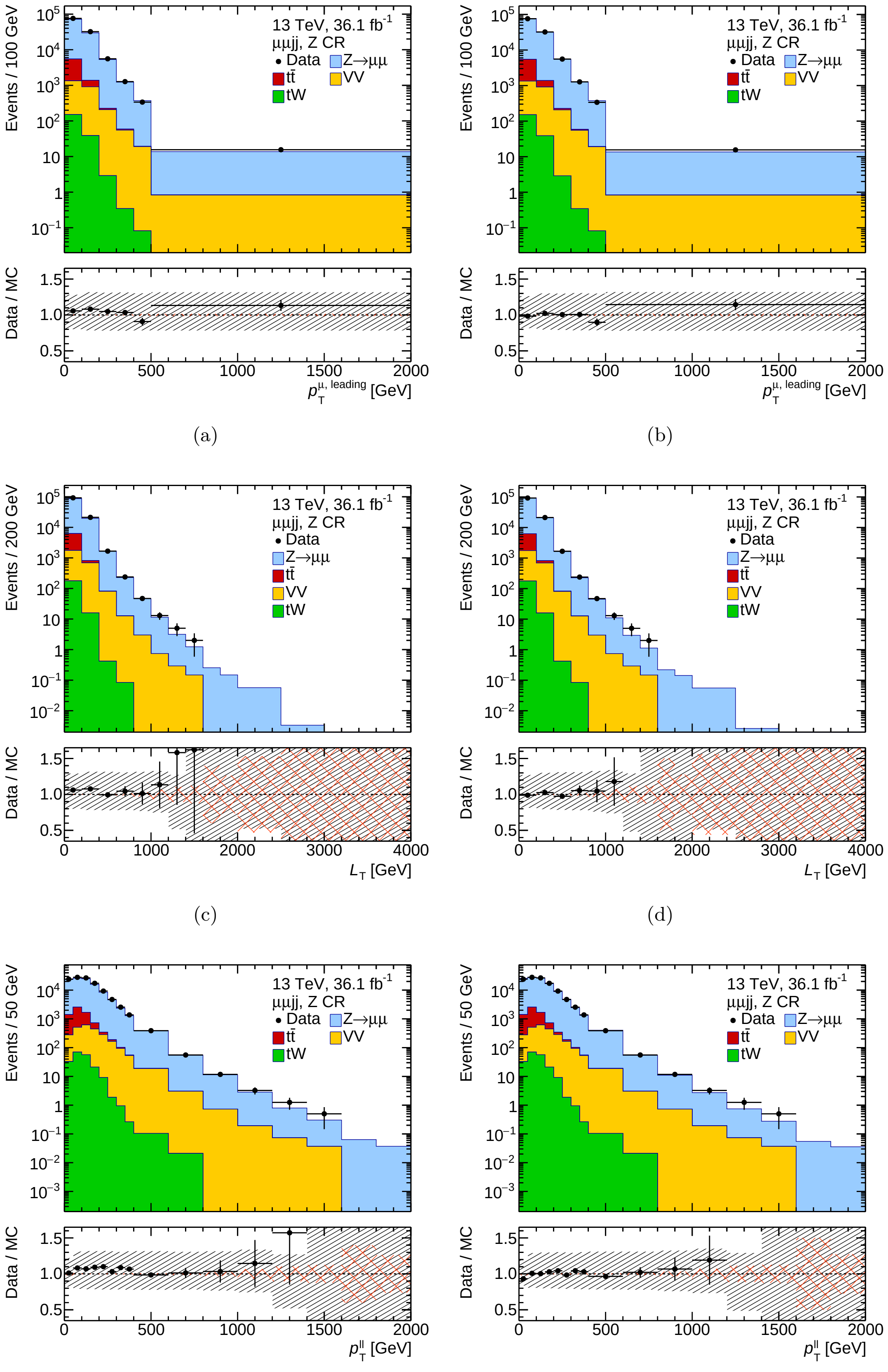

(a) (b)

(c) (d)

(e) (f)

Figure 7.19: *Distributions of* $p_T^{\mu,\ leading}$, L_T *and* p_T^{ll} *in the* Z *CR for the muon channel before (left) and after (right) reweighting in* m_{jj}. *The gray band displays the total systematic uncertainty. The hatched orange band shows the statistical uncertainty in the simulation.*

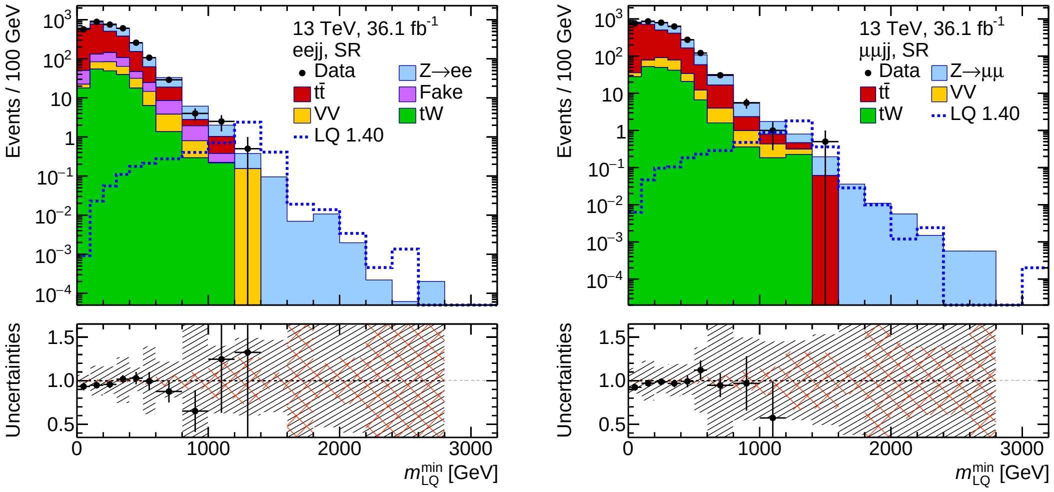

(a)

(b)

Figure 7.20: *Distributions of* m_{LQ}^{min} *variable in the SR for the (a) electron and (b) muon channel. The gray band displays the total systematic uncertainty. The hatched orange band shows the statistical uncertainty in the simulation.*

Chapter

8 Statistical interpretation

> *Your eyes can deceive you. Don't trust them.*
> Obi-Wan Kenobi from Star Wars: Episode IV - A New Hope

The interpretation of the analysis results is performed using the profile likelihood method, described in Section 8.1.3. This Chapter presents more details on the procedures, which are applied in the statistical interpretation. Section 8.1 describes the theory behind the limit setting procedure based on References [218–220], followed by the desciption of the systematics treatment presented in Section 8.2. Finally, Sections 8.3 and 8.4 summarize the results after the fit and after the actually limit setting, respectively. Both results are obtained using the HistFitter software framework for statistical analysis [221].

8.1 Theoretical background

8.1.1 Methodology and implementation aspects

The description of signal and backgrounds is done by a binned Probability Density Function (PDF), which is built using either two control regions (CRs) or one signal region (SR) in the electron and muon channel each. The two CRs are the Z+jets CR and a $t\bar{t}$ CR, as introduced in Section 7.5. Uncertainties are integrated in the PDFs as nuisance parameters $\boldsymbol{\theta}$. The signal strength μ_{SIG} is included in the PDF for the fit to the SR as parameter of interest.

The SR pushes the signal extraction forward, but it also adds negligible constraints on the background parameters. The CRs are enriched in background and have a negligible signal contamination. Therefore they are used for the normalisation of the predicted backgrounds to data. These adjustments of the normalisations in this setup are achieved by pulls of nuisance parameters. The definition of the different regions are given in Table 7.3.

There are two stages of the fit implementation. First, the fit is performed only including the CRs in order to extract the normalisation factors for the two main backgrounds. Then, the application of these normalisation factors in the SR is performed in the form of Gaussian nuisance parameters, which allow to change the respective background normalisation. However, there is no transfer of the constraints on other nuisance parameters coming from the CRs. In principle there is some loss of information in this way, but this procedure has more advantages than disadvantages by the simplification of the final fit. An important advantage is that this simplification allows to reduce the CPU time significantly, which is required for the fit execution and production of the diagnostic plots like PLL curves. Additionaly, the difficulties arising from the large CR statistics of the signal extraction fit are removed with this simplification.

In the Z CR one bin in m_{jj} is used covering the region from 0 GeV to 4000 GeV. In the $t\bar{t}$ CR one bin in $p_{\text{T}}^{\text{jet, leading}}$ is used covering the region from 0 GeV to 1500 GeV. In the SR, four bins in total in $m_{\mathrm{LQ}}^{\mathrm{min}}$ are used: three bins of 200 GeV width, covering the region from 600 GeV to 1200 GeV and one bin of 400 GeV width, covering the region from 1200 GeV to 1600 GeV.

All the statistical and systematic uncertainties were included by default as nuisance parameters, which are typically constrained by a Gaussian. Each constraint has the width, which is specified according to the prescription of each uncertainty.

When the PDF is fitted to data the optimal value and error of the signal strength and nuisance parameters including their correlations are calculated at the same time. In case the fit to data is minimally constrained, only the signal strength is adjusted, while the nuisance parameters are simply propagating the effect of the uncertainties. However, if the fit is over-constrained, then the nuisance parameters (their mean value and error) can be adjusted as well for the optimization of the description of data.

8.1.2 The likelihood

In order to constrain the MC expectation and the uncertainties with data a maximum likelihood fit is used. Another application of the likelihood covers the search for the presence of a signal using the CRs and the SR:

$$L\left(\mu, \boldsymbol{\theta}\right) = \prod_{j=1}^{N} \frac{\left(\mu s_j\left(\boldsymbol{\theta}\right) + b_j\left(\boldsymbol{\theta}\right)\right)^{n_j}}{n_j!} e^{-\left(\mu s_j(\boldsymbol{\theta}) + b_j(\boldsymbol{\theta})\right)} \prod_{l=1}^{M} \frac{u_l^{m_l}\left(\boldsymbol{\theta}\right)}{m_l!} e^{-u_l(\boldsymbol{\theta})}. \tag{8.1}$$

Here, N is the number of bins in the SR; in this analysis $N = 4$. M is the number of control regions; $M = 2$ in this analysis.

In Equation 8.1,

$$\mu s_i + b_i = E\left[n_i\right] \tag{8.2}$$

is the expectation of the Poisson distributed value n_i.

$$\mathbf{n} = \left(n_1, ..., n_N\right) \tag{8.3}$$

are the entries of a histogram with N bins built from the $m_{\mathrm{LQ}}^{\mathrm{min}}$ distribution in a SR.

$$u_l\left(\boldsymbol{\theta}\right) = E\left[m_l\right] \tag{8.4}$$

is the expectation of the Poisson distributed value m_l of events from the m_{jj} distribution in Z CR or the $p_{\mathrm{T}}^{\mathrm{jet,\ leading}}$ distribution in $t\bar{t}$ CR, so $l \in \left(Z \text{ CR},\ t\bar{t} \text{ CR}\right)$.

8.1.3 Hypothesis testing

Profile likelihood

The existence of a signal in a given dataset with predictions for signal and background contributions can be statistically tested. For this test the background-only null hypothesis against the background and signal alternative hypothesis are tested. According to the Neyman-Pearson lemma, the most powerful hypothesis test at a specified significance level is provided by the likelihood ratio

$$\lambda\left(\mu\right) = \frac{L\left(\mu, \hat{\hat{\boldsymbol{\theta}}}\right)}{L\left(\hat{\mu}, \hat{\boldsymbol{\theta}}\right)}, \tag{8.5}$$

where $\hat{\mu}$ and $\hat{\boldsymbol{\theta}}$ are the estimators, which maximise the likelihood, and $\hat{\hat{\boldsymbol{\theta}}}$ is the estimator, which maximises the likelihood for a given μ. The significance level indicates the probability for the rejection of the null hypothesis, if this hypothesis is true. However, the negative logarithm of this ratio is commonly used in order to try to reject the background hypothesis ($\mu = 0$) using

$$q_0 = \begin{cases} -2 \cdot \ln\lambda\left(0\right), & \hat{\mu} \geq 0 \\ 0, & \hat{\mu} < 0 \end{cases} \tag{8.6}$$

as a test statistic. The discrepancy between data and simulation for large values of q_0 can be measured by the calculation of the p-value and the significance, which are determined by

$$p_0 = \int_{q_{0,\text{observed}}}^{\infty} f\left(q_0|0\right) \mathrm{d}q_0 \text{ and } Z_0 = \Phi^{-1}\left(1 - p_0\right), \tag{8.7}$$

respectively, where $q_{0,\text{observed}}$ is the observed value of q_0, $f\left(q_0|0\right)$ is the probability density function of q_0 with $\mu = 0$, and Z_0 is the significance of the measurement using the inverse of the cumulative standard Gaussian function Φ.

For the usage of a profile likelihood fit to data the likelihood ratio is applied in order to gain best fit values for parameters of interest. These values are determined as values of parameters, which either minimise the negative logarithm of the likelihood ratio or maximise the likelihood ratio. A fit of this kind is performed across multiple CRs and SR in a full analysis. The effects of nuisance parameters are then constrained on the optimal way.

Limit setting

There exists another statistical method for the search of a signal, which is setting upper limits on the signal strength using a specified confidence level (CL) $(1 - \alpha)$, where α is the probability for the acceptance of the null hypothesis, if this hypothesis is incorrect. A CL represents the probability that an upper limit containing the true, but unknown value of the signal strength, is determined in $(1 - \alpha)$ of all measurements. A CL with the value of 95% is commonly used in particle physics. There is one more advantage of an upper limit setting. It can be used in order to compare the performance of different methods used for the signal search.

Using the Wald approximation (which requires the knowledge of the standard deviation) [222] a simplified test statistic

$$q_\mu = \begin{cases} \frac{(\mu - \hat{\mu}^2)}{\sigma^2}, & \hat{\mu} < \mu \\ 0, & \hat{\mu} > \mu \end{cases} \tag{8.8}$$

can be used for the calculation, where the best estimator $\hat{\mu}$ follows a Gaussian distribution with a central value and a standard deviation of σ. A formula for an upper limit on the signal strength at a specified CL of $(1 - \alpha)$ is an outcome of this simplification.

The test statistics

Equation 8.9 displays the test statistics, which is used for the exclusion fit in this thesis:

$$q_\mu = \begin{cases} -2 \cdot \ln\frac{L\left(\text{data}|\mu,\hat{\hat{\theta}}_\mu\right)}{L\left(\text{data}|\hat{\mu},\hat{\theta}\right)}, & \hat{\mu} < \mu \\ 0, & \hat{\mu} > \mu \end{cases}. \tag{8.9}$$

Here, $\hat{\mu}$ and $\hat{\theta}$ represent, respectively, the values of the signal strength and of the nuisance parameters, which maximise the likelihood. $\hat{\hat{\theta}}_\mu$ describe the values of the nuisance parameters, which maximise the likelihood for a given signal strength μ.

8.2 Treatment of systematic uncertainties

It is disallowed in this analysis, that the nuisance parameters corresponding to systematic uncertainties change the overall normalisation of the backgrounds which they affect. This restriction is selected in order to eliminate degeneracies with the background normalisation factors, which are extracted from the CRs. This leads to the fact, that the uncertainties may change the relative size of a given background in different regions, but, however, the total amount remains unchanged. This makes the uncertainties to be defined as shape uncertainties, although single-bin CRs are used in the statistical evaluation. In order to get this, the histograms corresponding to the systematically varied distributions are normalised on the way, that the total event number summed over all regions is conserved. The histograms were normalized in each bin i of the $m_{\mathrm{LQ}}^{\mathrm{min}}$, m_{jj} and $p_{\mathrm{T}}^{\mathrm{jet,\ leading}}$ distributions using the following formula:

$$\text{norm unc.}_i = \text{unc.}_i \times \frac{N_{\mathrm{nom}}}{N_{\mathrm{var}}}, \tag{8.10}$$

where unc.$_i$ (norm unc.$_i$) is the relative uncertainty in bin i before (after) the normalization and N_{nom} (N_{var}) is the sum of the events in all bins of $m_{\mathrm{LQ}}^{\mathrm{min}}$, m_{jj} and $p_{\mathrm{T}}^{\mathrm{jet,\ leading}}$ (four bins in $m_{\mathrm{LQ}}^{\mathrm{min}}$ and one bin each in m_{jj} and $p_{\mathrm{T}}^{\mathrm{jet,\ leading}}$, leading to six bins in total) for the nominal distribution (variation either in up or in down direction). The normalisation uncertainty is introduced via the normalisation scale factors and their uncertainties.

Experimental uncertainties are considered to be fully correlated between all processes and all regions, which are included in a given fit. Theory and modelling uncertainties are considered to be fully correlated between different regions in a fit, but, however, uncorrelated between processes.

The full list of systematics (with their corresponding names in the brackets used for example in Figures 8.2 and 8.3), which are all double-sided, is presented in the following:

- electron energy resolution (EG_Reso_All),
- electron isolation scale factor (EL_IsoSF),
- electron identification scale factor,
- electron reconstruction scale factor,
- electron trigger scale factor,
- muon momentum scale,
- muon momentum resolution from Inner Detector measurement (MUON_Reso_ID),
- muon momentum resolution from Muon Spectrometer measurement (MUON_Reso_MS),
- muon trigger efficiency scale factor, statistic uncertainty of the extraction method,
- muon trigger efficiency scale factor, systematic uncertainty of the extraction method,
- muon efficiency scale factor, statistic uncertainty of the extraction method (MUON_EffSF_SYST),
- muon efficiency scale factor, systematic uncertainty of the extraction method,
- muon isolation scale factor, statistic uncertainty of the extraction method,
- muon isolation scale factor, systematic uncertainty of the extraction method,

- muon track-to-vertex association scale factor, statistic uncertainty of the extraction method,
- muon track-to-vertex association scale factor, systematic uncertainty of the extraction method,
- scale of the muon momentum, the uncertainty originating from residual charge-dependent bias after track correction (MUON_Sagitta_Resbias),
- scale of the muon momentum, the uncertainty associated with the track correction applied during reconstruction (MUON_Sagitta_Rho),
- jet energy scale, η intercalibration (JES_EtaIntercalibration),
- jet energy scale, Nuisance Parameter 1 (JES_GroupedNP_1),
- jet energy scale, Nuisance Parameter 2 (JES_GroupedNP_2),
- jet energy scale, Nuisance Parameter 3 (JES_GroupedNP_3),
- jet energy resolution (JER_SingleNP),
- b-tagging (in)efficiency scale factor, b jets (btagSF_B),
- b-tagging (in)efficiency scale factor, c jets (btagSF_C),
- b-tagging (in)efficiency scale factor, light jets (btagSF_L),
- $t\bar{t}$ modelling: generator comparison (ttbar_unc_aMcAtNloPy8),
- $t\bar{t}$ modelling: shower description (ttbar_unc_PhH7),
- $t\bar{t}$ modelling: radiation parameter variations (ttbar_unc_radiation),
- $t\bar{t}$ modelling: PDF uncertainty (ttbar_unc_PDF),
- Z+jets: NNPDF intra-PDF uncertainty (Zll_unc_NNPDF),
- Z+jets: interPDF uncertainty (Zll_unc_interPDF),
- Z+jets: α_s uncertainty (Zll_unc_α_s),
- Z+jets: scale uncertainty (Zll_unc_scale),
- Z+jets: reweighting uncertainty (Vjets_unc_reweighting).

The $+1\sigma$ boundary of the jet energy resolution uncertainty band is calculated by increasing the energy resolution by 1σ. Since the jet energy resolution can not be decreased, the uncertainty is symmetrized in order to get the -1σ boundary of the uncertainty band.

In order to further simplify the setup and speed up limit calculation, systematics that are smaller than 3% in all bins are not included in the fit.

In the electron channel, this applies to the following list of nuisance parameters:

- identification scale factor,
- reconstruction scale factor,
- trigger scale factor.

And the following list of nuisance parameters applies to the muon channel:

- momentum scale,
- reconstruction scale factor (statistic uncertainty on the extraction method),
- isolation scale factor (statistic and systematic uncertainty on the extraction method),
- trigger scale factor (statistic and systematic uncertainty on the extraction method),
- track-to-vertex association scale factor (statistic and systematic uncertainty on the extraction method).

All systematics except the ones for fake electron background in electron channel were normalized using the formula 8.10. If the relative variations were higher than 100%, they were truncated to be exactly 100%. Finally, all systematics were symmetrized in each bin i of the $m_{\mathrm{LQ}}^{\mathrm{min}}$, m_{jj} and $p_{\mathrm{T}}^{\mathrm{jet,\ leading}}$ distributions using following description:

$$u_s = +A,\ d_s = -A \text{ with } A = \max\left(\mathrm{abs}\left(u\right), \mathrm{abs}\left(d\right)\right), \tag{8.11}$$

where u (d) is the relative up (down) variation before symmetrization and u_s (d_s) is the relative up (down) variation after symmetrization in a bin i.

Low statistics in the simulations in the signal region can lead to unphysical fluctuations and spikes in the systematic uncertainties. Thus, the systematics in the signal region have been smoothed as a function of $m_{\mathrm{LQ}}^{\mathrm{min}}$ before being fed to the fit. The smoothing[1] is done by inspecting each systematic as a function of $m_{\mathrm{LQ}}^{\mathrm{min}}$ and replacing the size in all bins with the size from first bin (from 600 GeV to 800 GeV), since the uncertainty from the first bin fluctuates less compared to the other bins. Figure 8.1 shows an example of the symmetrization and smoothing result.

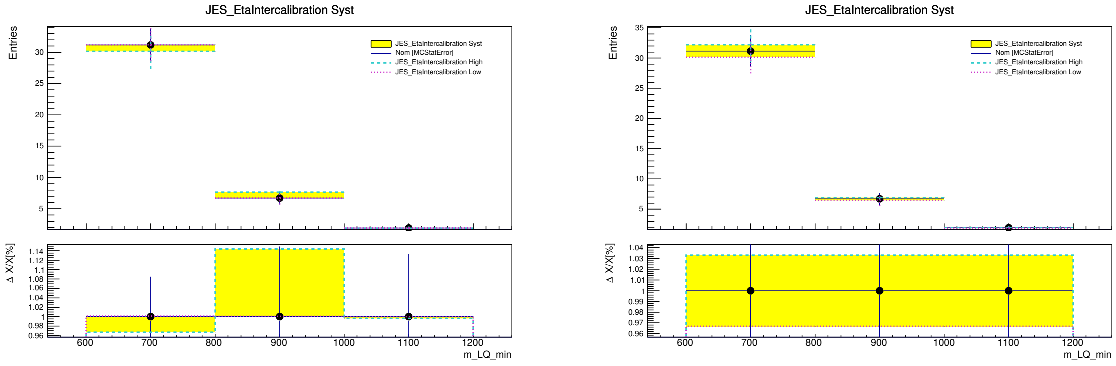

(a) (b)

Figure 8.1: *Jet energy scale (η intercalibration) uncertainty as a function of m_{LQ}^{min} before (left) and after (right) symmetrization and smoothing.*

In the electron channel only the following nuisance parameters were smoothed:

- all nuisance parameters in the signal,
- pile-up weight systematic for all contributions,
- reweighting of Z+jets uncertainty and all Z+jets modelling uncertainties for Z/γ^*+jets contribution,

---

[1] Actually, the word „smoothing“ is not the best one for the description of what is actually done, but since it was used internally during the analysis, where in the early stages the procedure was indeed similar to the real smoothing, it was kept at the end for simplicity.

- electron energy scale, PDF, generator variation, radiation for $t\bar{t}$ contribution.

In the muon channel, all nuisance parameters were smoothed except the following ones:

- reconstruction efficiency scale factor, systematic for all background contributions,
- 3^{rd} set of the JES, reweighting of Z+jets uncertainties, α_S, inter-PDF, scale Z+jets modelling uncertainties for Z/γ^*+jets contribution,
- generator variation for $t\bar{t}$ contribution.

8.3 Fit results

Figure 8.2(a) shows the signal strength and nuisance parameters after the combined fit to the SR and CRs for the example of a leptoquark with mass of 1.4 TeV in electron channel. The yellow marked range corresponds to a size of 1σ for reference. Figure 8.2(b) shows the correlation matrix of the fit parameters. Most nuisance parameters are not pulled (agree between observed data and background estimates) and remain unconstrained (the size of error bar remain 1σ). The pulls and constraints of the parameters corresponding to the (large) modelling uncertainties are not unexpected. The pull in the α`_puWeight_syst` NP is probably caused by a(n) (anti-)correlation of this parameter with the γ`_stat_SR1_m_LQ_min_bin_1` and $t\bar{t}$ generator variation uncertainty parameter. It is important that the signal strength parameter is essentially uncorrelated to all other nuisance parameters.

Figure 8.3(a) shows the signal strength and nuisance parameters after the combined fit to the SR and CRs for the example of a leptoquark with mass of 1.4 TeV in muon channel. Figure 8.3(b) shows the correlation matrix of the fit parameters. Here, most nuisance parameters are not pulled and remain unconstrained, and the signal strength parameter is uncorrelated to all other nuisance parameters as well.

Figure 8.4 shows the m_{jj} distribution in Z CR and $p_{\mathrm{T}}^{\text{jet, leading}}$ distribution in $t\bar{t}$ CR, both in electron channel, before and after the fit. Since both distributions contain only one bin, there is no shape change. As depicted in Figure 8.4(b) the MC simulated background describes the data better after the fit as expected. Figure 8.5 shows the $m_{\mathrm{LQ}}^{\mathrm{min}}$ distribution in the SR in the same channel. The distribution is separated into two different „regions“ due to different bin size. The first „region“ contains three bins with 200 GeV size each and after the fit the shape here is better described within the uncertainties than before fitting. The second „region“ contains only one bin with 400 GeV size and again the data is well described by the MC simulated background. The total uncertainty increases a bit in this last region after the fit.

Figure 8.6 shows the m_{jj} distribution in Z CR and $p_{\mathrm{T}}^{\text{jet, leading}}$ distribution in $t\bar{t}$ CR, both in muon channel, before and after the fit. The observation from the electron channel holds also in this channel. Figure 8.7 shows the $m_{\mathrm{LQ}}^{\mathrm{min}}$ distribution comparison in the SR in the muon channel, following the same structure as Figure 8.5. It can be seen, that the total uncertainty decreased in all three bins of the first „region“, but increased a bit in the single bin of the second „region“ due to the fit. Furthermore in the last two bins (of four in total) the data lies outside of the total uncertainty, which is also related to the negative μ_{SIG} value shown in Figure 8.3(a) meaning that for this particular fit configuration, the best agreement with data is achieved by „subtracting“ something from the background.

8.4 Exclusion limits

The expected and observed limits for the electron channel are shown in Figure 8.8. The limit on the cross section as a function of the LQ mass is shown in Figure 8.8(a) and the limits on

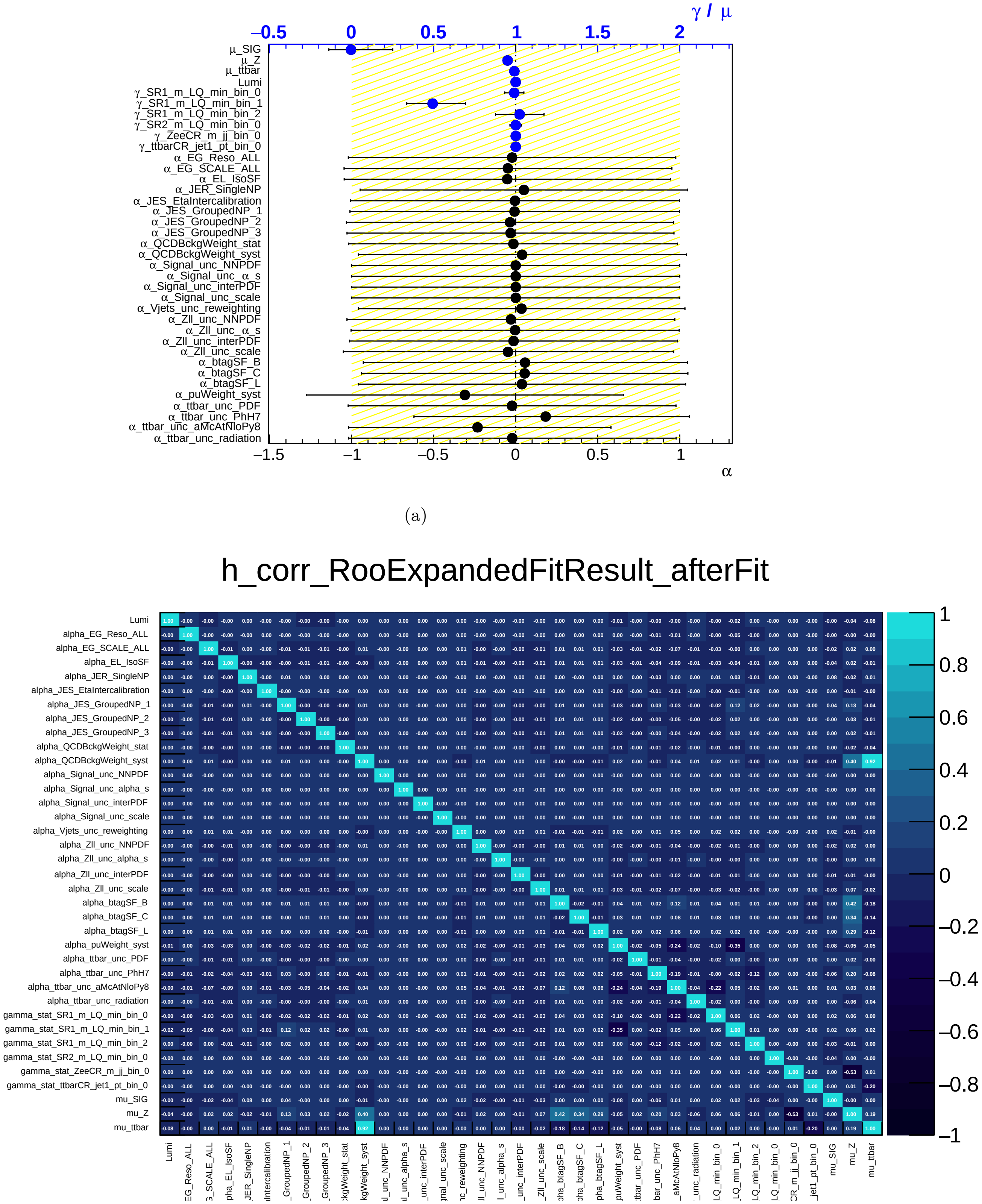

(a)

(b)

Figure 8.2: *Fit diagnostics for the example of an LQ mass hypothesis of 1.4 TeV in electron channel. (a): fit parameters, (b): correlation matrix.*

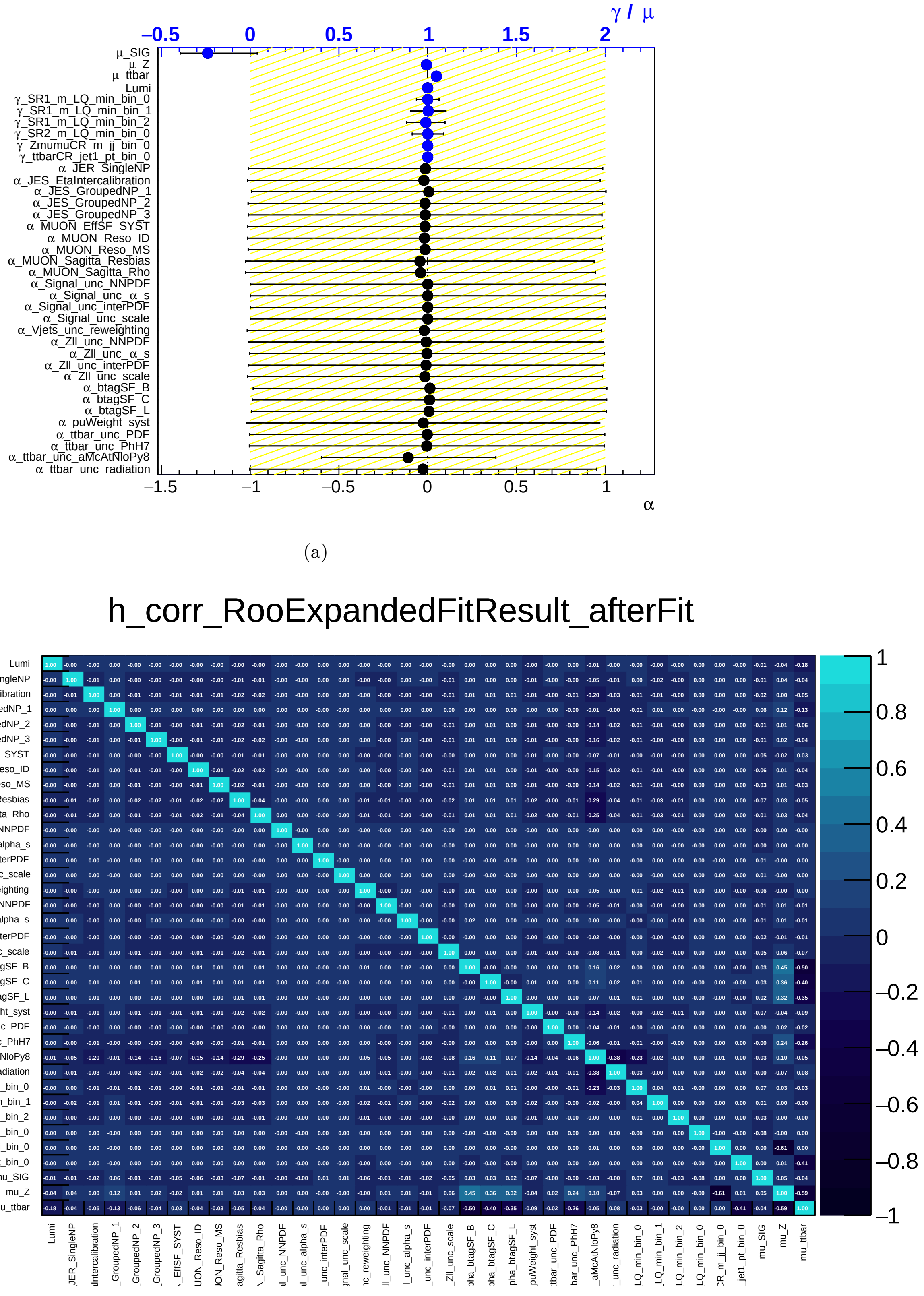

(a)

(b)

Figure 8.3: *Fit diagnostics for the example of an LQ mass hypothesis of 1.4 TeV in muon channel. (a): fit parameters, (b): correlation matrix.*

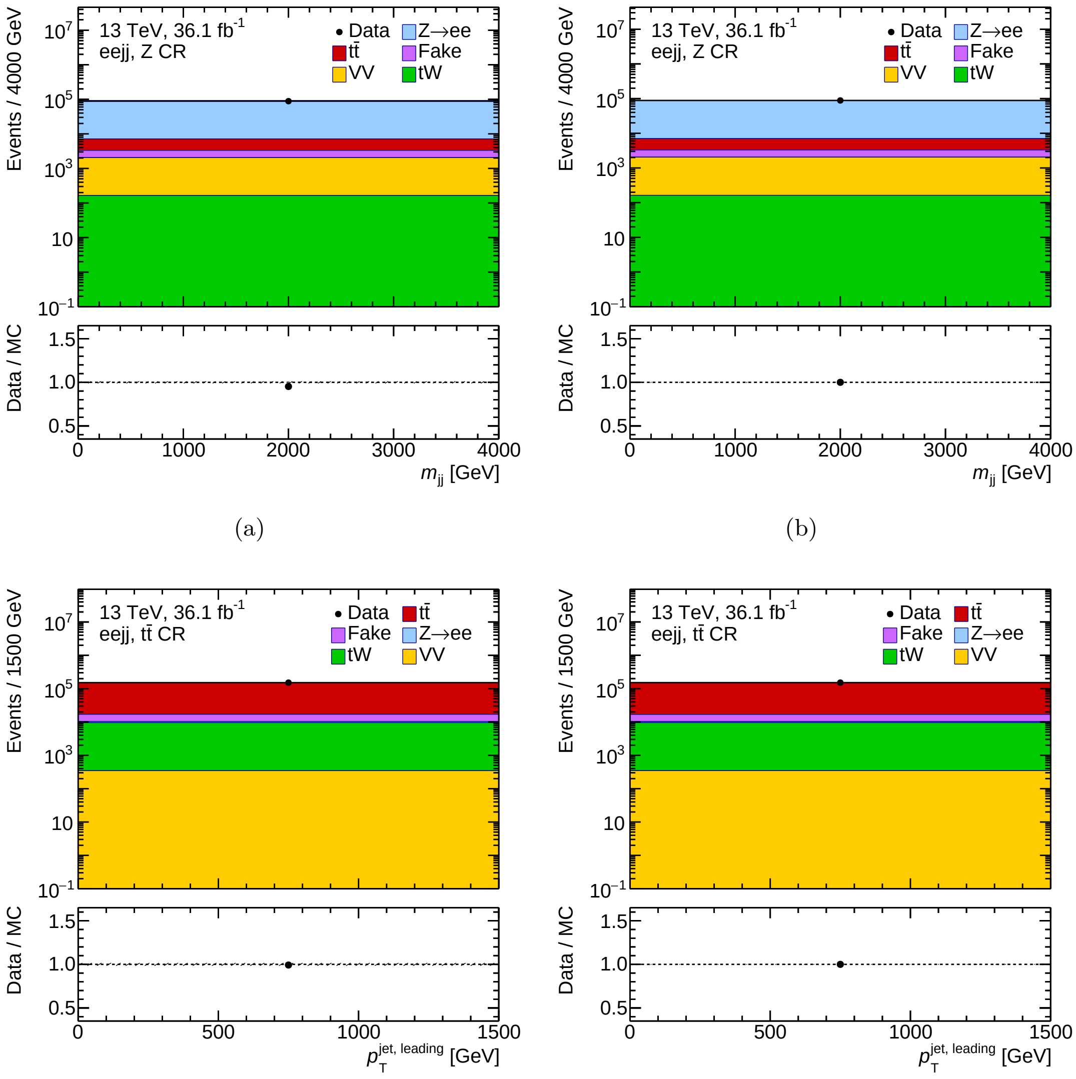

(a) (b)

(c) (d)

Figure 8.4: *Distributions for* m_{jj} *variable in Z CR and* $p_T^{jet,\ leading}$ *in* $t\bar{t}$ *CR in electron channel before (left) and after (right) fitting. The gray band displays the total systematic uncertainty.*

the plane of β and m_{LQ} in Figure 8.8(b). In addition there are two blue lines shown, which corresponds to the theoretical values. The dashed line is for the $\beta = 0.5$ case, while the solid one for the $\beta = 1.0$ case. The expected limit on the cross section in general falls with increasing LQ mass up to 1600 GeV and then increases. The observed limit follows the same behaviour except the low LQ mass region. There is a little gap for 800 GeV - 1050 GeV LQ mass region, which is however not essential for the final result.

The expected and observed limits for the muon channel are shown in Figure 8.9. The limit on the cross section as a function of the LQ mass are shown in Figure 8.9(a) and the limits on the plane of β and m_{LQ} in Figure 8.9(b). The overall Figure structure is similar to Figure 8.8. Exceptions here are that the observed limits above 1000 GeV lie below the expected limits, but still within 1σ band, and that there is different behaviour in low LQ mass region, which is again not dramatic for the final result.

The resulting limits on m_{LQ} for certain β values are summarized in Table 8.1.

The limits on the mass for the first generation LQs are in general a bit higher as the ones

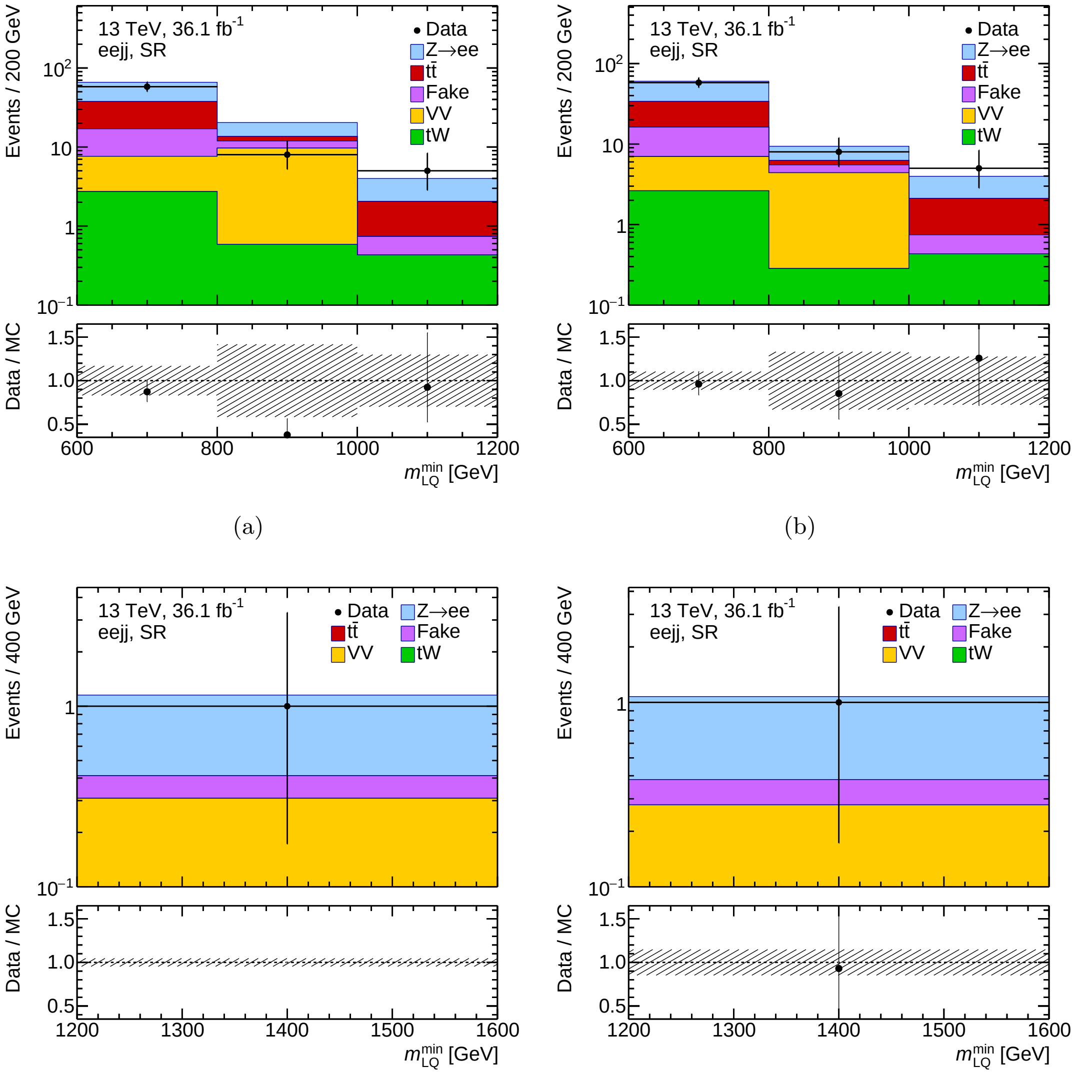

(a) (b)

(c) (d)

Figure 8.5: *Distributions for* m_{LQ}^{min} *variable in SR in electron channel before (left) and after (right) the fit. The gray band displays the total systematic uncertainty.*

Table 8.1: *Expected and observed 95% CL lower limits on first- and second-generation LQ masses for different values of* β*.*

β	95% CL limit on m_{LQ1} [GeV] Expected	95% CL limit on m_{LQ1} [GeV] Observed	95% CL limit on m_{LQ2} [GeV] Expected	95% CL limit on m_{LQ2} [GeV] Observed
1.0	1490	1490	1418	1475
0.5	1173	1146	1147	1208

for the second generation LQs, except the observed limits with $\beta = 0.5$ case. It can be seen by the behaviour of the red line representing the observed limit compared to the dashed black line representing the expected limit in Figures 8.8 and 8.9. However, the discrepancy here lies

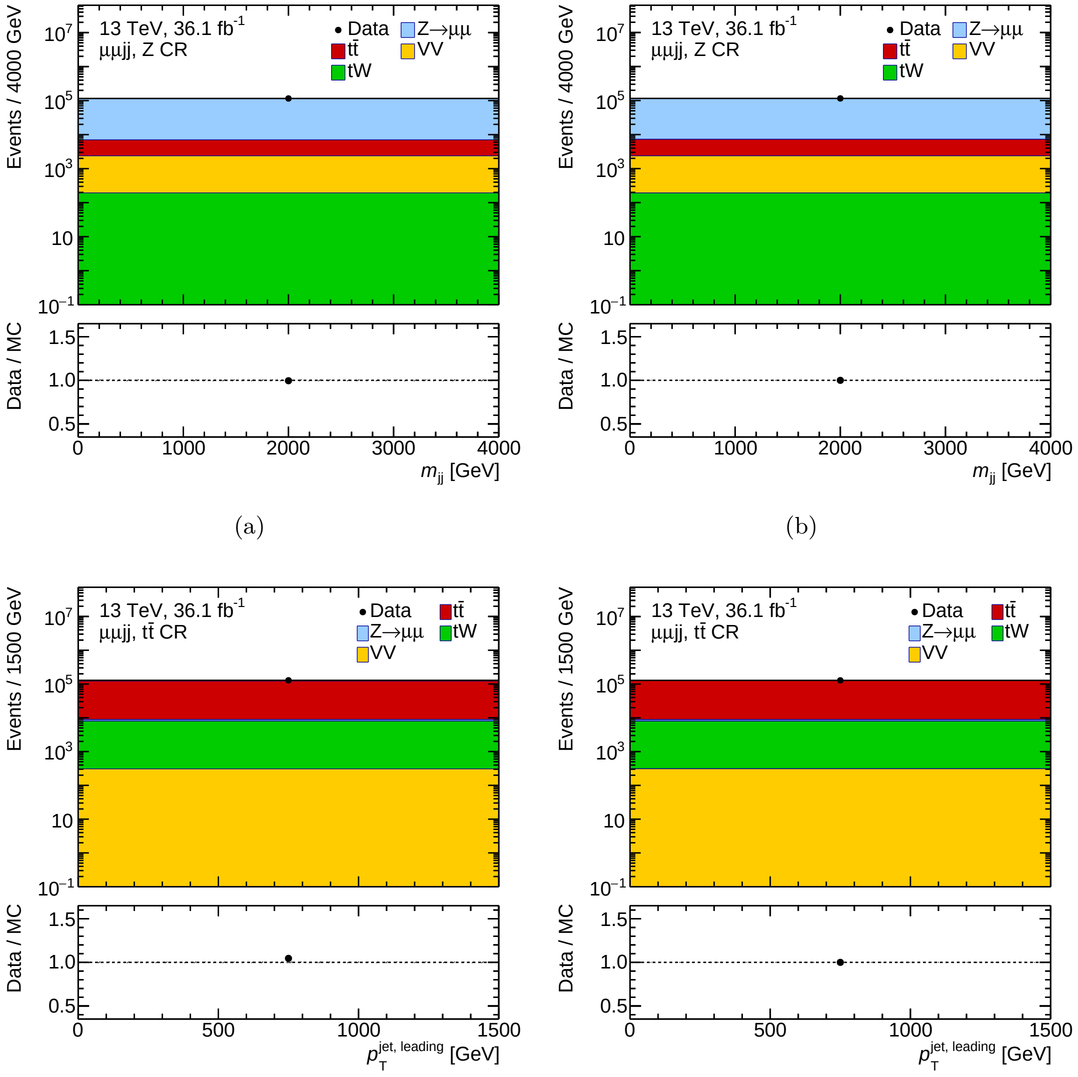

(a) (b)

(c) (d)

Figure 8.6: *Distributions for m_{jj} variable in Z CR and $p_T^{jet,\ leading}$ in $t\bar{t}$ CR in muon channel before (left) and after (right) the fit. The gray band displays the total systematic uncertainty.*

within the 1σ band and is therefore not important, since there is no indication on potential signal excess.

Compared to the previous ATLAS results using 3.2 fb^{-1} of data [168] the limits in all channels in this analysis are up to 400 GeV higher than before. The comparison with the recent ATLAS results using the same data as this analysis [163] deliver the observation that the obtained limits from both analyses are within the same order of magnitude. Within the minimal BRW model and assuming a branching ratio for the decay into a charged lepton and a quark of 100%, leptoquarks with masses up to 1.40 TeV (1.56 TeV) are excluded in electron (muon) channel in the analysis from Reference [163]. However, the comparison at this point is not quite fair since the observed limits from Reference [163] include additionally lepton-neutrino channel. In particular for lower values of β where the lepton-neutrino channel contributes significantly, the limits from Reference [163] are stronger as naively expected.

Finally, the most recent published results by CMS Collaboration are the following ones [223, 224]. Using 35.9 fb^{-1} of data collected at 13 TeV, the existence of scalar LQs with masses

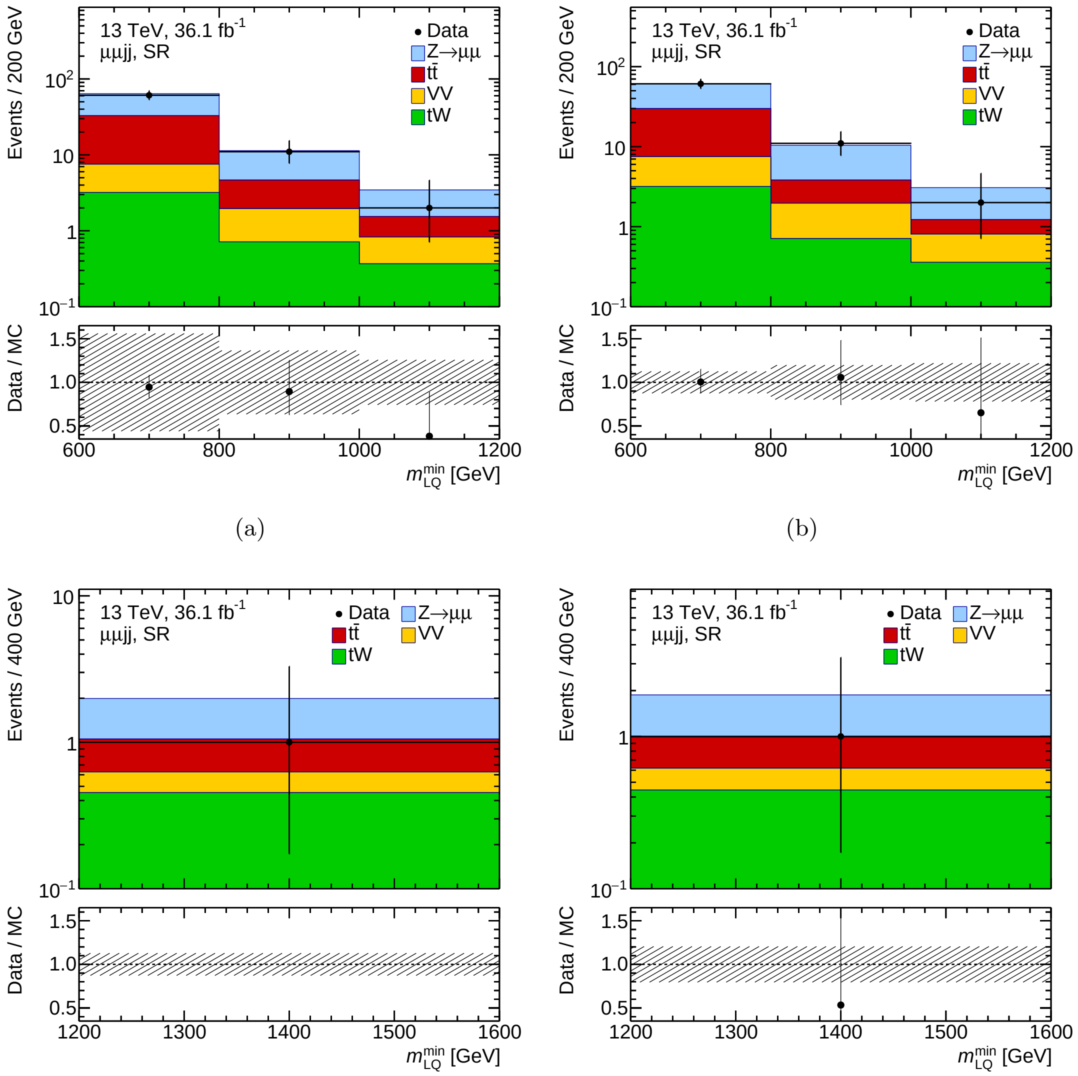

(a)

(b)

(c)

(d)

Figure 8.7: *Distributions for m_{LQ}^{min} variable in SR in muon channel before (left) and after (right) the fit. The gray band displays the total systematic uncertainty.*

below 1435 GeV (1270 GeV) for first-generation LQs at $\beta = 1\,(0.5)$ and, for second-generation LQs, 1530 GeV (1285 GeV) at $\beta = 1\,(0.5)$ is excluded at 95% CL. The limits obtained from the analysis described in this thesis are lower than the results gained by the CMS Collaboration except the limit on the LQ mass of the first generation with $\beta = 1.0$. However, the difference there is just 55 GeV, so the order of magnitude for the limits stays still the same.

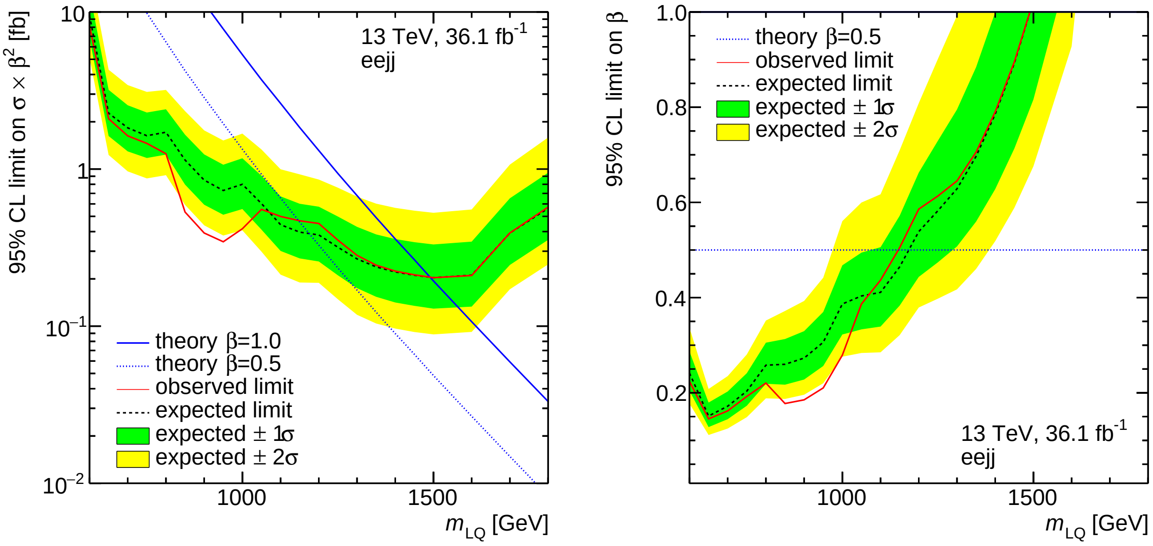

(a) (b)

Figure 8.8: *Limits on 1st generation LQs. Left: 95% CL limits on the cross section as a function of the LQ mass. Right: 95% CL limits in the β-m_{LQ}-plane. The dashed black line is the expected limit, the green and yellow band correspond to the $\pm 1\sigma$ and $\pm 2\sigma$ uncertainty band. The red line corresponds to the observed limit. The dashed (solid) blue line corresponds to the theoretical values if $\beta = 0.5$ ($\beta = 1.0$).*

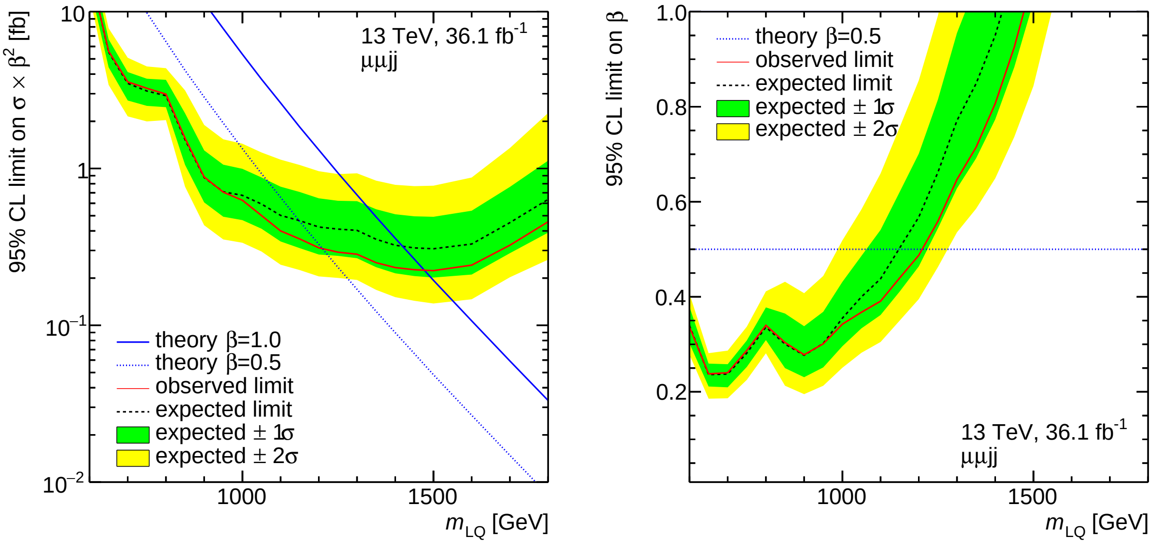

(a) (b)

Figure 8.9: *Limits on 2nd generation LQs. Left: 95% CL limits on the cross section as a function of the LQ mass. Right: 95% CL limits in the β-m_{LQ}-plane. The dashed black line is the expected limit, the green and yellow band correspond to the $\pm 1\sigma$ and $\pm 2\sigma$ uncertainty band. The red line corresponds to the observed limit. The dashed (solid) blue line corresponds to the theoretical values if $\beta = 0.5$ ($\beta = 1.0$).*

Chapter

9 Conclusion and outlook

> “*Difficult to see. Always in motion the future is.*”
> Yoda from Star Wars: Episode V - The Empire Strikes Back

The goal of this analysis was the search for pair-production of first- and second-generation leptoquarks in pp collisions at $\sqrt{s} = 13\,\text{TeV}$ which have been recorded using the ATLAS detector at LHC. The searches are based on a dataset corresponding to $36.1\,\text{fb}^{-1}$ of integrated luminosity and probe the lepton-quark channels. No significant excess above the SM background expectation is observed in any channel and exclusion limits have been evaluated. The results presented here significantly extend the sensitivity in mass compared to previous searches (before 2016). Within the minimal BRW model and assuming a branching ratio for the decay into a charged lepton and a quark of 50%, leptoquarks with masses up to 1.20 TeV are excluded at 95% CL in both channels.

The limiting factor of this analysis was controlling the systematics and performing of the fit. In order to achieve the results as they are, a lot of simplifications were done which might impact the result, for example the choice of the single binned CRs for the fit. However, with better MC simulated processes, the analysis could be done even better. For example Z+jets reweighting was introduced due to known mismodelling of the Z+jets simulations. Hopefully future analysis will have more success with better MC simulation processes and more importantly with more data collected by ATLAS in 2017, 2018 and beyond in Run 3 of LHC, currently scheduled to 2021.

The general search for leptoquarks is not over! Due to multiple independent measurements at Babar [225], Belle [226] and LHCb [86] leading to the discrepancies in both the charged current and neutral current interactions on the level of 4σ [227] an interest for leptoquarks, which could potentially explain these discrepancies, is rising and a bunch of more ATLAS searches is started. Few SUSY analyses try to perform the reinterpretation of their results in terms of leptoquarks of 3rd generation. The inclusion of the third generation will give insight to the charge of the LQs since the bottom and top quarks can be distinguished. The search for pair-production of first- and second-generation continues as well by expanding the analysis to the cross-generated channels (and therefore not using the minimal BRW model). The future will tell us if the leptoquarks can be finally found or we will have just stronger limits, which is not less important for the understanding of the BSM secrets.

Part IV

LAr purity monitoring system

Chapter

10

Motivation

> “*Much to learn, you still have.*”
>
> Yoda from Star Wars: Episode II - Attack of the Clones

The purity of liquid argon (LAr) is an important quantity during the operation of the LAr calorimeter. Electric negative impurity could lead to the reduction of the calorimeter signals amplitude and therefore to the worsening of the measured energy resolution, which is essential for the energy measurement of the particles. This electric negative impurity can arise from the degasing of the calorimeter and cryostate components after their installation or through the leaks in the cryostates during the operation. In order to be aware of this, the monitoring of the LAr purity is necessary. Known amount of charge is deposited in ionization chambers in order to measure the purity. Then the original amount of charge is reduced through electric negative impurity during the drift in the electric field. Therefore a degree for the LAr purity is given by the collected amount of charge after drift [228].

The measuring devices and the whole software for the data analysis, which enables the physicists to measure the purity, were developed by the ATLAS Mainz purity group at the end of the 20th century. Since then and especially after the installation of the LAr purity monitoring system to the ATLAS detector the members from ATLAS Mainz purity group - so-called purity experts - are responsible for the actual LAr purity monitoring and the corresponding system maintenance, even though the amount of group members decreased over time. During that time several places with LAr purity documentation were created, which led to a decentralisation of the information on the LAr purity monitoring system, making it more difficult to obtain an overall picture on the processes. In order to understand the current system several tests were performed and summarized in this thesis. Also, first steps towards a central purity documentation place are taken and briefly discussed here.

As a part of maintenance work it is important to keep the system operational in the future. In the next years the ATLAS detector will get several upgrades as a preparation for the upcoming LHC upgrade. There will be some changes which will directly affect the system, so it is already important to give thoughts to the upgrade of the LAr purity monitoring system.

CHAPTER

11 THEORETICAL AND SYSTEM DESCRIPTION

> “*Thee in luck, I'm the only one hereabouts who has one...*
> *but thee might as well buy a new ship. It would be cheaper,*
> *I think...* ”
> WATTO FROM STAR WARS: EPISODE I - THE PHANTOM MENACE

Two ionization chambers each containing a different radioactive source are used as a sensor for the LAr purity measurement. A measure of the LAr purity is then the ratio of the signals from these two chambers. These ionization chambers, high voltage electronics and the preamplifier represent together a system, which is denoted as basic monitor[1]. Thanks to the usage of two different source chambers, it is possible to measure the impurity with oxygen or oxygen-like molecules in a range up to 3 ppm[2] with an accuracy $<$ 100 ppb[3].

In the following the basics of the purity measurement are described in Section 11.1 based on Reference [228]. Section 11.2 gives more details about the hardware of the current LAr purity monitoring system followed by the discussion of the firmware in Section 11.3. The software chain of this system is briefly described in Section 11.4.

11.1 Physics behind LAr purity measurement

11.1.1 Ionization chamber

An ionization chamber consists of two parallel electrodes with the homogeneous electric field between them arising from the voltage between the electrodes. A mixture of gases, a liquid or a solid represent an active medium, which is also located between the electrodes. If a charged particle goes through this active medium, ions and electrons are created. They drift in the electric field to the electrodes and induce a change in charge, which can be detected by a charge sensitive preamplifier. The deposited energy of the particles is measured in the form of the charge released by ionization in the active detector layers.

An electric current $I = \frac{e}{t_d}$ flows during the drift time t_d for each electron-ion-pair (see Figure 11.1(a)). Here t_d is the time, which an electron needs in order to cover the distance d between cathode and anode with the constant drift velocity v_d. Since the mobility of ions is several magnitudes of order smaller than the velocity of electrons[4] the drift time of ions is larger than

---

[1] Also referred to as purity monitor, or in short just monitor.

[2] parts per million

[3] parts per billion

[4] The drift velocity of the ions and the electrons in a homogeneous electric field is $v_d^{\pm} = \mu^{\pm}|\vec{E}|$. Due to mass differences the mobility μ^- of the electrons is larger then the mobility μ^+ of the ions. The mobility of electrons in LAr is $\mu^- \approx 4000\,\mathrm{m^2\,V^{-1}\,s^{-1}}$. For a typical electric field of approximately $12\,\mathrm{kV\,cm^{-1}}$ the drift velocity amounts to $v_d^- \approx 5\,\mathrm{mm\,\mu s^{-1}}$ [229].

that of electrons. This leads to the fact that the ion contribution to the total amplitude of the electric current signal is negligible.

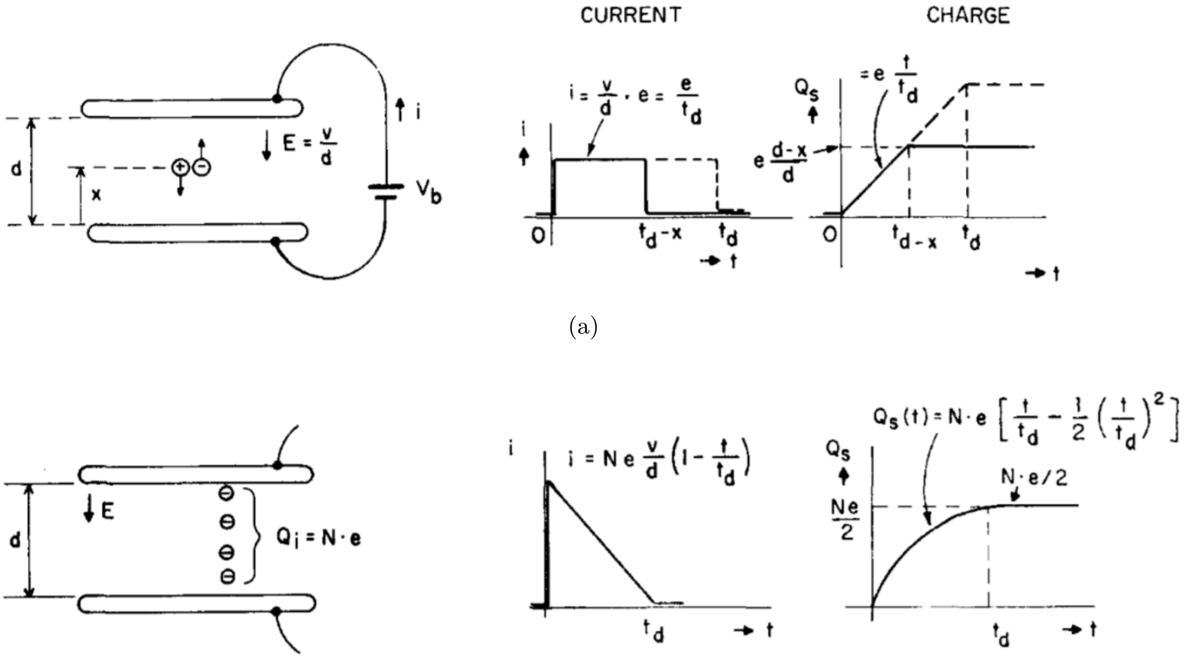

(a)

(b)

Figure 11.1: *Charge collection in LAr chamber, (a) single ion pair (solid lines), and for ions formed at the negatively biased plate (dashed lines); (b) uniform ionization [230].*

Assuming that N electrons, which are distributed homogeneously through the ionization trace, are available for the drift and the projection of the primary particle trace to the drift direction has the length d, the influenced electric current (see Figure 11.1(b)) can be measured as:

$$I(t) = Ne\frac{v_d}{d}\left(1 - \frac{t}{t_d}\right). \tag{11.1}$$

Through the integration of $I(t)$ and using $v_d = d/t_d$ it follows for the charge signal:

$$Q(t) = \int_0^{t_d} I(t)\,dt = \begin{cases} Ne\left(\frac{t}{t_d} - \frac{1}{2}\left(\frac{t}{t_d}\right)^2\right), & 0 \leq t \leq t_d \\ \frac{1}{2}Ne, & t > t_d \end{cases}. \tag{11.2}$$

This means that at least half of all previously produced charge carriers can be collected after the drift time t_d of the electrons. This result can be explained due to the neglection of the positive ion signal. If the ions would be considered and integrated over their very large drifting time, then they would contribute the other half to the total charge signal.

In a real ionization chamber the amount of electrons available for the drift is less than the amount of electrons produced during the ionization. First, the electron can recombine after the ionization with the „mother ion“ or during the drift time with some other ion. Second, there is still electric negative impurity in the active medium, where the drifting electrons can accumulate. These effects lead to the fact that the lifespan τ of the electrons during the drift time is not an infinite quantity anymore and only low amount of charge can be detected. Furthermore, these effects can be considered as two independent processes assuming that the recombinations during the drift time t_d occur in a short period of time and the attachment of the electrons occurs continuously to the electric negative molecules. In the following, these two effects are discussed and descriptive models are presented.

Charge loss through recombination

After the production of the amount of charge Q_{ini} through the ionization in an electric field, a part of the charge is lost due to the recombination and the amount of charge reduces to Q_0.

Initial recombination

L. Onsager reduces the problem of the recombination in his theory of initial recombination (also called as pairwise recombination) to the Brownian movement of a particle under the influence of the electric field of the „mother ion" and of the outer electric field [231]. On this way a possibility is neglected, that the electron can recombine during its drift time with some other ion. The combined Coulomb-potential, where the electron is located, can be defined as:

$$V = -e|\vec{E}|r\cos(\theta) - \frac{e^2}{\epsilon r}. \tag{11.3}$$

Here are e the elementary charge, $\vec{E}$ the outer electric field, r the distance between an electron and an ion, θ an angle between $\vec{E}$ and $\vec{r}$, and ϵ the permittivity of the active medium in the ionization chamber. The theory predicts for the low field strength the following behaviour:

$$\frac{N_0}{N_{\text{ini}}} = \frac{Q_0}{Q_{\text{ini}}} = e^{\frac{r_{kt}}{r_0}} \left(1 + |\vec{E}| \frac{e^3}{2\epsilon k^2 T^2}\right). \tag{11.4}$$

Here are $r_{kt} = \frac{e^2}{\epsilon kT}$ the Onsager-radius, r_0 the length of the thermalisation (the distance between the electron and the ion after the ionization), k the Boltzmann constant, and T the temperature. From the theory of the initial recombination it follows, that the amount of the electrons N_0 after the initial recombination changes linearly with the applied electric field (see Figure 11.2).

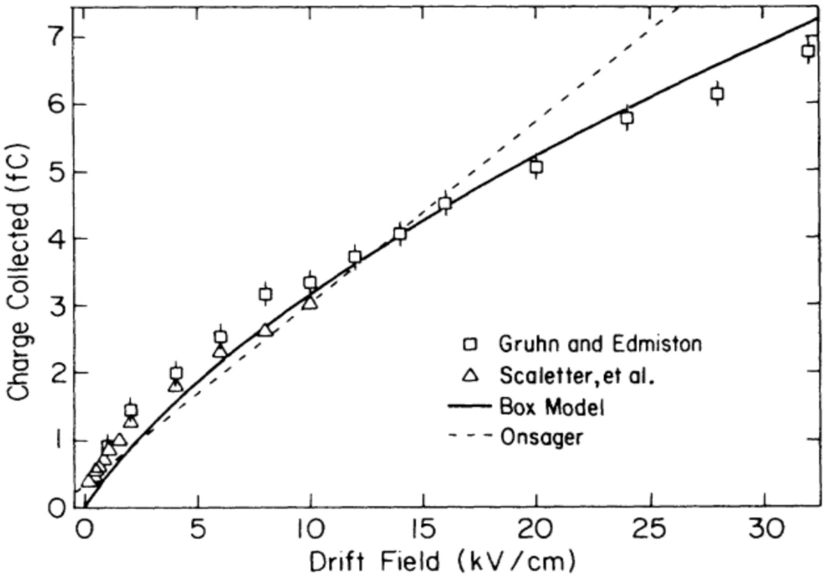

Figure 11.2: *Total charge Q_0 collected as a function of electric field after an alpha particle passes through LAr. The solid curve is a fit to the combined data sets from Scaletter et al. and Gruhn and Edmiston assuming no impurities and $E_0 = \xi|\vec{E}| = 470\ kV\ cm^{-1}$. The dashed line is the prediction for the Onsager theory of the initial recombination [232].*

Theory of columns in an electric field

The theory of columns in an electric field was presented by G. Jaffé in 1913 [233]. In this theory it is assumed, that an ionised particle creates a homogeneously distributed column of electrons and ions towards its trace. At the ionization time the density distribution $n_\pm\,(t = 0)$ of the ions and the electrons corresponds to the transverse Gaussian distribution with the width b:

$$n_{\pm}\left(t=0\right)=\frac{N}{nb^2}e^{-\frac{r^2}{b^2}}. \tag{11.5}$$

Here r is the distance from the trace of the primary particle and N the amount of charge carrier per unit length of the trace. The electrons and ions can recombine while the positive and negative charge carrier are separated due to an outer electric field. In contrast to the theory by L. Onsager the electron does not have to recombine with its „mother ion“ but rather with any ion from the column. In order to describe the temporal development of the ion density n_+ and the electron density n_- the following coupled differential Equations are established:

$$\frac{\partial n_{\pm}}{\partial t}=\underbrace{\mp\mu_{\pm}|\vec{E}|\sin\left(\phi\right)\frac{\partial n_{\pm}}{\partial x}}_{\text{drift}}+\underbrace{D_{\pm}\Delta n_{\pm}}_{\text{diffusion}}-\underbrace{k_r n_- n_+}_{\text{recombination}}. \tag{11.6}$$

Here $\mu_{\pm}$ is the mobility of ions or electrons, ϕ the angle between the external field $\vec{E}$ and the ionization trace, $D_{\pm}=\frac{\mu_{\pm}kT}{E}$ the diffusion coefficient and k_r the recombination coefficient. The first part on the right side of the Equations describes the particle drift in an electric field, the second part the diffusion in an active medium and the last part the recombination of the electrons and ions.

Since solving these Equations is complicated and delivers no clear results, G. Jaffé neglected first the recombination part and then treated it in the perturbation theory. Furthermore, an assumption was made, that the mobility of electrons is equal to the mobility of ions ($\mu_+=\mu_-$), even though it is not true, since the mass of ions is bigger than that of electrons and therefore the mobilities are different within several orders of magnitude ($\mu_+\ll\mu_-$).

However, H.A. Kramers showed in 1952 that the assumption of neglecting the recombination part is only valid for gases, but not for liquid noble gases. He solved Equation 11.6 by neglecting the diffusion part first and treating it later in the perturbation theory. With this approach the solution is:

$$\frac{N_0}{N_{\text{ini}}}=\frac{Q_0}{Q_{\text{ini}}}=\frac{2f}{\sqrt{\pi}}\int_0^{\infty}\frac{\sqrt{\zeta}}{fe^{\zeta}+1}\mathrm{d}\zeta \tag{11.7}$$

with

$$f=\frac{|\vec{E}|b\,\sin\left(\phi\right)}{4\sqrt{\pi}eN_{\text{ini}}}. \tag{11.8}$$

The Box model

The column theory by G. Jaffé and H.A. Kramers failed to describe the recombination part for liquid noble gases due to the assumption that the mobilities for electrons and ions are equal ($\mu_+=\mu_-$).

In 1987 J. Thomas and D.A. Imel measured the dependence of the electron-ion-pair-recombination to the external electric field in LAr and liquid xenon. They observed that the results are incompatible with the pairwise recombination model by L. Onsager [232]. Therefore they developed a so-called Box model using the differential Equations raised by G. Jaffé. Assuming, that in LAr and in liquid xenon the diffusion part is small (the diffusion rate of the electrons is on the order of magnitude of a few millimeters per meter drift) and the drift velocity of the ions and electrons have a difference of several orders of magnitude, the diffusion part was neglected and the mobility of ions was set to zero ($\mu_+=0$). This results to the following system of differential Equations:

$$\frac{\partial n_+}{\partial t}=-k_r n_- n_+, \tag{11.9}$$

$$\frac{\partial n_-}{\partial t}=\mu_-|\vec{E}|\sin\left(\phi\right)\frac{\partial n_-}{\partial x}-k_r n_- n_+. \tag{11.10}$$

The system of Equations 11.9 and 11.10 could be solved using the assumptions, that every electron-ion-pair is isolated and N_0 electrons and ions are equally distributed in a „box“ with an edge width a at time point $t = 0$:

$$\frac{Q_0}{Q_{\text{ini}}} = \frac{1}{\xi} \ln\left(1 + \xi\right). \tag{11.11}$$

Here ξ is the only parameter of the Box model:

$$\xi = \frac{N k_r}{4a^2 \mu_- |\vec{E}|}. \tag{11.12}$$

This parameter was defined by adaptation to the measurement data as:

$$E_0 := \xi|\vec{E}| = 470\,\mathrm{kV\,cm^{-1}} \text{ for the } \alpha\text{-source } \left({}^{241}\mathrm{Am}\right),$$
$$\xi|\vec{E}| = 0.8\,\mathrm{kV\,cm^{-1}} \text{ for the } \beta\text{-source } \left({}^{113}\mathrm{Sn}\right).$$

Using the Box model it is possible to predict the produced amount of charge Q_{ini} after the ionization assuming that the quantities of the electric field and Q_0 are known. Since the recombination of the electrons with the ions from the previous ionization events is not considered, a correction factor was multiplied to Q_{ini} which was, however, determined empirically.

Charge loss through attachment

The amount of electrons during the drift through the ionization chamber decreases not only due to the recombination loss but also due to the attachment to the electric negative molecules. This results in the reduction of the gained charge and therefore in the reduction of the signal amplitude. However, the ion contribution to the electric current signal can be neglected since it is low compared to the electrons. The temporal dynamics of the electron density can be described with the following differential equation:

$$\frac{dn_e}{dt} = -k_s n_s\left(t\right) n_e\left(t\right). \tag{11.13}$$

Here n_e is the electron density, n_s the number density of the electric negative impurity and k_s the attachment coefficient. The solution of Equation 11.13 with the homogeneous distribution of the electric negative atoms or molecules is:

$$n_e\left(t\right) = n_e\left(t_0\right) e^{-\frac{t}{\tau_s}}, \tag{11.14}$$

where $\tau_s = \frac{1}{k_s n_s(t)}$ is a measure which shows how fast the electron density reduces over time. k_s is the so-called attachment constant, which depends on factors like the type of impurity, environment (for example liquid xenon, LAr), the temperature and the energy of the drifting electrons. In order to be able to describe the attachment of the electrons to the electric negative atoms or molecules well, it is better to know these factors as precisely as possible. The attachment constant for oxygen in LAr was measured by M. Adams et al. (see Figure 11.3) [234].

In order to describe the concentration p_{O_2} of the oxygen impurity the mean free path can be parameterized by using

$$\lambda = v_d \tau_s = \mu_e |\vec{E}| \tau_s \tag{11.15}$$

with μ_e as the mobility of electrons as

$$\lambda = \alpha \frac{|\vec{E}|}{n_s}. \tag{11.16}$$

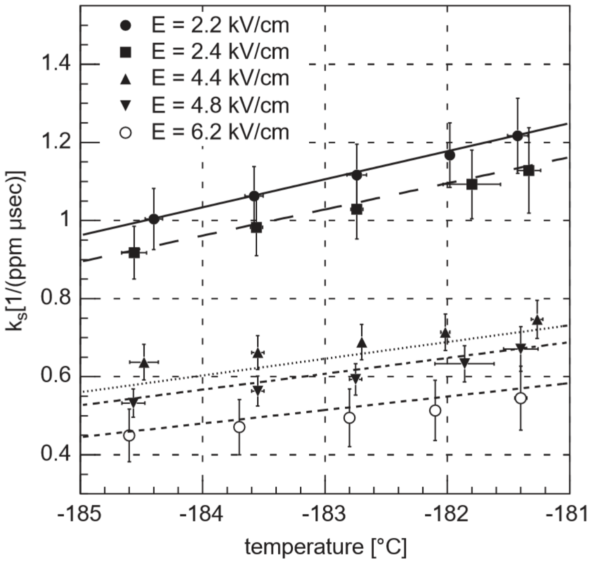

Figure 11.3: *The attachment rate k_s as a function of the temperature of the LAr and different values of the electric field strength [234].*

Here $\alpha = \frac{\mu_e}{k_s}$ is assumed as a constant parameter, which was determined by Hofmann et al. experimentally [235]:

$$\alpha_\alpha = (0.14 \pm 0.03)\,\frac{\text{ppm cm}}{\text{kV/cm}} \text{ for the } \alpha\text{-source,}$$
$$\alpha_\beta = (0.15 \pm 0.03)\,\frac{\text{ppm cm}}{\text{kV/cm}} \text{ for the } \beta\text{-source.}$$

The measurements were performed with impurity concentration of $\sim$ 1 ppm and electric field strength of $10\,\text{kV}\,\text{cm}^{-1}$. The proportionality $\lambda \approx n_s^{-1}$ was approved for the ionization by the β-source. However, deviations for the ionization by the α-source were found, which led to the calculation of the influence of impurity on the recombination.

If the type of impurity is unknown, then using the measured free mean path or rather lifespan of the electrons leads to the following determination of the impurity $p_{O_2} \equiv p$ in oxygen:

$$p_{O_2} := n_s = \alpha \frac{|\vec{E}|}{\lambda} = \alpha \frac{|\vec{E}|}{v_d \tau_s}. \tag{11.17}$$

Since the type of impurity is unknown, the attachment constant k_s for oxygen and the impurity p are used for the purity calculation. For example the N_2 concentration has to be approximately 100 times bigger than that of oxygen for the same reduction of the gained charge [236].

Electric current signal of the ionization chamber under influence of electric negative impurity

If the influence of the electric negative impurity to the electric current signal of the ionization chamber has to be taken into account, then Equation 11.1 should be modified. Addition of the finite lifespan τ of the electrons leads to the following electric current:

$$I(t) = I_0 e^{-\frac{t}{\tau}} \left(1 - \frac{t}{t_d}\right). \tag{11.18}$$

The integration of Equation 11.18 leads to:

$$Q(t) = \begin{cases} Q_0 \frac{\tau}{t_d} \left[-\frac{t}{t_d} e^{-\frac{t}{\tau}} + \left(e^{-\frac{t}{\tau}} - 1 \right) \left(1 - \frac{\tau}{t_d} \right) \right], & 0 \le t \le t_d \\ Q_0 \frac{\tau}{t_d} \left[-\frac{\tau}{t_d} \left(1 - e^{-\frac{t_d}{\tau}} \right) - 1 \right], & t > t_d \end{cases}. \tag{11.19}$$

Figure 11.4 shows the time trend of the strength of the electric current and the integrated charge.

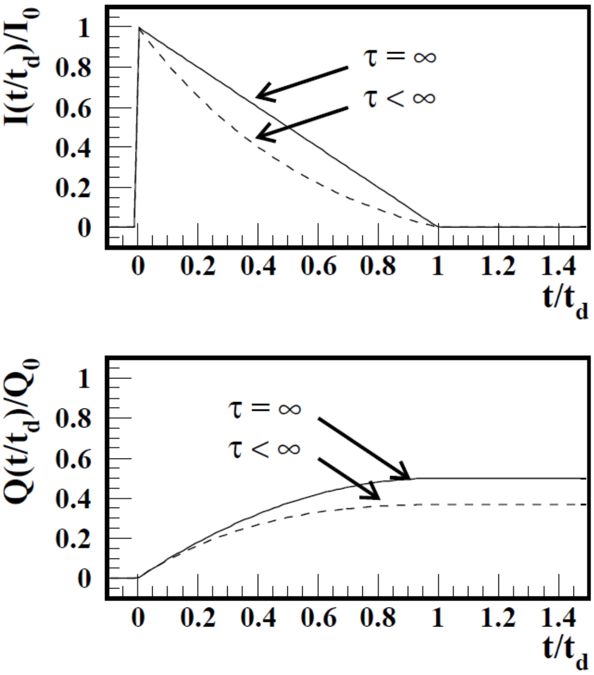

Figure 11.4: *Expected electric current signal (at the top) and charge signal (the bottom) of an ionization chamber for finite and infinite lifespan of electrons [229].*

11.1.2 Basic monitor

In order to measure the electric negative impurity in LAr the basic monitor was developed in Mainz. It consists of two ionization chambers, the high voltage electronics and the charge sensitive preamplifier, which integrates the electric current signals from the ionization chambers. In one chamber the α source (^{241}Am) is installed, in the other the β source (^{207}Bi).

The coverage of the components of the basic monitor as well as the introduction of a model for the purity calculation from the chamber signals are described in the following.

Am chamber

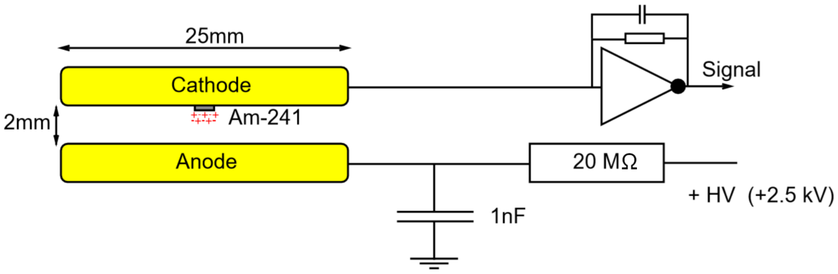

Figure 11.5: *Schematic view of the ^{241}Am-cell, in which α-particles of $\approx$ 5.5 MeV ionize the LAr close to the source [234].*

Figure 11.5 shows the schematic view of the ^{241}Am-chamber. The electrodes consist of stainless steel discs with a diameter of 25 mm, which are fixed with a holder from SINTIMID[5] and are

---

[5] A radiation hard synthetic substance with small expansion coefficient.

located at a distance of 2 mm. With typically used running voltages of 2.5 kV an electric field of $12.5\,\mathrm{kV\,cm^{-1}}$ is applied between the electrodes.

A thin layer of ^{241}Am mounted on the cathode is the α source. A spectrum of ^{241}Am is shown in Figure 11.6. ^{241}Am has a half-life of 432 years. The three α lines which are close together (5.49 MeV (85.2%), 5.44 MeV (12.8%) and 5.39 MeV (1.4%)) can not be separated due to low resolution of the chamber and used electronics, and thus combine into one peak [237].

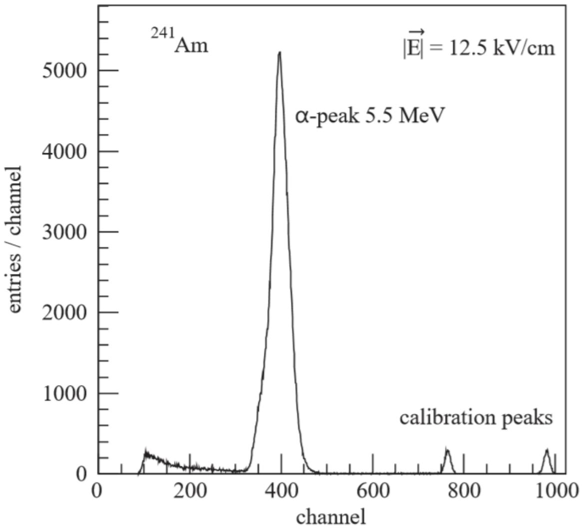

Figure 11.6: *Signal spectrum of the ^{241}Am-cell recorded with the CERN testbeam setup ($p \approx 0.3\,\mathrm{ppm}_{O_2}$). Calibration peaks are used to monitor the stability of the electronics chain [234].*

The range of the α-particles in LAr is approximately 100 µm [238]. So the secondary electrons are well located and build so to say a point-shaped charge distribution. The consideration of all effects, which occur for larger charge expansion, is therefore not necessary. This leads to the simple chamber geometry. The high voltage is undocked with a resistor of 20 MΩ and capacitor of 1 nF, which build together low-pass filter, in order to reduce the disturbing influences coming from this high voltage. The influenced electric current signal is read out and integrated from the charge sensitive preamplifier over the cathode.

The signal form of the ^{241}Am chamber

The electrons, which are produced due to α particles, influence the following electric current signal as they lead to drifts in the electric field:

$$I(t) = \begin{cases} \frac{Q_0}{t_d} e^{-\frac{t}{\tau}}, & 0 \le t \le t_d \\ 0, & t > t_d \end{cases} . \tag{11.20}$$

Here Q_0 is the amount of charge after the recombination, t_d the drift time and τ the lifespan of the electrons in LAr. In case the electric current is integrated, which is true for the charge sensitive preamplifier, then it follows:

$$Q(t) = \int_0^t I(t)\,dt = \begin{cases} Q_0 \frac{\tau}{t_d}\left(1 - e^{-\frac{t}{\tau}}\right), & t < t_d \\ Q_0 \frac{\tau}{t_d}\left(1 - e^{-\frac{t_d}{\tau}}\right), & t \ge t_d \end{cases} . \tag{11.21}$$

The drift time can be calculated as $t_d = \frac{d}{v_d}$ since the distance d between the electrodes and the drift velocity v_d are known. Furthermore τ equals $\frac{1}{k_s n_s}$ as discussed in Section 11.1.1. It follows from Equation 11.21:

$$Q(n_s) = Q_0 \frac{v_d}{d \cdot k_s \cdot n_s}\left(1 - e^{-\frac{d \cdot k_s \cdot n_s}{v_d}}\right). \tag{11.22}$$

Applying the Box model introduced in Section 11.1.1 results in the charge available after recombination:

$$Q_0 = Q_{\text{ini}} \frac{|\vec{E}|}{E_0} \ln\left(1 + \frac{E_0}{|\vec{E}|}\right). \tag{11.23}$$

Here Q_{ini} is the total amount of charge after the ionization and $E_0 = 470\,\text{kV}\,\text{cm}^{-1}$ (for ^{241}Am) is the model parameter experimentally determined by Thomas and Imel (see Section 11.1.1). This leads to the gained charge Q dependent on $|\vec{E}|$ and $n_s \equiv p$:

$$Q\left(|\vec{E}|, p\right) = Q_{\text{ini}} \frac{|\vec{E}|}{E_0} \ln\left(1 + \frac{E_0}{|\vec{E}|}\right) \frac{v_d}{d \cdot k_s \cdot p}\left(1 - e^{-\frac{d \cdot k_s \cdot p}{v_d}}\right). \tag{11.24}$$

Figure 11.7 shows the dependence of charge in the impurity. Here the integrated charge $Q\left(|\vec{E}|, p\right)$ is proportional to the reciprocal value of the impurity p due to simple chamber geometry. The amount of charge, which is created during the ionization, is $Q_{\text{ini}} = 37.3\,\text{fC}$. This charge was calculated from the knowledge of the deposited energy of 5.5 MeV in LAr [229].

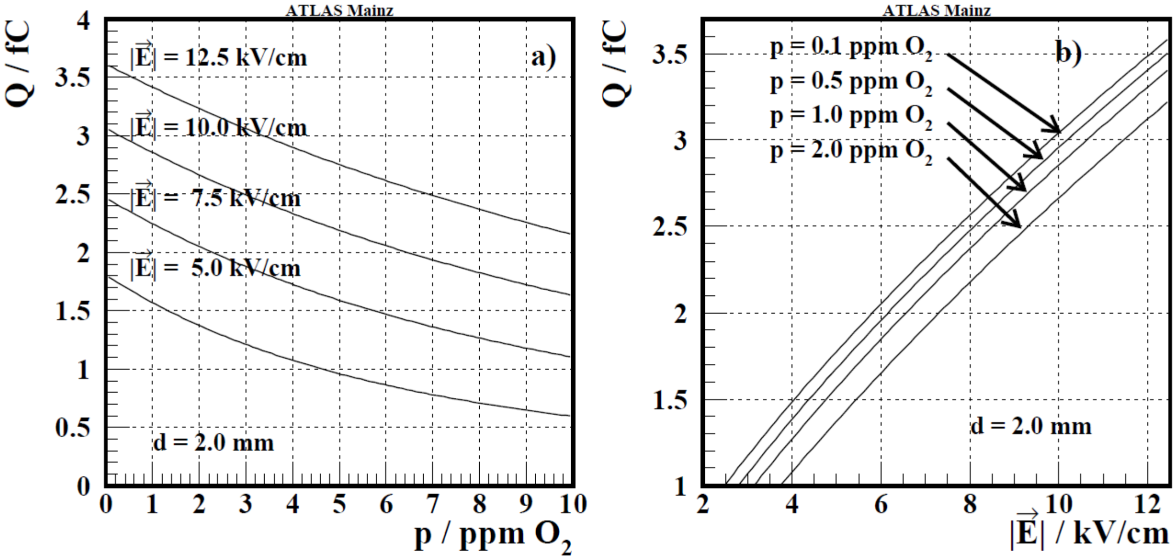

Figure 11.7: *The expected signal height of the* ^{241}*Am chamber (a) as a function of the impurity concentration p for different electric field strengths* $|\vec{E}|$ *and (b) as a function of the applied electric field strength* $|\vec{E}|$ *for different concentrations of the impurity p [229].*

Bi chamber

Figure 11.8 shows the schematic view of the ^{207}Bi-chamber. The dimensions of the electrodes correspond to the ones of the Am chamber with only difference that a ^{207}Bi source was evaporated. The chamber consists of two electrodes and a Frisch-grid, which is fixed between the anode and the cathode. The distance between the cathode and the grid is 5 mm and between the grid and the anode it is 1 mm.

The energy spectrum of ^{207}Bi is shown in Figure 11.9. The important lines of the ^{207}Bi spectrum are the three γ-lines at 569 keV, 1064 keV and 1770 keV. The measured peaks are the conversion electron peak at 481 keV and the peaks used for the purity calculation at 975 keV and 1047 keV. The two last mentioned peaks can not be resolved separately in the chamber and result into one peak. Furthermore, the Compton spectra and photons are measured as well [237].

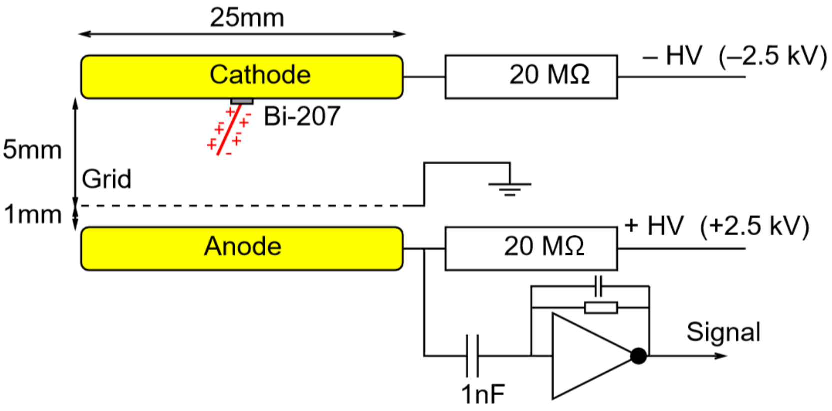

Figure 11.8: *Schematic view of the* ^{207}*Bi-cell. Conversion electrons of* $\approx$ *1 MeV ionize the LAr along their* $\approx$ *3 mm long tracks in front of the cathode. Only electrons drifting between the grid and the anode are taken into account for the signal [234].*

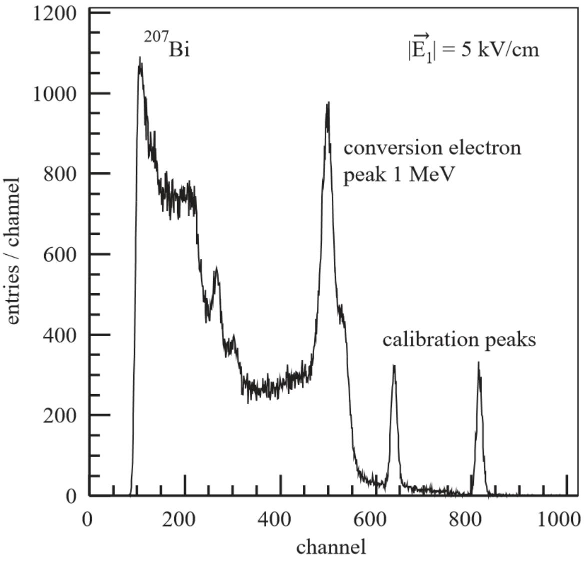

Figure 11.9: *Signal spectrum of the* ^{207}*Bi-cell recorded with the CERN testbeam setup (p* $\approx$ *0.3 ppm*$_{O_2}$*). The two conversion electron lines at 1047 keV and 976 keV are not resolved separately and form the largest peak. The* γ*-line at 1064 keV is strongly suppressed. The background on the left from it consists of the Compton continuum with the Compton-edge at 858 keV and the contributions to the* γ*-line at 569 keV. Calibration peaks are used to monitor the stability of the electronics chain [234].*

Since the conversion electrons have a range of 3 mm in LAr the volume expansion of the charge has to be considered. For this reason the ionization chamber is subdivided into a drift room and a measuring room. The drift room is installed between the cathode and the Frisch-grid[6] and has a length of 5 mm. On this way the conversion electron can deposit its complete energy. The drift room has the field strength of 5 kV cm^{-1} at 2.5 kV. The measuring room has a space between the grid and the anode and a distance of 1 mm which corresponds to a field of 25 kV cm^{-1} at 2.5 kV. The detection of the electric current signal is performed by the anode. This signal is integrated through the preamplifier, which is separated from the high voltage through a capacitor with a capacity of 1 nF.

---

[6] The Frisch-grid shields the electric field of the drifted electrons in the drift room from the anode.

The following applies to the produced amount of charge after the ionization:

$$Q_0 = \int_0^{z_0} \rho_0\left(z\right) dz \text{ with } 0 < z_0 \leq z_{\text{max}}. \tag{11.25}$$

Here $z_0 = z_{\text{max}} \cos\left(\alpha\right)$ is the projection of the trace to the drifting direction in an electric field, α is the angle between the ionization trace and the drifting direction, Q_0 is the amount of charge, which is available after the recombination, and $\rho_0\left(z\right)$ is the charge density after recombination at position z. The charge density, which is available after recombination at the position of the Frisch-grid, is:

$$\rho_1\left(z\right) = \rho_0\left(z\right) e^{-\frac{(d_1 - z)/v_d}{\tau}} = \rho_0\left(z\right) e^{-\frac{d_1 - z}{\lambda_1}} \text{ with } 0 < z < z_0. \tag{11.26}$$

Here λ_1 is the mean free path in the first drifting room and d_1 is its length. Analogously to Equation 11.25 the total charge of the electrons which are coming to the Frisch-grid can be expressed as:

$$Q_1 = \int_0^{z_0} \rho_1\left(z\right) dz = \int_0^{z_0} \rho_o\left(z\right) e^{-\frac{d_1 - z}{\lambda_1}} dz. \tag{11.27}$$

The drifting electrons influence the electric current signal to the anode in the second drifting room. This results to the integrated charge:

$$Q_2 = Q_1 \frac{\lambda_2}{d_2} \left(1 - e^{-\frac{d_2}{\lambda_2}}\right), \tag{11.28}$$

where d_2 is the length and λ_2 is the mean free path of the second drifting room. Assuming a homogeneous charge density distribution $\rho_0 = \frac{Q_0}{z_0}$ towards the ionization trace it follows from Equation 11.25:

$$Q_1 = Q_0 \frac{\lambda_1}{z_0} e^{-\frac{d_1}{\lambda_1}} \left(e^{\frac{z_0}{\lambda_1}} - 1\right). \tag{11.29}$$

Using Equation 11.29 on Equation 11.28 it follows:

$$Q_2 = Q_0 \frac{\lambda_1}{z_0} \frac{\lambda_2}{d_2} e^{-\frac{d_1}{\lambda_1}} \left(e^{\frac{z_0}{\lambda_1}} - 1\right) \left(1 - e^{-\frac{d_2}{\lambda_2}}\right). \tag{11.30}$$

Insert λ_1 and λ_2 from Equation 11.16 and Q_0 from the prognosis using the Box model (see Section 11.1.1), it follows for Equation 11.30:

$$Q_2\left(p, |\vec{E}|\right) = Q_{\text{ini}} \frac{|\vec{E}_1|}{E_0} \ln\left(1 + \frac{E_0}{|\vec{E}_1|}\right) \frac{\alpha^2 |\vec{E}_1| |\vec{E}_2|}{p^2 z_0 d_2} e^{-\frac{p d_1}{\alpha |\vec{E}_1|}} \left(e^{\frac{p z_0}{\alpha |\vec{E}_1|}} - 1\right) \left(1 - e^{-\frac{p d_2}{\alpha |\vec{E}_2|}}\right). \tag{11.31}$$

Since the electron is acting as an ionizing particle, it can be assumed that α is defined to be $(0.15 \pm 0.03)\, \frac{\text{ppm cm}}{\text{kV/cm}}$ according to Reference [235]. Figure 11.10 shows the expected charge Q_2 for a typical field dependent on the electric negative impurity p.

The integrated charge $Q_2\left(p, |\vec{E}|\right)$ is proportional to the reciprocal value of p^2 due to the complicated geometry of the ^{207}Bi chamber (compared to the one from ^{241}Am chamber). Therefore the integrated charge of the ^{207}Bi chamber falls faster with increasing impurity p compared to ^{241}Am chamber.

Purity determination

In order to measure the purity the combination of both ionization chambers is used since advantages of both ionization chambers can be used. Figures 11.7 and 11.10 show the expected amplitudes from the ^{241}Am and ^{207}Bi chamber respectively. The sensitivity to the changes of the impurity p is for the ^{207}Bi chamber in the range of 1 ppm which is high compared to the ^{241}Am

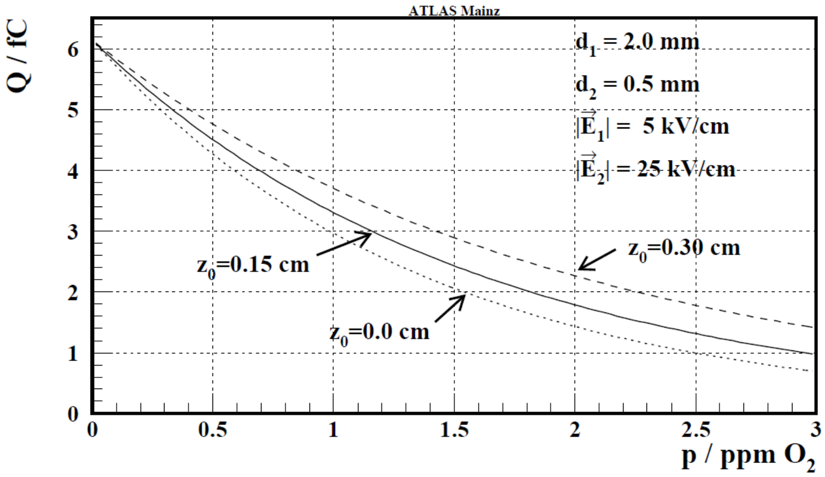

Figure 11.10: *The expected signal amplitude of the ^{207}Bi chamber as a function of the impurity p for different projections z_0. The specified values for the electric field and the length of the drifting room correspond to the real values used in the basic monitor [229].*

chamber. However, the ^{241}Am chamber is complementary to the ^{207}Bi chamber and allows for measurements over a wide range of p.

Figure 11.11 shows schematically the electric construction. Since the readout of the chamber signals in ^{241}Am chamber is performed over the cathode and in ^{207}Bi chamber over the anode, the corresponding influenced electric current has opposite directions. Therefore the signals have different polarity after the integration from the preamplifier. The respective chamber, where the signal is created, can be identified by using the common linear and symmetric preamplifier.

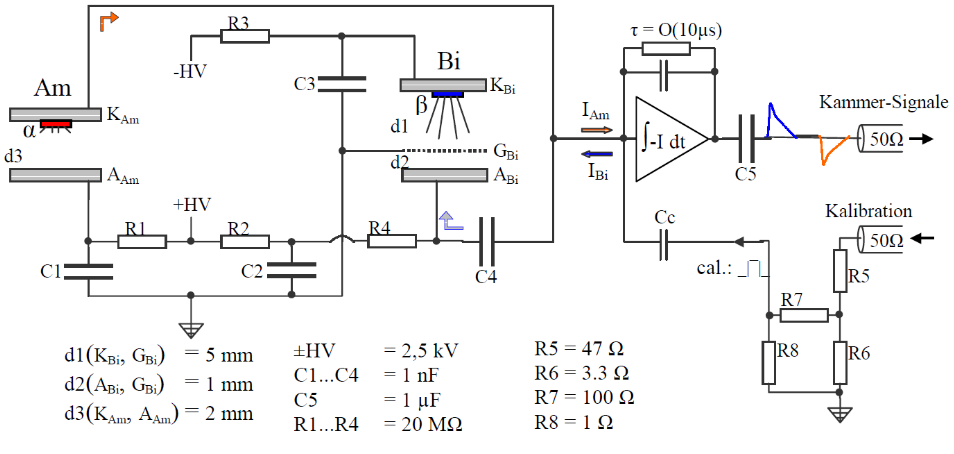

Figure 11.11: *Schematic presentation of the basic monitor [239].*

For the determination of the absolute purity the ratio of the integrated charge from the ^{207}Bi chamber to the one from the ^{241}Am chamber is calculated in the purity monitoring system. Figure 11.12 shows the ratio $Q_{\mathrm{Bi}}/Q_{\mathrm{Am}}$ dependence on the impurity p for different temperature values.

The parametrization of the ratio is represented by a fit of the model function of different models discussed in Section 11.1.1 to the data points, allowing the recombination of the ^{241}Am cell and the attachment rate to vary. Furthermore, an overall offset of the ratio has been added as an additional fit parameter. The fit emphasizes, that the recombination in the Box model is overestimated by 10%. The inconsistency of the model function with the measured data could

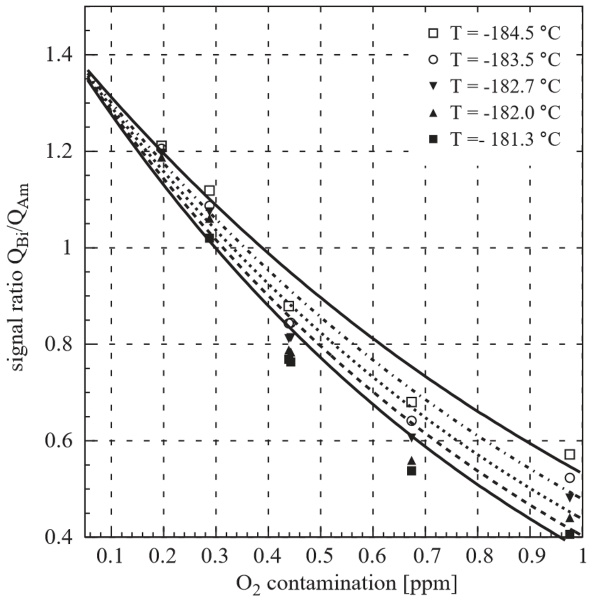

Figure 11.12: *The measured ratio of the signal amplitudes of the* ^{207}*Bi-cell* ($|\vec{E}_1| = 4.5$ *kV/cm*, $|\vec{E}_2| = 25$ *kV/cm) and* ^{241}*Am-cell* ($|\vec{E}| = 10$ *kV/cm) for different temperatures as a function of the oxygen contamination. The lines correspond to the prediction of the models discussed in Section 11.1.1 [234].*

be explained by shortcomings of the recombination model and the assumption of a homogeneous charge deposition along the track of the conversion electrons. The measured signal ratio hints at a steeper dependence on the oxygen content for low impurities and a smaller gradient for impurities around 1 ppm [234]. For a fixed oxygen contamination value, the measured signal ratio is larger with lower temperature.

For the operation of the LAr calorimeter a long-term stable impurity of approximately up to 1 ppm is acceptable [100], which means that the LAr purity monitoring system has to be operational in the measuring range under 1 ppm in order to see the worsening of the purity. Basic monitor makes it possible to measure the impurity up to 3 ppm with a statistical uncertainty of 7.4 ppb and an estimated systematic uncertainty of 21% [234]. Therefore it satisfies the asked requirements.

11.2 Current hardware chain

The purity measurement in ATLAS detector works generally in the way described in Section 11.1.2. One of many goals during the development of the LAr purity monitoring system was the realization of an automated system. Therefore a series of several systems was developed in Mainz, all of which together make the automated operation possible. An overview of the current LAr purity monitoring system and its functionality is given in the following.

Figure 11.13 shows the schematic representation of the electronic and software components from the current LAr purity monitoring system. Here the basic monitor (BM) is a sensor, which gives the analog signals containing the information about the LAr purity. These signals are sent over FEB[7] to the PFEB[8], where they are digitized, processed and sent to the PC[9], which calculate the LAr purity under usage of data (HV and temperature) from DCS[10] and sent it to the DCS.

---

[7] Front-End Board

[8] Purity Front-End Board

[9] The data collecting, processing and archiving software WinCC OA using OPC UA is located on the PC.

[10] Detector Control System

The shown voltage flow will be described in the next Sections.

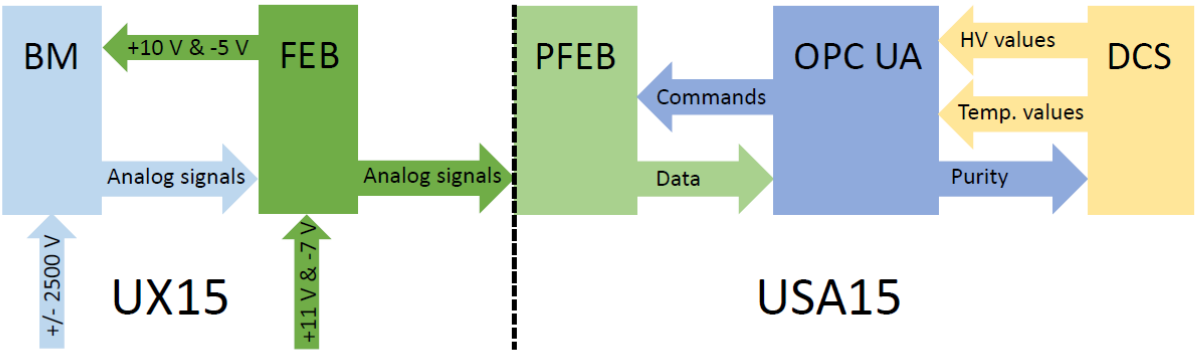

Figure 11.13: *Schematic representation of the data and voltage flow of the LAr purity monitoring system.*

11.2.1 Realization of the basic monitor

The ^{241}Am and ^{207}Bi chambers described in Section 11.1.2 are located on one plate together with high voltage electronics and charge sensitive preamplifier. The electronic components are four capacitors with 1 nF each, and four resistors with 20 MΩ each, all labeled in Figure 11.14, which shows also all the other components of basic monitor on the plate together. The description of the components is based on the convention given in Figure 11.11.

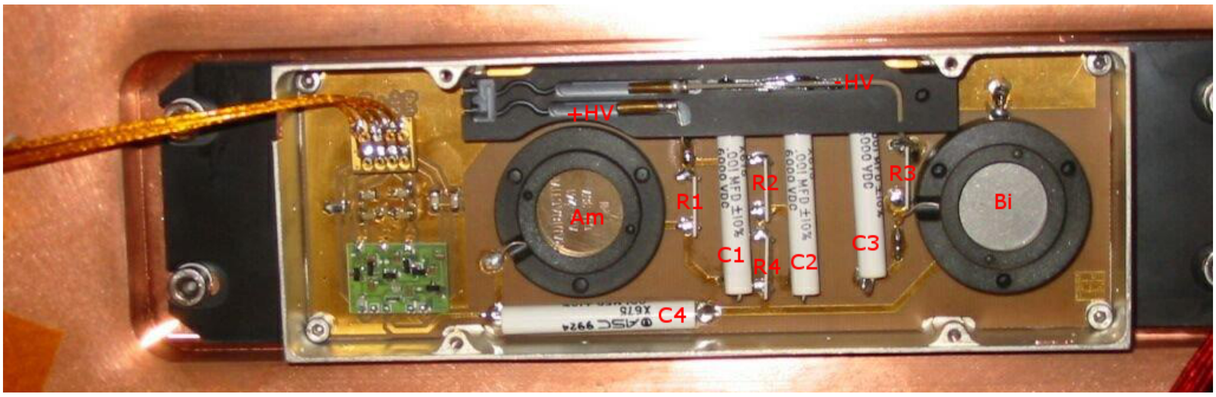

Figure 11.14: *The standard configuration of the basic monitor as it is used in ATLAS detector (here just before complete construction) [240]. The red description of the components is based on the convention given in Figure 11.11.*

The advantage of the transport of the signals from the chambers over one line as described in Section 11.1.2 is that the whole electronic chain influences both chamber signals in the same way. It is therefore not necessary to consider the impact through several electronic components to both signals from the chambers separately.

The absolute charge calibration[11] with used preamplifier was proven to be difficult [238]. This problem was bypassed by taking the ratio $Q_{\mathrm{Bi}}/Q_{\mathrm{Am}}$ from Equations 11.24 and 11.31. On this way all the factors coming from the charge calibration cancel each other.

Since the produced amount of charge in the chambers is just a matter of few fC, a charge sensitive preamplifier ($\approx 1\,\mathrm{mV\,fC^{-1}}$) is used, which is optimized for the operational temperature

---

[11] The voltage amplitudes as an output from the preamplifier are the measure of the integrated charge. In order to connect these two quantities, the preamplifier has to be calibrated.

range between 86 K and 90 K. The development and production of this preamplifier was made by V. Radeka from Brookhaven National Laboratory, which is the reason why this preamplifier is also called Radeka-preamplifier.

The cable pipe described earlier includes four coaxial cables. One cable carries the signal from the chambers to Front-End Board, the other three receive from the Front-End Board positive low voltage (+10 V) and negative low voltage (-5 V) for Radeka-preamplifer and the calibration pulses. Lastly the HV of ±2.5 kV is provided to the chambers from HV feedthrougs installed in the ATLAS detector. The provided HV is used by both ionization chambers.

There are two different configurations of basic monitors which are installed in the cryostates of the ATLAS detector. The previously described configuration is also referred to as standard configuration of the basic monitor, which consists of ^{241}Am-chamber, ^{207}Bi-chamber, high voltage electronics and charge sensitive preamplifier. In addition, there is a so-called FCAL configuration. It refers to the basic monitors, where the preamplifier input and the chamber output are connected via an approximately 4.5 m coaxial cable[12] [241]. The preamplifier lies in a separate box in a place with less „radiation“ inside of the cryostates. There are two types of the monitors with FCAL configuration. One of them consists of two different ionisation chambers, the other only of a ^{241}Am chamber. However, all monitors with FCAL configuration could not be considered to be operational since they never delivered the purity data.

11.2.2 Front-End Board

The Front-End Board (FEB), also known as driver board or read out board, is the hardware step between BM and PFEB deployed in UX15. Figure 11.15 shows a block diagram of the functionality of the FEB.

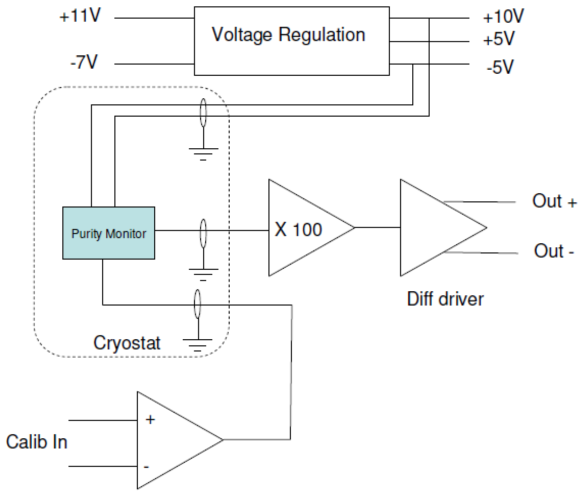

Figure 11.15: *Block diagram of the functionality of the FEB [242].*

Each FEB has to provide the following functionality [242]:

- Provide the +10 V and -5 V power for the Radeka-preamplifiers in BMs;
- Provide the ±5 V for the OpAmps;
- Receive the signal[13] of the purity monitor;

---

[12] Actually, there are two different coaxial cables which in total have a length of 4.5 m. However, both have the same capacity and therefore the same impact on the preamplifier. So, they can be considered as one piece of the coaxial cable.

[13] The signal has an impedance of 50 Ω.

- Boost this signal by a factor of 100 in total[14];
- Drive the signals differentially to USA15;
- Send the calibration signal to the Radeka-preamplifier.

All above mentioned voltages are currently derived from +11 V and -7 V rail of the Front-End Crate power bus. Both voltages from the power bars are fused with 0.5 A. The protection against overvoltage and voltage reversal is ensured by avalanche diodes. The board utilizes the radiation hard regulators ST4913LHC and ST7913LHC for the above mentioned low voltage for the Radeka-preamplifiers in BMs and the OpAmps. Each preamplifier is provided with a separate regulator in order to avoid any coupling between the channels.

There are in total 12 FEBs. Each of them consists of several electronic components. The active ones are OpAmps (HFA1135), voltage regulators and protection diodes for incoming voltages (of type SA12A). These active elements have been certified for the use at the level of the Front-End Crate (up to 300 fb^{-1}). Other components of the board are ceramic SMD capacitors, SMD resistors and fuses, and several connectors. The connections of each board are three pairs of twisted pair cable for the signal (approximately of 150 m length) and one twisted pair cable for calibration. More detailed information for FEB can be found in Reference [242].

11.2.3 Purity Front-End Board

The Purity Front-End Board (PFEB) is the so-called brain of the LAr purity monitoring system, which is placed in USA15 in order to reduce the radioactivity impact on the board and also save space on the ATLAS detector. A PFEB is responsible for following tasks:

- Signal processing (digitization, triggering, analysis and histogramming of the signal pulses);
- Deployment of calibration signal to UX15.

The PFEB can digitize up to six input channels with 40 Ms and 10 Bits. Figure 11.16 shows a PFEB in the last known version. The FADCs[15] are connected to a Xilinx FPGA which takes care of the triggering, calculates the amplitude utilizing a digital filter and histograms the pulses in external memory. The data are made available via CAN-bus to the computer.

There are 6 PFEBs in total. The detailed assignment of the PFEBs to the corresponding FEBs and BMs is summarized in Table 11.1. The assignment of the PFEB6, which is connected to the FCAL monitors only, is not listed there since these monitors are ignored anyway.

The communication between FPGA and a computer with software is established using CAN-protocol. A CAN-controller (SLIO[16]) is used in order to produce the CAN-frames and to transpose the physical layers. The SLIO consists of an internal RC-resonant circuit which is used for clocking. This resonant circuit should be adjusted every 30 ms in order to keep the stable clock pulse frequency. The clock pulse generation is performed using the definite CAN-frame which is produced by an external electronics called PicSync. The PicSync consists of the Microchip Pic microcontroller and a CAN-controller. The Pic has a bidirectional connection to the controller, which can unzip or pack the data using CAN-specifications and sent them to the bus. Furthermore, the microcontroller is connected with a time controlled relay which is able to interrupt the voltage supply of all PFEBs for 15 s. The control is performed via CAN-frame,

---

[14] The coaxial signal is received by an OpAmp of type HFA1135 (Intersil), which boosts the signal by a factor of 10. A second OpAmp of the same type provides an additional factor of 10. Hence the output signal is approximately 200 mV in amplitude. The bandwidth of this stage is approximately 60 MHz.

[15] Flash Analog-to-Digital Converter

[16] CAN Serial Linked I/O device with digital and analog port functions

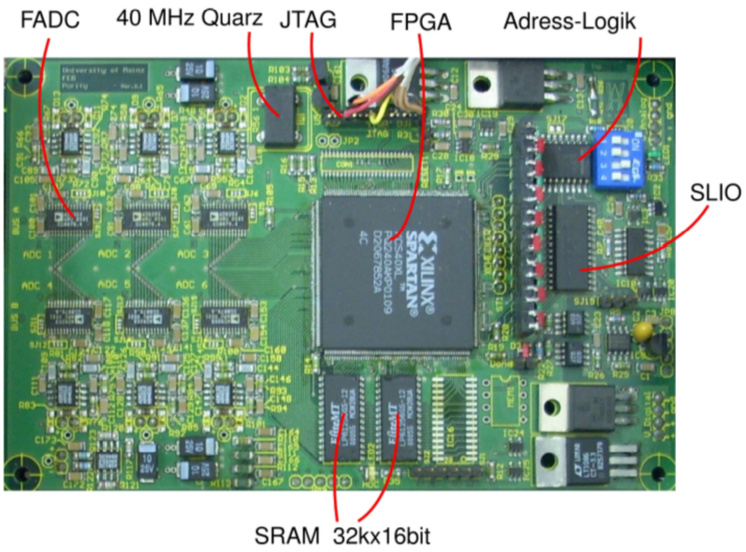

Figure 11.16: *Purity Front-End Board and its components [243].*

which can be produced from the PC. On this way, the whole CAN-bus-system can be restored remotely from Mainz in case of a failure.

The charge sensitive preamplifier has two inputs in a basic monitor. Both inputs go to the electronics, which should be amplified, while one of them is connected via a 1 pF capacitor (see Figure 11.11). By applying of the square-wave voltage a δ-like electric current pulse can be produced with the help of the capacitor. On this way the pulse answer can be measured on the output of the preamplifier. This input is called calibration input and is used in order to check the functionality of the analog and digital electronic chain. The calibration pulses are produced in FPGA in the time period of $T = 1.6$ ms which reduce the voltage amplitude via voltage divider and guide it to the calibration input.

The Pic-microcontroller contains a non-volatile flash memory in order to store the program code and has to be configured only once. This is performed using special hardware[17]. In order to configure the FPGA, the firmware, which will be discussed in Section 11.3 in more detail, can be loaded via CAN-frame. The rate of the data transfer is, however, relatively slow, and the transmission lasts about 50 s. In very rare cases, if the voltage supply of the PFEB was interrupted (mainly due to some maintenance works), the firmware should be loaded again after the interruption in order to establish the full functionality of the LAr purity monitoring system again.

11.3 Firmware for the FPGA

Due to planned long running time of the ATLAS experiment it is important to design and develop the systems to not only be modifiable but also to have maximum maintainability. The choice of the FPGA as signal processing unit fulfills these requirements for the LAr purity monitoring system, since FPGA is a chip which can work long and be modified with new functions without affecting already existing functions. Furthermore the current firmware designed in VHDL[18] by E. Ertel in 2009 [228] replaced the older version of the firmware.

The firmware was designed as far as possible independently of the hardware related components, and the functionality was described on the register-transfer-plane from the behavioural point

---

[17] A machine which can load a firmware.

[18] A language for the hardware description.

UX15		USA15
BM	FEB	PFEB
Barrel A1	I05L slot 14B	PFEB1
Barrel A2		
Barrel A3		
Barrel A4	I13L slot 14B	
Barrel A5		
Barrel C1	H05L slot 14B	PFEB2
Barrel C2		
Barrel C3		
Barrel C4	H13L slot 14B	
Barrel C5		
HEC 1AA	A07R slot 14B	PFEB3
HEC 1AB		
HEC 1AC		
HEC 2AA	A07R slot 14A	
HEC 2AB		
HEC 2AC		
EMEC AT	A13L slot 14B	PFEB4
EMEC AB		
HEC 2CA	C01R slot 14A	
HEC 2CB		
HEC 2CC		
EMEC CT	C08L slot 14B	PFEB5
EMEC CB		
HEC 1CA	C08L slot 14A	
HEC 1CB		
HEC 1CC		

Table 11.1: *The assignment of the PFEBs to the corresponding FEBs and the basic monitors (BMs).*

of view. It means that the illustration of the behavioural description on the chip architecture is decided by the synthesis tool, and the quality of the synthesized circuit depends on this decision. The current firmware contains no clearly structured modules which are interconnected, but rather behavioural description, which characterizes the transmission behaviour and can be divided in many different functions. In order to synthesize the VHDL code the Xilinx Foundation Tool was used. It was also responsible for the Place and Route[19].

11.3.1 The filtering system

A crucial function of the firmware is the preparation of the raw data delivered from FADC. The raw data passes through three filter stages. First, the data stream is formed by a differential filter. Second, the differentiated data is averaged by a summation filter. Third, the difference making procedure is performed. The first two filter stages have the task to deliver values for

---

[19] The final stage of the design of a circuit, which is carried out via automatic tools in case of FPGA. This phase consists of two different steps: placement and routing. In a placement step it is decided using an algorithm which position the certain logic components receive in the FPGA. After the placement step, these logic components are interconnected.

the trigger. With the last difference making procedure it is possible to get the amplitude of the signal by usage of the simple logic. The separate description of these filter stages follows in more detail.

Differential filter

In the first filter stage the data coming from FADC goes through the difference making procedure. In order to build the difference, where the minuend and the subtrahend are the data values which correspond to different time points, a delay has to be implemented which can be realized using shift registers. The data will be pushed with every clock one position further in the shift register with the depth of $(p_1 + 1)$ bits. In order to calculate the difference the date (D) on the last place (p_1) is subtracted from the date on the first place (0) in the shift register:

$$Q_i\left(i\right) = D\left(i\right) - D\left(i - p_1\right). \tag{11.32}$$

Figure 11.17 shows the difference making procedure of the raw signal with the edge rising of 100 values per 25 samples for different values of the filter parameter p_1. The low-frequency components, in which the cut-off frequency is determined by the parameter p_1, are suppressed due to calculation of the difference $Q_1\left(i\right)$. In this way the filter can be associated as the digital high pass. The cut-off frequency changes to larger values with lower values of p_1 because the edges are steeper with high-frequency signals than with low-frequency signals and therefore the maximum difference between $D\left(i\right)$ and $D\left(i - j\right)$ is available after few samples j. The parameter p_1 is chosen so that the difference $Q_i\left(i\right)$ is maximal for the typical signal and the parameter p_1 is minimal for it since the value of p_1 is directly connected with the value of the delay logic and the required FPGA resources. Furthermore the pile-up effects are suppressed by the filter, so that measurements with high rates could be possible (see Figure 11.18). In this way the minimization of p_1 is motivated additionaly, since two fast consecutive signals can not be distinguished if the value of p_1 is too high.

A value of 512 is added to every value of $Q_1\left(i\right)$ because it is easier to build the logic if it works with unsigned values. Due to drift time t_d of the electrons, the time, which is expected for the slope, is approximately 700 µs. It corresponds to 28 samples with typical clock frequency of 40 MHz. The parameter p_1 of the filter is set to the value $p_1 = 48$. In this way the filter covers the expected time, in which the edges rise.

Summation filter

In the second filter stage the data $Q_1\left(i\right)$ coming from the first filter stage is summed over p_2 samples to:

$$Q_2\left(i\right) = \sum_{\mu=1}^{p_2} Q_1\left(i - \mu\right). \tag{11.33}$$

The main purpose of this filter stage is the suppression of the high-frequency components by averaging over p_2 values. The filter can be associated as low pass which performs the smoothing on the data stream $Q_i\left(i\right)$ (see Figure 11.19). In this way gained data $Q_2\left(i\right)$ are used for triggering. The advantage is that the amplitude rises through the summation and therefore the vertical resolution gets better. In this way the fine tuning of the trigger threshold is possible, which is crucial for low signal-to-noise ratios.

The parameter p_2 is set to $p_2 = 24$ in the firmware. It means, that the zero line should be $24 \times 512 = 12288$. However, the zero line is reduced to 6144 since the last bin is cut away by a division by two.

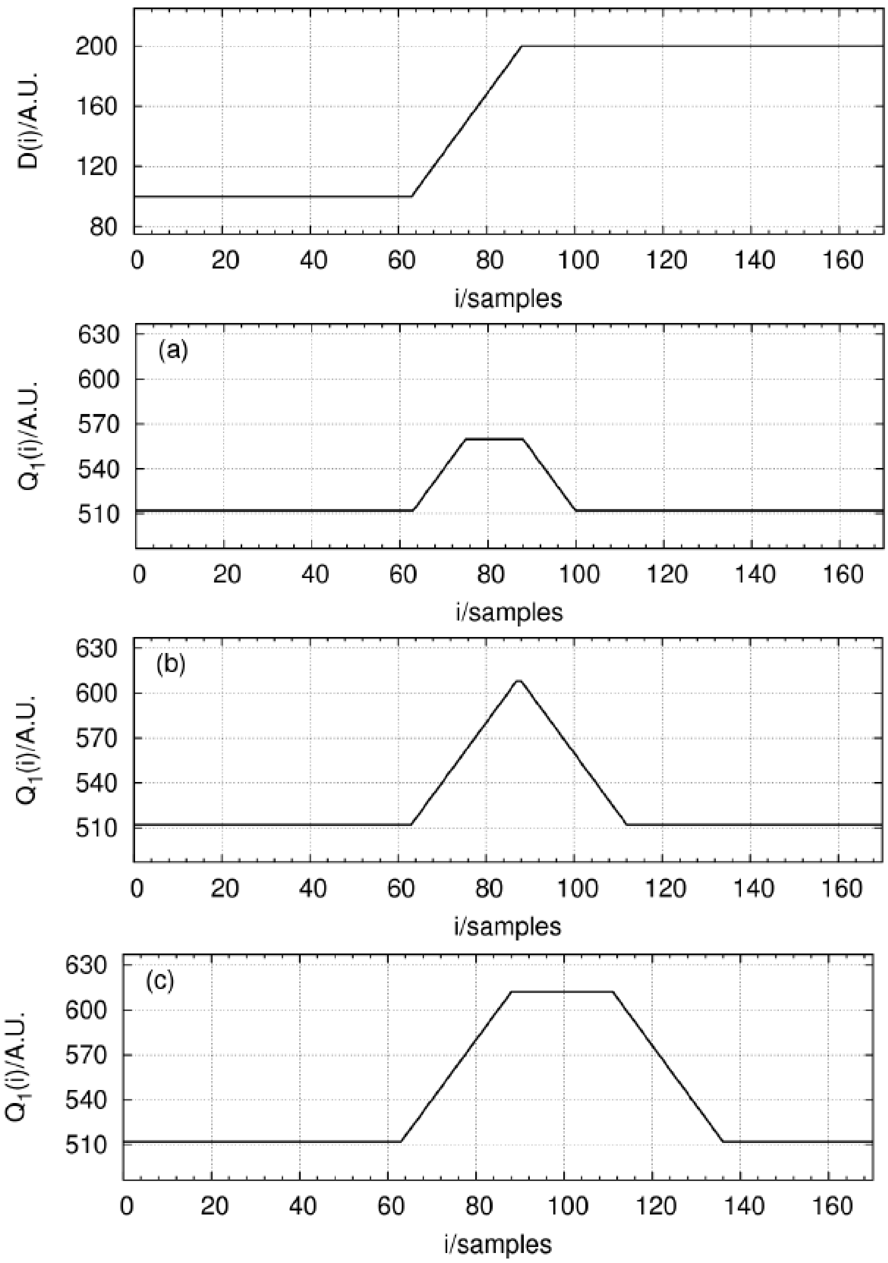

Figure 11.17: *Data stream as output of the differential filter for different values of filter parameter p_1 (a) 12, (b) 24, (c) 48. The edge of the input signal is linear and rises in the range of 25 samples by 100 values [228].*

Formation of a bipolar signal using a differential filter

The result of the differentiation is positive for rising edges and negative for falling edges. The result $Q_2(i)$ of the summation in the signal range contains a rising edge and a falling edge right after that. Calculating the difference with values of $Q_2(i)$:

$$Q_3(i) = Q_2(i) - Q_2(i - p_3) \tag{11.34}$$

leads to the bipolar signal (see Figure 11.20). The amplitude can be determined with a simple logic since the zero line is not necessary. The parameter p_3 is set to $p_3 = 48$ in the firmware. After the differentiation a value of 32768 is added to $Q_3(i)$ in order to guarantee unsigned values.

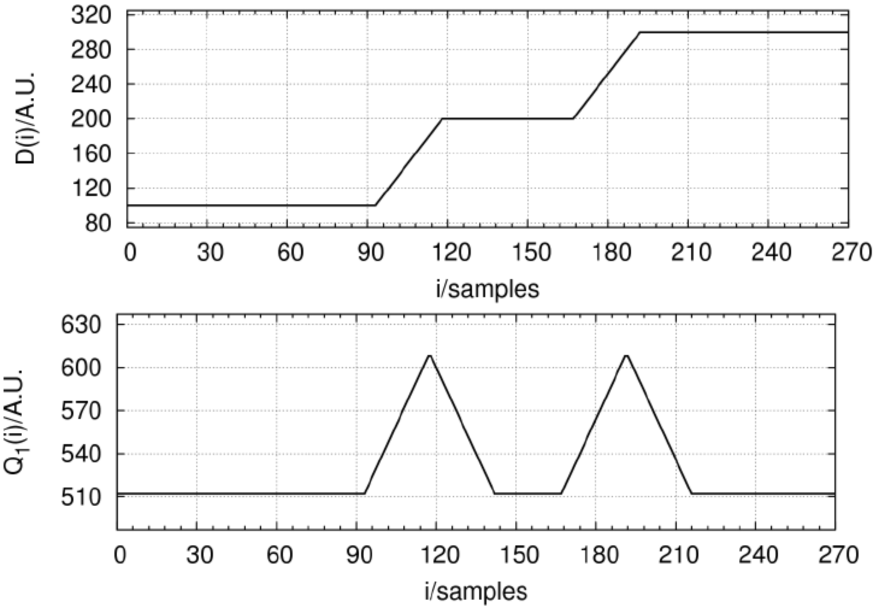

Figure 11.18: *Pile-up effect: two consecutive edges in a short time before (top) and after (bottom) the formation of the difference [228].*

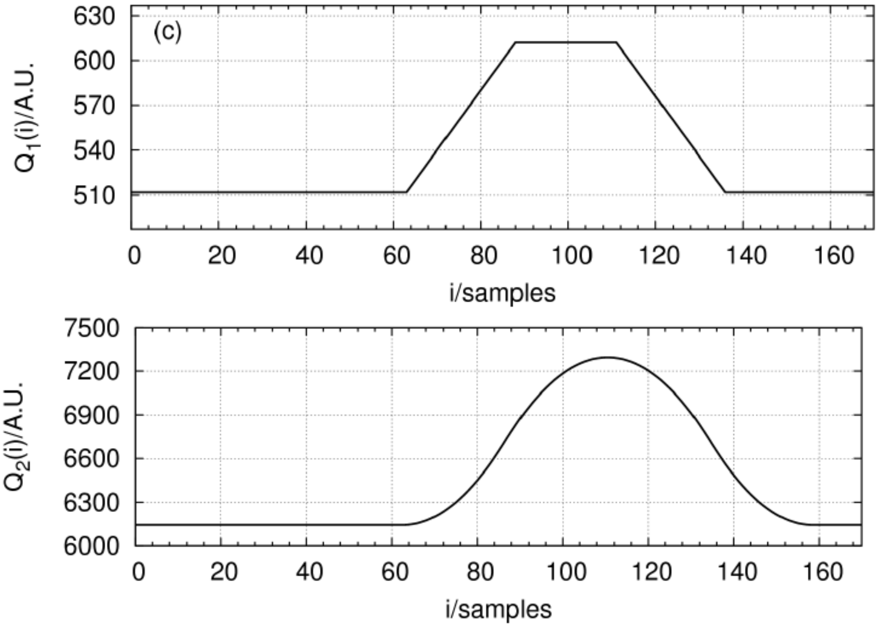

Figure 11.19: *Summation of the differentiated data $Q_1(i)$ with $p_2 = 24$ [228].*

11.3.2 Trigger logic

In addition to the values of $Q_2(i)$ the trigger uses some information from the configuration file stored on the production machine. This information is sent to the FPGA. The used information is the trigger thresholds for ^{241}Am and ^{207}Bi signals and the paralyse value, which defines the time window in which the amplitude should be determined.

The trigger compares the given thresholds with the resulting values $Q_2(i)$ after the summation. If $Q_2(i)$ is larger (lower) then the ^{241}Am (^{207}Bi) threshold, the trigger triggers. At the same time a bit is set, which carries the information about the origin of the chamber signals.

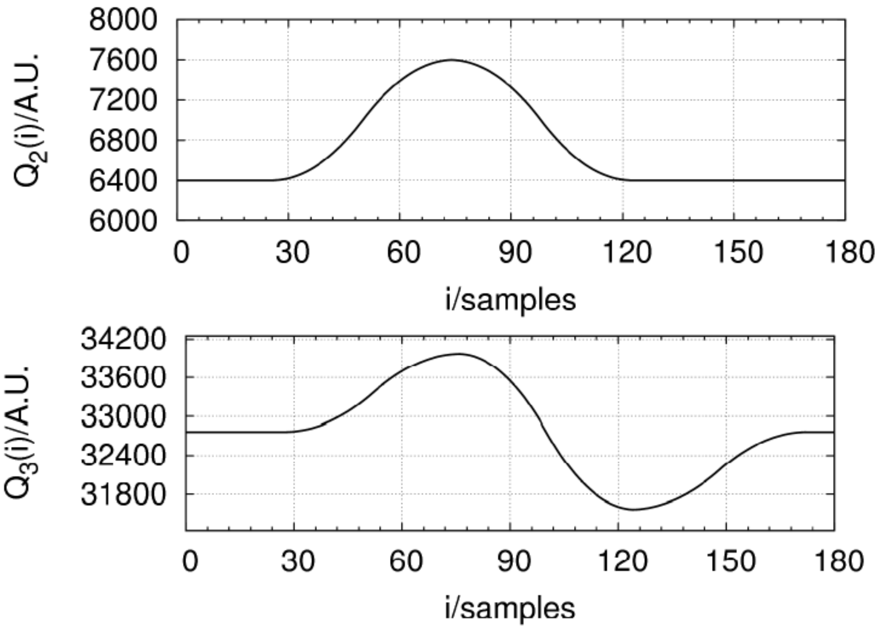

Figure 11.20: *Formation of the bipolar signal [228].*

A counter begins to work after triggering and stops after reaching the paralyse value. By reaching the paralyse time the histogramming procedure of the determined amplitude starts. A paralyse time is approximately 3 µs.

11.3.3 Amplitude determination

In order to determine the amplitude the maximal and minimal value of $Q_3(i)$ are determined first and then the difference is calculated. The time window for the amplitude determination is set by the paralyse value in the configuration file. In order to reduce the value further the result is additionaly divided by two.

11.3.4 Configuration of FPGA

The required information for the operation of PFEBs is received in FPGA and written into register. This information is stored in the configuration file on the production machine. There are 16 register with a width of 8 bits which are used for the storage of data. In the following the purpose of the parameters in the configuration file is explained:

1. *Choice of ADC*: There are 6 ADCs on one PFEB which can be selected by FPGA separately. The received value corresponds to the number of the equivalent ADC.
2. *Histogram statistics*: The value sets the amount of entries in the histograms.
3. *Calibration pulse*: The value sets the amplitude of the calibration pulse on the output of PFEB. There are 16 valid values which correspond to the output voltages of 0 mV to 200 mV. The configuration values are linear between these voltages.
4. *Operation mode*: There are three operation modes available. Histogram mode records the histograms, row data mode records data at the entrance of the filter, bipolar mode records data at the exit of the filter.
5. *First und last RAM-address*: These values set the RAM address range of the FPGA.

6. ^{207}*Bi trigger threshold*: A value that should be smaller than the zero line (6144). The resulting negative difference is the actual threshold.

7. ^{241}*Am trigger threshold*: A value that should be larger than the zero line. The resulting positive difference is the actual threshold.

8. *Paralyse*: This value sets the time needed for the amplitude determination in histogram mode. In row data and bipolar modes it corresponds to the shift of the recorded data with increasing value to the left.

11.4 Current software chain

In order to evaluate the histograms the data are sent to the PC. This PC contains a chain of different programs which evaluate the histograms and visualize the results. This Section gives an overview of the different components of this software chain.

11.4.1 OPC UA server

The OPC UA server is the main part of the purity system since it is responsible for the communication with the PFEBs, management of the histograms and estimation of the peak positions. The basic design structure is shown in Figure 11.21. A more detailed schematic is shown in Appendix C.

The OPC UA server design is hardware oriented. This means that there is one MainPurity system, which holds objects of the different PFEBs[20]. Each of these PFEBs objects holds up to 6 BasicMonitors. The configuration of all shown properties is made via an .xml configuration file (which configures at the end the FPGA as written in Section 11.3.4). A short description of the single properties is listed in Table 11.2.

The OPC UA server manages the CAN communication between the FPGA and PC. More information about this can be found in References [243, 244].

The peak position estimation is implemented using ROOT functions from Reference [245] in a so-called peak finding algorithm[21]:

1. Search for the peak in the range 500-900 of the histogram. For the reference, the full range of the histogram is 0-1000.

2. If no peak could be found, extend the range to 350-900.

3. If again no peak could be found or there was found more than one peak at some stage (even in the range 500-900), then the peak finding algorithm failed. Otherwise the value of the found peak is used for the further procedures like purity calculation.

11.4.2 WinCC OA

In order to communicate between OPC UA server and the actual DCS, a software suite using WinCC OA (several scripts and panels) was created. It is also a small part of the FSM[22], an abstract representation of the ATLAS experiment. It allows to control the mapping between hardware and software components and helps to visualize the values of the ^{241}Am and ^{207}Bi peak positions and the calculated purity values. The values for the temperature and high voltage are

---

[20] The class „PurityFrondEndBoard“ refers to the Purity Front-End Board even though there is a spelling error in the class name.

[21] This algorithm is the same for both ^{241}Am and ^{207}Bi spectra.

[22] Finite State Machine

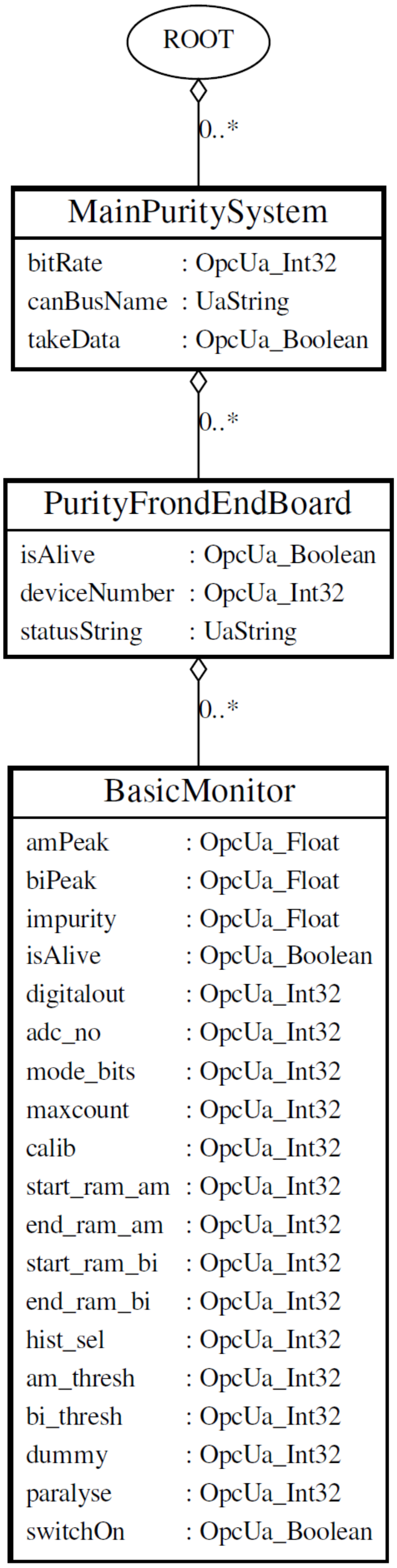

Figure 11.21: *Basic OPC UA server design [243].*

taken from the DCS for this. After the calculation of the purity values, they are provided to the DCS over the OPC UA server.

Parameter	Explanation
MainPuritySystem	
bitRate	bit rate of CAN bus (should be 125000)
canBusName	name of the CAN bus
takeData	true=DAQ starts, false=DAQ holds
PurityFrondEndBoard	
isAlive	true=is alive, false=is dead and will be skipped in DAQ
deviceNumber	number pf PFEB (has to correspond with the 4-bit switch on the board)
status string	status of PFEB (like sending, ioMode, sleep...)
BasicMonitor	
amPeak	^{241}Am peak position
biPeak	^{207}Bi peak position
impurity	impurity (calculated with dummy temperature and HV)
isAlive	true=is alive, false=is dead and will be skipped at DAQ
digitalout	unknown, is set to 0
adc__no	number of BM on PFEB
mode__bits	unknown, is set to 1
start__ram__am	where to start ^{241}Am histogram in RAM
end__ram__am	where to end ^{241}Am histogram in RAM (difference is number of bins)
start__ram__bi	where to start ^{207}Bi histogram in RAM
end__ram__bi	where to end ^{207}Bi histogram in RAM (difference is number of bins)
hist__sel	0=take ^{207}Bi histogram, 1=take ^{241}Am histogram
am__thresh	signal amplitude threshold for ^{241}Am signal
bi__thresh	signal amplitude threshold for ^{207}Bi signal
dummy	unknown, is set to 255
paralyse	time for the amplitude determination in histogram mode
switchOn	true=on, false=off and will be skipped at DAQ

Table 11.2: *Description of the single properties [243].*

11.4.3 Detector Control System

The DCS is used for the monitoring and control of the ATLAS detector. Several properties like voltage, temperature, pressure or device status are listed and recorded. On this way the current status of the detector can be seen. The long-term behaviour of the parameters and detector components can be observed, so failures can be recognized earlier. For the purity calculation recorded data from the database are used, which are delivered by the DCS.

Chapter

12

MAINTENANCE

> “*I can help! I can fix anything!*”
>
> Anakin Skywalker from Star Wars: Episode I - The Phantom Menace

In order to judge the status of the LAr purity monitoring system efficiently it is important to see the actual spectra of the Am and Bi sources[1] of all LAr purity monitors. After comparing them with the expectation a statement on the current functionality of the LAr purity monitor can be given. This visualization was previously very complicated. The improvement of the visualization procedure is realized by implementing a so-called LAr purity „expert panel“. Both previous and current visualization approaches are described in Section 12.1. It was figured out that the calibration pulses were running all the time. The study behind calibration is presented in Section 12.2. Furthermore, by coincidence it was found that some spectra look unexpected if the HV of the monitors is off. Since this could be an indication of errors of the HV mapping, a test on the issue was performed. The approach of this test and its results are discussed in Section 12.3. In order to understand the behaviour of some issues during the test, it was decided to take the spectra including all the noise. The description of this procedure, including the results is summarized in Section 12.4. Finally, in order to save all gained knowledge about the LAr purity monitoring system a completely new TWiki page was created with some informations on the purity monitoring approach. The topics of this documentation are briefly described in Section 12.5.

12.1 Spectra visualization

The current LAr purity monitoring system saves the spectra as a series of numbers in a .txt-files directly on the production machine. Each „histogram“ in such a file contains the following information:

- Full timestamp (from the year down to the seconds) of the record.
- The value of the peak position found by the peak finding algorithm implemented in the OPC UA server.
- 1000 numbers which represent 1000 equidistant bins in a „histogram“. Each of these numbers corresponds to the amount of entries for the given bin.

Each .txt-file contains all stored „histograms“ for Am or Bi source of the given LAr purity monitor. If the file would contain only one histogram the file size would be approximately 2.3 kilobyte. It is obvious that the file size increases with every „histogram“ written in the file. In order to actually visualize these histograms more implementation steps on the user side are needed.

---

[1] For the simplicity ^{241}Am and ^{207}Bi sources are called shortly Am and Bi in all further appearancies.

12.1.1 Previous approach

The previous approach was developed by M. Becker - a former LAr purity expert. Figure 12.1 summarizes all the needed steps, which are also described below.

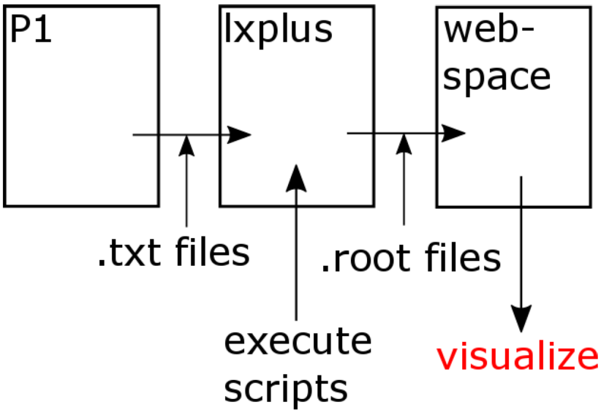

Figure 12.1: *Summary of the steps from the previous visualization approach.*

1. The .txt-files should be copied from the production machine (P1) to the lxplus (private) storage area[2].
2. Execute the scripts written using python [246] programming language[3], which transforms the .txt-files into the .root-files containing the actual spectra.
3. Reload previously written website, which take an information from the .root-files and shows the spectra on the screen.

This approach has several disadvantages. First of all, it is complex. In order to see the spectra the user should copy files, execute scripts and open a specific site in the internet browser. Second of all, it is non-general. Almost every step was connected to the private area of M. Becker leading to the fact that everything was connected to one single person whose availability at ATLAS was limited. The implementation of LAr purity „expert panel“ was primarly designed to solve these problems.

12.1.2 LAr purity „expert panel“

The LAr purity „expert panel“ was designed using features and tools from WinCC OA 3.15 [247]. Figure 12.2 shows this panel with exemplary Am and Bi spectra of HEC 1CA LAr purity monitor, which look similar to the theoretical expectations shown in Figures 11.6 and 11.9 (single peak for Am spectrum and two peaks with the Compton continuum in between for Bi spectrum, where the last peak is used for the purity calculation).

The functionality of this panel is driven by the following scripts:

- Clicked script for Selected monitor button.
- Clicked script for Change the status button.
- Initialize and text changed scripts for Path field.

---

[2] The storage area should be not necessary the private one, but since lxplus area is directly connected to some user and not for example to an institution, the lxplus area can be considered as private by definition.

[3] The scripts were written by M. Becker.

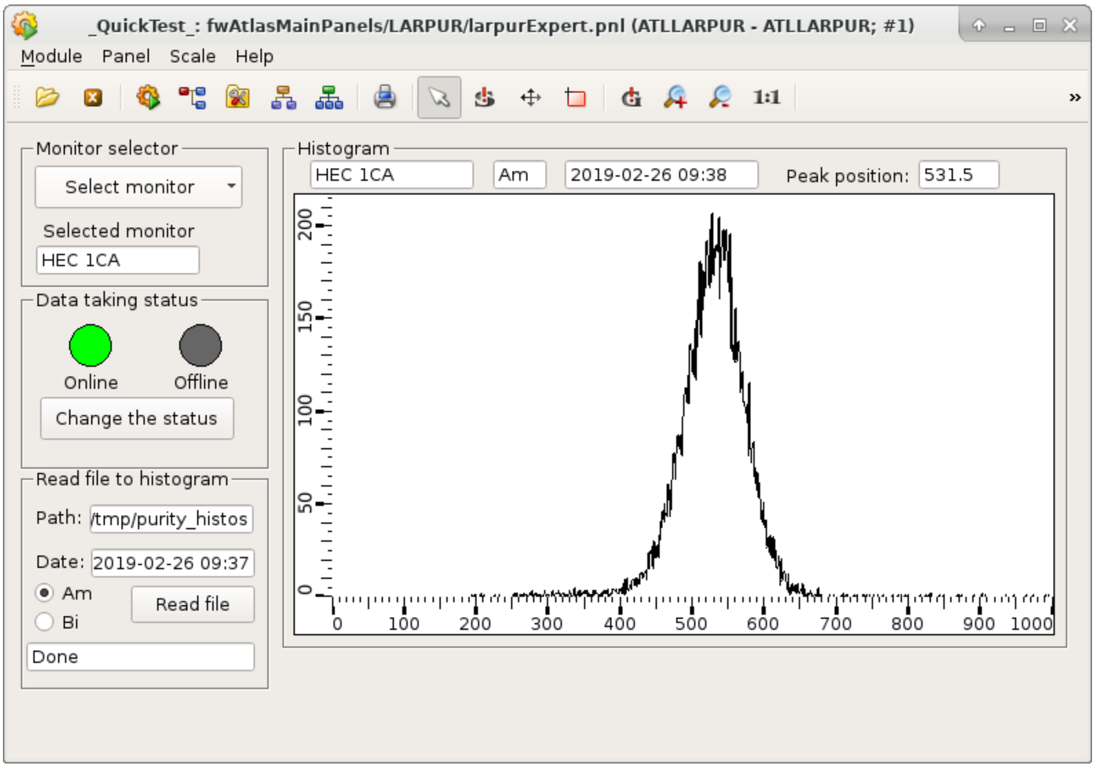

QuickTest: fwAtlasMainPanels/LARPUR/larpurExpert.pnl (ATLLARPUR - ATLLARPUR; #1)

Selected monitor
HEC 1CA

Path: /tmp/purity_histos
Date: 2019-02-26 09:37
● Am
○ Bi
Done

HEC 1CA | Am | 2019-02-26 09:38 | Peak position: 531.5

(a) Am spectrum.

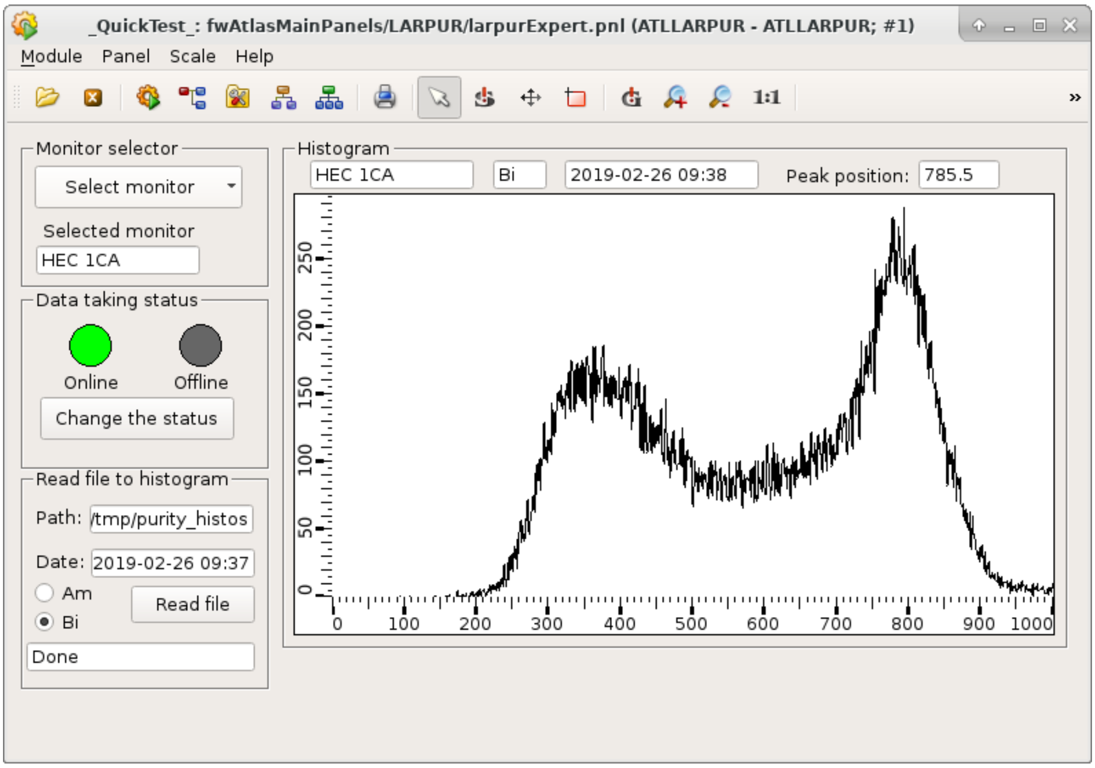

QuickTest: fwAtlasMainPanels/LARPUR/larpurExpert.pnl (ATLLARPUR - ATLLARPUR; #1)

Selected monitor
HEC 1CA

Path: /tmp/purity_histos
Date: 2019-02-26 09:37
○ Am
● Bi
Done

HEC 1CA | Bi | 2019-02-26 09:38 | Peak position: 785.5

(b) Bi spectrum.

Figure 12.2: *LAr purity „expert panel". The left part of the panel is responsible for several settings, which the user can select, and the majority of the right part of the panel serves as an actual visualization part by showing the spectrum and few information about it.*

- Initialize and text changed scripts for Date field.
- Clicked script for Read file button.

Since this panel was integrated as a part of the official LAr purity monitoring software which lies in P1, it can directly use the .txt-files and visualize them without other complicated steps. Furthermore it can be started from everyone who has access to P1 and is therefore no longer connected to a private area. After the start, the usage of this panel is pretty straight forward, but just in case the full description is written below:

1. Select the monitor from the menu. The name of the selected monitor and its data taking status (online or offline) are the displayed.
2. The data taking status can be changed by clicking on Change the status button. If the data taking is stopped for some monitor, then this monitor is skipped during the read-out process. However, it does not mean that the monitor went offline completely.
3. Write down the path to the stored .txt-files (or use the default[4] one, where the .txt.-files are stored as default).
4. Put the date including time after which you are looking for the histogram in the exact following format: „YYYY-MM-DD HH:MM“. Here is YYYY, MM, DD, HH and MM corresponds to the year, month, day, hour (in 24 hour format) and minute respectively[5]. Ignore this field to get the most recent stored spectrum of the chosen monitor.
5. Choose the source (either Am or Bi) and press Read file button.
6. If everything is done correctly, the message Done will be shown in the status field on the bottom of the panel and on the right side the histogram will be shown with some information about it (monitor name, selected source, time stamp of the histogram and the peak position[6]). If the status field shows something different from Done, then there is something wrong and the text in the status field should give a first hint about what went wrong.

The LAr purity „expert panel“ is a practicable and less complicated way to visualize the stored spectra, but there is still one aspect which impacts the performance of the panel: the size of the stored .txt-files. The visualization takes more time the bigger the file to read is. In order to speed up the performance of the panel (and to reduce the amount of used disc space on P1) it is recommended to copy the .txt-files at least once per year to some other storage place and delete them on P1. The stored files on P1 could be automatically deleted due to back-up works performed centrally by the ATLAS DCS team[7], so it is highly appreciated to follow up to the announcements of these works and copy the files before back-up works proceed.

12.2 Calibration

With rising information about the LAr purity monitoring system it was found that on this system the calibration pulses were running along to the signal pulses. It is not a problem for the monitors which deliver proper purity data, since the calibration pulses are significantly lower

---

[4] /localdisk/tmp/purity_histos

[5] It should be mentioned since the system which stores the .txt-files uses different time zone for the timesteps, the displayed time on the LAr „expert panel“ is a bit different from the time displayed on the FSM. In fact: FSM time = panel time + 1 hour.

[6] -1 for the peak position means, that the peak was not found.

[7] In this case the team usually provides the list of folders which might be deleted. If the /tmp folder is on this list, then the action is needed.

than the signal pulses. However, the calibration can explain the strange spectra with several peaks almost at the same height, like in Figure 12.3, which shows the Am and Bi spectra for Barrel A1 LAr purity monitor[8].

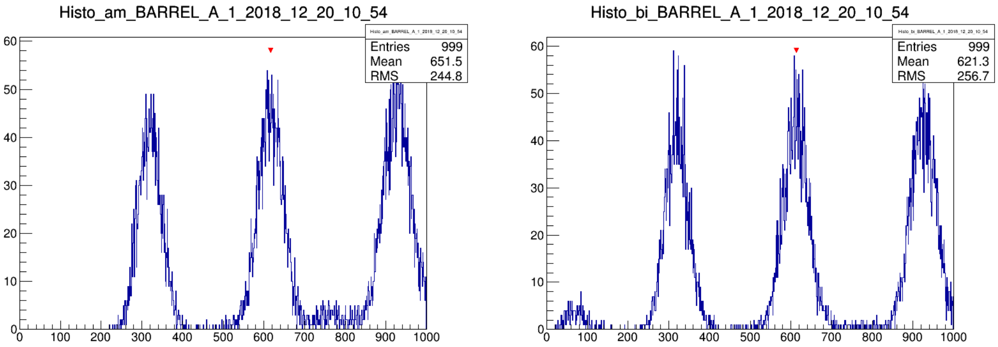

(a) Calibration value = 16.

(b) Calibration value = 16.

Figure 12.3: *Am (left) and Bi (right) spectra for Barrel A1 LAr purity monitor. The calibration value is set to 16 and HV is off.*

It turned out that these spectra were made with the calibration value, which was set to 16 - the default value up to that time point. A test was performed for this monitor, where the calibration value was changed from 0 to 16. With the value 0 no spectra for Barrel A1 could be stored (most probably due to default high thresholds for Am and Bi sources as it was found out later, since otherwise the noise spectra would be visible[9]), the spectra with values 1-3 are shown in Figure 12.4, the other spectra can be found in Appendix D.

Judging from the results shown in Figures 12.3 and 12.4, the calibration value 16 provides a series of the calibration pulses, more accurate a sum of the calibration pulses from the values 1-15 (since the amplitudes for the values 1-3 are much higher as the ones for the values 4-15, the three peaks from the values 1-3 are seen in Figure 12.3 while the contributions from the values 4-15 are visible as the „noise“ between the peaks). However, since it makes no further sense to have calibration online during the proper purity measurement, the decision was made, to switch calibration off permanently. Technically, the calibration value = 0 is now the new default. Figure 12.5 shows the direct comparison of the Am and Bi spectra before and after switching calibration off for HEC 1CA LAr purity monitor.

It can be seen, that the small calibration peaks around the signal peak seen in Figure 12.5(a) are gone in Figure 12.5(c). The Bi spectrum after the calibration shutdown looks a bit smoother in the middle range of the spectrum.

The Am and Bi spectra with these new nominal settings are summarized in Appendix E for reference.

12.3 HV mapping test

During the test with the calibration for Barrel A1 monitor it was found that switching HV for Barrel A1 monitor impacts impurity measurement for Barrel A3 monitor. Furthermore switching

---

[8] It should be mentioned that these spectra looked the same no matter if HV modules for Barrel A1 monitor were on or off. This observation was the main motivation to check this monitor closer. As it turned out later during the HV mapping test described in Section 12.3 the monitor Barrel A1 did not receive HV during the whole calibration tests.

[9] However, this hypothesis was not tested.

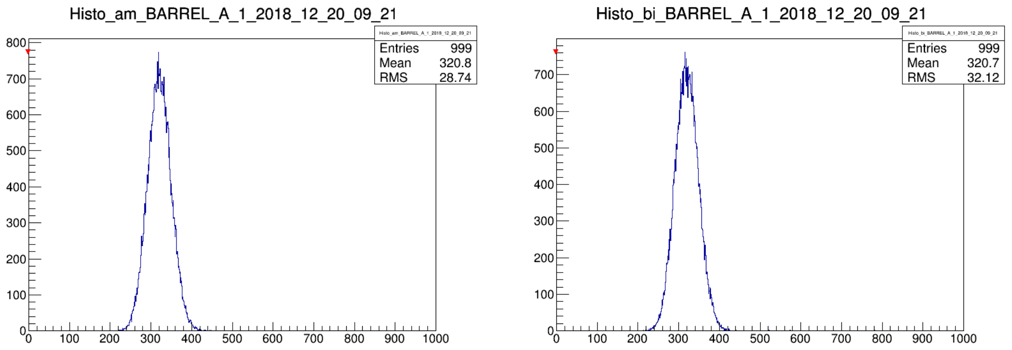

(a) Calibration value = 1. (b) Calibration value = 1.

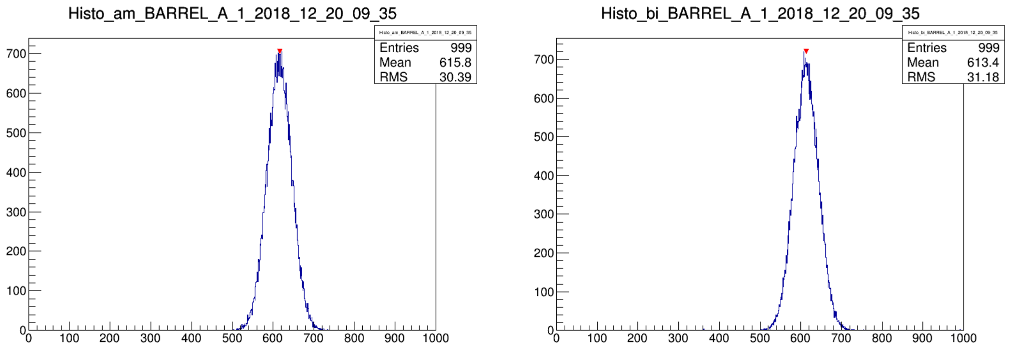

(c) Calibration value = 2. (d) Calibration value = 2.

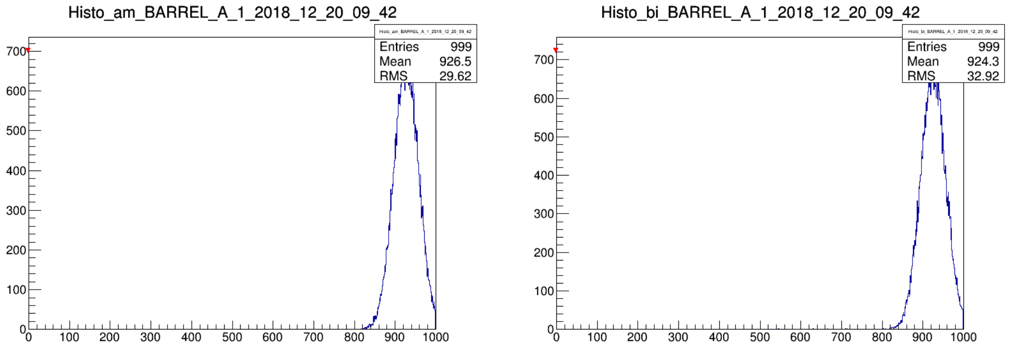

(e) Calibration value = 3. (f) Calibration value = 3.

Figure 12.4: *Am (left) and Bi (right) spectra for Barrel A1 LAr purity monitor. The calibration value is set to 1, 2 and 3 on the top, in the middle and on the bottom, respectively, and HV is off.*

HV for HEC 1AA monitor impacts impurity measurement for HEC 2AA monitor in a similar way. The idea of an HV mapping test was born, which was done in a few parts in total of two days (the test time was limited by some other ATLAS maintenance constraints).

The initial idea was to switch HV off for every LAr purity monitor except for one HV module. This way in theory only one spectrum should be stored and then visualized using LAr purity „expert panel“ - the one which is directly connected with the HV module. However, this idea did not work since values for Am and Bi peaks seem to be updated only if new values for the Am peak exist. (Probably the idea would work anyway if the trigger thresholds would be set to the zero line[10]. The knowledge about this was gained only after the end of this HV mapping

---

[10] However, again this hypothesis was not tested.

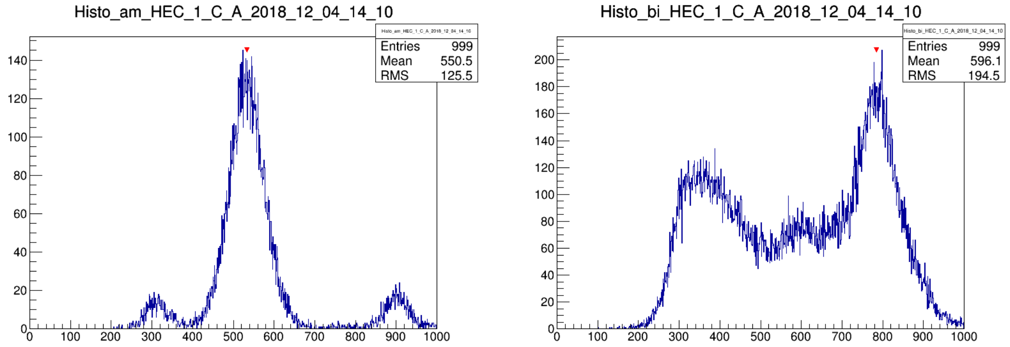

(a) Calibration is on.

(b) Calibration is on.

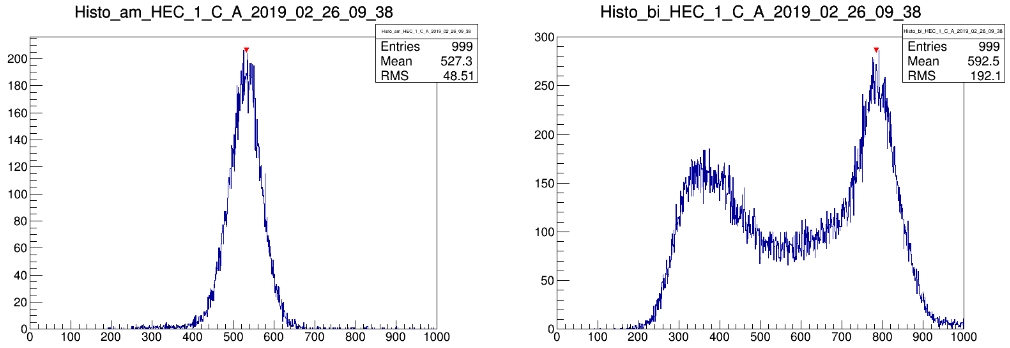

(c) Calibration is off.

(d) Calibration is off.

Figure 12.5: *Am (left) and Bi (right) spectra for HEC 1CA LAr purity monitor. The calibration is switched on on the top (off on the bottom).*

test.) So a slightly different approach was used.

For every HV purity module in HEC A area the HV was switched on. It was proven that every purity monitor in HEC A area delivered the expected data and the other monitors did not deliver purity data. Then HV was switched off for one Bi HV module from that area. After some time the Am spectrum looked as expected for the default situation, but the Bi spectrum missed the peak on the right side of the spectrum (see Figure 12.6), and the HV mapping could be established. Repeating this procedure for Am HV module led to the situation that both Am and Bi spectra were not stored and combining this result with the information gained from the Bi HV module test the HV mapping could be established. Using this algorithm the complete mapping on the HEC A side could be noted. However, the procedure was changed for the rest of the test.

Moving to HEC C area, it was found out, that the algorithm used for HEC A area did not work. Switching HV off for Bi spectrum led to the situation that both Am and Bi spectra were not stored. The HV mapping between Am and Bi HV modules was not possible anymore. (Again, this is most probably due to default high thresholds for Am and Bi sources, since otherwise the noise spectra would be visible[11].) Assuming that Am and Bi HV modules from any purity monitor were connected to only one monitor and not to two different monitors, the algorithm was changed as follows. The HV was switched off for every LAr purity monitor except for the Am and Bi HV modules assigned to the same monitor. As a result the two stored spectra could be clearly identified to which monitor they were assigned. This new algorithm was kept for all the other monitors except for EMEC AB and EMEC CT (since LV was off for them in the test

---

[11] This hypothesis was not tested.

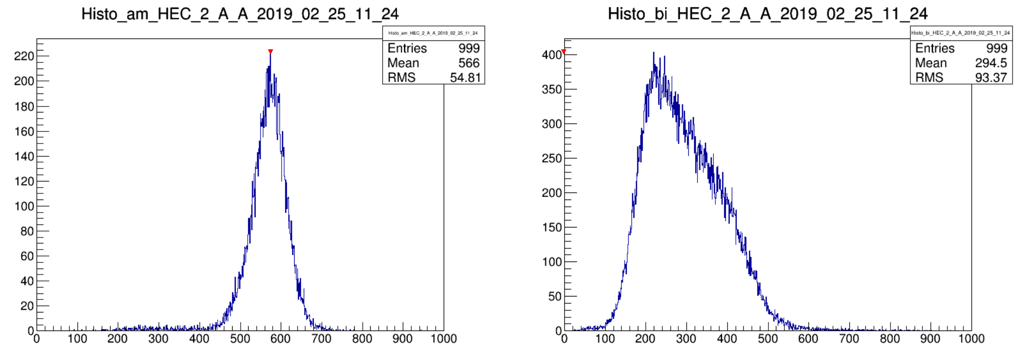

(a) Am spectrum of HEC 2AA monitor.

(b) Bi spectrum of HEC 2AA monitor.

Figure 12.6: *Am (left) and Bi (right) spectra for HEC 2AA LAr purity monitor. HV module for Bi source of HEC 1AA monitor is switched off. So, Bi HV module of HEC 1AA monitor impacts Bi spectrum of HEC 2AA monitor.*

period), and for Barrel C4 and EMEC CT (since they are declared to be dead).

Figure 12.7 summarizes the observations for HEC 2CB and HEC 2CC monitors. First HV modules only for HEC 2CB were switched on and the spectra shown in Figures 12.7(a) and 12.7(b) were seen, then HV modules only for HEC 2CC monitor were switched on and the spectra shown in Figures 12.7(c) and 12.7(d) were seen. So, a swap between these monitors is observed.

Figure 12.8 summarizes all results.

HV assigned to the HEC 1A* monitors impact the HEC 2A* monitors and vice versa. Furthermore there seems to be a switch between HEC *AB and HEC *AC monitors. HEC C area looks a bit better. There is no connection between HEC 1C and HEC 2C monitors as it should be and two monitors (HEC 1CA and HEC 2CA) are even connected properly. There is still a switch between HEC *CB and HEC *CC like in HEC A area. EMEC CB and Barrel C5 monitors are connected properly as well. The other Barrel C monitors (except Barrel C4, which was not tested) seem to have a swap between themselfes: 1→3, 2→1, 3→2. The same swap is observed in Barrel A area assuming that HV modules of Barrel A3 monitor impact Barrel A2 monitor which is dead and therefore do not store the data. Barrel A4 and Barrel A5 monitors seem to be swaped as well.

Overall, given that the swaps seem to have a „structure“ within them, it is more likely that the connection between HV modules and the purity monitors was accidently switched at some point. The question is: when and at which level the swaps were „implemented“? The first question is important to understand how much impurity data was archived using broken HV mapping and the last question is important to understand the problem. There are several possibilities:

- HV mapping on the LAr purity software side could be wrong (checked and it seems to be consistent to the previous mapping).
- HV mapping on the LAr purity hardware side could be wrong (since no interventions were made on the hardware side, it is unlikely that the fault is here [248]).
- Patch panel, where channels from HV devices are distributed to the cables, could be wrongly connected [249].
- The assignment of the signals from the monitors in a purity software could be wrong [249].

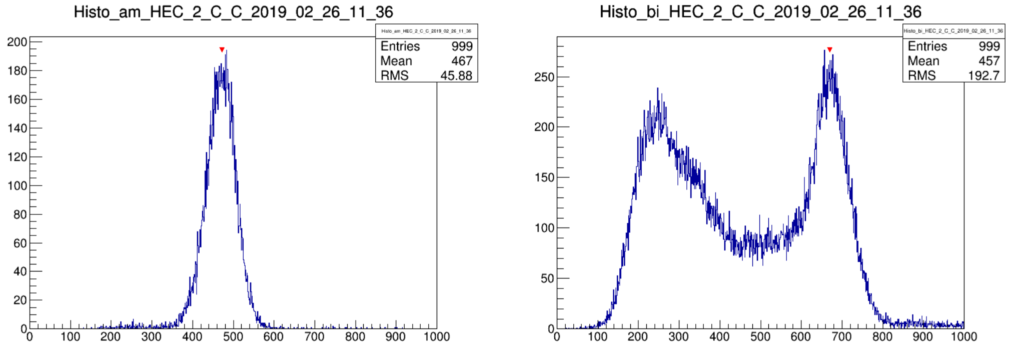

(a) Am spectrum of HEC 2CC monitor.

(b) Bi spectrum of HEC 2CC monitor.

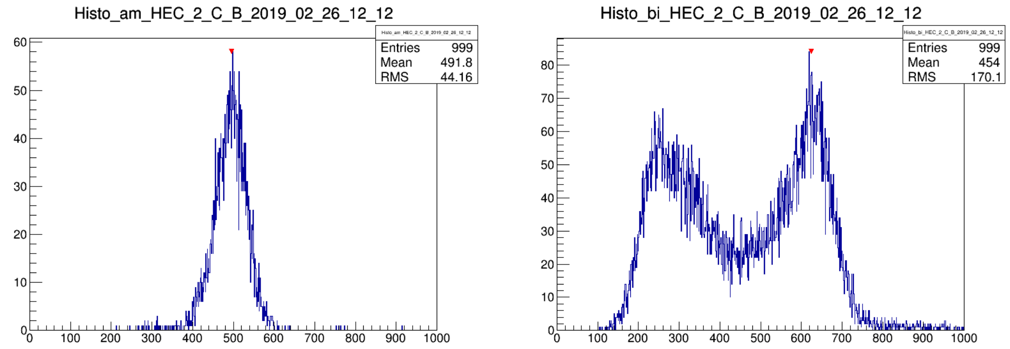

(c) Am spectrum of HEC 2CB monitor.

(d) Bi spectrum of HEC 2CB monitor.

Figure 12.7: *Am (left) and Bi (right) spectra for HEC 2CC (top) and HEC 2CB (bottom) LAr purity monitors. First HV modules only for HEC 2CB were switched on and the spectra on top were seen, then HV modules only for HEC 2CC were switched on and the spectra on the bottom were seen.*

One of the last two possibilities, seems to be the reason for the issue, but they were not checked, yet. Since it is odd, that it could be impossible to distinguish between Am and Bi HV mapping during the test, it was decided to make another test by decreasing the trigger threshold of the monitors and see if the spectrum will be stored then.

12.4 Noise spectra

Table 12.1 summarizes the values required for the trigger thresholds, stored in the configuration file, which is used by the running LAr purity monitoring system in order to configure the FPGAs. The actual trigger threshold has to be calculated using 6144 as a zero line (see Section 11.3 for more technical details about the FPGA firmware).

In order to record the noise spectra, the HV was set to be offline and both values in the configuration file (for Am and Bi) were set to 6144 for all LAr purity monitors. Figure 12.9 shows as an example Am and Bi spectra for HEC 1CA LAr purity monitor which are marked in blue. The spectra for the other LAr purity monitors look similar and can be found in Appendix F.

By fitting these spectra using a Gaussian fit

$$f(x) = p_0 e^{-\frac{1}{2}\left(\frac{x-p_1}{p_2}\right)^2} \tag{12.1}$$

the parameters p_0 (height of the curve), p_1 (mean of the curve) and p_2 (width of the curve) could

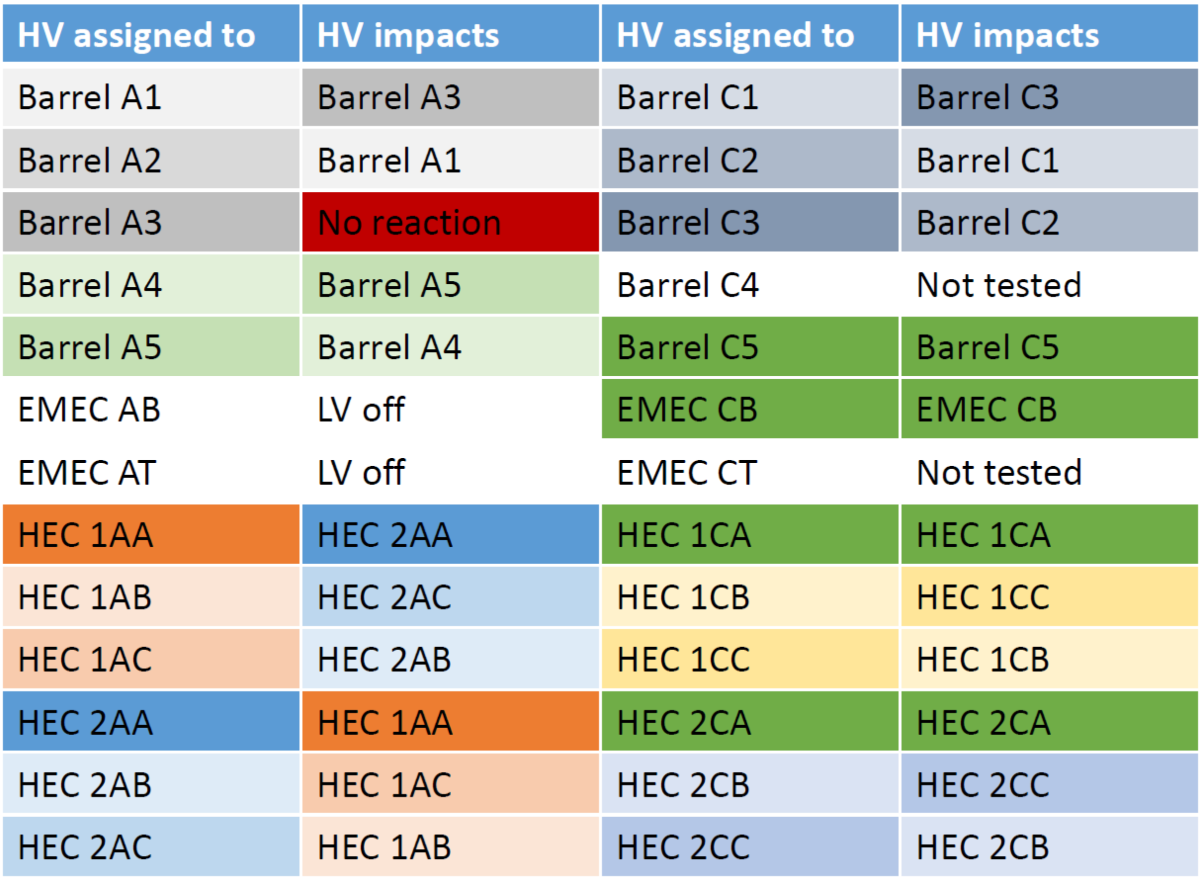

HV assigned to	HV impacts	HV assigned to	HV impacts
Barrel A1	Barrel A3	Barrel C1	Barrel C3
Barrel A2	Barrel A1	Barrel C2	Barrel C1
Barrel A3	No reaction	Barrel C3	Barrel C2
Barrel A4	Barrel A5	Barrel C4	Not tested
Barrel A5	Barrel A4	Barrel C5	Barrel C5
EMEC AB	LV off	EMEC CB	EMEC CB
EMEC AT	LV off	EMEC CT	Not tested
HEC 1AA	HEC 2AA	HEC 1CA	HEC 1CA
HEC 1AB	HEC 2AC	HEC 1CB	HEC 1CC
HEC 1AC	HEC 2AB	HEC 1CC	HEC 1CB
HEC 2AA	HEC 1AA	HEC 2CA	HEC 2CA
HEC 2AB	HEC 1AC	HEC 2CB	HEC 2CC
HEC 2AC	HEC 1AB	HEC 2CC	HEC 2CB

Figure 12.8: *Results of the HV mapping test. Mapping for EMEC AB and EMEC AT monitors could not be tested since LV in the testing period was off. Barrel C4 and EMEC CT monitors were not tested as well, because these monitors are declared to be dead.*

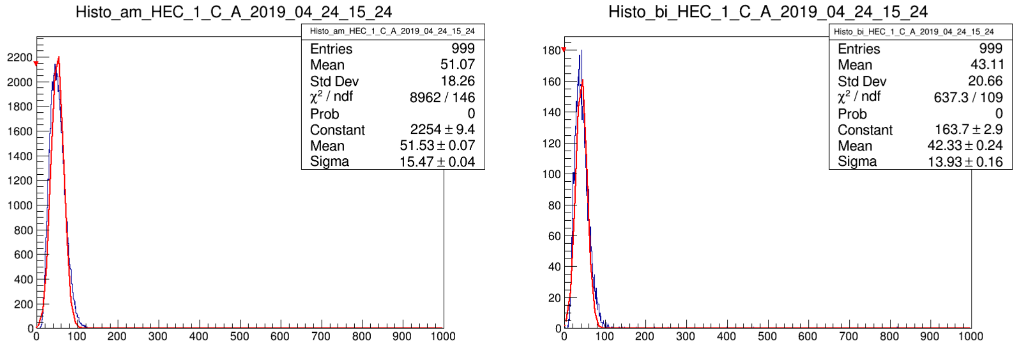

(a) Am spectrum.

(b) Bi spectrum.

Figure 12.9: *Am (left) and Bi (right) spectra for HEC 1CA LAr purity monitor marked in blue. The HV was switched off and trigger threshold is set to the zero line. The Gaussian fit curve is marked in red.*

be determined. Figure 12.9 shows the Gaussian fit curve marked in red[12]. They are summarized in Table 12.2 excluding the values for p_0 since the height of the curve is not relevant for the peak position.

Figure 12.10 shows the gained parameters nicely summarized in two plots. If the LAr purity monitor is dead or the corresponding LV modules were offline, then the parameters were set to

---

[12] The plots in Appendix F are shown without Gaussian fit curves.

Monitor	Am threshold	Bi threshold	PFEB
Barrel A1	7200	5100	PFEB1
Barrel A3	7200	5000	
Barrel A4	7200	5200	
Barrel A5	8000	4600	
Barrel C1	7200	4900	PFEB2
Barrel C2	7200	4900	
Barrel C3	7200	4900	
Barrel C4	6900	4900	
Barrel C5	6900	4900	
HEC 1AA	7000	5400	PFEB3
HEC 1AB	7000	5400	
HEC 1AC	7000	5400	
HEC 2AA	7000	5400	
HEC 2AB	7000	5400	
HEC 2AC	7000	5400	
EMEC AT	7000	5400	PFEB4
EMEC AB	6900	5400	
HEC 2CA	6900	5400	
HEC 2CB	7100	5300	
HEC 2CC	6900	5400	
HEC 1CA	7200	5000	PFEB5
HEC 1CB	7200	5000	
HEC 1CC	7200	5000	
EMEC CT	6900	5500	
EMEC CB	7200	5400	

Table 12.1: *Trigger threshold values for every LAr purity monitor. The entire line for Barrel A2 monitor is not included in the configuration file.*

zero in these plots.

Comparing the p_1 and p_2 parameters between Am and Bi spectra, the parameters for Am spectrum are a bit higher then the ones for Bi spectrum. The possible explanation can be found in the hardware setup of the corresponding ionization chambers since the noise rises linearly with the capacity of the ionization chamber [250]. The capacity of the ionization chamber can be estimated as the capacity C of the plate condensator:

$$C \sim \frac{A}{d}, \tag{12.2}$$

where A is the surface of the plate and d is the distance between the plates. Since the surface of the anode and cathode are the same in both Am and Bi ionization chambers, $C \sim d^{-1}$. The distance between anode and cathode in the Am ionization chamber is smaller than the one in the Bi ionization chamber, which leads to the larger capacity in the Am ionization chamber.

Since there is no possibility to take the corresponding spectra for a time period before 2019, there is no way to say if the measured spectra changed over time or stayed stable. This would be interesting in order to estimate the possible growth of the noise with time for the future LHC runs.

BM	Am spectrum		Bi spectrum	
	p_1	p_2	p_1	p_2
Barrel A1	53.72±0.07	16.79±0.04	44.08±0.24	14.86±0.17
Barrel A3	50.76±0.07	15.31±0.04	42.23±0.22	14.07±0.14
Barrel A4	54.11±0.07	16.23±0.04	44.41±0.24	15.40±0.20
Barrel A5	54.20±0.10	17.21±0.04	43.66±0.25	14.61±0.17
Barrel C1	52.18±0.07	15.22±0.04	42.87±0.28	14.44±0.19
Barrel C2	52.54±0.07	15.32±0.04	42.49±0.22	14.02±0.15
Barrel C3	52.81±0.07	16.34±0.04	43.69±0.24	14.62±0.16
HEC 2CA	47.07±0.07	13.83±0.03	38.31±0.23	13.31±0.16
HEC 2CB	40.96±0.11	13.17±0.07	36.13±0.39	12.79±0.28
HEC 2CC	44.67±0.06	13.99±0.04	36.61±0.20	11.98±0.12
HEC 1CA	51.53±0.07	15.47±0.04	42.33±0.24	13.93±0.16
HEC 1CB	54.89±0.07	16.79±0.04	44.47±0.26	14.42±0.17
HEC 1CC	51.89±0.07	15.94±0.04	43.08±0.25	13.67±0.16
EMEC CB	53.49±0.07	15.84±0.04	43.61±0.23	16.55±0.20
EMEC CT	4.02±0.01	1.40±0.00	3.87±0.01	1.35±0.01

Table 12.2: *Gaussian fit parameters p_1 and p_2. The parameter p_0 from the fit is not listed here.*

12.5 Documentation

An important aspect of the maintenance is the documentation. The previous LAr purity expert already started to writing it, but never released it[13]. His work was extended with few points and stored on Reference [244], which can be accessed by everyone from the ATLAS community.

This documentation contains the information about the following topics:

- Starter guide and library of the technical commands for new LAr purity expert in Mainz[14];
- General setup;
- Hardware and CAN communication;
- OPC UA server;
- WinCC OA.

Especially the last point was largely developed with time by some practical information like how to switch HV off or on for the test reasons, or how to change the mapping for the temperature probe if it is needed due to inavailability of some of them. This documentation could be edited by everyone from the ATLAS community as well and should be kept up to date by the next LAr purity expert.

This thesis can be used as an extension of this documentation.

---

[13] His notes are available only internally in Mainz as Reference [243].

[14] This information is stored in a file which can be found on the documentation page.

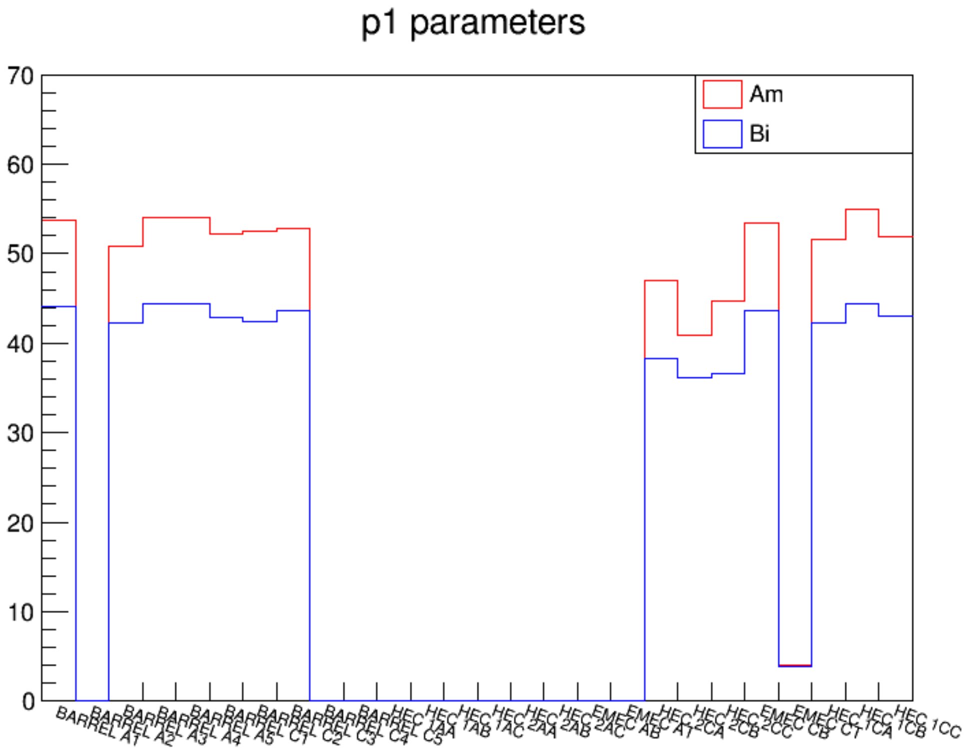

(a) p_1 parameters.

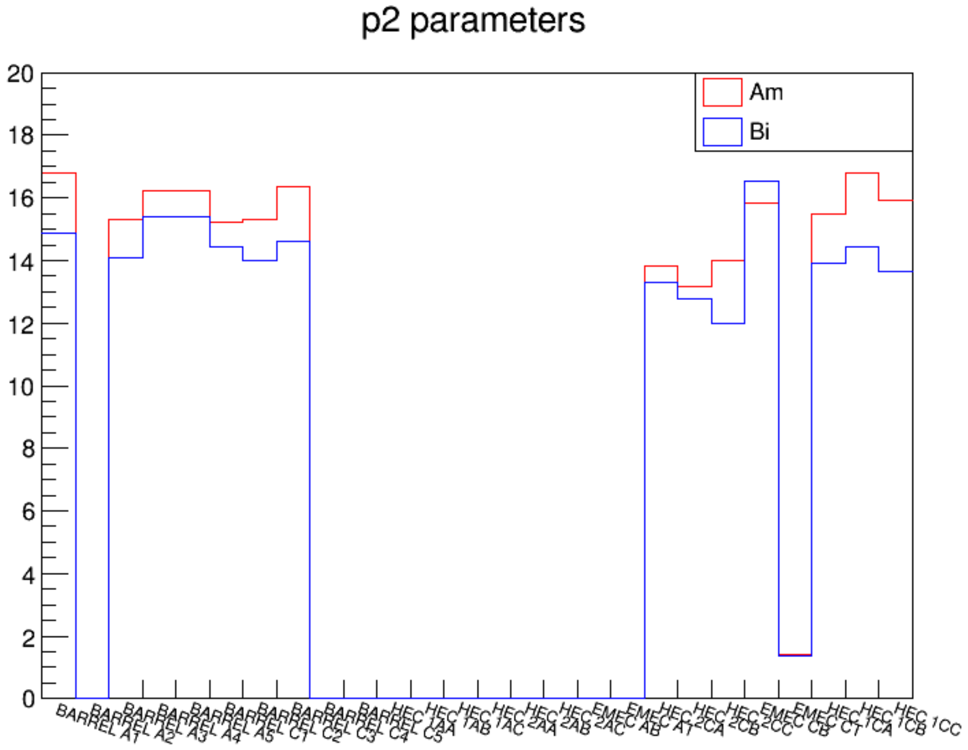

(b) p_2 parameters.

Figure 12.10: *Summary of p_1 and p_2 Gaussian parameters gained for all LAr purity monitors. The parameters are set to zero if the monitor is dead or the corresponding LV modules are offline.*

CHAPTER

13

UPGRADE DEVELOPMENT

> “*We need more troops.*”
> STORMTROOPER FROM STAR WARS: EPISODE VII - THE FORCE AWAKENS

ATLAS will be upgraded during the so-called upgrade Phases. An overview over the different planned projects for Phase-I and Phase-II is given in Section 13.1. This means for LAr purity monitoring system, that it should be kept on track with these upgrades. But first it should be checked if it can survive the expected challenges during the next collisions or not. Many related questions and answers to them are discussed in Section 13.2. Section 13.3 briefly mentions the problem for the current LAr purity system which has to be adressed in the future due to changed voltage supplies in the ATLAS detector. The discussion about the possibilites to handle this situation is written in Section 13.4.

13.1 Overview of the upgrade Phases

Run 2 of the LHC ended in 2018. Since then the Long Shutdown 2 (LS2) of the LHC is ongoing and so-called Phase-I of the upgrade activities started. The goal is to end with Phase-I just before the start of Run 3 of the LHC which is scheduled for 2021. However, already now the planning for Phase-II, scheduled for late 2022, is started since there are major plans for Run 4 of the LHC, including the HL-HLC project. In the following Sections an overview of planned ATLAS upgrades in both Phases is given based on Reference [251].

13.1.1 Phase-I

The main goal of detector improvements for Phase-I is the integration of $\sim$300 fb^{-1} by 2023. For this the possibility to reach peak instantaneous luminosities of up to $2.2 \times 10^{34}\,\text{cm}^{-2}\,\text{s}^{-1}$ will be exploited. The focus of the improvements lies on the enhancement of the trigger capabilities in order to maintain good physics selectivity by much higher data and background rates. Design of the most of these upgrades includes the satisfaction of Phase-II requirements, while the upgrades themselves will continue operating in ATLAS throughout the High-Luminosity phase of the LHC.

The following four major ATLAS Phase-I Upgrade projects were approved by the CERN Research Board in March 2014: ATLAS New Small Wheel, ATLAS Fast Tracker, ATLAS Liquid Argon Calorimeter Phase-I Upgrade, Phase-I Upgrade of the ATLAS TDAQ System. Furthermore, the approval of the AFP (ATLAS Forward Proton) project was followed in June 2015. Detailed technical descriptions of these projects were presented in the Technical Design Reports [252–256], which include among other information also cost estimates, construction schedules and information on project organisation.

While most of these projects are now largely progressing according to plan, there is a significant delay with the New Small Wheel and the Fast Tracker.

The ATLAS Fast Tracker (FTK) is designed to provide fast tracking information, which will serve as input to the high-level trigger. For this purpose data from the Pixel and SCT Detectors as well as from the new Insertable B-Layer Pixel Detector will be used by FTK. Furthermore, track reconstruction will be moved by FTK into a hardware system with huge parallel processing, which produces global track reconstruction with good resolution to be used by further trigger.

The New Small Wheel (NSW) is designed to replace the so-called Small Wheels, which are the current innermost stations of the endcap Muon Spectrometer, with a new detector assembly with improved performance. The NSW uses two detector technologies, which provide tracking and triggering capabilities: Micro-Mesh Gaseous Structures (Micromegas, MM) and small-strip Thin Gap Chambers (sTGC).

The goal of the LAr Phase-I upgrade is the improvement of the Level-1 calorimeter decision for Run 3 and beyond via enhancement of jet rejection and pile-up subtraction capabilities. In order to achieve this, the trigger will use for its decision more information about the calorimeter energy depositions in both the transverse and longitudinal directions. For this purpose 10 „supercells“ will be defined for each of the previous trigger towers. This new information is digitized on the detector and transmitted by optical fibers off the detector to back-end electronics. Then it is processed further, calibrated and transferred to the new Phase-I Level-1 calorimeter trigger system.

The main focus of the Phase-I TDAQ upgrades is on the Level-1 calorimeter trigger in order to fully benefit of the finer segmentation, which will be available after the Phase-I LAr upgrade. More sophisticated algorithms are implemented in new Feature Extractor processors (FEX) for electron/photon reconstruction, jet reconstruction and for global variables. Furthermore, the new data acquisition infrastructure will be used by all Phase-I detectors. It will be evolved in order to handle the Phase-II DAQ functions.

The AFP project promises to allow tag and measure the momentum and emission angle of very forward protons, and therefore significantly extend the physics goal of ATLAS. This makes it possible to observe and measure a number of processes that are otherwise difficult or impossible to study, where one or both photons remain intact.

13.1.2 Phase-II

The main goal of detector improvements in preparation for the HL-LHC era is the integration of a total of $3000\,\mathrm{fb}^{-1}$, exploiting a nominal levelled luminosity of approximately $5 \times 10^{34}\,\mathrm{cm}^{-2}\,\mathrm{s}^{-1}$, and an ultimate levelled luminosity of $7.5 \times 10^{34}\,\mathrm{cm}^{-2}\,\mathrm{s}^{-1}$, which results $250\,\mathrm{fb}^{-1}$ to $300\,\mathrm{fb}^{-1}$ integrated luminosity per year with high radiation and event pile-up levels as a consequence. In the HL-LHC environment the high particle densities and substantial integrated radiation are expected. In order to achieve the required sensitivity for physics measurements many highly innovative technology developments are required. In order to be able to work with the higher trigger and readout rates required at the HL-LHC much of the electronics on the detector systems will need major upgrades. Furthermore, the current inner tracker has to be replaced.

A total of six Phase-II TDRs [257–262] were submitted to the LHCC and UCG starting in December 2016. These TDRs were reviewed by the UCG in 2017 and 2018. These reviews include the review of cost, schedule, resources and risks. Finally, after all six TDRs were approved by the LHCC, UCG, and the CERN Research Board the process was completed in April 2018. Next step for these projects is the Phase-II technical and schedule review process of ATLAS, which is currently underway. The technical reviews proceed the chain from Specifications to Preliminary Design, followed by Final Design, and finally Production Readiness.

The first post-TDR project is the ITk Strip project. Initially designed five barrel layers of the strip system were reduced to four, the amount of discs in the forward region has been decreased from seven to six and lastly the so-called stub layer has been removed. After all, since entering the post-TDR phase in June 2017, the community of this project has made excellent progress in all areas.

The second post-TDR project is the Phase-II upgrade of the Muon Spectrometer. The replacement of a large fraction of the front-end and on- and off-detector readout and trigger electronics for the Resistive Plate Chambers, Thin Gap Chambers, and Monitored Drift Tube chambers is planned in order to ensure the compatibility with the higher trigger rates and longer latencies, which are necessary for the new level-0 trigger.

The third post-TDR project is the Phase-II LAr upgrade, which is entirely an upgrade of the electronics. The final goal for the calorimeters is to completely replace the front-end electronics. The Front-End Board (FEB2) is the critical on-detector component, which includes a new preamp/shaper ASIC, followed by a 14-bit 40 MHz ADC, for each readout channel of the LAr calorimeter. A second-generation prototype for the preamp/shaper is now being developed as a joint effort.

The fourth post-TDR project is the Phase-II Tile Calorimeter upgrade. This is an extremely large upgrade since the mechanics, electronics, power supplies, and about 10% of the PMTs will be upgraded or replaced.

The fifth post-TDR project is the Phase-II ITk Pixel Tracker. This is the most technologically ambitious project, which includes multiple new technologies. For example, the detailed layout of the Pixel tracker has been simplified and finalized in recent months. It is now almost entirely based on a single quad-ASIC module design.

The last post-TDR project is the Phase-II TDAQ upgrade. This project controls a wide range of interfaces, which have to be agreed on by all the detector projects in order to have a functional data acquisition, trigger, and control/configuration system. In order to achieve this the community has developed a detailed Detector - TDAQ Interface document, which has been reviewed across all the Phase-II projects, and is now approved. The community works on the further progress in order to finalize all of their user requirements and specification documents, so that they can move into the detailed design phase.

13.2 Survival questions and answers

Specifically for LAr purity monitoring system there are the following major points to be considered:

- Will the LAr purity monitoring electronics be able to survive the huge increase of coming integrated luminosity and radiation?
- Is the LAr purity monitoring system affected by the planned replacement of the front-end electronics in the calorimeters?

The general problem of the current LAr purity monitoring system is that it was designed to handle with the designed LHC integrated luminosity which will be reached in Run 3. At the development time no one considered runs beyond Run 3, so it is not guaranteed, that the LAr purity monitors will be further fully operational at Run 4 and beyond. The next problem is that the LAr purity monitors are installed inside of the cryostates and therefore are stuck there by definition since no opening of the cryostates is planned for the next years due to the costs which might arise from this operation. It means, that these monitors can not be exchanged.

Given all this information, the first question to be answered is: Will the LAr purity monitors survive Run 4? Of course a definite answer can not be given, however, it is still possible to make at least a qualitatively guess. The points to consider are:

- Half-life time of the Am and Bi source;
- Age of the electronics;
- Radiation to the electronics.

The half-life of Am source is 432 years, so there is no worry about it. The half-life time of Bi source is much less, only 33 years. However, this should not be an issue. The age of the electronics might be an issue.

More interesting is the question about the radiation increase since some electronics are sensitive to the radiation (Radeka amplifier, which is designed for 300 fb^{-1}). In order to check the impact of the radiation on the electronics, simulations from References [263, 264] were used. Table 13.1 summarizes the results for the neutron fluence and Table 13.2 shows values for the total ionising dose. All these values were obtained from simulations for 1 fb^{-1} and then extrapolated to values comparable to data collected in Run 2 and in Run 4 of LHC .

Region	$1\,\mathrm{fb}^{-1}$	$300\,\mathrm{fb}^{-1}$	$4000\,\mathrm{fb}^{-1}$
Barrel, EMEC	$10^{11}\,\mathrm{cm}^{-2}$	$3 \times 10^{13}\,\mathrm{cm}^{-2}$	$4 \times 10^{14}\,\mathrm{cm}^{-2}$
HEC 1	$2 \times 10^{10}\,\mathrm{cm}^{-2}$	$6 \times 10^{12}\,\mathrm{cm}^{-2}$	$8 \times 10^{13}\,\mathrm{cm}^{-2}$
HEC 2	$2 \times 10^{9}\,\mathrm{cm}^{-2}$	$6 \times 10^{11}\,\mathrm{cm}^{-2}$	$8 \times 10^{12}\,\mathrm{cm}^{-2}$
FCAL	$2 \times 10^{13}\,\mathrm{cm}^{-2}$	$6 \times 10^{15}\,\mathrm{cm}^{-2}$	$8 \times 10^{16}\,\mathrm{cm}^{-2}$

Table 13.1: *Neutron fluence obtained from the simulations for 1 fb^{-1} of integrated luminosity and extrapolated to other practicable luminosity values.*

Region	$1\,\mathrm{fb}^{-1}$	$300\,\mathrm{fb}^{-1}$	$4000\,\mathrm{fb}^{-1}$
Barrel, EMEC	$1\,\mathrm{Gy}$	$3 \times 10^{2}\,\mathrm{Gy}$	$4 \times 10^{3}\,\mathrm{Gy}$
HEC 1	$10^{-1}\,\mathrm{Gy}$	$3 \times 10^{1}\,\mathrm{Gy}$	$4 \times 10^{2}\,\mathrm{Gy}$
HEC 2	$3 \times 10^{-2}\,\mathrm{Gy}$	$9\,\mathrm{Gy}$	$1.2 \times 10^{2}\,\mathrm{Gy}$
FCAL	$10^{2}\,\mathrm{Gy}$	$3 \times 10^{4}\,\mathrm{Gy}$	$4 \times 10^{5}\,\mathrm{Gy}$

Table 13.2: *Total ionising dose obtained from the simulations for 1 fb^{-1} of integrated luminosity and extrapolated to other practicable luminosity values.*

It can be seen that the highest radiation is expected to be in barrel and EMEC region (the FCAL region can be ignored, since no functional LAr purity monitor is sitting there). A cross-check with Reference [265] gives the values for barrel front-end crate to be expected for Run 4:

- 1.8 kGy on the total ionising dose.
- $3.6 \times 10^{13}\,\mathrm{cm}^{-2}$ on the neutron fluence.

The electronic components which are sensitive to the ionising dose and the neutron fluence are the active components (see also Section 11.2): ST voltage regulators, OpAmps[1] and protection diodes.

- ST voltage are good up to $\sim 5 \times 10^{13}\,\mathrm{cm}^{-2}$ and $\sim 13\,\mathrm{kGy}$ [266].
- OpAmps were tested up to $\sim 3.2 \times 10^{13}\,\mathrm{cm}^{-2}$ and $\sim 8.7\,\mathrm{kGy}$ [266].

---

[1] Operational Amplifier which amplify the signal coming from BMs over FEBs to PFEBs.

- Protection diodes were tested up to $\sim 2.66 \times 10^{13}\,\mathrm{cm}^{-2}$ and $\sim 16.8\,\mathrm{kGy}$ [267].

Judging from these numbers, the purity boards might still survive the increasing total ionization dose in Run 4 since the expectation on the radiation is much lower then it was during the performed tests. However, the increasing radiation can lead to increasing noise produced via several electronic components in the hardware chain of the LAr purity monitoring system (like Radeka amplifier). The expected neutron fluence is partially larger than it was during the performed tests, but since the order of magnitude remains the same, it might not be a big deal.

13.3 Problem with negative voltage

It is clear now, that LAr purity monitoring system might survive the coming increase of the integrated luminosity, but will it stay compatible to the rest of the ATLAS electronics? Unfortunately not.

As shown in Figure 11.13, all FEBs have currently the low voltage input of $-7\,\mathrm{V}$ and $+11\,\mathrm{V}$ coming from the Front-End Crate power bus, which is used not only by some electronic components (line drivers) on the FEB itself but also transferred to the BMs where it is used by the Radeka preamplifier. In this connection the negative low voltage is mandatory because it is needed for the „negative“ signal output coming from the Bi ionization chamber. By knowing that the signal is „negative“ the system can judge that it can be associated with the signal from Bi ionization chamber.

However, as stated in Section 13.1 the goal for the calorimeters is to completely replace the front-end electronics. In particular, it includes the increase of the positive low voltage and the removal of the negative low voltage source at least in the barrel area. More precisely, there is still no consensus if $+24\,\mathrm{V}$ or $+48\,\mathrm{V}$ will be provided by the Front-End Crate LVPS, but it is known already, that there will be no negative low voltage [266]. However, provision of the negative voltage is essential for the current LAr purity monitoring system, so this system needs to be upgraded. First thoughts about this upgrade are given in the next Section.

13.4 First upgrade thoughts

It is definitely a problem, that the negative voltage source will be gone in the future. For the current LAr purity monitoring system negative low voltage has to be provided for the OpAmps on FEB ($-5\,\mathrm{V}$) and further for the Radeka amplifier placed in the BMs ($-5\,\mathrm{V}$ as well). Figure 13.1 shows the current low voltage flow through one FEB to the three BMs[2]. The electronic components not related to the voltage are not shown. Every „regulators“ box summarizes two regulators (one is for positive voltage, another one for the negative). Furthermore there are three empty spaces which were initially designed for usage of another three OpAmps, but were not used at the end.

It is obvious that the negative voltage should be provided to FEB, but where to get it from? As already mentioned in Section 13.3 it is still unknown, which voltage will be provided by the Front-End Crate LVPS instead of $-7\,\mathrm{V}$ & $+11\,\mathrm{V}$. It will be either $+24\,\mathrm{V}$ or $+48\,\mathrm{V}$. There are the following possibilities for further development considering this new input:

- Get negative voltage from other subsystems, if they could provide it (very unlikely).
- Modify the existing FEBs.

---

[2] There are also few FEBs operational which provide low voltage to only two BMs.

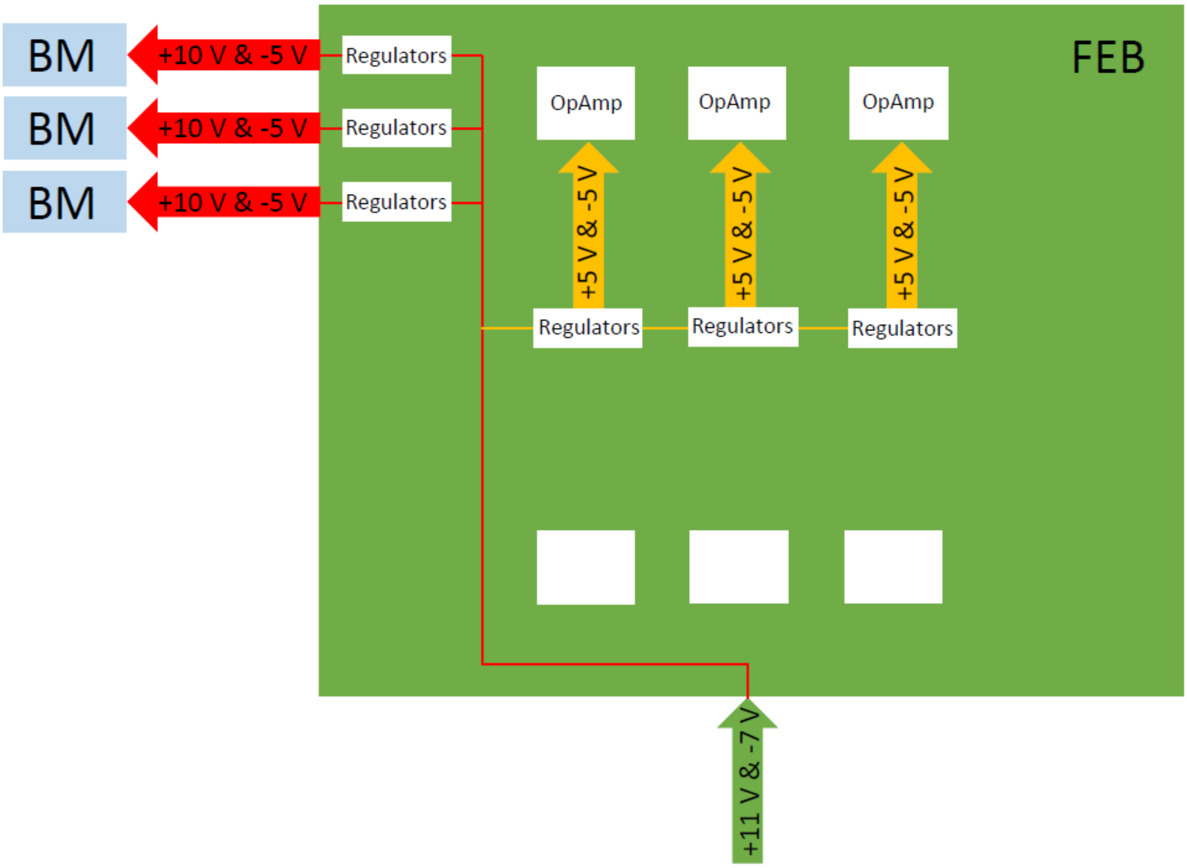

Figure 13.1: *Schematic overview of the low voltage flow on FEB. The electronic components not related to the voltage are not shown.*

  - Change existing OpAmps (not preferred option due to lack of manpower). However, it would not solve the problem with the voltage for the Radeka preamplifier sitting on BMs, but it might be at least a partial solution.
  - Add additional components to the free space of FEB in order to provide the needed voltage.
    - Usage of the negative voltage transferred via twisted pair cables (with the calibration signal) from the PFEBs. However, this option was declined due to its non-triviality for the implementation and for the tests.
    - Usage of the 48 V/12 V DC/DC converter from Milano Design [268] (in order to reduce the incoming voltage to +12 V) with usage of an additional voltage inverter[3] (in order to invert it to the needed negative voltage values). See Figure 13.2 for the visualization of this proposal[4].

- Change the FEBs completely (not preferred option since it would require a lot of planning and testing work by people which are simply not available).

The most likely option will be to use the DC/DC converter, which is still under development by ATLAS Milano group. This converter could be placed on the free place of the FEB and will be able to provide +12 V for the usage by LAr purity FEBs. This value could be converted to

---

[3] However the inverter would be installed with a diode leading to reduced amount of incoming voltage to its half which is even better for the LAr purity system needs.

[4] The inverter is meant to be installed with a diode which is not shown on Figure. The inverter together with the diode are summarized as inverter from now on.

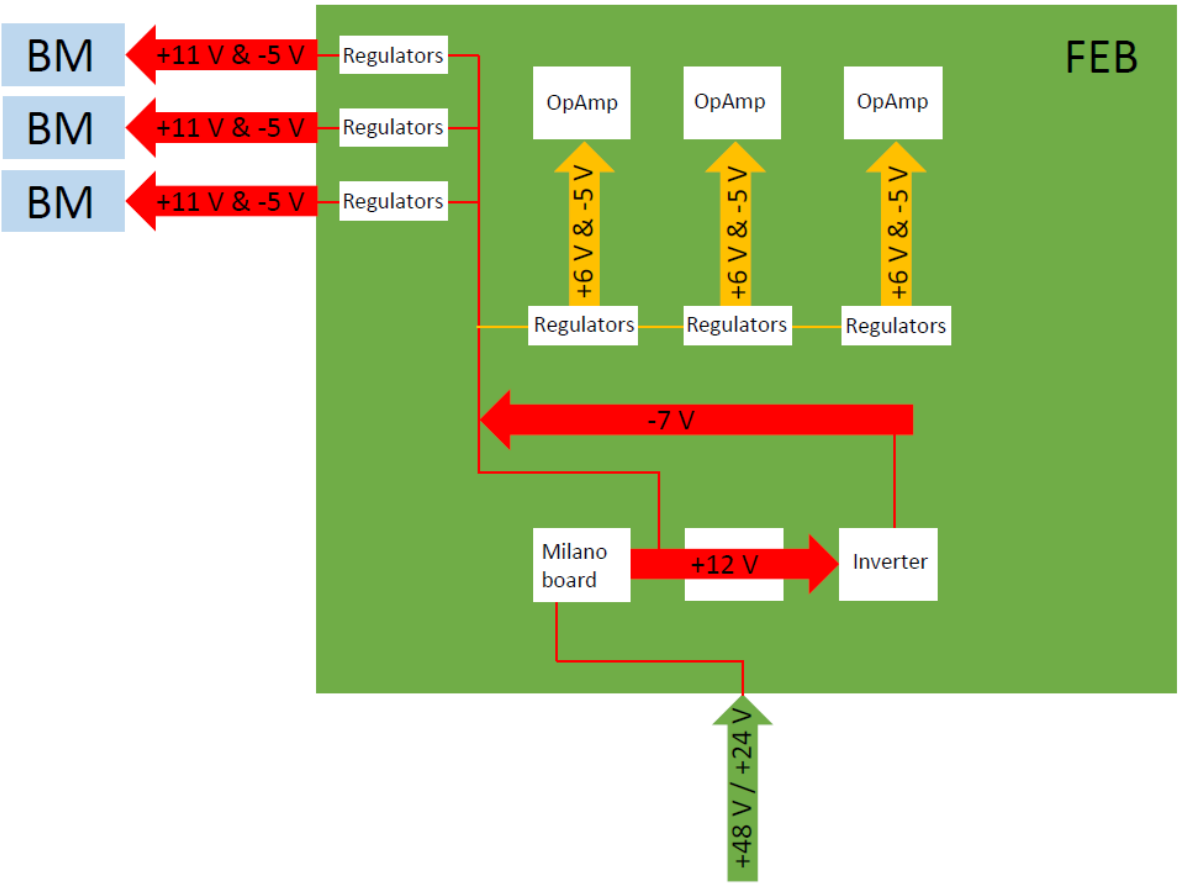

Figure 13.2: *Schematic overview of the low voltage flow on FEB using converter from ATLAS Milano group and voltage inverter. The electronic components not related to the voltage are not shown.*

$-7\,\mathrm{V}$, which is still fine (Radeka amplifier can handle this voltage as well) by using of voltage inverter which could be placed for example on another free place of the FEB. However, usage of voltage inverters means to produce additional noise which needs to be studied in the future. The positive voltage used by Radeka amplifiers in BMs and OpAmps on FEBs would increase by $\sim 1\,\mathrm{V}$ since the output from Milano converter would be a bit larger then the current input to the FEBs, but it is still sustainable.

Chapter

14

Conclusion and outlook

> “*Difficult to see. Always in motion the future is.*”
> Yoda from Star Wars: Episode V - The Empire Strikes Back

The goals of the work with LAr purity monitoring system in this thesis were the understanding and maintenance of the current system, as well as first discussions about the future of the system and possibilities for the related upgrade.

In order to be able to see the Am and Bi spectra instantly and directly from the production machine the LAr purity „expert panel“ was designed, implemented, installed and deployed to the production machine to be ready to use. During the general maintenance the current HV mapping was questioned and therefore a test with almost all LAr purity monitors was performed. The results showed that indeed there is something odd in the current mapping, however it is not clear since when the fault exists and most important where exactly. The final solution to this problem is therefore not decided yet, but the possible sources for the problem are listed. From the LAr purity expert point of view the easiest solution would be to change the mapping scripts according to the observed results. However, it might be still the case that this changed mapping would be not the true one, but in the combination with the still-to-be-discovered bug source the misconnections will cancel out and the problem would be solved. For the education purposes and as a reference for the future the noise spectra were recorded and summarized in this thesis. In order to make the life for the next LAr purity expert easier and to collect all the gained information, an official documentation place was created, where everyone from the ATLAS community can access the documentation and even edit it.

As the ATLAS detector is being upgraded to meet all the challenges facing the LHC in the coming years, the LAr purity monitoring system should also be upgraded. In particular because otherwise the system will not be operational since the negative voltage will be gone, which is very important for the LAr purity monitoring system. As an aggressive solution, the full replacement of the system is not possible since many parts of it (the actual monitors) are inside of the cryostates which will remain closed. However, these parts should be still functional according to the thoughts based on the previous tests and simulated data. The replacement of the accessable parts is not an option. One of the most likely solutions will be the usage of the new DC/DC converter developed by ATLAS Milano group with additional electronic parts, but there is still room for further discussions. The integrity of this converter to the current LAr purity monitoring system should be checked once the final design of the converter will be available, and study of the noise after integrity should be performed. If everything will be running smoothly, only the age of the current electronics could pose a problem.

SUMMARY

> “*I’ve been waiting for this day for a long time.*”
> KYLO REN FROM STAR WARS: EPISODE VII - THE FORCE AWAKENS

The Large Hadron Collider (LHC) at CERN delivered data from proton-proton collisions up to the 13 TeV center of mass energy so far. In the future the energy is even planned to grow. The collected data allows for making more precise measurements of the known physics and the search of new physics. It is essential to make sure that this data was collected under the best conditions of the ATLAS detector. In this thesis two different topics are covered. On the one hand the search for pair-produced first and second generation scalar leptoquarks in *pp* collisions at 13 TeV with ATLAS detector is described. On the other hand the work with the liquid argon purity monitoring system of the ATLAS detector is summarized.

The search for pair-produced first and second generation scalar leptoquarks in *pp* collisions at 13 TeV has been carried out using data with an integrated luminosity of 36.1 fb^{-1}. It is motivated among other things by the models adressing some of the recent *b*-flavours anomalies. The search used events with at least two jets and two only charged same-flavour leptons (electrons or muons). The events with neutrinos in the final state were not considered in this thesis, even though many relevant aspects for example region definitions are taken from the search where these events were considered. However that search used different analysis strategy at the end. The expected amount of background from Standard Model processes has been estimated using Monte Carlo simulations and methods based on data. It has been compared to data and the results were interpreted using the profile likelihood method. The background estimation based fully on Monte Carlo simulations would be a difficult task since the fake background determination would require better Monte Carlo simulation production with more events for better statistics. For the statistical interpretation the framework HISTFITTER was used, which is only one of many frameworks which might be used, even if it is probably the most common one for the ATLAS community. No significant excess above the SM background expectation is observed in any channel and exclusion limits have been evaluated. Within the minimal BRW model and assuming a branching ratio for the decay into a charged lepton and a quark of 50%, leptoquarks with masses up to 1.20 TeV are excluded at 95% CL in both searched channels. Compared to the previous ATLAS results using 3.2 fb^{-1} of data the limits in all channels could be setted in this search up to $\sim$ 400 GeV higher as before. However, the general search for leptoquarks is not over since there are several efforts ongoing not only limited to ATLAS experiment and including even more channels.

The work with the liquid argon purity monitoring system turned out to be a difficult, but interesting task. The system consists of 30 monitors installed in the ATLAS detector, the software chain outside of the detector and several hardware components in between. In the most monitors the Am and Bi ionization chambers are available. In order to be able to see the Am and Bi spectra instantly and directly from the production machine the expert panel was designed from scratch and implemented to be ready to use. The possibilities of this panel are small (visualize the spectrum), but it is enough for the motivated purpose. However, the panel could be improved by implementing new features like the possibility to restart the OPC UA server. This feature would be useful and difficult to implement at the same time. Following by some indications seen on the spectra, the investigation on the high voltage mapping was performed with unexpected results leading to mismatching on the mapping. The possible sources for this problem are listed which has to be followed up in the future in order to develop a better solution. Furthermore, the noise spectra were taken for all monitors except the ones where the measurement was not possible due to other maintenance works on the ATLAS experiment which require the partially shutdown of low voltage relevant for Radeka amplifier on basic monitors. It would be at least interesting to record the missing noise spectra. In the course of the ATLAS detector upgrade to be ready for the future Runs of LHC every subsystem has to be prepared for it. The LAr purity monitoring system is no exception since it is already known that there will be no negative low voltage provided centrally to the FEBs which is important for the mentioned Radeka amplifier on basic monitors. The first thoughts about the possible upgrade steps are summarized in this thesis after making sure that the system can stay fully operational at least theoretically based on the simulations and thoughts.

Appendix

A DETAILED INFORMATION ABOUT MC SAMPLES

The following Appendix provides tables with information about the Monte Carlo samples used in the pair-produced LQ search. The Monte Carlo samples are described in detail in section 7.2.2. This Appendix consists of two Chapters. Chapter A.1 lists the DSID, cross section, filter efficiency, k-factor and higher order cross section of the MC samples. Chapter A.2 lists amount of the generated events for these MC samples.

A.1 General information

Tables A.1, A.2, A.3, A.4 and A.5 list information about the background samples. Cross section and filter efficiency for each sample was defined using AMI interface. Other information comes from Reference [269]. The information about the signal samples is collected in Table A.6 for the first and in Table A.7 for the second generation samples.

Name	DSID	σ [pb]	Filt. Eff.	k-fac.	H.o. σ [pb]
ttbar_hdamp258p75_nonallhad	410501	730.17	0.544	1.139	452.336
ttbar_hdamp258p75_dil	410503	76.93	1.0	1.139	87.626

Table A.1: *$t\bar{t}$ MC samples.*

Name	DSID	σ [pb]	Filt. Eff.	k-fac.	H.o. σ [pb]
singletop_tchan_lept_top	410011	43.739	1.0	1.010	44.152
singletop_tchan_lept_antitop	410012	25.778	1.0	1.020	26.276
Wt_inclusive_top	410013	34.009	1.0	1.054	35.845
Wt_inclusive_antitop	410014	33.989	1.0	1.054	35.824
Wt_dilepton_top	410015	3.583	1.0	1.054	3.777
Wt_dilepton_antitop	410016	3.581	1.0	1.054	3.775
SingleTopSchan_noAllHad_top	410025	2.051	1.0	1.005	2.061
SingleTopSchan_noAllHad_antitop	410026	1.262	1.0	1.022	1.289

Table A.2: *Single top MC samples.*

Name	DSID	σ [pb]	Filt. Eff.	k-fac.	H.o. σ [pb]
llll	361063	12.805	1.0	0.91	11.653
lllvSFMinus	361064	1.844	1.0	0.91	1.678
lllvOFMinus	361065	3.625	1.0	0.91	3.299
lllvSFPlus	361066	2.562	1.0	0.91	2.331
lllvOFPlus	361067	5.025	1.0	0.91	4.573
llvv	361068	13.998	1.0	0.91	12.738
lvvv	361088	3.396	1.0	0.91	3.091
WplvWmqq_SHv21_improved	361091	24.893	1.0	0.91	22.653
WpqqWmlv_SHv21_improved	361092	24.898	1.0	0.91	22.657
WlvZqq_SHv21_improved	361093	11.500	1.0	0.91	10.465
WqqZll_SHv21_improved	361094	3.426	1.0	0.91	3.117
ZqqZll_SHv21_improved	361096	16.433	0.144	0.91	2.149

Table A.3: *Diboson MC samples.*

Name	DSID	σ [pb]	Filt. Eff.	k-fac.	H.o. σ [pb]
Zmumu_MAXHTPTV0_70_CVetoBVeto	364100	1982.500	0.822	0.975	1588.496
Zmumu_MAXHTPTV0_70_CFilterBVeto	364101	1982.200	0.114	0.975	219.474
Zmumu_MAXHTPTV0_70_BFilter	364102	1981.500	0.066	0.975	126.937
Zmumu_MAXHTPTV70_140_CVetoBVeto	364103	109.140	0.690	0.975	73.423
Zmumu_MAXHTPTV70_140_CFilterBVeto	364104	108.980	0.197	0.975	20.897
Zmumu_MAXHTPTV70_140_BFilter	364105	101.540	0.111	0.975	10.990
Zmumu_MAXHTPTV140_280_CVetoBVeto	364106	39.870	0.599	0.975	23.304
Zmumu_MAXHTPTV140_280_CFilterBVeto	364107	39.857	0.235	0.975	9.144
Zmumu_MAXHTPTV140_280_BFilter	364108	36.187	0.158	0.975	5.583
Zmumu_MAXHTPTV280_500_CVetoBVeto	364109	8.526	0.560	0.975	4.657
Zmumu_MAXHTPTV280_500_CFilterBVeto	364110	8.526	0.266	0.975	2.215
Zmumu_MAXHTPTV280_500_BFilter	364111	8.522	0.177	0.975	1.469
Zmumu_MAXHTPTV500_1000	364112	1.787	1.0	0.975	1.743
Zmumu_MAXHTPTV1000_E_CMS	364113	0.148	1.0	0.975	0.144

Table A.4: *$Z \rightarrow \mu\mu$ MC samples.*

Name	DSID	σ [pb]	Filt. Eff.	k-fac.	H.o. σ [pb]
Zee_MAXHTPTV0_70_CVetoBVeto	364114	1981.600	0.821	0.975	1587.022
Zee_MAXHTPTV0_70_CFilterBVeto	364115	1981.500	0.114	0.975	219.996
Zee_MAXHTPTV0_70_BFilter	364116	1982.000	0.066	0.975	127.085
Zee_MAXHTPTV70_140_CVetoBVeto	364117	110.640	0.694	0.975	74.900
Zee_MAXHTPTV70_140_CFilterBVeto	364118	110.500	0.189	0.975	20.316
Zee_MAXHTPTV70_140_BFilter	364119	110.460	0.118	0.975	12.739
Zee_MAXHTPTV140_280_CVetoBVeto	364120	40.645	0.616	0.975	24.420
Zee_MAXHTPTV140_280_CFilterBVeto	364121	40.671	0.233	0.975	9.237
Zee_MAXHTPTV140_280_BFilter	364122	40.674	0.153	0.975	6.081
Zee_MAXHTPTV280_500_CVetoBVeto	364123	8.670	0.567	0.975	4.797
Zee_MAXHTPTV280_500_CFilterBVeto	364124	8.667	0.266	0.975	2.250
Zee_MAXHTPTV280_500_BFilter	364125	8.681	0.177	0.975	1.494
Zee_MAXHTPTV500_1000	364126	1.809	1.0	0.975	1.764
Zee_MAXHTPTV1000_E_CMS	364127	0.149	1.0	0.975	0.145

Table A.5: *$Z \to ee$ MC samples.*

Mass [GeV]	DSID	σ [pb]
200	306708	58.332
250	306709	19.868
300	306710	7.8616
350	306711	3.5079
400	306712	1.7089
450	306713	0.88169
500	306714	0.48193
550	306715	0.27535
600	306716	0.16308
650	306717	0.099096
700	306718	0.061969
750	306719	0.039377
800	306720	0.025775
850	306721	0.016902
900	306722	0.011419
950	306723	0.0077933
1000	306724	0.005352
1050	306725	0.0037047
1100	306726	0.0026187
1150	306727	0.0018387
1200	306728	0.0013122
1250	306729	0.00093708
1300	306730	0.00067823
1350	306731	0.00049102
1400	306732	0.00035895
1450	306733	0.00026501
1500	306734	0.00019405
1600	306735	0.00010676
1700	306736	5.9233e-05
1800	306737	3.3157e-05

Table A.6: *Signal MC samples for first generation.*

Mass [GeV]	DSID	σ [pb]
200	306742	58.321
250	306743	19.869
300	306744	7.8754
350	306745	3.5078
400	306746	1.7087
450	306747	0.88173
500	306748	0.48123
550	306749	0.27533
600	306750	0.163
650	306751	0.099098
700	306752	0.061852
750	306753	0.039378
800	306754	0.025775
850	306755	0.016902
900	306756	0.011413
950	306757	0.0077933
1000	306758	0.0053518
1050	306759	0.0037112
1100	306760	0.0026188
1150	306761	0.0018387
1200	306762	0.0013137
1250	306763	0.00093751
1300	306764	0.00067825
1350	306765	0.00049102
1400	306766	0.00035888
1450	306767	0.00026404
1500	306768	0.00019359
1600	306769	0.00010677
1700	306770	5.9234e-05
1800	306771	3.3154e-05

Table A.7: *Signal MC samples for second generation.*

A.2 Amount of generated events

Tables A.8, A.9, A.10, A.11 and A.12 list information about the background samples. The amount of generated events for each sample was defined using AMI interface. Additionaly, DAOD format is given since the amount of generated events depends on the DAOD format of the MC sample. The information about the signal samples is collected in Tables A.13 and A.14 for the first and in Tables A.15 and A.16 for the second generation samples.

Name	DSID	EXOT	# events
ttbar_hdamp258p75_nonallhad	410501	9	17808357
ttbar_hdamp258p75_dil	410503	12	6438699

Table A.8: *$t\bar{t}$ MC samples with their DSIDs and amount of generated events.*

Name	DSID	EXOT	# events
singletop_tchan_lept_top	410011	9	856648
singletop_tchan_lept_antitop	410012	9	894770
Wt_inclusive_top	410013	9	917188
Wt_inclusive_antitop	410014	9	915328
Wt_dilepton_top	410015	12	325251
Wt_dilepton_antitop	410016	12	324596
SingleTopSchan_noAllHad_top	410025	9	165285
SingleTopSchan_noAllHad_antitop	410026	9	170558

Table A.9: *Diboson MC samples with their DSIDs and amount of generated events.*

Name	DSID	EXOT	# events
llll	361063	9	200910
		12	434479
lllvSFMinus	361064	9	44589
		12	39408
lllvOFMinus	361065	9	83121
		12	65836
lllvSFPlus	361066	9	59494
		12	52573
lllvOFPlus	361067	9	113880
		12	90782
llvv	361068	9	1764655
		12	1344084
lvvv	361088	9	366115
WplvWmqq_SHv21_improved	361091	9	661000
WpqqWmlv_SHv21_improved	361092	9	707628
WlvZqq_SHv21_improved	361093	9	732061
WqqZll_SHv21_improved	361094	9	1586642
		12	1363690
ZqqZll_SHv21_improved	361096	9	1601925
		12	1417141

Table A.10: *All MC samples with their DSIDs and amount of generated events.*

Name	DSID	EXOT	# events
Zmumu_MAXHTPTV0_70_CVetoBVeto	364100	9	1252876
		12	3148325
Zmumu_MAXHTPTV0_70_CFilterBVeto	364101	9	1055571
		12	2153913
Zmumu_MAXHTPTV0_70_BFilter	364102	9	1864377
		12	3829273
Zmumu_MAXHTPTV70_140_CVetoBVeto	364103	9	3385454
		12	2756643
Zmumu_MAXHTPTV70_140_CFilterBVeto	364104	9	1136951
		12	966538
Zmumu_MAXHTPTV70_140_BFilter	364105	9	3513361
		12	3087397
Zmumu_MAXHTPTV140_280_CVetoBVeto	364106	9	3466770
		12	2490933
Zmumu_MAXHTPTV140_280_CFilterBVeto	364107	9	2037446
		12	1527735
Zmumu_MAXHTPTV140_280_BFilter	364108	9	8634914
		12	6709648
Zmumu_MAXHTPTV280_500_CVetoBVeto	364109	9	1445943
		12	1083592
Zmumu_MAXHTPTV280_500_CFilterBVeto	364110	9	713129
		12	543335
Zmumu_MAXHTPTV280_500_BFilter	364111	9	1446208
		12	1138215
Zmumu_MAXHTPTV500_1000	364112	9	2271645
		12	1759032
Zmumu_MAXHTPTV1000_E_CMS	364113	9	813602
		12	651353

Table A.11: *$Z \to \mu\mu$ MC samples with their DSIDs and amount of generated events.*

Name	DSID	EXOT	# events
Zee_MAXHTPTV0_70_CVetoBVeto	364114	9	1160838
		12	2753388
Zee_MAXHTPTV0_70_CFilterBVeto	364115	9	996755
		12	1900690
Zee_MAXHTPTV0_70_BFilter	364116	9	1754903
		12	3379762
Zee_MAXHTPTV70_140_CVetoBVeto	364117	9	3262170
		12	2434208
Zee_MAXHTPTV70_140_CFilterBVeto	364118	9	1101463
		12	860855
Zee_MAXHTPTV70_140_BFilter	364119	9	3391884
		12	2737797
Zee_MAXHTPTV140_280_CVetoBVeto	364120	9	3372260
		12	2238880
Zee_MAXHTPTV140_280_CFilterBVeto	364121	9	1989313
		12	1377802
Zee_MAXHTPTV140_280_BFilter	364122	9	8429087
		12	6078768
Zee_MAXHTPTV280_500_CVetoBVeto	364123	9	1381858
		12	958414
Zee_MAXHTPTV280_500_CFilterBVeto	364124	9	695899
		12	491409
Zee_MAXHTPTV280_500_BFilter	364125	9	1415657
		12	1035091
Zee_MAXHTPTV500_1000	364126	9	2216639
		12	1583618
Zee_MAXHTPTV1000_E_CMS	364127	9	792603
		12	580683

Table A.12: *$Z \rightarrow ee$ MC samples with their DSIDs and amount of generated events.*

Mass [GeV]	DSID	EXOT	# events
200	306708	9	93461
		12	29512
250	306709	9	97916
		12	30533
300	306710	9	101795
		12	31602
350	306711	9	104525
		12	32689
400	306712	9	105692
		12	33134
450	306713	9	95310
		12	30140
500	306714	9	99620
		12	31831
550	306715	9	107822
		12	34533
600	306716	9	97589
		12	31410
650	306717	9	108766
		12	34942
700	306718	9	86967
		12	28209
750	306719	9	107806
		12	35264
800	306720	9	108019
		12	35095
850	306721	9	107111
		12	35050
900	306722	9	108178
		12	35704

Table A.13: *Signal MC samples for first generation with their DSIDs and amount of generated events, part I.*

Mass [GeV]	DSID	EXOT	# events
950	306723	9	109849
		12	36148
1000	306724	9	109041
		12	36122
1050	306725	9	110014
		12	36421
1100	306726	9	110069
		12	36712
1150	306727	9	110193
		12	36516
1200	306728	9	106678
		12	35626
1250	306729	9	105430
		12	35325
1300	306730	9	109662
		12	36940
1350	306731	9	110372
		12	37259
1400	306732	9	105394
		12	35615
1450	306733	9	80918
		12	27348
1500	306734	9	77265
		12	26174
1600	306735	9	110257
		12	37655
1700	306736	9	110769
		12	38026
1800	306737	9	109364
		12	37835

Table A.14: *Signal MC samples for first generation with their DSIDs and amount of generated events, part II.*

Mass [GeV]	DSID	EXOT	# events
200	306742	9	89199
		12	31224
250	306743	9	99119
		12	34329
300	306744	9	97525
		12	33891
350	306745	9	103952
		12	36339
400	306746	9	104316
		12	36703
450	306747	9	105731
		12	37670
500	306748	9	105125
		12	37876
550	306749	9	106821
		12	38713
600	306750	9	103059
		12	37852
650	306751	9	107390
		12	39410
700	306752	9	107606
		12	39790
750	306753	9	105015
		12	39066
800	306754	9	108122
		12	40362
850	306755	9	107905
		12	40724
900	306756	9	100731
		12	38089

Table A.15: *Signal MC samples for second generation with their DSIDs and amount of generated events, part I.*

Mass [GeV]	DSID	EXOT	# events
950	306757	9	108047
		12	41092
1000	306758	9	107426
		12	40713
1050	306759	9	100986
		12	38605
1100	306760	9	107961
		12	41792
1150	306761	9	108235
		12	41674
1200	306762	9	90284
		12	35103
1250	306763	9	107790
		12	42118
1300	306764	9	108182
		12	42294
1350	306765	9	108343
		12	42718
1400	306766	9	108504
		12	42472
1450	306767	9	104737
		12	41446
1500	306768	9	97450
		12	38675
1600	306769	9	107173
		12	42571
1700	306770	9	106242
		12	42606
1800	306771	9	103267
		12	41876

Table A.16: *Signal MC samples for second generation with their DSIDs and amount of generated events, part II.*

Appendix

B DETAILS ON THE PURITY CALCULATION

The following Appendix provides the needed formulae for the purity calculation as they implemented and therefore used by the current LAr purity monitoring system. These formulae were directly extracted from the scripts using in the production machine and extended with some words in order to understand the using quantities and where their values are coming from.

B.1 Drift velocity

Needs T_e (in °C) and E (in $\mathrm{kV\,cm^{-1}}$) as an input.

$$T = 273.15 + T_e - 90.371, \tag{B.1}$$

$$v = (-0.01481 \cdot T + 1) \cdot \left(0.141 \cdot E \cdot \log\left(1 + \frac{12.4}{E}\right) + 1.627 \cdot E^{0.317}\right) - 0.0075 \cdot T. \tag{B.2}$$

The values for the formula B.2 are taken from Reference [229][1].

B.2 Attachment constant

Needs T_e (in °C) and E (in $\mathrm{kV\,cm^{-1}}$) as an input.

$$T = T_e + 184, \tag{B.3}$$

$$k_s = 1.71 \cdot \left(0.172 + e^{0.498 - E \cdot 0.305} + e^{20 - E \cdot 10.21} + T \cdot \left(e^{-1.431 - E \cdot 0.643} + 0.03\right)\right). \tag{B.4}$$

Alternative formula from Reference [234]:

$$k_s = \frac{25.44 + 0.128 \cdot T_e}{E} + (2.73 + 0.014 \cdot T_e). \tag{B.5}$$

However the formula B.5 is valid for a LAr temperature between −181 °C and −185 °C and an electric field between $2.2\,\mathrm{kV\,cm^{-1}}$ and $6.2\,\mathrm{kV\,cm^{-1}}$. The highest measured electric field is $25\,\mathrm{kV\,cm^{-1}}$ for Bi ionization chamber. So, this alternative formula is not used by the system.

B.3 Charge for ^{207}Bi source

Needs HV_{neg} (in V), HV_{pos} (in V), T_e (in °C) and n_s (impurity) as an input.

---

[1] The current system has the value $E^{0.371}$, and not $E^{0.317}$, probably due to mistake. However the difference is negligible.

v_1 is drift velocity using T_e and $E_1 = \frac{HV_{\text{neg}}}{1000 \cdot d_1}$;
v_2 is drift velocity using T_e and $E_2 = \frac{HV_{\text{pos}}}{1000 \cdot d_2}$;
k_{s1} uses T_e and E_1; k_{s2} uses T_e and E_2;
$d_{11} = d_1 \cdot 10$ and $d_{21} = d_2 \cdot 10$.

$$Q_1 = Q_{\text{ini}}^{\text{Bi}} \cdot \frac{E_1}{E_0^{\text{Bi}}} \cdot \log\left(1 + \frac{E_0^{\text{Bi}}}{E_1}\right) \cdot \frac{v_1}{z_0 \cdot k_{s1} \cdot n_s} \cdot e^{-\frac{d_{11} \cdot k_s \cdot n_s}{v_1}} \cdot \left(e^{\frac{z_0 \cdot k_{s1} \cdot n_s}{v_1}} - 1\right), \tag{B.6}$$

$$Q_{\text{Bi}} = Q_1 \cdot \frac{v_2}{d_{21} \cdot k_{s2} \cdot n_s} \cdot \left(1 - e^{-\frac{d_{21} \cdot k_{s2} \cdot n_s}{v_2}}\right), \tag{B.7}$$

with $d_1 = 0.52\,\text{cm}$ (distance between cathode and grid), $d_2 = 0.1\,\text{cm}$ (distance between grid and anode), $E_0^{\text{Bi}} = 0.8\,\text{kV}\,\text{cm}^{-1}$, $Q_{\text{ini}}^{\text{Bi}} = 6.7\,\text{fC}$, $z_0 = 0.15\,\text{cm}$ (projection of the track on the drift direction in the electric field).

B.4 Charge for ^{241}Am source

Needs HV_{pos} (in V), T_e (in °C) and n_s (impurity) as an input.

v is drift velocity using T_e (in °C) and $E = \frac{HV_{\text{pos}}}{1000 \cdot d}$;
k_s uses T_e (in °C) and E;
$d_{sc} = d \cdot 10$.

$$E_0 = 416 \cdot \left(1 - 0.5 \cdot e^{-0.198 \cdot E}\right), \tag{B.8}$$

$$Q_{\text{Am}} = Q_{\text{ini}}^{\text{Am}} \cdot \frac{E}{E_0} \cdot \log\left(1 + \frac{E_0}{E}\right) \cdot \frac{v}{d_{sc} \cdot k_s \cdot n_s} \cdot \left(1 - e^{-\frac{d_{sc} \cdot k_s \cdot n_s}{v}}\right), \tag{B.9}$$

with $d = 0.2\,\text{cm}$ (distance between the electrods), $Q_{\text{ini}}^{\text{Am}} = 37.3\,\text{fC}$.

B.5 Purity calculation algorithm

$min\_pur = 0$ and $max\_pur = 2$, $test\_pur = min\_pur$;
$inc = 0.2$;
$cur\_prec = 1$ and $precision = 10^{-5}$.

First the energy spectra of both sources are recorded. Then the peaks for 1 MeV line of Bi source and 5.5 MeV line of Am source are determined. Next the ratio of the peaks is builded and compared with the ratio of the calculated charges. Then through the iteration the impurity n_s is determined at the calculation of the charges. Both ratios should be nearly the same with *precision* value as a precision. This algorithm is written below in more detail.

1. Check if $cur\_prec > precision$ and $test\_pur > max\_pur$.
2. If not, the purity value is $test\_pur$. Otherwise go to the next step.
3. Check if the overall calculation time exceeded 28 seconds.
4. If so, the purity value is -1. Otherwise go to the next step.
5. Define $test\_pur = test\_pur + inc$.
6. Calculate $\frac{Q_{\text{Bi}}}{Q_{\text{Am}}}$ using formulae B.7 and B.9 with $test\_pur$ as n_s.

7. Set $cur\_prec = \left|\frac{Q_{\mathrm{Bi}}}{Q_{\mathrm{Am}}} - \frac{p_{\mathrm{Bi}}}{p_{\mathrm{Am}}}\right|$, where p_{Bi} (p_{Am}) is measured peak position for Bi (Am) source.
8. Check if $\frac{Q_{\mathrm{Bi}}}{Q_{\mathrm{Am}}} < \frac{p_{\mathrm{Bi}}}{p_{\mathrm{Am}}}$.
9. If so, set $test\_pur = test\_pur - inc$ and $inc = \frac{inc}{2}$.
10. Return to the step 1.

Appendix

C

MORE DETAILED OPC UA SERVER DESIGN

The following Appendix contains a schematic of more detailed OPC UA server design shown in Figure C.1. The actual OPC UA server design can be found in the middle of this Figure. On the bottom are the connections to the hardware aspects (PFEBs and BMs) of LAr purity monitoring system shown. On top are the connections with WinCC OA objects listed. The last ones can be used for direct searching of the corresponding current values in the FSM.

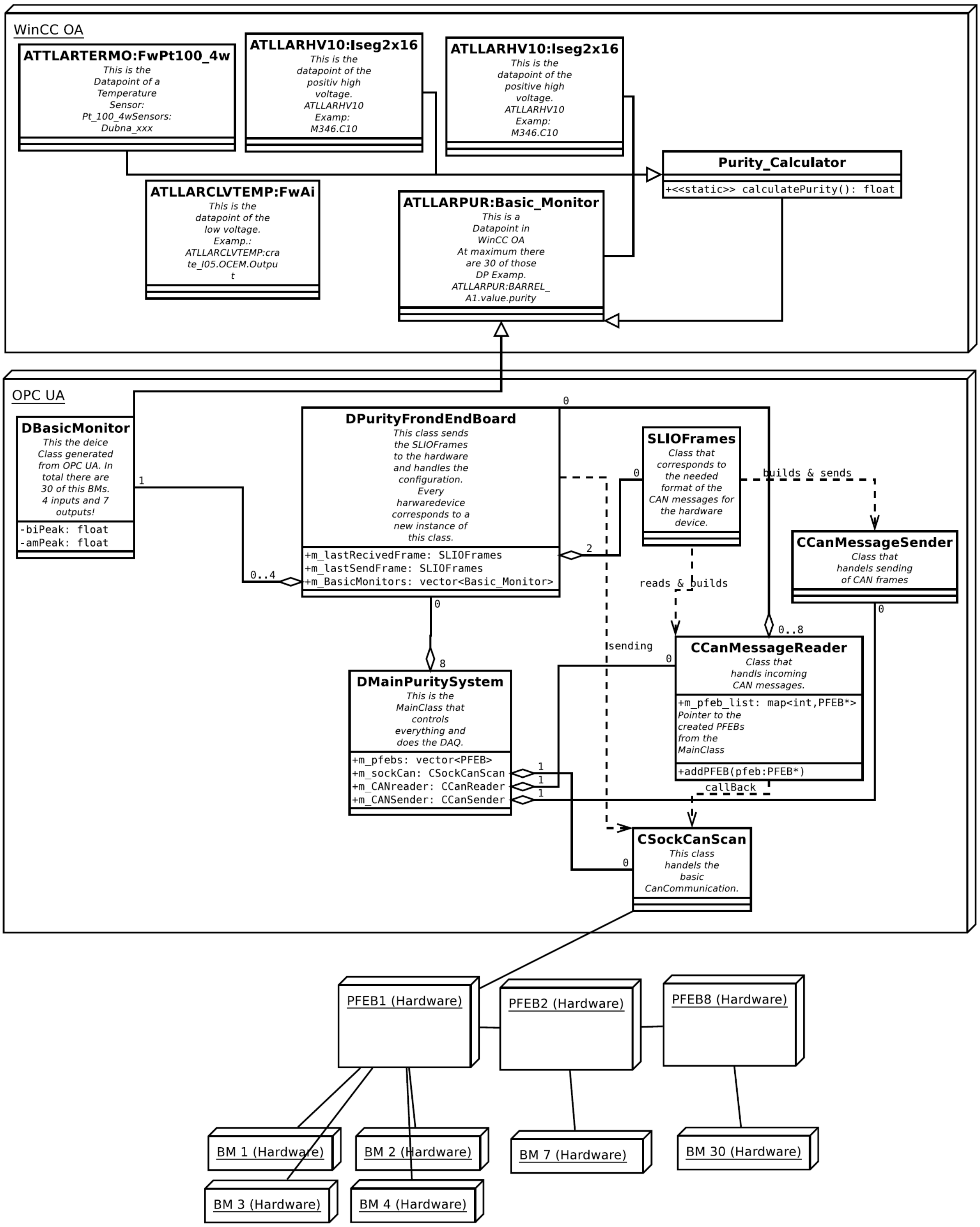

Figure C.1: *More detailed OPC UA server design [243].*

Appendix

D

Barrel A1 spectra during calibration test

The following Appendix provides Am and Bi spectra for Barrel A1 LAr purity monitor with different calibration values. The spectra with calibration values 4 and 5 are shown in Figure D.1. Figure D.2 summarize the spectra with calibration values 6-9. Figure D.3 and Figure D.4 show the spectra with calibration values 10-13 and 14-15, respectively. For all these spectra the HV was switched off.

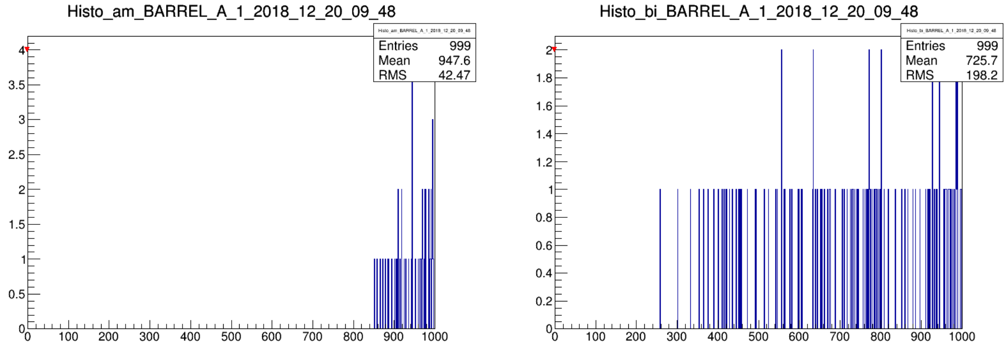

(a) Calibration value = 4.

(b) Calibration value = 4.

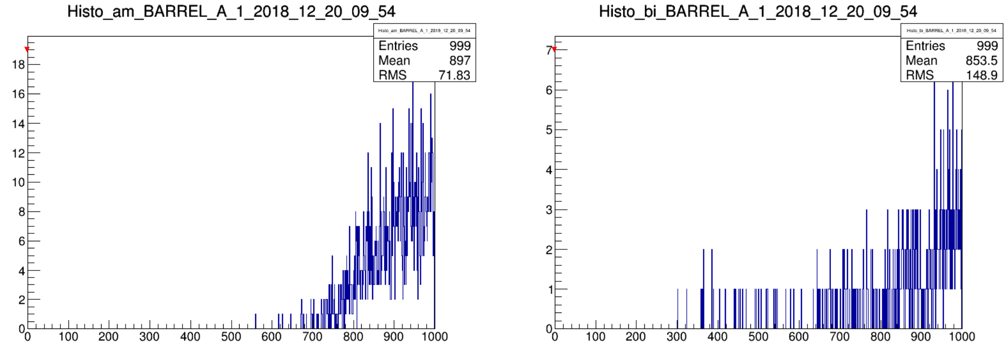

(c) Calibration value = 5.

(d) Calibration value = 5.

Figure D.1: *Am (left) and Bi (right) spectra for Barrel A1 LAr purity monitor. The calibration value is setted to 4 (top) and 5 (bottom), and HV is off.*

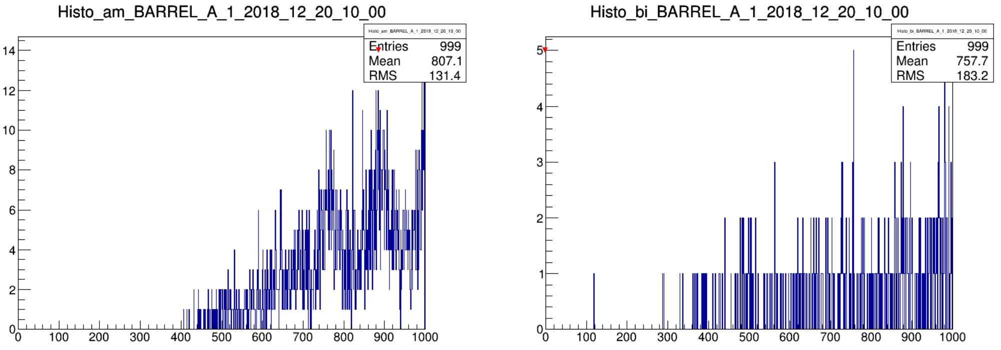

(a) Calibration value = 6.

(b) Calibration value = 6.

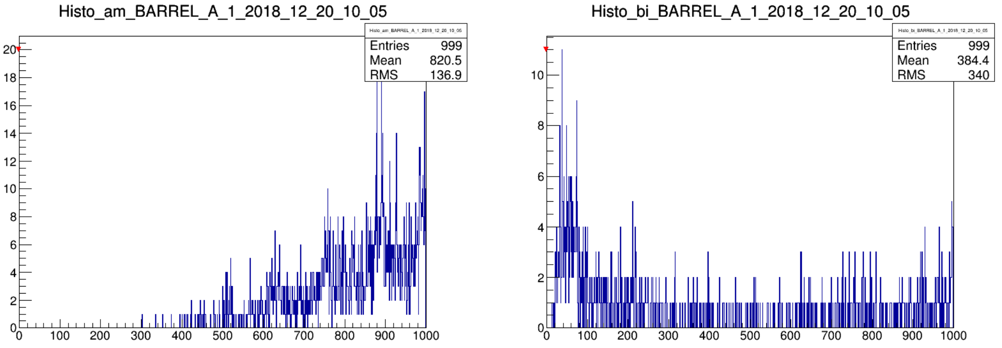

(c) Calibration value = 7.

(d) Calibration value = 7.

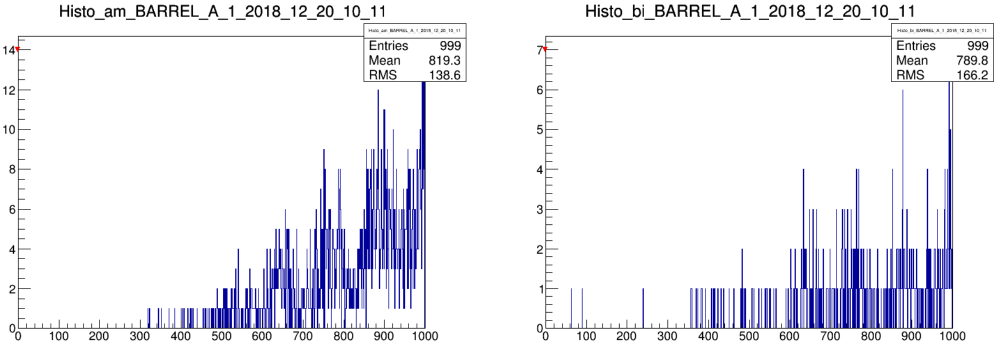

(e) Calibration value = 8.

(f) Calibration value = 8.

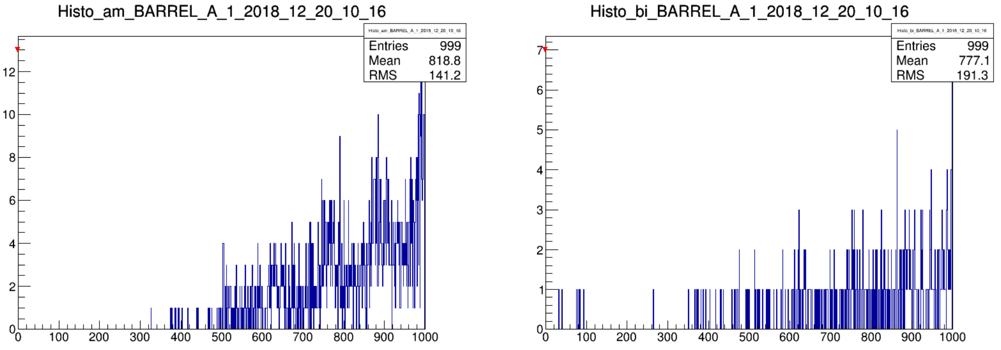

(g) Calibration value = 9.

(h) Calibration value = 9.

Figure D.2: *Am (left) and Bi (right) spectra for Barrel A1 LAr purity monitor. The calibration value is setted to 6, 7, 8, 9 from the first row to the last, and HV is off.*

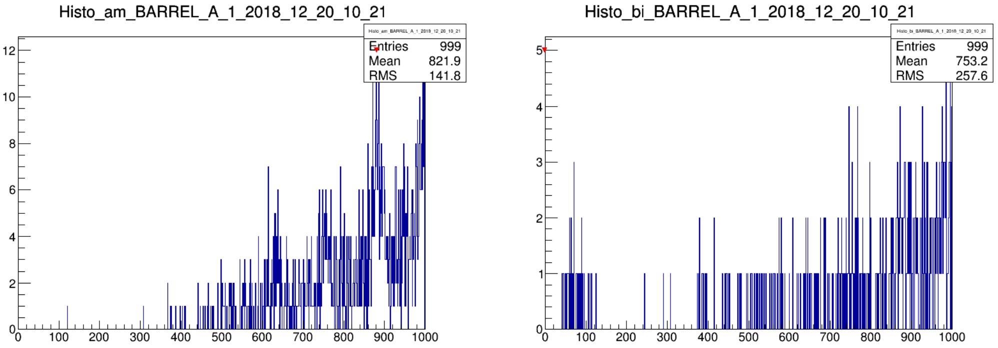

(a) Calibration value = 10.

(b) Calibration value = 10.

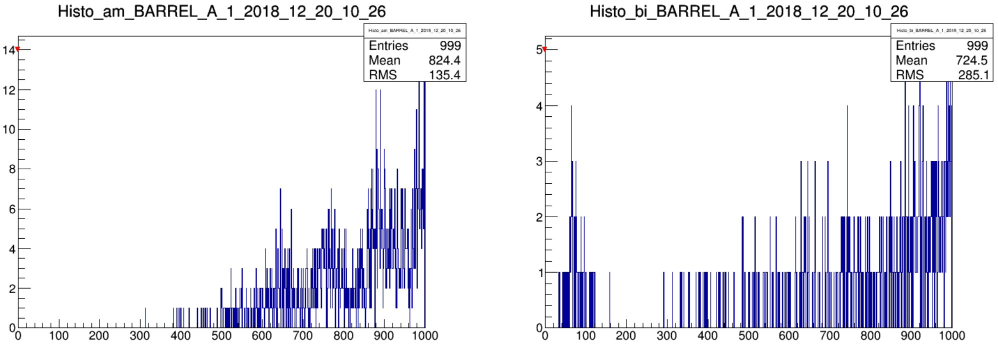

(c) Calibration value = 11.

(d) Calibration value = 11.

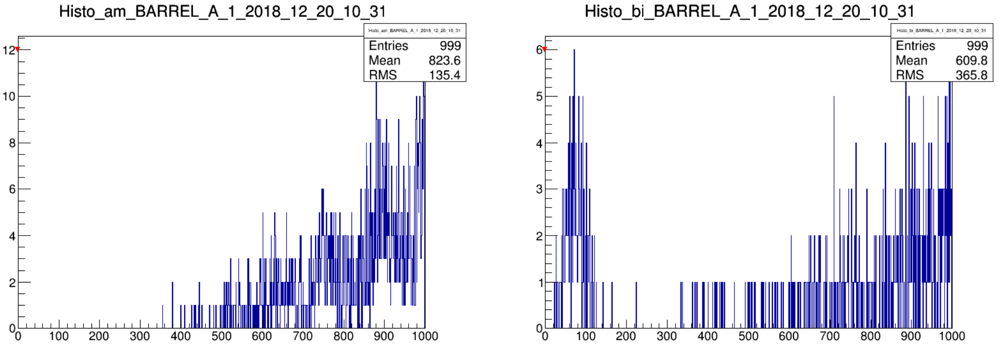

(e) Calibration value = 12.

(f) Calibration value = 12.

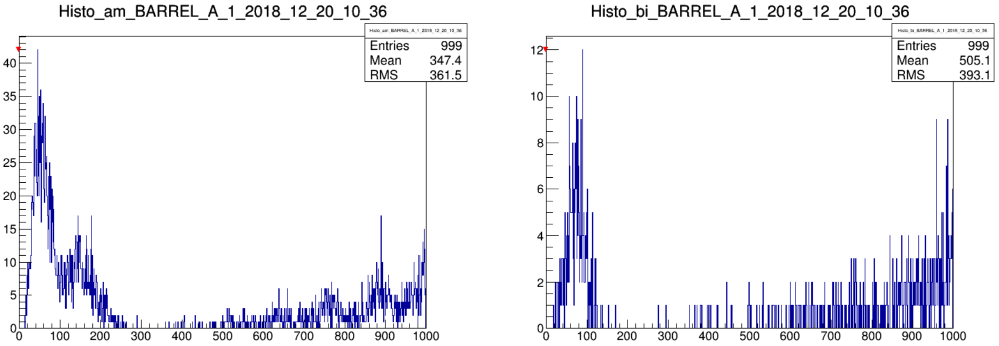

(g) Calibration value = 13.

(h) Calibration value = 13.

Figure D.3: *Am (left) and Bi (right) spectra for Barrel A1 LAr purity monitor. The calibration value is setted to 10, 11, 12, 13 from the first row to the last, and HV is off.*

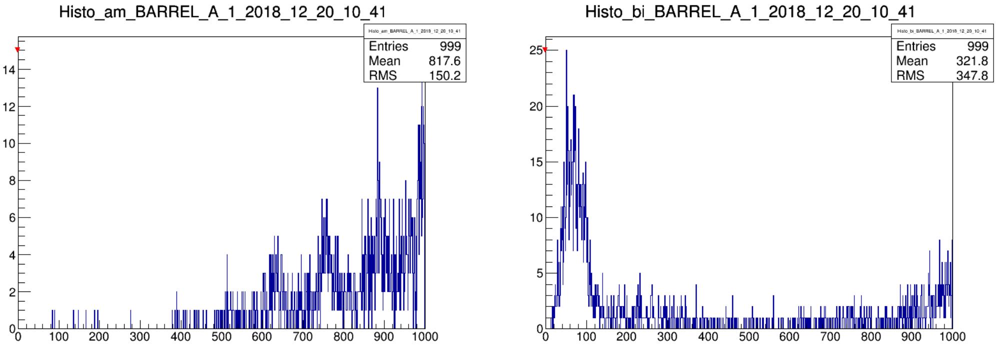

(a) Calibration value = 14.

(b) Calibration value = 14.

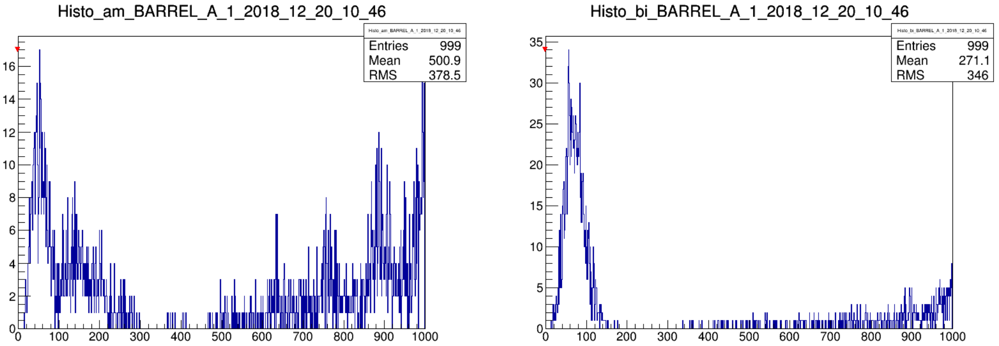

(c) Calibration value = 15.

(d) Calibration value = 15.

Figure D.4: *Am (left) and Bi (right) spectra for Barrel A1 LAr purity monitor. The calibration value is setted to 14 (top) and 15 (bottom), and HV is off.*

Appendix

E Nominal spectra

The following Appendix provides the Am and Bi spectra with nominal settings taken during the HV mapping test described in Section 12.3. However, due to other maintenance works on the ATLAS detector, which were beyond of my control, the LV for some monitors was off for a long time and did not switch back on during writing of this thesis, so the corresponding plots are not included here.

Figures are sorted by the mapping to the PFEBs. Figure E.1 shows the spectra for Barrel A1 and Barrel A3 monitors, Figure E.2 - for Barrel A4 and Barrel A5, Figure E.3 - for Barrel C1, C2, C3 and C5, Figure E.4 - for HEC 1AA, 1AB and 1AC, Figure E.5 - for HEC 2AA, 2AB and 2AC, Figure E.6 - for HEC 2CA, 2CB and 2CC, Figure E.7 - for EMEC CB, HEC 1CA, HEC 1CB and HEC 1CC.

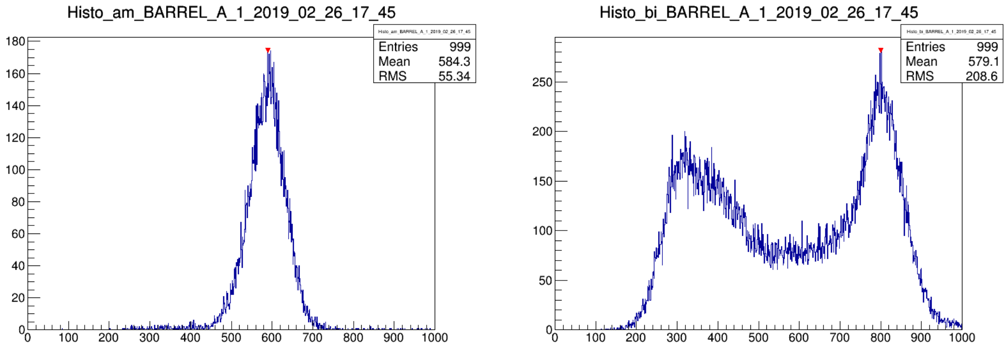

(a) Barrel A1 Am spectrum. (b) Barrel A1 Bi spectrum.

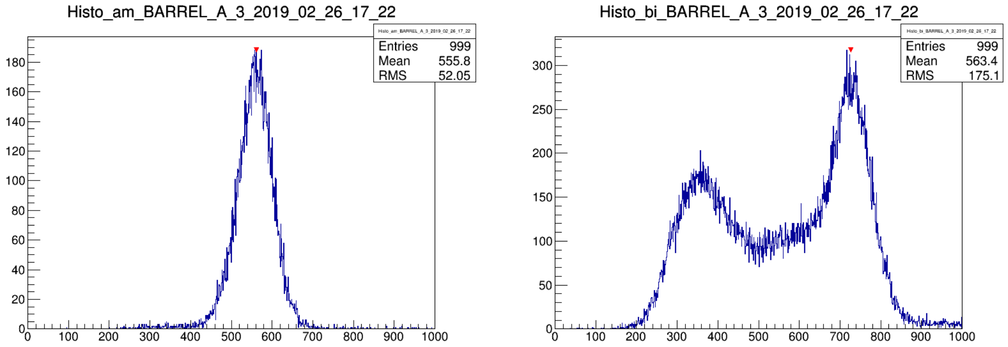

(c) Barrel A3 Am spectrum. (d) Barrel A3 Bi spectrum.

Figure E.1: *PFEB 1, part I.*

All plots look similar to the theoretical expectations shown in Figures 11.6 and 11.9 (single peak for Am spectrum and two peaks with the Compton continuum in between for Bi spectrum, where the last peak is used for the purity calculation). Remarkable additions to these main

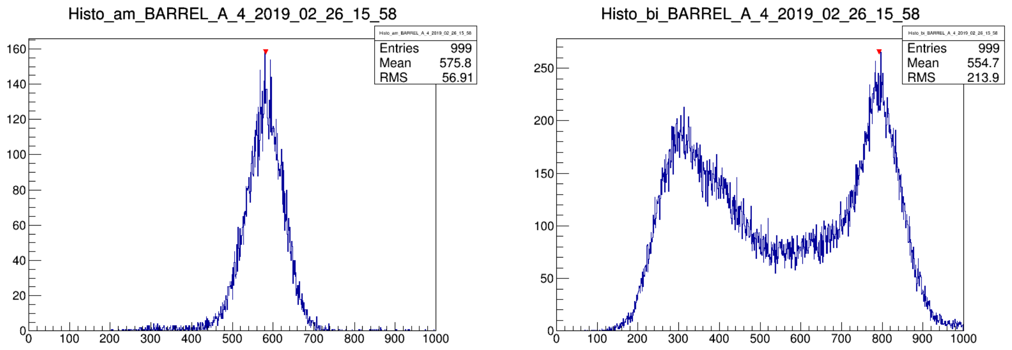

(a) Barrel A4 Am spectrum.

(b) Barrel A4 Bi spectrum.

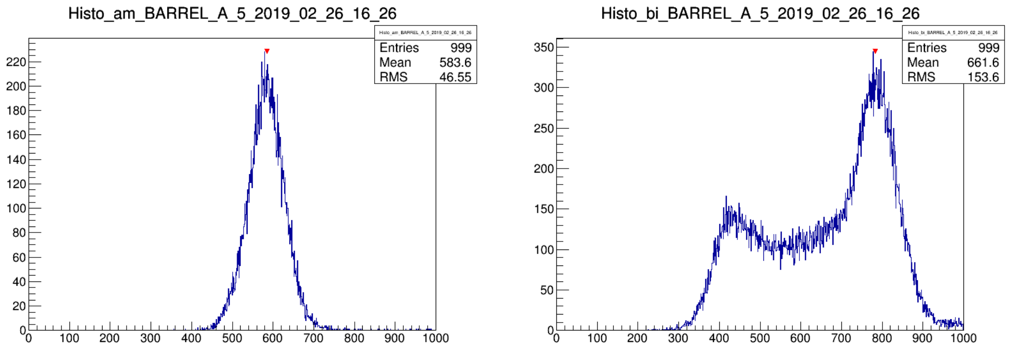

(c) Barrel A5 Am spectrum.

(d) Barrel A5 Bi spectrum.

Figure E.2: *PFEB 1, part II.*

spectra are few secondary peaks in the low regions of the spectrum in Am spectrum of Barrel C5 monitor (Figure E.3(g)) and Bi spectra of HEC 2AB (Figure E.5(d)), HEC 2AC (Figure E.5(f)) and EMEC CB (Figure E.7(b)) monitors. The origin of these secondary peaks is not yet understood, but it can not be the calibration since it was switched off (by setting the calibration value to 0 for all LAr purity monitors). However, they do not affect the purity calculation since the peak finding algorithm works in the higher region of the spectrum.

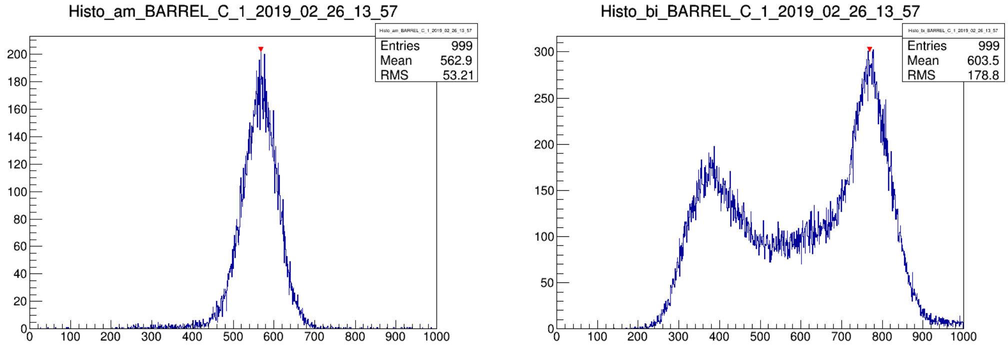

(a) Barrel C1 Am spectrum.

(b) Barrel C1 Bi spectrum.

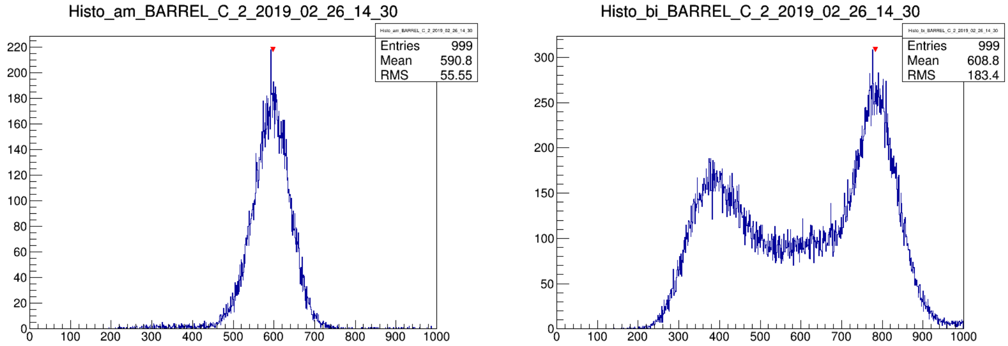

(c) Barrel C2 Am spectrum.

(d) Barrel C2 Bi spectrum.

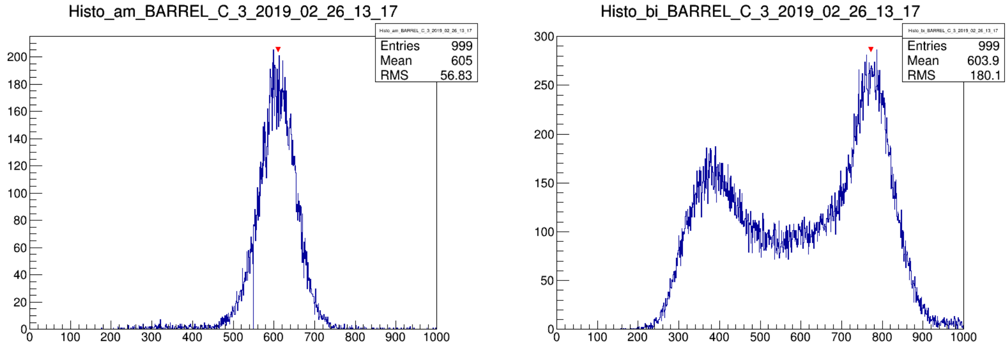

(e) Barrel C3 Am spectrum.

(f) Barrel C3 Bi spectrum.

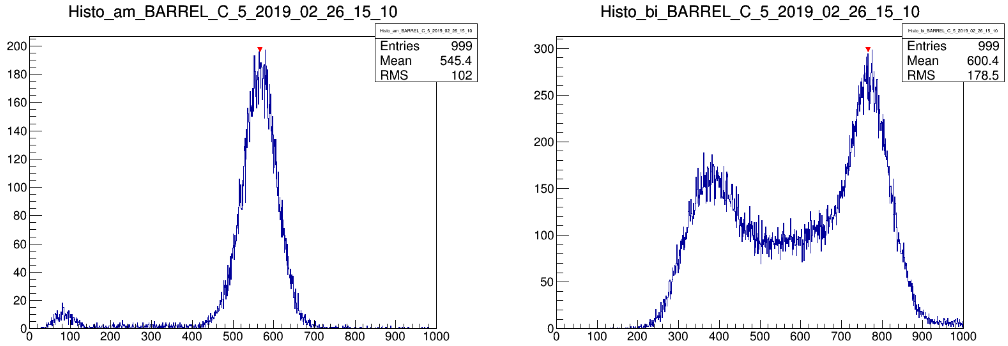

(g) Barrel C5 Am spectrum.

(h) Barrel C5 Bi spectrum.

Figure E.3: *PFEB 2.*

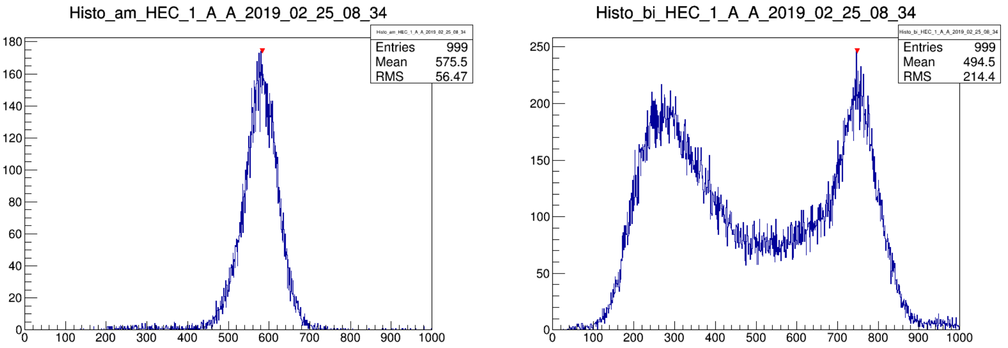

(a) HEC 1AA Am spectrum.

(b) HEC 1AA Bi spectrum.

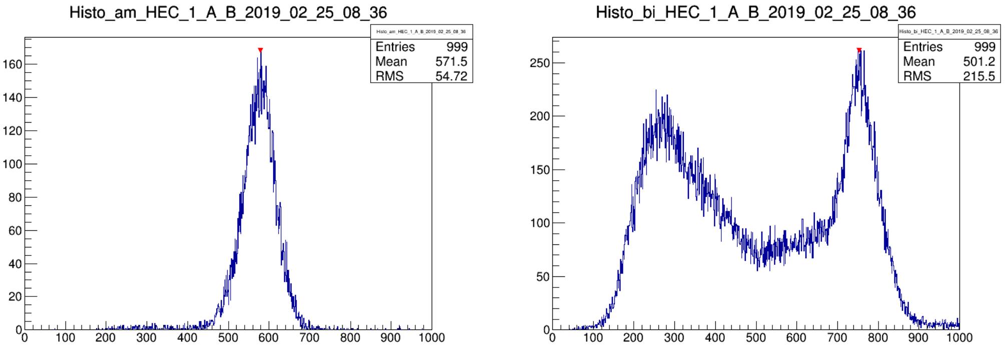

(c) HEC 1AB Am spectrum.

(d) HEC 1AB Bi spectrum.

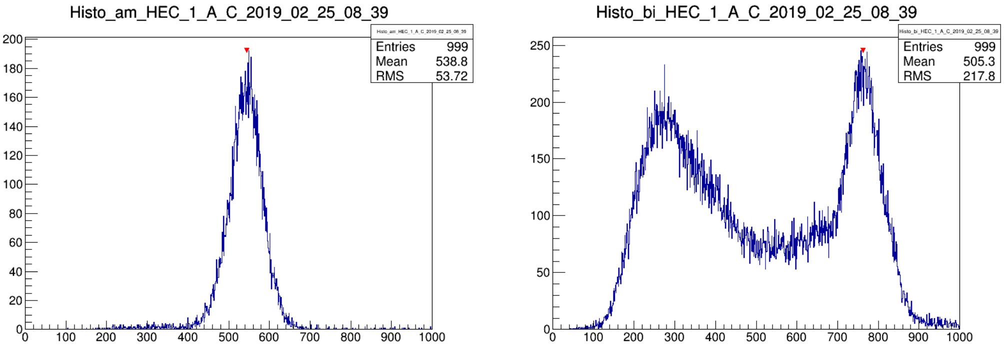

(e) HEC 1AC Am spectrum.

(f) HEC 1AC Bi spectrum.

Figure E.4: *PFEB 3, part I.*

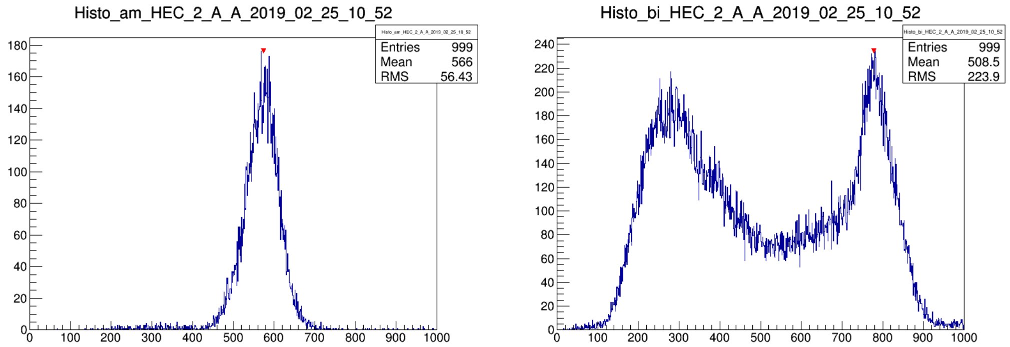
Histo_am_HEC_2_A_A_2019_02_25_10_52

Histo_bi_HEC_2_A_A_2019_02_25_10_52

(a) HEC 2AA Am spectrum.

(b) HEC 2AA Bi spectrum.

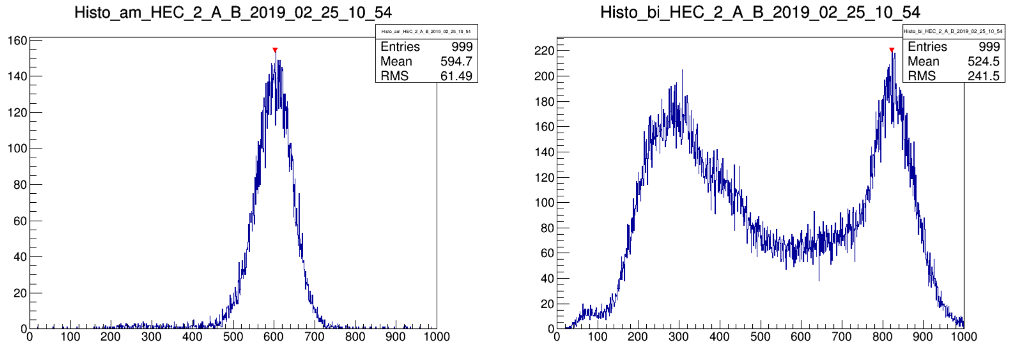
Histo_am_HEC_2_A_B_2019_02_25_10_54

Histo_bi_HEC_2_A_B_2019_02_25_10_54

(c) HEC 2AB Am spectrum.

(d) HEC 2AB Bi spectrum.

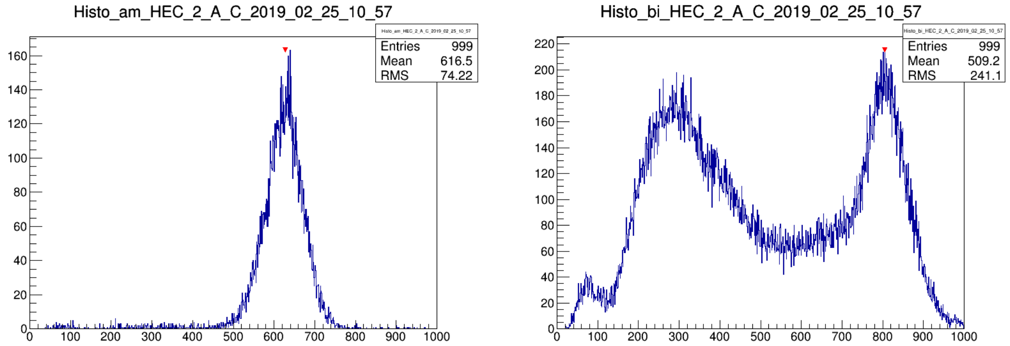
Histo_am_HEC_2_A_C_2019_02_25_10_57

Histo_bi_HEC_2_A_C_2019_02_25_10_57

(e) HEC 2AC Am spectrum.

(f) HEC 2AC Bi spectrum.

Figure E.5: *PFEB 3, part II.*

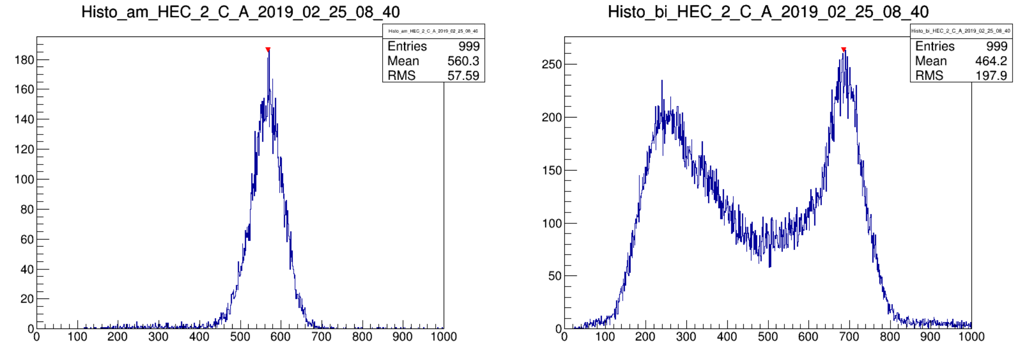

(a) HEC 2CA Am spectrum.

(b) HEC 2CA Bi spectrum.

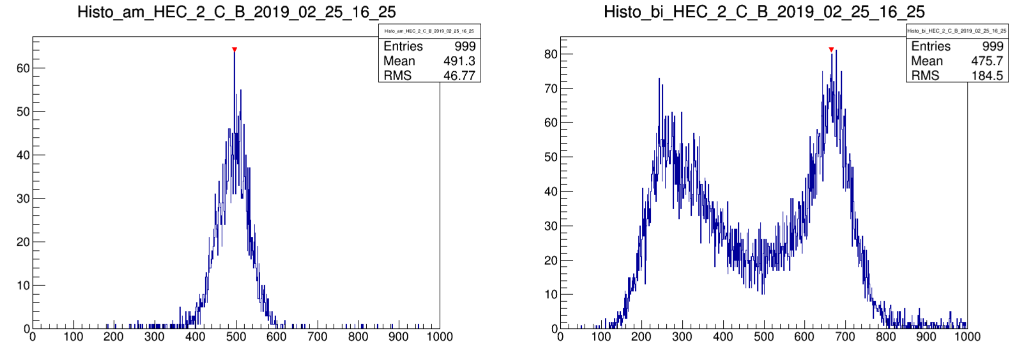

(c) HEC 2CB Am spectrum.

(d) HEC 2CB Bi spectrum.

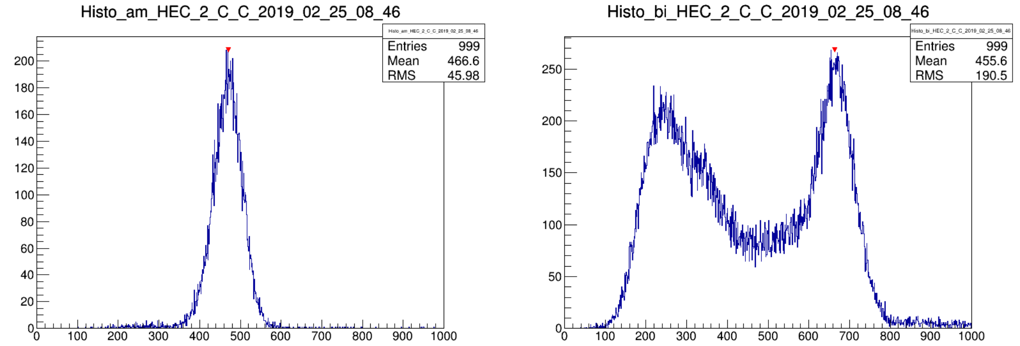

(e) HEC 2CC Am spectrum.

(f) HEC 2CC Bi spectrum.

Figure E.6: *PFEB 4.*

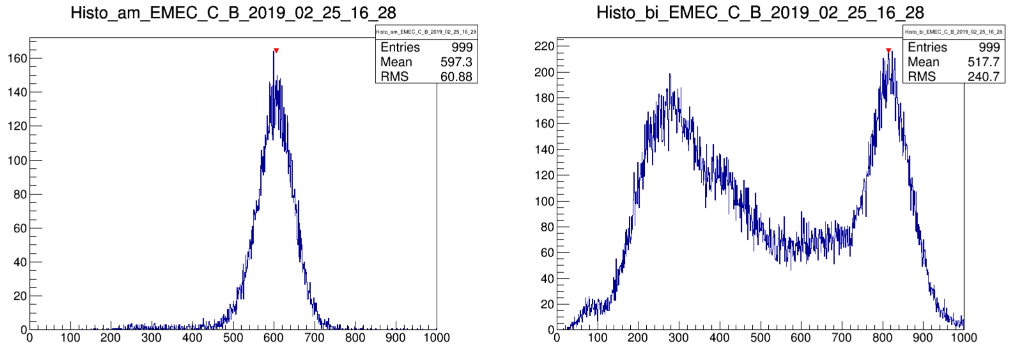

(a) EMEC CB Am spectrum.

(b) EMEC CB Bi spectrum.

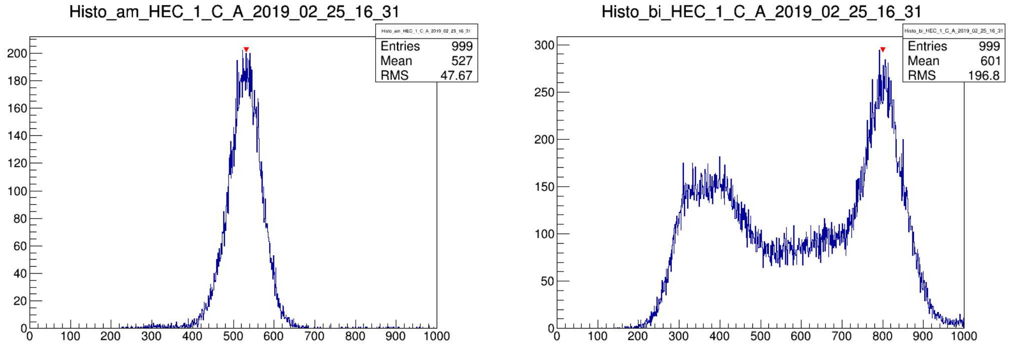

(c) HEC 1CA Am spectrum.

(d) HEC 1CA Bi spectrum.

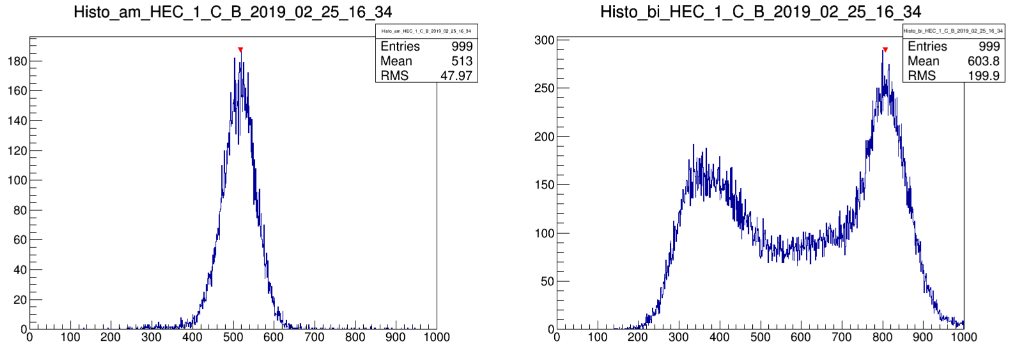

(e) HEC 1CB Am spectrum.

(f) HEC 1CB Bi spectrum.

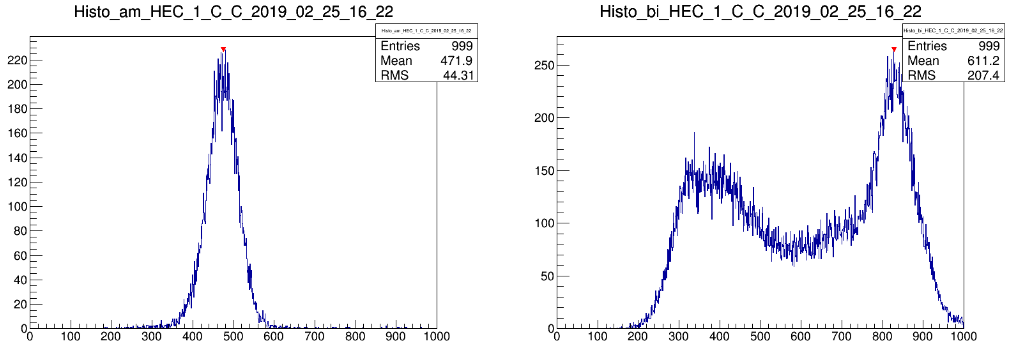

(g) HEC 1CC Am spectrum.

(h) HEC 1CC Bi spectrum.

Figure E.7: *PFEB 5.*

Appendix

F NOISE SPECTRA

The following Appendix provides the noise spectra of Am and Bi for all LAr purity monitors. In order to collect these histograms both Am and Bi thresholds were set to the zero line (6144 in the configuration file) and HV was switched off, so only LV was kept to be onine. However, due to other maintenance works on the ATLAS detector, which were beyond of my control, the LV for some monitors was off for a long time and did not switch back on during writing of this thesis, so the corresponding plots are not included here.

Figures are sorted by the mapping to the PFEBs. Figure F.1 shows the spectra for Barrel A1 and Barrel A3 monitors, Figure F.2 - for Barrel A4 and Barrel A5, Figure F.3 - for Barrel C1, C2 and C3, Figure F.4 - for HEC 2CA, 2CB and 2CC, Figure F.5 - for EMEC CB, HEC 1CA, HEC 1CB and HEC 1CC.

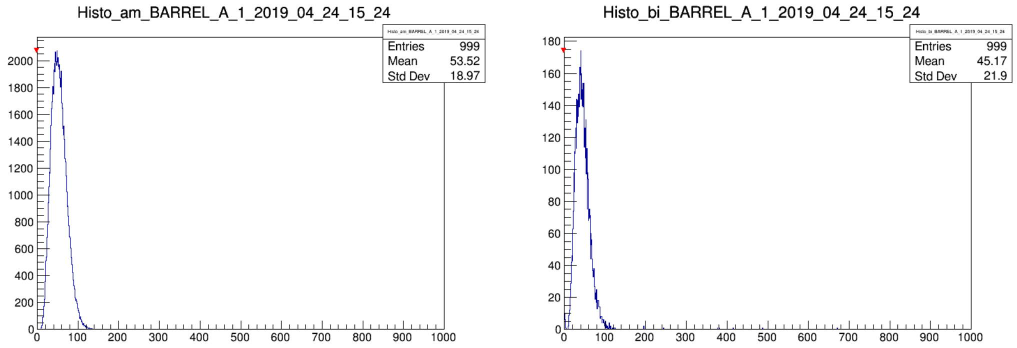

(a) Barrel A1 Am spectrum. (b) Barrel A1 Bi spectrum.

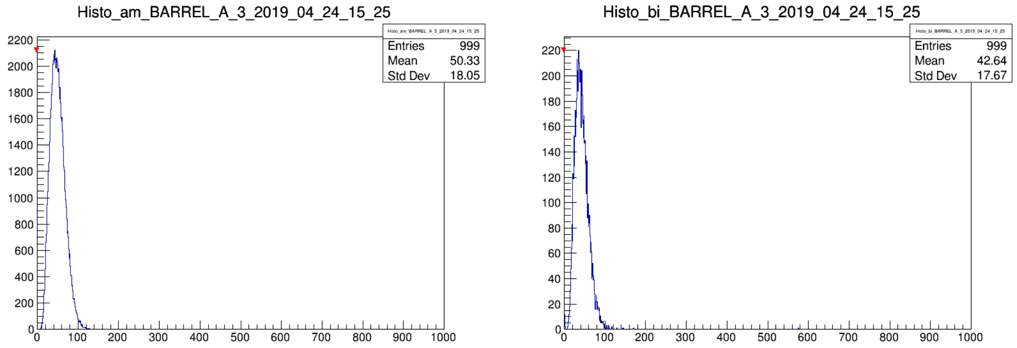

(c) Barrel A3 Am spectrum. (d) Barrel A3 Bi spectrum.

Figure F.1: *PFEB 1, part I.*

An exceptional behavior of the Bi spectrum for EMEC CB monitor (see Figure F.5(b)) is not yet understood.

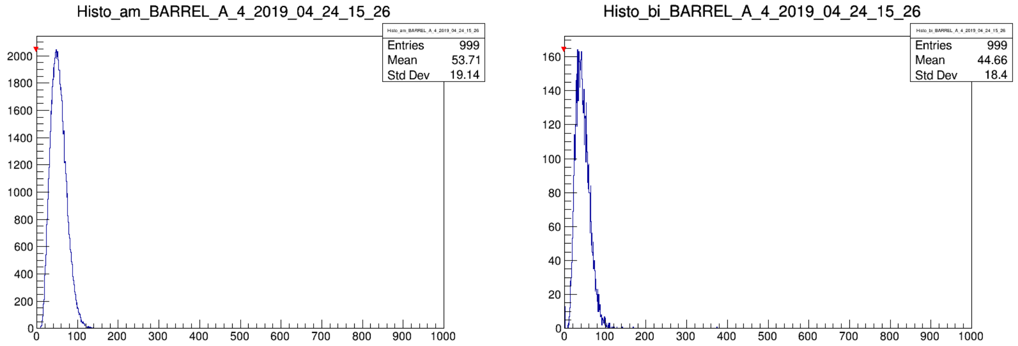

(a) Barrel A4 Am spectrum.

(b) Barrel A4 Bi spectrum.

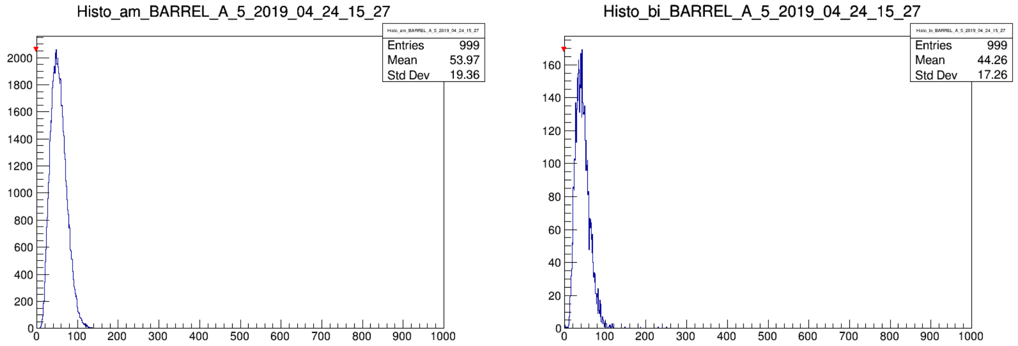

(c) Barrel A5 Am spectrum.

(d) Barrel A5 Bi spectrum.

Figure F.2: *PFEB 1, part II.*

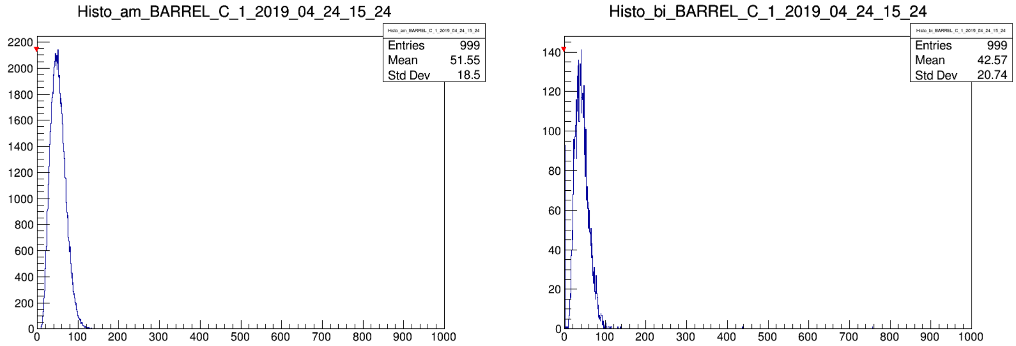

(a) Barrel C1 Am spectrum.

(b) Barrel C1 Bi spectrum.

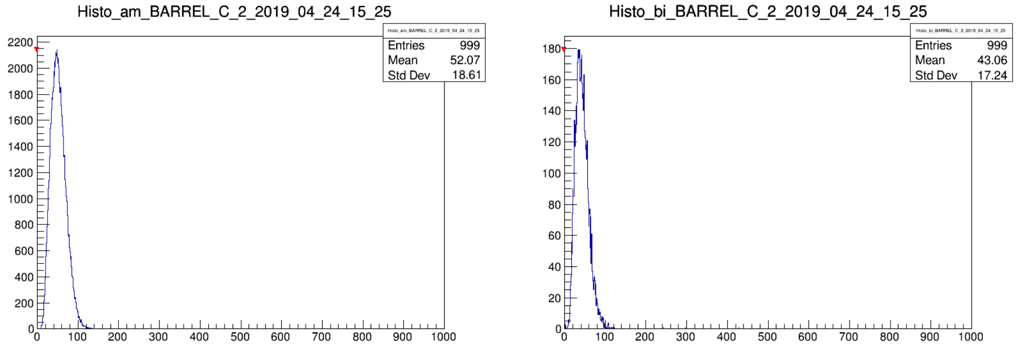

(c) Barrel C2 Am spectrum.

(d) Barrel C2 Bi spectrum.

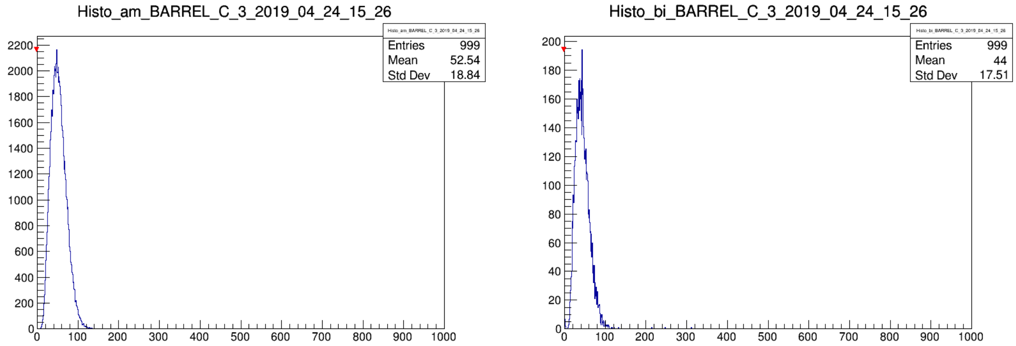

(e) Barrel C3 Am spectrum.

(f) Barrel C3 Bi spectrum.

Figure F.3: *PFEB 2, part I.*

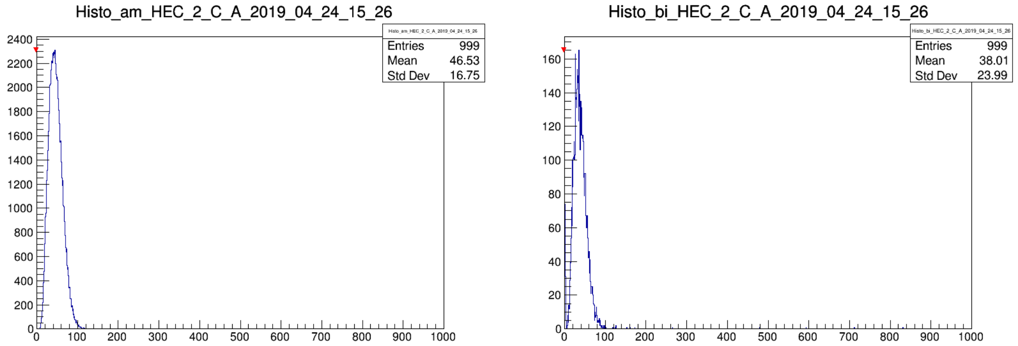

(a) HEC 2CA Am spectrum.

(b) HEC 2CA Bi spectrum.

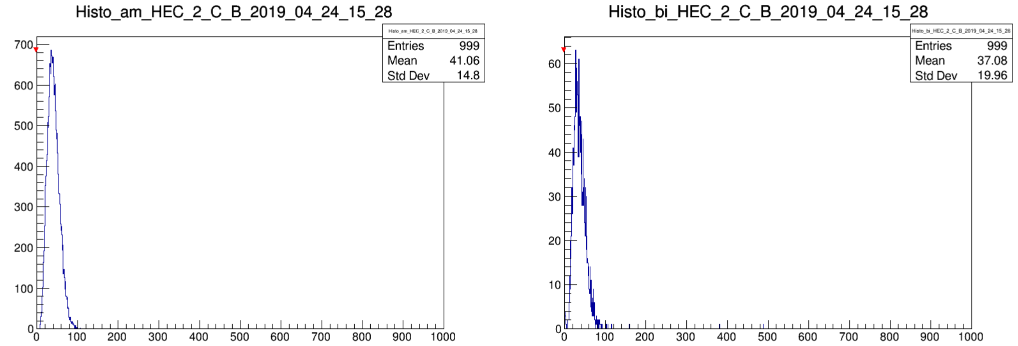

(c) HEC 2CB Am spectrum.

(d) HEC 2CB Bi spectrum.

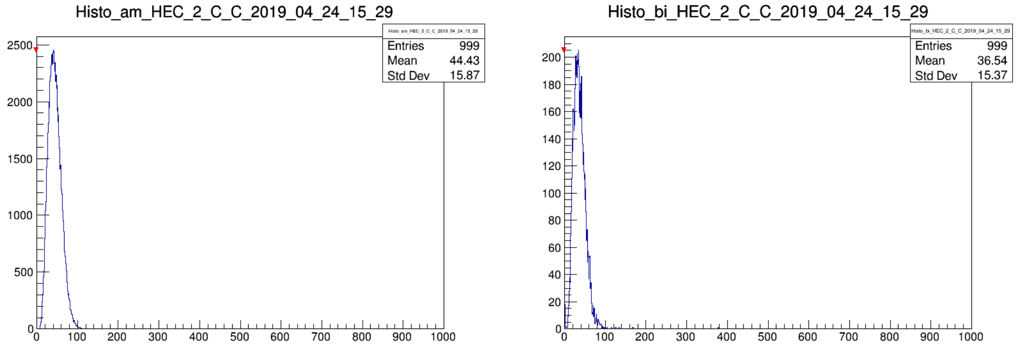

(e) HEC 2CC Am spectrum.

(f) HEC 2CC Bi spectrum.

Figure F.4: *PFEB 4, part II.*

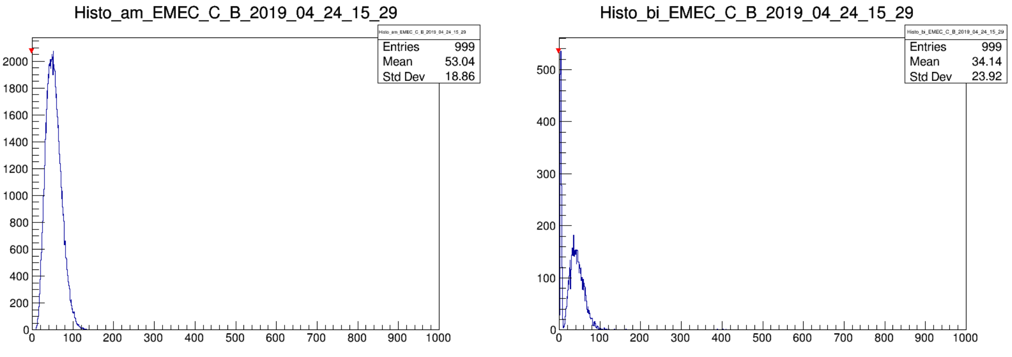

(a) EMEC CB Am spectrum.

(b) EMEC CB Bi spectrum.

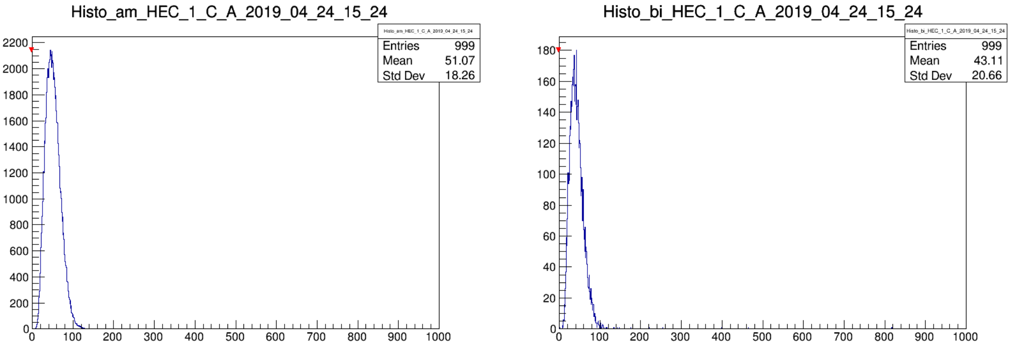

(c) HEC 1CA Am spectrum.

(d) HEC 1CA Bi spectrum.

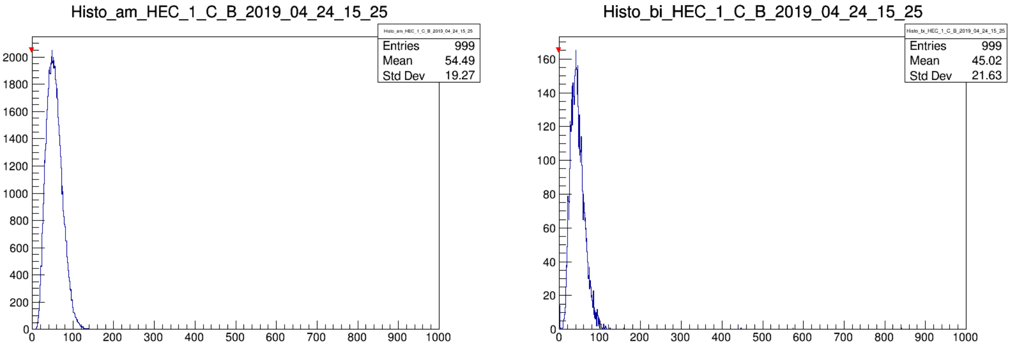

(e) HEC 1CB Am spectrum.

(f) HEC 1CB Bi spectrum.

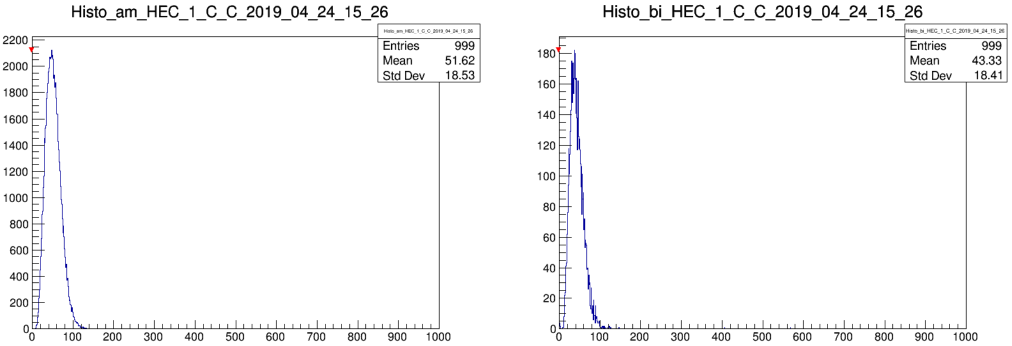

(g) HEC 1CC Am spectrum.

(h) HEC 1CC Bi spectrum.

Figure F.5: *PFEB 5.*

BIBLIOGRAPHY

References for Chapter : Introduction

[1] J. Law and R. Rennie. *A Dictionary of Physics*. Oxford University Press, 2015. ISBN: 978-0-198-71474-3 *Cited on page 1.*

[2] J. J. Thomson M.A. F.R.S. "XL. Cathode Rays". In: *The London, Edinburgh, and Dublin Philosophical Magazine and Journal of Science* 44.269 (1897), pp. 293–316. DOI: 10.1080/14786449708621070 *Cited on page 1.*

[3] Professor E. Rutherford F.R.S. "LXXIX. The scattering of α and β particles by matter and the structure of the atom". In: *The London, Edinburgh, and Dublin Philosophical Magazine and Journal of Science* 21.125 (1911), pp. 669–688. DOI: 10.1080/14786440508637080 *Cited on page 1.*

[4] J. Chadwick. "Possible Existence of a Neutron". In: *Nature* 129 (1932), p. 312. DOI: 10.1038/129312a0 *Cited on page 1.*

[5] M. Gell-Mann. "A schematic model of baryons and mesons". In: *Physics Letters* 8.3 (1964), pp. 214–215. ISSN: 0031-9163. DOI: doi.org/10.1016/S0031-9163(64)92001-3 *Cited on page 1.*

[6] G. Zweig. "An SU(3) model for strong interaction symmetry and its breaking. Version 2". In: *Developments in the Quark Theory of Hadrons, Volume 1. 1964 - 1978*. Ed. by D.B. Lichtenberg and S. P. Rosen. http://inspirehep.net/record/4674/files/cern-th-412.pdf. 1964, pp. 22–101 *Cited on page 1.*

[7] M. Breidenbach et al. "Observed Behavior of Highly Inelastic Electron-Proton Scattering". In: *Phys. Rev. Lett.* 23 (16 Oct. 1969), pp. 935–939. DOI: 10.1103/PhysRevLett.23.935 *Cited on page 1.*

[8] E. D. Bloom et al. "High-Energy Inelastic $e-p$ Scattering at 6° and 10°". In: *Phys. Rev. Lett.* 23 (16 Oct. 1969), pp. 930–934. DOI: 10.1103/PhysRevLett.23.930 *Cited on page 1.*

[9] R. Brandelik et al. "Evidence for planar events in e^+e^- annihilation at high energies". In: *Physics Letters B* 86.2 (1979), pp. 243–249. ISSN: 0370-2693. DOI: doi.org/10.1016/0370-2693(79)90830-X *Cited on page 2.*

[10] D. P. Barber et al. "Discovery of Three-Jet Events and a Test of Quantum Chromodynamics at PETRA". In: *Phys. Rev. Lett.* 43 (12 Sept. 1979), pp. 830–833. DOI: 10.1103/PhysRevLett.43.830 *Cited on page 2.*

[11] C. Berger et al. "Evidence for gluon bremsstrahlung in e^+e^- annihilations at high energies". In: *Physics Letters B* 86.3 (1979), pp. 418–425. ISSN: 0370-2693. DOI: doi.org/10.1016/0370-2693(79)90869-4 *Cited on page 2.*

[12] W. Bartel et al. "Observation of planar three-jet events in e^+e^- annihilation and evidence for gluon bremsstrahlung". In: *Physics Letters B* 91.1 (1980), pp. 142–147. ISSN: 0370-2693. DOI: doi.org/10.1016/0370-2693(80)90680-2 *Cited on page 2.*

[13] G. Arnison et al. “Experimental observation of isolated large transverse energy electrons with associated missing energy at s=540 GeV”. In: *Physics Letters B* 122.1 (1983), pp. 103–116. ISSN: 0370-2693. DOI: doi.org/10.1016/0370-2693(83)91177-2 *Cited on pages 2, 14.*

[14] M. Banner et al. “Observation of single isolated electrons of high transverse momentum in events with missing transverse energy at the CERN pp collider”. In: *Physics Letters B* 122.5 (1983), pp. 476–485. ISSN: 0370-2693. DOI: doi.org/10.1016/0370-2693(83)91605-2 *Cited on pages 2, 14.*

[15] G. Arnison et al. “Experimental observation of lepton pairs of invariant mass around 95 GeV/c^2 at the CERN SPS collider”. In: *Physics Letters B* 126.5 (1983), pp. 398–410. ISSN: 0370-2693. DOI: doi.org/10.1016/0370-2693(83)90188-0 *Cited on pages 2, 14.*

[16] P. Bagnaia et al. “Evidence for $Z^0 \to e^+e^-$ at the CERN pp collider”. In: *Physics Letters B* 129.1 (1983), pp. 130–140. ISSN: 0370-2693. DOI: doi.org/10.1016/0370-2693(83)90744-X *Cited on pages 2, 14.*

[17] D0 Collaboration. “Observation of the top quark”. In: *Phys. Rev. Lett.* 74 (1995), pp. 2632–2637. DOI: 10.1103/PhysRevLett.74.2632. arXiv: hep-ex/9503003 [hep-ex] *Cited on page 2.*

[18] D0 Collaboration. “Measurement of the Electric Charge of the Top Quark in $t\bar{t}$ Events”. In: *Phys. Rev.* D90.5 (2014). [Erratum: Phys. Rev.D90,no.7,079904(2014)], p. 051101. DOI: 10.1103/PhysRevD.90.051101,10.1103/PhysRevD.90.079904. arXiv: 1407.4837 [hep-ex] *Cited on page 2.*

[19] P. C. Bhat, H. Prosper, and S. S. Snyder. “Top quark physics at the Tevatron”. In: *Int. J. Mod. Phys.* A13 (1998), pp. 5113–5218. DOI: 10.1142/S0217751X98002389. arXiv: hep-ex/9809011 [hep-ex] *Cited on page 2.*

[20] CDF Collaboration. “Observation of top quark production in $\bar{p}p$ collisions”. In: *Phys. Rev. Lett.* 74 (1995), pp. 2626–2631. DOI: 10.1103/PhysRevLett.74.2626. arXiv: hep-ex/9503002 [hep-ex] *Cited on page 2.*

[21] ATLAS Collaboration. “A Particle Consistent with the Higgs Boson Observed with the ATLAS Detector at the Large Hadron Collider”. In: *Science* 338.6114 (2012), pp. 1576–1582. ISSN: 0036-8075. DOI: 10.1126/science.1232005. eprint: http://science.sciencemag.org/content/338/6114/1576.full.pdf *Cited on page 2.*

[22] W. de Boer. “The Discovery of the Higgs Boson with the CMS Detector and its Implications for Supersymmetry and Cosmology”. In: *Time and Matter 2013 (TAM2013) Venice, Italy*. 2013. arXiv: 1309.0721 [hep-ph] *Cited on page 2.*

[23] R. Pöttgen. “Search for Dark Matter in events with a highly energetic jet and missing transverse momentum in proton-proton collisions at $\sqrt{s} = 8$ TeV with the ATLAS Detector”. PhD thesis. Johannes Gutenberg-Universität Mainz, Oct. 2014 *Cited on pages 2, 31, 46.*

[24] M. Zinser. “Search for new heavy charged bosons and measurement of high-mass Drell-Yan production in proton-proton collisions”. PhD thesis. Johannes Gutenberg-Universität Mainz, Aug. 2016 *Cited on pages 2, 16, 29, 33, 47, 59.*

[25] M. Becker. “Measurement of ZZ production and search for anomalous neutral triple gauge couplings in pp collisions at $\sqrt{s} = 13$ TeV with the ATLAS experiment”. PhD thesis. Johannes Gutenberg-Universität Mainz, Dec. 2017 *Cited on pages 2, 7, 47.*

[26] S. Schmitz. “Search for New Resonances in Lepton-Antilepton Final States in Proton-Proton Collisions at $\sqrt{s}$ = 13 TeV with the ATLAS Experiment”. PhD thesis. Johannes Gutenberg-Universität Mainz, May 2018 *Cited on pages 2, 31, 33, 35, 47, 66.*

References for Chapter 1: The Standard Model

[13] G. Arnison et al. “Experimental observation of isolated large transverse energy electrons with associated missing energy at s=540 GeV”. In: *Physics Letters B* 122.1 (1983), pp. 103–116. ISSN: 0370-2693. DOI: `doi.org/10.1016/0370-2693(83)91177-2` *Cited on pages 2, 14.*

[14] M. Banner et al. “Observation of single isolated electrons of high transverse momentum in events with missing transverse energy at the CERN pp collider”. In: *Physics Letters B* 122.5 (1983), pp. 476–485. ISSN: 0370-2693. DOI: `doi.org/10.1016/0370-2693(83)91605-2` *Cited on pages 2, 14.*

[15] G. Arnison et al. “Experimental observation of lepton pairs of invariant mass around 95 GeV/c^2 at the CERN SPS collider”. In: *Physics Letters B* 126.5 (1983), pp. 398–410. ISSN: 0370-2693. DOI: `doi.org/10.1016/0370-2693(83)90188-0` *Cited on pages 2, 14.*

[16] P. Bagnaia et al. “Evidence for $Z^0 \to e^+e^-$ at the CERN pp collider”. In: *Physics Letters B* 129.1 (1983), pp. 130–140. ISSN: 0370-2693. DOI: `doi.org/10.1016/0370-2693(83)90744-X` *Cited on pages 2, 14.*

[24] M. Zinser. “Search for new heavy charged bosons and measurement of high-mass Drell-Yan production in proton-proton collisions”. PhD thesis. Johannes Gutenberg-Universität Mainz, Aug. 2016 *Cited on pages 2, 16, 29, 33, 47, 59.*

[25] M. Becker. “Measurement of ZZ production and search for anomalous neutral triple gauge couplings in pp collisions at $\sqrt{s} = 13$ TeV with the ATLAS experiment”. PhD thesis. Johannes Gutenberg-Universität Mainz, Dec. 2017 *Cited on pages 2, 7, 47.*

[27] R. Caputo. “A Search for First Generation Leptoquarks at the ATLAS detector”. PhD thesis. Stony Brook University, Aug. 2011 *Cited on pages 7, 21.*

[28] A. Zannoni. “On the Quantization of the Monoatomic Ideal Gas”. In: *arXiv e-prints* (Dec. 1999). arXiv: `cond-mat/9912229 [cond-mat.stat-mech]` *Cited on page 7.*

[29] P. A. M. Dirac and R. H. Fowler. “On the theory of quantum mechanics”. In: *Proceedings of the Royal Society of London. Series A, Containing Papers of a Mathematical and Physical Character* 112 (Oct. 1926). DOI: `10.1098/rspa.1926.0133` *Cited on page 7.*

[30] M. Fukugita, M. Tanimoto, and T. Yanagida. “Atmospheric neutrino oscillation and a phenomenological lepton mass matrix”. In: *Phys. Rev.* D57 (1998), pp. 4429–4432. DOI: `10.1103/PhysRevD.57.4429`. arXiv: `hep-ph/9709388 [hep-ph]` *Cited on page 7.*

[31] LHCb Collaboration. “Observation of the resonant character of the $Z(4430)^-$ state”. In: *Phys. Rev. Lett.* 112.22 (2014), p. 222002. DOI: `10.1103/PhysRevLett.112.222002`. arXiv: `1404.1903 [hep-ex]` *Cited on page 8.*

[32] BESIII Collaboration. “Observation of a Charged Charmoniumlike Structure in $e^+e^- \to \pi^+\pi^-\ J/\psi$ at $\sqrt{s}$ =4.26 GeV”. In: *Phys. Rev. Lett.* 110 (2013), p. 252001. DOI: `10.1103/PhysRevLett.110.252001`. arXiv: `1303.5949 [hep-ex]` *Cited on page 8.*

[33] LHCb Collaboration. “Observation of $J/\psi p$ Resonances Consistent with Pentaquark States in $\Lambda_b^0 \to J/\psi K^- p$ Decays”. In: *Phys. Rev. Lett.* 115 (2015), p. 072001. DOI: 10.1103/PhysRevLett.115.072001. arXiv: 1507.03414 [hep-ex] *Cited on page 8.*

[34] M. Tanabashi et al. “Review of Particle Physics”. In: *Phys. Rev. D* 98 (3 Aug. 2018), p. 030001. DOI: 10.1103/PhysRevD.98.030001 *Cited on pages 8, 60.*

[35] Bose. “Plancks Gesetz und Lichtquantenhypothese”. In: *Zeitschrift für Physik* 26.1 (Dec. 1924), pp. 178–181. ISSN: 0044-3328. DOI: 10.1007/BF01327326 *Cited on page 8.*

[36] D. H. Perkins. *Introduction to High Energy Physics.* 4th ed. Cambridge University Press, 2000. DOI: 10.1017/CBO9780511809040 *Cited on page 8.*

[37] James Clerk Maxwell. *A Treatise on Electricity and Magnetism.* Vol. 1. Cambridge Library Collection - Physical Sciences. Cambridge University Press, 2010. DOI: 10.1017/CBO9780511709333 *Cited on page 8.*

[38] E. Fermi. “Versuch einer Theorie der β-Strahlen. I”. In: *Zeitschrift für Physik* 88.3 (Mar. 1934), pp. 161–177. ISSN: 0044-3328. DOI: 10.1007/BF01351864 *Cited on page 9.*

[39] H. Fritzsch, M. Gell-Mann, and H. Leutwyler. “Advantages of the color octet gluon picture”. In: *Physics Letters B* 47.4 (1973), pp. 365–368. ISSN: 0370-2693. DOI: doi.org/10.1016/0370-2693(73)90625-4 *Cited on page 9.*

[40] M. E. Peskin and D. V. Schroeder. *An Introduction to quantum field theory.* Reading, USA: Addison-Wesley, 1995. ISBN: 978-0-201-50397-5 *Cited on page 9.*

[41] F. Halzen and A. D. Martin. *Quarks and Leptons: An Introductory Course in Modern Particle Physics.* New York, USA: Wiley, 1984. ISBN: 978-0-471-88741-6 *Cited on page 9.*

[42] E. Noether. “Invariante Variationsprobleme”. In: *Nachrichten von der Gesellschaft der Wissenschaften zu Göttingen, Mathematisch-Physikalische Klasse* (1918). http://eudml.org/doc/59024, pp. 235–257 *Cited on page 10.*

[43] R. P. Feynman. “The Theory of Positrons”. In: *Phys. Rev.* 76 (6 Sept. 1949), pp. 749–759. DOI: 10.1103/PhysRev.76.749 *Cited on page 10.*

[44] E. Fermi. *Nuclear Physics: A Course Given by Enrico Fermi at the University of Chicago.* University Of Chicago Press, 1974. ISBN: 978-0-226-24365-8 *Cited on page 11.*

[45] A. Pich. “Quantum chromodynamics”. In: *High energy physics. Proceedings, 2nd European School, Sorrento, Italy, August 29-September 1, 1994. Vol. 1, 2.* 1995, pp. 157–207. arXiv: hep-ph/9505231 [hep-ph] *Cited on page 13.*

[46] D. Griffiths. *Introduction to Elementary Particles.* Wiley, Oct. 2008. ISBN: 978-3-527-40601-2 *Cited on page 13.*

[47] S. Weinberg. “A Model of Leptons”. In: *Phys. Rev. Lett.* 19 (21 Nov. 1967), pp. 1264–1266. DOI: 10.1103/PhysRevLett.19.1264 *Cited on page 13.*

[48] W. Hollik. “Electroweak Theory”. In: *Journal of Physics: Conference Series* 53 (Nov. 2006), pp. 7–43. DOI: 10.1088/1742-6596/53/1/002 *Cited on pages 13, 15.*

[49] E. D. Commins and P. H. Bucksbaum. *Weak Interactions of Leptons and Quarks.* Cambridge, USA: Univ. Pr., 1983. ISBN: 978-0-521-27370-1 *Cited on page 14.*

[50] S. Dawson. "Introduction to electroweak symmetry breaking". In: *Proceedings, Summer School in High-energy physics and cosmology: Trieste, Italy, June 29-July 17, 1998*. 1998, pp. 1–83. arXiv: `hep-ph/9901280 [hep-ph]` *Cited on page 14.*

[51] P.W. Higgs. "Broken symmetries, massless particles and gauge fields". In: *Physics Letters* 12.2 (1964), pp. 132–133. ISSN: 0031-9163. DOI: `doi.org/10.1016/0031-9163(64)91136-9` *Cited on page 15.*

[52] ATLAS Collaboration. "Observation of a new particle in the search for the Standard Model Higgs boson with the ATLAS detector at the LHC". In: *Phys. Lett.* B716 (2012), pp. 1–29. DOI: `10.1016/j.physletb.2012.08.020`. arXiv: `1207.7214 [hep-ex]` *Cited on page 15.*

[53] CMS Collaboration. "Observation of a new boson at a mass of 125 GeV with the CMS experiment at the LHC". In: *Phys. Lett.* B716 (2012), pp. 30–61. DOI: `10.1016/j.physletb.2012.08.021`. arXiv: `1207.7235 [hep-ex]` *Cited on page 15.*

[54] ATLAS Collaboration. "Measurement of the Higgs boson mass in the $H \rightarrow ZZ^* \rightarrow 4\ell$ and $H \rightarrow \gamma\gamma$ channels with $\sqrt{s}$=13TeV pp collisions using the ATLAS detector". In: (2017). ATLAS-CONF-2017-046 *Cited on page 15.*

[55] H. Yukawa. "Quantum Theory of Non-Local Fields. Part I. Free Fields". In: *Phys. Rev.* 77 (2 Jan. 1950), pp. 219–226. DOI: `10.1103/PhysRev.77.219` *Cited on page 16.*

References for Chapter 2: Proton-proton collisions

[56] T. Hülsing. "Probing Quantum Chromodynamics with the ATLAS Detector: Charged-Particle Event Shape Variables and the Dijet Cross-Section". PhD thesis. Johannes Gutenberg-Universität Mainz, Sept. 2014 *Cited on page 17.*

[57] S. D. Drell and T.-M. Yan. "Partons and their applications at high energies". In: *Annals of Physics* 66.2 (1971), pp. 578–623. ISSN: 0003-4916. DOI: `doi.org/10.1016/0003-4916(71)90071-6` *Cited on page 17.*

[58] G. Altarelli and G. Parisi. "Asymptotic freedom in parton language". In: *Nuclear Physics B* 126.2 (1977), pp. 298–318. ISSN: 0550-3213. DOI: `doi.org/10.1016/0550-3213(77)90384-4` *Cited on page 18.*

[59] C. Adloff et al. "Measurement of neutral and charged current cross-sections in positron proton collisions at large momentum transfer". In: *Eur. Phys. J.* C13 (2000), pp. 609–639. DOI: `10.1007/s100520000316`. arXiv: `hep-ex/9908059 [hep-ex]` *Cited on page 18.*

[60] S. Chekanov et al. "Measurement of the neutral current cross-section and F(2) structure function for deep inelastic e + p scattering at HERA". In: *Eur. Phys. J.* C21 (2001), pp. 443–471. DOI: `10.1007/s100520100749`. arXiv: `hep-ex/0105090 [hep-ex]` *Cited on page 18.*

[61] L. N. Lipatov. "The parton model and perturbation theory". In: *Sov. J. Nucl. Phys.* 20 (1975). [Yad. Fiz.20,181(1974)], pp. 94–102 *Cited on page 18.*

[62] V. N. Gribov and L. N. Lipatov. "Deep inelastic e p scattering in perturbation theory". In: *Sov. J. Nucl. Phys.* 15 (1972). [Yad. Fiz.15,781(1972)], pp. 438–450 *Cited on page 18.*

[63] Y. L. Dokshitzer. “Calculation of the Structure Functions for Deep Inelastic Scattering and e+ e- Annihilation by Perturbation Theory in Quantum Chromodynamics.” In: *Sov. Phys. JETP* 46 (1977). [Zh. Eksp. Teor. Fiz.73,1216(1977)], pp. 641–653 *Cited on page 18.*

[64] A. D. Martin et al. “Parton distributions for the LHC”. In: *Eur. Phys. J.* C63 (2009), pp. 189–285. DOI: `10.1140/epjc/s10052-009-1072-5`. arXiv: `0901.0002 [hep-ph]` *Cited on pages 19, 64.*

[65] J. Stirling. *MSTW PDFs: key plots.* `https://mstwpdf.hepforge.org/plots/plots.html` *Cited on page 18.*

[66] F. Siegert. “Monte-Carlo event generation for the LHC”. `http://etheses.dur.ac.uk/484/`. PhD thesis. Durham University, Sept. 2010 *Cited on page 20.*

References for Chapter 3: Beyond the Standard Model

[27] R. Caputo. “A Search for First Generation Leptoquarks at the ATLAS detector”. PhD thesis. Stony Brook University, Aug. 2011 *Cited on pages 7, 21.*

[67] S. Davidson, D. C. Bailey, and B. A. Campbell. “Model independent constraints on leptoquarks from rare processes”. In: *Z. Phys.* C61 (1994), pp. 613–644. DOI: `10.1007/BF01552629`. arXiv: `hep-ph/9309310 [hep-ph]` *Cited on pages 22, 24.*

[68] M. Kramer et al. “Pair production of scalar leptoquarks at the CERN LHC”. In: *Phys. Rev.* D71 (2005), p. 057503. DOI: `10.1103/PhysRevD.71.057503`. arXiv: `hep-ph/0411038 [hep-ph]` *Cited on pages 22, 25.*

[69] J. Blümlein and R. Rückl. “Production of scalar and vector leptoquarks in e+e- annihilation”. In: *Physics Letters B* 304.3 (1993), pp. 337–346. ISSN: 0370-2693. DOI: `doi.org/10.1016/0370-2693(93)90306-3` *Cited on page 22.*

[70] D. E. Acosta and S. K. Blessing. “Leptoquark Searches at HERA and the Tevatron”. In: *Annual Review of Nuclear and Particle Science* 49.1 (1999), pp. 389–434. DOI: `10.1146/annurev.nucl.49.1.389` *Cited on page 23.*

[71] J. C. Pati and A. Salam. “Lepton Number as the Fourth Color”. In: *Phys. Rev.* D10 (1974). [Erratum: Phys. Rev.D11,703(1975)], pp. 275–289. DOI: `10.1103/PhysRevD.10.275,10.1103/PhysRevD.11.703.2` *Cited on pages 24, 59.*

[72] H. Georgi and S. L. Glashow. “Unity of All Elementary-Particle Forces”. In: *Phys. Rev. Lett.* 32 (8 Feb. 1974), pp. 438–441. DOI: `10.1103/PhysRevLett.32.438` *Cited on pages 24, 59.*

[73] E. Witten. “Symmetry breaking patterns in superstring models”. In: *Nuclear Physics B* 258 (1985), pp. 75–100. ISSN: 0550-3213. DOI: `doi.org/10.1016/0550-3213(85)90603-0` *Cited on page 24.*

[74] M. Dine et al. “Superstring model building”. In: *Nuclear Physics B* 259.4 (1985), pp. 549–571. ISSN: 0550-3213. DOI: `doi.org/10.1016/0550-3213(85)90001-X` *Cited on page 24.*

[75] J. L. Hewett and T. G. Rizzo. “Much ado about leptoquarks: A Comprehensive analysis”. In: *Phys. Rev.* D56 (1997), pp. 5709–5724. DOI: `10.1103/PhysRevD.56.5709`. arXiv: `hep-ph/9703337 [hep-ph]` *Cited on pages 24, 59.*

[76] K. Lane. “Two lectures on technicolor”. In: (2002). arXiv: `hep-ph/0202255 [hep-ph]` *Cited on page 24.*

[77] W. Buchmüller, R. Rückl, and D. Wyler. “Leptoquarks in lepton-quark collisions”. In: *Physics Letters B* 191.4 (1987), pp. 442–448. ISSN: 0370-2693. DOI: `10.1016/0370-2693(87)90637-X` *Cited on pages 26, 59.*

[78] V. A. Mitsou et al. “Prospects for scalar leptoquark discovery at the LHC”. In: *Czech. J. Phys.* 55 (2005), B659–B666. arXiv: `hep-ph/0411189 [hep-ph]` *Cited on pages 26, 60.*

[79] D. Milstead et al. *Search for first and second generation scalar leptoquarks in pp collisions at $\sqrt{s}$ = 13 TeV with the ATLAS detector at the LHC.* Tech. rep. ATL-COM-PHYS-2016-1690. `https://cds.cern.ch/record/2234245` (Internal documentation). Nov. 2016 *Cited on pages 26, 64, 67, 71, 72, 78.*

References for Chapter 4: The Large Hadron Collider

[23] R. Pöttgen. “Search for Dark Matter in events with a highly energetic jet and missing transverse momentum in proton-proton collisions at $\sqrt{s} = 8$ TeV with the ATLAS Detector”. PhD thesis. Johannes Gutenberg-Universität Mainz, Oct. 2014 *Cited on pages 2, 31, 46.*

[24] M. Zinser. “Search for new heavy charged bosons and measurement of high-mass Drell-Yan production in proton-proton collisions”. PhD thesis. Johannes Gutenberg-Universität Mainz, Aug. 2016 *Cited on pages 2, 16, 29, 33, 47, 59.*

[26] S. Schmitz. “Search for New Resonances in Lepton-Antilepton Final States in Proton-Proton Collisions at $\sqrt{s}$ = 13 TeV with the ATLAS Experiment”. PhD thesis. Johannes Gutenberg-Universität Mainz, May 2018 *Cited on pages 2, 31, 33, 35, 47, 66.*

[80] L. Evans and P. Bryant. “LHC Machine”. In: *Journal of Instrumentation* 3.08 (Aug. 2008), S08001–S08001. DOI: `10.1088/1748-0221/3/08/s08001` *Cited on page 29.*

[81] O. Endner. “Search for New Physics using Jets in Proton-Proton Collisions”. PhD thesis. Johannes Gutenberg-Universität Mainz, Dec. 2015 *Cited on pages 30, 55.*

[82] G. Papotti. *Lessons learnt in LHC operation in 2015.* `https://indico.cern.ch/event/448109/contributions/1942059/attachments/1216261/1793941/2015overview_paper.pdf`. 2016 *Cited on page 31.*

[83] D. Nisbet. *LHC Operation in 2016.* `https://indico.cern.ch/event/580313/contributions/2359285/attachments/1396590/2135891/Operation_in_2016_v1_1.pdf`. 2016 *Cited on page 31.*

[84] ATLAS Collaboration. “The ATLAS Experiment at the CERN Large Hadron Collider”. In: *Journal of Instrumentation* 3.08 (Aug. 2008), S08003–S08003. DOI: `10.1088/1748-0221/3/08/s08003` *Cited on pages 31, 33.*

[85] CMS Collaboration. “The CMS experiment at the CERN LHC”. In: *Journal of Instrumentation* 3.08 (Aug. 2008), S08004–S08004. DOI: `10.1088/1748-0221/3/08/s08004` *Cited on page 31.*

[86] LHCb Collaboration. “The LHCb Detector at the LHC”. In: *Journal of Instrumentation* 3.08 (Aug. 2008), S08005–S08005. DOI: `10.1088/1748-0221/3/08/s08005` *Cited on pages 31, 111.*

[87] ALICE Collaboration. “The ALICE experiment at the CERN LHC”. In: *Journal of Instrumentation* 3.08 (Aug. 2008), S08002–S08002. DOI: `10.1088/1748-0221/3/08/s08002` *Cited on page 31.*

[88] TOTEM Collaboration. “The TOTEM Experiment at the CERN Large Hadron Collider”. In: *Journal of Instrumentation* 3.08 (Aug. 2008), S08007–S08007. DOI: 10.1088/1748-0221/3/08/s08007 *Cited on page 31.*

[89] LHCf Collaboration. “The LHCf detector at the CERN Large Hadron Collider”. In: *Journal of Instrumentation* 3.08 (Aug. 2008), S08006–S08006. DOI: 10.1088/1748-0221/3/08/s08006 *Cited on page 31.*

[90] J. Pinfold et al. *Technical Design Report of the MoEDAL Experiment*. Tech. rep. CERN-LHCC-2009-006. MoEDAL-TDR-001. https://cds.cern.ch/record/1181486. June 2009 *Cited on page 31.*

References for Chapter 5: The ATLAS experiment

[23] R. Pöttgen. “Search for Dark Matter in events with a highly energetic jet and missing transverse momentum in proton-proton collisions at $\sqrt{s} = 8$ TeV with the ATLAS Detector”. PhD thesis. Johannes Gutenberg-Universität Mainz, Oct. 2014 *Cited on pages 2, 31, 46.*

[24] M. Zinser. “Search for new heavy charged bosons and measurement of high-mass Drell-Yan production in proton-proton collisions”. PhD thesis. Johannes Gutenberg-Universität Mainz, Aug. 2016 *Cited on pages 2, 16, 29, 33, 47, 59.*

[25] M. Becker. “Measurement of ZZ production and search for anomalous neutral triple gauge couplings in pp collisions at $\sqrt{s} = 13$ TeV with the ATLAS experiment”. PhD thesis. Johannes Gutenberg-Universität Mainz, Dec. 2017 *Cited on pages 2, 7, 47.*

[26] S. Schmitz. “Search for New Resonances in Lepton-Antilepton Final States in Proton-Proton Collisions at $\sqrt{s} = 13$ TeV with the ATLAS Experiment”. PhD thesis. Johannes Gutenberg-Universität Mainz, May 2018 *Cited on pages 2, 31, 33, 35, 47, 66.*

[81] O. Endner. “Search for New Physics using Jets in Proton-Proton Collisions”. PhD thesis. Johannes Gutenberg-Universität Mainz, Dec. 2015 *Cited on pages 30, 55.*

[84] ATLAS Collaboration. “The ATLAS Experiment at the CERN Large Hadron Collider”. In: *Journal of Instrumentation* 3.08 (Aug. 2008), S08003–S08003. DOI: 10.1088/1748-0221/3/08/s08003 *Cited on pages 31, 33.*

[91] CERN. *Computer generated image of the whole ATLAS detector*. CERN Document server. https://mediastream.cern.ch/MediaArchive/Photo/Public/2008/0803012/0803012_01/0803012_01-A4-at-144-dpi.jpg. 2008 *Cited on page 33.*

[92] E. Scifo. “Measurement of the Brout-Englert-Higgs boson couplings in its diphoton decay channel with the ATLAS detector at the LHC”. PhD thesis. Université Paris-Sud, July 2014 *Cited on page 34.*

[93] S. Haywood et al. *ATLAS inner detector: Technical Design Report, 2*. Technical Design Report ATLAS. http://cds.cern.ch/record/331064. Geneva: CERN, 1997 *Cited on page 36.*

[94] *ATLAS central solenoid: Technical Design Report*. Technical Design Report ATLAS. https://cds.cern.ch/record/331067. Geneva: CERN, 1997 *Cited on page 36.*

[95] CERN. *Computer generated image of the ATLAS inner detector*. CERN Document server. https://mediastream.cern.ch/MediaArchive/Photo/Public/2008/0803014/0803014_01/0803014_01-A4-at-144-dpi.jpg. 2008 *Cited on page 37.*

[96] K. Potamianos. “The upgraded Pixel detector and the commissioning of the Inner Detector tracking of the ATLAS experiment for Run-2 at the Large Hadron Collider”. In: *PoS* EPS-HEP2015 (2015), p. 261. arXiv: `1608.07850 [physics.ins-det]` *Cited on page 37.*

[97] N. Wermes and G. Hallewel. *ATLAS pixel detector: Technical Design Report*. Technical Design Report ATLAS. `https://cds.cern.ch/record/381263`. Geneva: CERN, 1998 *Cited on page 36.*

[98] M. Capeans et al. *ATLAS Insertable B-Layer Technical Design Report*. Tech. rep. CERN-LHCC-2010-013. ATLAS-TDR-19. `http://cds.cern.ch/record/1291633`. Sept. 2010 *Cited on page 37.*

[99] CERN. *Computer Generated image of the ATLAS calorimeter*. CERN Document server. `https://mediastream.cern.ch/MediaArchive/Photo/Public/2008/0803015/0803015_01/0803015_01-A4-at-144-dpi.jpg`. 2008 *Cited on page 39.*

[100] *ATLAS liquid-argon calorimeter: Technical Design Report*. Technical Design Report ATLAS. `https://cds.cern.ch/record/331061`. Geneva: CERN, 1996 *Cited on pages 38, 129.*

[101] *ATLAS calorimeter performance: Technical Design Report*. Technical Design Report ATLAS. `https://cds.cern.ch/record/331059`. Geneva: CERN, 1996 *Cited on page 38.*

[102] ATLAS Collaboration. “Electron and photon energy calibration with the ATLAS detector using LHC Run 1 data”. In: *Eur. Phys. J.* C74.10 (2014), p. 3071. DOI: `10.1140/epjc/s10052-014-3071-4`. arXiv: `1407.5063 [hep-ex]` *Cited on page 39.*

[103] *ATLAS tile calorimeter: Technical Design Report*. Technical Design Report ATLAS. `https://cds.cern.ch/record/331062`. Geneva: CERN, 1996 *Cited on page 40.*

[104] A. Artamonov et al. “The ATLAS Forward Calorimeter”. In: *Journal of Instrumentation* 3.02 (Feb. 2008), P02010–P02010. DOI: `10.1088/1748-0221/3/02/p02010` *Cited on page 40.*

[105] *ATLAS muon spectrometer: Technical Design Report*. Technical Design Report ATLAS. `https://cds.cern.ch/record/331068`. Geneva: CERN, 1997 *Cited on page 40.*

[106] *ATLAS magnet system: Technical Design Report, 1*. Technical Design Report ATLAS. `https://cds.cern.ch/record/338080`. Geneva: CERN, 1997 *Cited on page 40.*

[107] J. P. Badiou et al. *ATLAS barrel toroid: Technical Design Report*. Technical Design Report ATLAS. `https://cds.cern.ch/record/331065`. Geneva: CERN, 1997 *Cited on page 40.*

[108] *ATLAS end-cap toroids: Technical Design Report*. Technical Design Report ATLAS. `https://cds.cern.ch/record/331066`. Geneva: CERN, 1997 *Cited on page 40.*

[109] CERN. *Computer generated image of the ATLAS Muons subsystem*. CERN Document server. `https://mediastream.cern.ch/MediaArchive/Photo/Public/2008/0803017/0803017_01/0803017_01-A4-at-144-dpi.jpg`. 2008 *Cited on page 41.*

[110] *ATLAS level-1 trigger: Technical Design Report*. Technical Design Report ATLAS. `http://cds.cern.ch/record/381429`. Geneva: CERN, 1998 *Cited on page 42.*

[111] P. Jenni et al. *ATLAS high-level trigger, data-acquisition and controls: Technical Design Report*. Technical Design Report ATLAS. `http://cds.cern.ch/record/616089`. Geneva: CERN, 2003 *Cited on page 42.*

[112] ATLAS Collaboration. “Performance of the ATLAS Trigger System in 2015”. In: *Eur. Phys. J.* C77.5 (2017), p. 317. DOI: `10.1140/epjc/s10052-017-4852-3`. arXiv: `1611.09661 [hep-ex]` *Cited on pages 43, 66.*

[113] G. Lehmann Miotto et al. “Configuration and control of the ATLAS trigger and data acquisition”. In: *Nuclear Instruments and Methods in Physics Research Section A: Accelerators, Spectrometers, Detectors and Associated Equipment* 623.1 (2010). 1st International Conference on Technology and Instrumentation in Particle Physics, pp. 549–551. ISSN: 0168-9002. DOI: `doi.org/10.1016/j.nima.2010.03.066` *Cited on page 44.*

[114] C. Eck et al. *LHC computing Grid: Technical Design Report. Version 1.06 (20 Jun 2005)*. Technical Design Report LCG. `https://cds.cern.ch/record/840543`. Geneva: CERN, 2005 *Cited on page 44.*

[115] R.W.L. Jones. “ATLAS computing and the GRID”. In: *Nuclear Instruments and Methods in Physics Research Section A: Accelerators, Spectrometers, Detectors and Associated Equipment* 502.2 (2003). Proceedings of the VIII International Workshop on Advanced Computing and Analysis Techniques in Physics Research, pp. 372–375. ISSN: 0168-9002. DOI: `doi.org/10.1016/S0168-9002(03)00446-7` *Cited on page 44.*

[116] R. Brun and F. Rademakers. “ROOT — An object oriented data analysis framework”. In: *Nuclear Instruments and Methods in Physics Research Section A: Accelerators, Spectrometers, Detectors and Associated Equipment* 389.1 (1997). New Computing Techniques in Physics Research V, pp. 81–86. ISSN: 0168-9002. DOI: `doi.org/10.1016/S0168-9002(97)00048-X` *Cited on page 44.*

[117] High Performance Computing Group. Johannes Gutenberg-Universität Mainz. `https://hpc.uni-mainz.de/` *Cited on page 45.*

[118] ATLAS Collaboration. “Improved luminosity determination in pp collisions at sqrt(s) = 7 TeV using the ATLAS detector at the LHC”. In: *Eur. Phys. J.* C73.8 (2013), p. 2518. DOI: `10.1140/epjc/s10052-013-2518-3`. arXiv: `1302.4393 [hep-ex]` *Cited on page 45.*

[119] P. Jenni et al. “ATLAS Forward Detectors for Measurement of Elastic Scattering and Luminosity”. In: (2008) *Cited on page 45.*

[120] V. Balagura. “Notes on van der Meer Scan for Absolute Luminosity Measurement”. In: *Nucl. Instrum. Meth.* A654 (2011), pp. 634–638. DOI: `10.1016/j.nima.2011.06.007`. arXiv: `1103.1129 [physics.ins-det]` *Cited on page 45.*

[121] ATLAS Luminosity Group. *LuminosityForPhysics*. TWiki page. `https://twiki.cern.ch/twiki/bin/viewauth/Atlas/LuminosityForPhysics` (Internal documentation). 2018 *Cited on pages 45, 62, 73.*

[122] ATLAS Experiment - public results. *Data Quality Information for Data*. TWiki page. `https://twiki.cern.ch/twiki/bin/view/AtlasPublic/RunStatsPublicResults2010`. 2018 *Cited on page 46.*

[123] S. Agostinelli et al. “GEANT4: A Simulation toolkit”. In: *Nuclear Instruments and Methods in Physics Research Section A: Accelerators, Spectrometers, Detectors and Associated Equipment* 506.3 (2003), pp. 250–303. ISSN: 0168-9002. DOI: `10.1016/S0168-9002(03)01368-8` *Cited on pages 46, 64.*

[124] Z. Marshall. “Simulation of Pile-up in the ATLAS Experiment”. In: *Journal of Physics: Conference Series* 513.2 (June 2014), p. 022024. DOI: `10.1088/1742-6596/513/2/022024` *Cited on page 46.*

[125] ATLAS Public Results. *LuminosityPublicResultsRun2*. TWiki page. `https://twiki.cern.ch/twiki/bin/view/AtlasPublic/LuminosityPublicResultsRun2`. 2018 *Cited on pages 46, 63.*

[126] T. Cornelissen et al. *Concepts, Design and Implementation of the ATLAS New Tracking (NEWT)*. Tech. rep. ATL-SOFT-PUB-2007-007. ATL-COM-SOFT-2007-002. `https://cds.cern.ch/record/1020106`. Mar. 2007 *Cited on page 47.*

[127] R. Frühwirth. "Application of Kalman filtering to track and vertex fitting". In: *Nuclear Instruments and Methods in Physics Research Section A: Accelerators, Spectrometers, Detectors and Associated Equipment* 262.2 (1987), pp. 444–450. ISSN: 0168-9002. DOI: `doi.org/10.1016/0168-9002(87)90887-4` *Cited on page 47.*

[128] ATLAS Collaboration. "Performance of the ATLAS Track Reconstruction Algorithms in Dense Environments in LHC Run 2". In: *Eur. Phys. J.* C77.10 (2017), p. 673. DOI: `10.1140/epjc/s10052-017-5225-7`. arXiv: `1704.07983 [hep-ex]` *Cited on page 48.*

[129] ATLAS Collaboration. *Vertex Reconstruction Performance of the ATLAS Detector at $\sqrt{s}$ = 13 TeV*. Tech. rep. ATL-PHYS-PUB-2015-026. `https://cds.cern.ch/record/2037717`. July 2015 *Cited on page 48.*

[130] ATLAS Collaboration. *Electron efficiency measurements with the ATLAS detector using the 2015 LHC proton-proton collision data*. Tech. rep. ATLAS-CONF-2016-024. `https://cds.cern.ch/record/2157687`. June 2016 *Cited on pages 48, 67.*

[131] W. Lampl et al. *Calorimeter Clustering Algorithms: Description and Performance*. Tech. rep. ATL-LARG-PUB-2008-002. ATL-COM-LARG-2008-003. `http://cds.cern.ch/record/1099735`. Apr. 2008 *Cited on page 48.*

[132] T. G. Cornelissen et al. "The global χ^2 track fitter in ATLAS". In: *Journal of Physics: Conference Series* 119.3 (July 2008), p. 032013. DOI: `10.1088/1742-6596/119/3/032013` *Cited on page 49.*

[133] ATLAS Collaboration. *Improved electron reconstruction in ATLAS using the Gaussian Sum Filter-based model for bremsstrahlung*. Tech. rep. ATLAS-CONF-2012-047. `https://cds.cern.ch/record/1449796`. May 2012 *Cited on page 49.*

[134] ATLAS Collaboration. *Electron and photon energy calibration with the ATLAS detector using data collected in 2015 at* $\sqrt{s} = 13$ TeV. Tech. rep. ATL-PHYS-PUB-2016-015. `http://cds.cern.ch/record/2203514`. Aug. 2016 *Cited on page 51.*

[135] ATLAS Collaboration. "Muon reconstruction performance of the ATLAS detector in proton–proton collision data at $\sqrt{s}$ =13 TeV". In: *Eur. Phys. J.* C76.5 (2016), p. 292. DOI: `10.1140/epjc/s10052-016-4120-y`. arXiv: `1603.05598 [hep-ex]` *Cited on pages 51, 54, 67, 68, 73.*

[136] J. Illingworth and J. Kittler. "A survey of the Hough Transform". In: *Computer Vision, Graphics, and Image Processing* 44.1 (1988), pp. 87–116. ISSN: 0734-189X. DOI: `doi.org/10.1016/S0734-189X(88)80033-1` *Cited on page 51.*

[137] ATLAS Collaboration. "Measurements of Higgs boson production and couplings in the four-lepton channel in pp collisions at center-of-mass energies of 7 and 8 TeV with the ATLAS detector". In: *Phys. Rev.* D91.1 (2015), p. 012006. DOI: `10.1103/PhysRevD.91.012006`. arXiv: `1408.5191 [hep-ex]` *Cited on page 53.*

[138] ATLAS Collaboration. "Search for high-mass dilepton resonances in pp collisions at $\sqrt{s} = 8$ TeV with the ATLAS detector". In: *Phys. Rev.* D90.5 (2014), p. 052005. DOI: `10.1103/PhysRevD.90.052005`. arXiv: `1405.4123 [hep-ex]` *Cited on page 54.*

[139] ATLAS Collaboration. "Search for new particles in events with one lepton and missing transverse momentum in *pp* collisions at $\sqrt{s} = 8$ TeV with the ATLAS detector". In: *JHEP* 09 (2014), p. 037. DOI: `10.1007/JHEP09(2014)037`. arXiv: `1407.7494 [hep-ex]` *Cited on page 54.*

[140] ATLAS Collaboration. "Jet energy measurement with the ATLAS detector in proton-proton collisions at $\sqrt{s} = 7$ TeV". In: *Eur. Phys. J.* C73.3 (2013), p. 2304. DOI: `10.1140/epjc/s10052-013-2304-2`. arXiv: `1112.6426 [hep-ex]` *Cited on page 54.*

[141] A. Hrynevich. "ATLAS jet and missing energy reconstruction, calibration and performance in LHC Run-2". In: *Journal of Instrumentation* 12.06 (June 2017), pp. C06038–C06038. DOI: `10.1088/1748-0221/12/06/c06038` *Cited on pages 54, 56.*

[142] M. Cacciari, G. P. Salam, and G. Soyez. "The anti-k_t jet clustering algorithm". In: *JHEP* 04 (2008), p. 063. DOI: `10.1088/1126-6708/2008/04/063`. arXiv: `0802.1189 [hep-ph]` *Cited on pages 54, 68.*

[143] ATLAS Collaboration. "Jet reconstruction and performance using particle flow with the ATLAS Detector". In: *Eur. Phys. J.* C77.7 (2017), p. 466. DOI: `10.1140/epjc/s10052-017-5031-2`. arXiv: `1703.10485 [hep-ex]` *Cited on page 55.*

[144] ATLAS Collaboration. "Jet energy measurement and its systematic uncertainty in proton-proton collisions at $\sqrt{s} = 7$ TeV with the ATLAS detector". In: *Eur. Phys. J.* C75 (2015), p. 17. DOI: `10.1140/epjc/s10052-014-3190-y`. arXiv: `1406.0076 [hep-ex]` *Cited on page 55.*

[145] ATLAS Collaboration. "Topological cell clustering in the ATLAS calorimeters and its performance in LHC Run 1". In: *Eur. Phys. J.* C77 (2017), p. 490. DOI: `10.1140/epjc/s10052-017-5004-5`. arXiv: `1603.02934 [hep-ex]` *Cited on page 55.*

[146] ATLAS Collaboration. *Data-driven determination of the energy scale and resolution of jets reconstructed in the ATLAS calorimeters using dijet and multijet events at $\sqrt{s} = 8$ TeV*. Tech. rep. ATLAS-CONF-2015-017. `https://cds.cern.ch/record/2008678`. Apr. 2015 *Cited on page 55.*

[147] T. H. Park. "Jet energy resolution measurement of the ATLAS detector using momentum balance". MA thesis. Carleton University, Aug. 2018 *Cited on page 55.*

[148] ATLAS Collaboration. *Jet Calibration and Systematic Uncertainties for Jets Reconstructed in the ATLAS Detector at $\sqrt{s} = 13$ TeV*. Tech. rep. ATL-PHYS-PUB-2015-015. `https://cds.cern.ch/record/2037613`. July 2015 *Cited on page 55.*

[149] ATLAS Collaboration. "Performance of algorithms that reconstruct missing transverse momentum in $\sqrt{s} = 8$ TeV proton-proton collisions in the ATLAS detector". In: *Eur. Phys. J.* C77.4 (2017), p. 241. DOI: `10.1140/epjc/s10052-017-4780-2`. arXiv: `1609.09324 [hep-ex]` *Cited on page 56.*

[150] ATLAS Collaboration. "Performance of pile-up mitigation techniques for jets in *pp* collisions at $\sqrt{s} = 8$ TeV using the ATLAS detector". In: *Eur. Phys. J.* C76.11 (2016), p. 581. DOI: `10.1140/epjc/s10052-016-4395-z`. arXiv: `1510.03823 [hep-ex]` *Cited on page 56.*

[151] ATLAS Collaboration. *Forward Jet Vertex Tagging: A new technique for the identification and rejection of forward pileup jets*. Tech. rep. ATL-PHYS-PUB-2015-034. `https://cds.cern.ch/record/2042098`. Aug. 2015 *Cited on page 56.*

References for Chapter 6: Motivation

[24] M. Zinser. “Search for new heavy charged bosons and measurement of high-mass Drell-Yan production in proton-proton collisions”. PhD thesis. Johannes Gutenberg-Universität Mainz, Aug. 2016 *Cited on pages 2, 16, 29, 33, 47, 59.*

[34] M. Tanabashi et al. “Review of Particle Physics”. In: *Phys. Rev. D* 98 (3 Aug. 2018), p. 030001. DOI: `10.1103/PhysRevD.98.030001` *Cited on pages 8, 60.*

[71] J. C. Pati and A. Salam. “Lepton Number as the Fourth Color”. In: *Phys. Rev.* D10 (1974). [Erratum: Phys. Rev.D11,703(1975)], pp. 275–289. DOI: `10.1103/PhysRevD.10.275,10.1103/PhysRevD.11.703.2` *Cited on pages 24, 59.*

[72] H. Georgi and S. L. Glashow. “Unity of All Elementary-Particle Forces”. In: *Phys. Rev. Lett.* 32 (8 Feb. 1974), pp. 438–441. DOI: `10.1103/PhysRevLett.32.438` *Cited on pages 24, 59.*

[75] J. L. Hewett and T. G. Rizzo. “Much ado about leptoquarks: A Comprehensive analysis”. In: *Phys. Rev.* D56 (1997), pp. 5709–5724. DOI: `10.1103/PhysRevD.56.5709`. arXiv: `hep-ph/9703337 [hep-ph]` *Cited on pages 24, 59.*

[77] W. Buchmüller, R. Rückl, and D. Wyler. “Leptoquarks in lepton-quark collisions”. In: *Physics Letters B* 191.4 (1987), pp. 442–448. ISSN: 0370-2693. DOI: `10.1016/0370-2693(87)90637-X` *Cited on pages 26, 59.*

[78] V. A. Mitsou et al. “Prospects for scalar leptoquark discovery at the LHC”. In: *Czech. J. Phys.* 55 (2005), B659–B666. arXiv: `hep-ph/0411189 [hep-ph]` *Cited on pages 26, 60.*

[152] S. Dimopoulos and L. Susskind. “Mass without scalars”. In: *Nuclear Physics B* 155.1 (1979), pp. 237–252. ISSN: 0550-3213. DOI: `10.1016/0550-3213(79)90364-X` *Cited on page 59.*

[153] S. Dimopoulos. “Technicoloured signatures”. In: *Nuclear Physics B* 168.1 (1980), pp. 69–92. ISSN: 0550-3213. DOI: `10.1016/0550-3213(80)90277-1` *Cited on page 59.*

[154] E. Eichten and K. Lane. “Dynamical breaking of weak interaction symmetries”. In: *Physics Letters B* 90.1 (1980), pp. 125–130. ISSN: 0370-2693. DOI: `10.1016/0370-2693(80)90065-9` *Cited on page 59.*

[155] V.D. Angelopoulos et al. “Search for new quarks suggested by the superstring”. In: *Nuclear Physics B* 292 (1987), pp. 59–92. ISSN: 0550-3213. DOI: `10.1016/0550-3213(87)90637-7` *Cited on page 59.*

[156] W. Buchmüller and D. Wyler. “Constraints on SU(5)-type leptoquarks”. In: *Physics Letters B* 177.3 (1986), pp. 377–382. ISSN: 0370-2693. DOI: `10.1016/0370-2693(86)90771-9` *Cited on page 59.*

[157] B. Diaz, M. Schmaltz, and Y.-M. Zhong. “The leptoquark Hunter’s guide: Pair production”. In: *JHEP* 10 (2017), p. 097. DOI: `10.1007/JHEP10(2017)097`. arXiv: `1706.05033 [hep-ph]` *Cited on page 59.*

[158] B. Gripaios, M. Nardecchia, and S. A. Renner. “Composite leptoquarks and anomalies in *B*-meson decays”. In: *JHEP* 05 (2015), p. 006. DOI: `10.1007/JHEP05(2015)006`. arXiv: `1412.1791 [hep-ph]` *Cited on page 59.*

[159] J. M. Cline. “B decay anomalies and dark matter from vectorlike confinement”. In: *Phys. Rev.* D97.1 (2018), p. 015013. DOI: `10.1103/PhysRevD.97.015013`. arXiv: `1710.02140 [hep-ph]` *Cited on page 59.*

[160] L. Di Luzio and M. Nardecchia. “What is the scale of new physics behind the B-flavour anomalies?” In: *Eur. Phys. J.* C77.8 (2017), p. 536. DOI: `10.1140/epjc/s10052-017-5118-9`. arXiv: `1706.01868 [hep-ph]` *Cited on page 59.*

[161] B. Schrempp and F. Schrempp. “Light leptoquarks”. In: *Physics Letters B* 153.1 (1985), pp. 101–107. ISSN: 0370-2693. DOI: `10.1016/0370-2693(85)91450-9` *Cited on page 59.*

[162] A. Belyaev et al. “Leptoquark single and pair production at LHC with CalcHEP/CompHEP in the complete model”. In: *JHEP* 09 (2005), p. 005. DOI: `10.1088/1126-6708/2005/09/005`. arXiv: `hep-ph/0502067 [hep-ph]` *Cited on pages 59, 63.*

[163] ATLAS Collaboration. “Searches for scalar leptoquarks and differential cross-section measurements in dilepton-dijet events in proton-proton collisions at a centre-of-mass energy of $\sqrt{s} = 13$ TeV with the ATLAS experiment”. In: *Eur. Phys. J.* C79.9 (2019), p. 733. DOI: `10.1140/epjc/s10052-019-7181-x`. arXiv: `1902.00377 [hep-ex]` *Cited on pages 60, 61, 63, 68, 69, 108.*

[164] ATLAS Collaboration. “Search for pair production of first or second generation leptoquarks in proton-proton collisions at $\sqrt{s} = 7$ TeV using the ATLAS detector at the LHC”. In: *Phys. Rev.* D83 (2011), p. 112006. DOI: `10.1103/PhysRevD.83.112006`. arXiv: `1104.4481 [hep-ex]` *Cited on page 60.*

[165] ATLAS Collaboration. “Search for first generation scalar leptoquarks in pp collisions at $\sqrt{s} = 7$ TeV with the ATLAS detector”. In: *Phys. Lett.* B709 (2012). [Erratum: *Phys. Lett.* B711,442 (2012)], pp. 158–176. DOI: `10.1016/j.physletb.2012.03.023,10.1016/j.physletb.2012.02.004`. arXiv: `1112.4828 [hep-ex]` *Cited on page 60.*

[166] ATLAS Collaboration. “Search for second generation scalar leptoquarks in pp collisions at $\sqrt{s} = 7$ TeV with the ATLAS detector”. In: *Eur. Phys. J.* C72 (2012), p. 2151. DOI: `10.1140/epjc/s10052-012-2151-6`. arXiv: `1203.3172 [hep-ex]` *Cited on page 60.*

[167] ATLAS Collaboration. “Searches for scalar leptoquarks in pp collisions at $\sqrt{s} = 8$ TeV with the ATLAS detector”. In: *Eur. Phys. J.* C76.1 (2016), p. 5. DOI: `10.1140/epjc/s10052-015-3823-9`. arXiv: `1508.04735 [hep-ex]` *Cited on page 60.*

[168] ATLAS Collaboration. “Search for scalar leptoquarks in pp collisions at $\sqrt{s} = 13$ TeV with the ATLAS experiment”. In: *New J. Phys.* 18.9 (2016), p. 093016. DOI: `10.1088/1367-2630/18/9/093016`. arXiv: `1605.06035 [hep-ex]` *Cited on pages 60, 61, 108.*

[169] CMS Collaboration. “Search for Pair Production of First-Generation Scalar Leptoquarks in pp Collisions at $\sqrt{s} = 7$ TeV”. In: *Phys. Rev. Lett.* 106 (2011), p. 201802. DOI: `10.1103/PhysRevLett.106.201802`. arXiv: `1012.4031 [hep-ex]` *Cited on page 60.*

[170] CMS Collaboration. “Search for First Generation Scalar Leptoquarks in the $e\nu$jj channel in pp collisions at $\sqrt{s} = 7$ TeV”. In: *Phys. Lett.* B703 (2011), pp. 246–266. DOI: `10.1016/j.physletb.2011.07.089`. arXiv: `1105.5237 [hep-ex]` *Cited on page 60.*

[171] CMS Collaboration. "Search for Pair Production of Second-Generation Scalar Leptoquarks in pp Collisions at $\sqrt{s} = 7$ TeV". In: *Phys. Rev. Lett.* 106 (2011), p. 201803. DOI: `10.1103/PhysRevLett.106.201803`. arXiv: `1012.4033 [hep-ex]` *Cited on page 60.*

[172] CMS Collaboration. "Search for pair production of first- and second-generation scalar leptoquarks in pp collisions at $\sqrt{s} = 7$ TeV". In: *Phys. Rev.* D86 (2012), p. 052013. DOI: `10.1103/PhysRevD.86.052013`. arXiv: `1207.5406 [hep-ex]` *Cited on page 60.*

[173] CMS Collaboration. "Search for pair production of first and second generation leptoquarks in proton-proton collisions at $\sqrt{s} = 8$ TeV". In: *Phys. Rev.* D93.3 (2016), p. 032004. DOI: `10.1103/PhysRevD.93.032004`. arXiv: `1509.03744 [hep-ex]` *Cited on page 60.*

[174] CMS Collaboration. *Search for pair-production of first generation scalar leptoquarks in pp collisions at* $\sqrt{s} = 13$ TeV *with* 2.6 fb^{-1}. Tech. rep. CMS-PAS-EXO-16-043. `https://cds.cern.ch/record/2205285`. 2016 *Cited on page 60.*

[175] CMS Collaboration. *Search for pair-production of second-generation scalar leptoquarks in pp collisions at* $\sqrt{s} = 13$ TeV *with the CMS detector*. Tech. rep. CMS-PAS-EXO-16-007. `https://cds.cern.ch/record/2139349`. 2016 *Cited on page 60.*

References for Chapter 7: Analysis

[26] S. Schmitz. "Search for New Resonances in Lepton-Antilepton Final States in Proton-Proton Collisions at $\sqrt{s} = 13$ TeV with the ATLAS Experiment". PhD thesis. Johannes Gutenberg-Universität Mainz, May 2018 *Cited on pages 2, 31, 33, 35, 47, 66.*

[64] A. D. Martin et al. "Parton distributions for the LHC". In: *Eur. Phys. J.* C63 (2009), pp. 189–285. DOI: `10.1140/epjc/s10052-009-1072-5`. arXiv: `0901.0002 [hep-ph]` *Cited on pages 19, 64.*

[79] D. Milstead et al. *Search for first and second generation scalar leptoquarks in pp collisions at $\sqrt{s} = 13$ TeV with the ATLAS detector at the LHC*. Tech. rep. ATL-COM-PHYS-2016-1690. `https://cds.cern.ch/record/2234245` (Internal documentation). Nov. 2016 *Cited on pages 26, 64, 67, 71, 72, 78.*

[112] ATLAS Collaboration. "Performance of the ATLAS Trigger System in 2015". In: *Eur. Phys. J.* C77.5 (2017), p. 317. DOI: `10.1140/epjc/s10052-017-4852-3`. arXiv: `1611.09661 [hep-ex]` *Cited on pages 43, 66.*

[121] ATLAS Luminosity Group. *LuminosityForPhysics*. TWiki page. `https://twiki.cern.ch/twiki/bin/viewauth/Atlas/LuminosityForPhysics` (Internal documentation). 2018 *Cited on pages 45, 62, 73.*

[123] S. Agostinelli et al. "GEANT4: A Simulation toolkit". In: *Nuclear Instruments and Methods in Physics Research Section A: Accelerators, Spectrometers, Detectors and Associated Equipment* 506.3 (2003), pp. 250–303. ISSN: 0168-9002. DOI: `10.1016/S0168-9002(03)01368-8` *Cited on pages 46, 64.*

[125] ATLAS Public Results. *LuminosityPublicResultsRun2*. TWiki page. `https://twiki.cern.ch/twiki/bin/view/AtlasPublic/LuminosityPublicResultsRun2`. 2018 *Cited on pages 46, 63.*

[130] ATLAS Collaboration. *Electron efficiency measurements with the ATLAS detector using the 2015 LHC proton-proton collision data*. Tech. rep. ATLAS-CONF-2016-024. `https://cds.cern.ch/record/2157687`. June 2016 *Cited on pages 48, 67.*

[135] ATLAS Collaboration. "Muon reconstruction performance of the ATLAS detector in proton–proton collision data at $\sqrt{s}$ =13 TeV". In: *Eur. Phys. J.* C76.5 (2016), p. 292. DOI: `10.1140/epjc/s10052-016-4120-y`. arXiv: `1603.05598 [hep-ex]` *Cited on pages 51, 54, 67, 68, 73.*

[142] M. Cacciari, G. P. Salam, and G. Soyez. "The anti-k_t jet clustering algorithm". In: *JHEP* 04 (2008), p. 063. DOI: `10.1088/1126-6708/2008/04/063`. arXiv: `0802.1189 [hep-ph]` *Cited on pages 54, 68.*

[162] A. Belyaev et al. "Leptoquark single and pair production at LHC with CalcHEP/CompHEP in the complete model". In: *JHEP* 09 (2005), p. 005. DOI: `10.1088/1126-6708/2005/09/005`. arXiv: `hep-ph/0502067 [hep-ph]` *Cited on pages 59, 63.*

[163] ATLAS Collaboration. "Searches for scalar leptoquarks and differential cross-section measurements in dilepton-dijet events in proton-proton collisions at a centre-of-mass energy of $\sqrt{s}$ = 13 TeV with the ATLAS experiment". In: *Eur. Phys. J.* C79.9 (2019), p. 733. DOI: `10.1140/epjc/s10052-019-7181-x`. arXiv: `1902.00377 [hep-ex]` *Cited on pages 60, 61, 63, 68, 69, 108.*

[168] ATLAS Collaboration. "Search for scalar leptoquarks in pp collisions at $\sqrt{s}$ = 13 TeV with the ATLAS experiment". In: *New J. Phys.* 18.9 (2016), p. 093016. DOI: `10.1088/1367-2630/18/9/093016`. arXiv: `1605.06035 [hep-ex]` *Cited on pages 60, 61, 108.*

[176] ATLAS Collaboration. "Luminosity determination in pp collisions at $\sqrt{s}$ = 8 TeV using the ATLAS detector at the LHC". In: *Eur. Phys. J.* C76.12 (2016), p. 653. DOI: `10.1140/epjc/s10052-016-4466-1`. arXiv: `1608.03953 [hep-ex]` *Cited on pages 62, 73.*

[177] G. Avoni et al. "The new LUCID-2 detector for luminosity measurement and monitoring in ATLAS". In: *JINST* 13.07 (2018), P07017. DOI: `10.1088/1748-0221/13/07/P07017` *Cited on page 62.*

[178] F. Maltoni and T. Stelzer. "MadEvent: Automatic event generation with MadGraph". In: *JHEP* 02 (2003), p. 027. DOI: `10.1088/1126-6708/2003/02/027`. arXiv: `hep-ph/0208156 [hep-ph]` *Cited on page 63.*

[179] T. Mandal, S. Mitra, and S. Seth. "Pair Production of Scalar Leptoquarks at the LHC to NLO Parton Shower Accuracy". In: *Phys. Rev.* D93.3 (2016), p. 035018. DOI: `10.1103/PhysRevD.93.035018`. arXiv: `1506.07369 [hep-ph]` *Cited on page 63.*

[180] P. Artoisenet et al. "Automatic spin-entangled decays of heavy resonances in Monte Carlo simulations". In: *JHEP* 03 (2013), p. 015. DOI: `10.1007/JHEP03(2013)015`. arXiv: `1212.3460 [hep-ph]` *Cited on page 63.*

[181] T. Sjostrand, S. Mrenna, and P. Z. Skands. "A Brief Introduction to PYTHIA 8.1". In: *Comput. Phys. Commun.* 178 (2008), pp. 852–867. DOI: `10.1016/j.cpc.2008.01.036`. arXiv: `0710.3820 [hep-ph]` *Cited on page 63.*

[182] ATLAS Collaboration. *ATLAS Run 1 Pythia8 tunes*. Tech. rep. ATL-PHYS-PUB-2014-021. `https://cds.cern.ch/record/1966419`. Nov. 2014 *Cited on page 63.*

[183] R. D. Ball et al. “Parton distributions for the LHC Run II”. In: *JHEP* 04 (2015), p. 040. DOI: 10.1007/JHEP04(2015)040. arXiv: 1410.8849 [hep-ph] *Cited on page 63.*

[184] ATLAS Collaboration. *Monte Carlo Generators for the Production of a W or Z/γ^* Boson in Association with Jets at ATLAS in Run 2*. Tech. rep. ATL-PHYS-PUB-2016-003. https://cds.cern.ch/record/2120133. Jan. 2016 *Cited on page 64.*

[185] T. Gleisberg et al. “Event generation with SHERPA 1.1”. In: *JHEP* 02 (2009), p. 007. DOI: 10.1088/1126-6708/2009/02/007. arXiv: 0811.4622 [hep-ph] *Cited on page 64.*

[186] T. Gleisberg and S. Hoeche. “Comix, a new matrix element generator”. In: *JHEP* 12 (2008), p. 039. DOI: 10.1088/1126-6708/2008/12/039. arXiv: 0808.3674 [hep-ph] *Cited on page 64.*

[187] F. Cascioli, P. Maierhofer, and S. Pozzorini. “Scattering Amplitudes with Open Loops”. In: *Phys. Rev. Lett.* 108 (2012), p. 111601. DOI: 10.1103/PhysRevLett.108.111601. arXiv: 1111.5206 [hep-ph] *Cited on page 64.*

[188] S. Hoeche et al. “QCD matrix elements + parton showers: The NLO case”. In: *JHEP* 04 (2013), p. 027. DOI: 10.1007/JHEP04(2013)027. arXiv: 1207.5030 [hep-ph] *Cited on page 64.*

[189] H.-L. Lai et al. “New parton distributions for collider physics”. In: *Phys. Rev.* D82 (2010), p. 074024. DOI: 10.1103/PhysRevD.82.074024. arXiv: 1007.2241 [hep-ph] *Cited on page 64.*

[190] P. Nason. “A New method for combining NLO QCD with shower Monte Carlo algorithms”. In: *JHEP* 11 (2004), p. 040. DOI: 10.1088/1126-6708/2004/11/040. arXiv: hep-ph/0409146 [hep-ph] *Cited on page 64.*

[191] S. Frixione, P. Nason, and C. Oleari. “Matching NLO QCD computations with Parton Shower simulations: the POWHEG method”. In: *JHEP* 11 (2007), p. 070. DOI: 10.1088/1126-6708/2007/11/070. arXiv: 0709.2092 [hep-ph] *Cited on page 64.*

[192] S. Alioli et al. “A general framework for implementing NLO calculations in shower Monte Carlo programs: the POWHEG BOX”. In: *JHEP* 06 (2010), p. 043. DOI: 10.1007/JHEP06(2010)043. arXiv: 1002.2581 [hep-ph] *Cited on page 64.*

[193] S. Alioli, S.-O. Moch, and P. Uwer. “Hadronic top-quark pair-production with one jet and parton showering”. In: *JHEP* 01 (2012), p. 137. DOI: 10.1007/JHEP01(2012)137. arXiv: 1110.5251 [hep-ph] *Cited on page 64.*

[194] T. Sjostrand, S. Mrenna, and P. Z. Skands. “PYTHIA 6.4 Physics and Manual”. In: *JHEP* 05 (2006), p. 026. DOI: 10.1088/1126-6708/2006/05/026. arXiv: hep-ph/0603175 [hep-ph] *Cited on page 64.*

[195] J. Pumplin et al. “New generation of parton distributions with uncertainties from global QCD analysis”. In: *JHEP* 07 (2002), p. 012. DOI: 10.1088/1126-6708/2002/07/012. arXiv: hep-ph/0201195 [hep-ph] *Cited on page 64.*

[196] P. Z. Skands. “Tuning Monte Carlo Generators: The Perugia Tunes”. In: *Phys. Rev.* D82 (2010), p. 074018. DOI: 10.1103/PhysRevD.82.074018. arXiv: 1005.3457 [hep-ph] *Cited on page 64.*

[197] D. J. Lange. “The EvtGen particle decay simulation package”. In: *Nuclear Instruments and Methods in Physics Research Section A: Accelerators, Spectrometers, Detectors and Associated Equipment* 462.1 (2001). BEAUTY2000, Proceedings of the 7th Int. Conf. on B-Physics at Hadron Machines, pp. 152–155. ISSN: 0168-9002. DOI: `10.1016/S0168-9002(01)00089-4` *Cited on page 64.*

[198] R. D. Ball et al. “Parton distributions with LHC data”. In: *Nucl. Phys.* B867 (2013), pp. 244–289. DOI: `10.1016/j.nuclphysb.2012.10.003`. arXiv: `1207.1303 [hep-ph]` *Cited on page 64.*

[199] ATLAS Collaboration. *Summary of ATLAS Pythia 8 tunes*. Tech. rep. ATL-PHYS-PUB-2012-003. `https://cds.cern.ch/record/1474107`. Aug. 2012 *Cited on page 64.*

[200] ATLAS Collaboration. “The ATLAS Simulation Infrastructure”. In: *Eur. Phys. J.* C70 (2010), pp. 823–874. DOI: `10.1140/epjc/s10052-010-1429-9`. arXiv: `1005.4568 [physics.ins-det]` *Cited on page 64.*

[201] ATLAS Collaboration. *The simulation principle and performance of the ATLAS fast calorimeter simulation FastCaloSim*. Tech. rep. ATL-PHYS-PUB-2010-013. `https://cds.cern.ch/record/1300517`. Oct. 2010 *Cited on page 64.*

[202] ATLAS Production Group. *DataPeriods*. TWiki page. `https://twiki.cern.ch/twiki/bin/viewauth/AtlasProtected/DataPeriods` (Internal documentation). 2018 *Cited on page 66.*

[203] S. Schramm. “Searching for Dark Matter with the ATLAS Detector in Events with an Energetic Jet and Large Missing Transverse Momentum”. PhD thesis. University of Toronto, Feb. 2015 *Cited on page 66.*

[204] ATLAS Collaboration. “Measurement of the muon reconstruction performance of the ATLAS detector using 2011 and 2012 LHC proton–proton collision data”. In: *Eur. Phys. J.* C74.11 (2014), p. 3130. DOI: `10.1140/epjc/s10052-014-3130-x`. arXiv: `1407.3935 [hep-ex]` *Cited on page 67.*

[205] M. Morgenstern. “Performance of the ATLAS Muon Trigger in Run 2”. In: (Feb. 2018). `https://cds.cern.ch/record/2304213` *Cited on page 68.*

[206] ATLAS Collaboration. “Jet energy scale measurements and their systematic uncertainties in proton-proton collisions at $\sqrt{s} = 13$ TeV with the ATLAS detector”. In: *Phys. Rev.* D96.7 (2017), p. 072002. DOI: `10.1103/PhysRevD.96.072002`. arXiv: `1703.09665 [hep-ex]` *Cited on page 68.*

[207] ATLAS Collaboration. *Selection of jets produced in 13TeV proton-proton collisions with the ATLAS detector*. Tech. rep. ATLAS-CONF-2015-029. `https://cds.cern.ch/record/2037702`. July 2015 *Cited on page 68.*

[208] ATLAS Collaboration. “Performance of b-Jet Identification in the ATLAS Experiment”. In: *JINST* 11.04 (2016), P04008. DOI: `10.1088/1748-0221/11/04/P04008`. arXiv: `1512.01094 [hep-ex]` *Cited on page 68.*

[209] ATLAS Collaboration. *Optimisation of the ATLAS b-tagging performance for the 2016 LHC Run*. Tech. rep. ATL-PHYS-PUB-2016-012. `https://cds.cern.ch/record/2160731`. June 2016 *Cited on page 68.*

[210] ATLAS Collaboration. “Search for new resonances in events with one lepton and missing transverse momentum in pp collisions at $\sqrt{s} = 13$ TeV with the ATLAS detector”. In: *Phys. Lett.* B762 (2016), pp. 334–352. DOI: `10.1016/j.physletb.2016.09.040`. arXiv: `1606.03977 [hep-ex]` *Cited on page 69.*

[211] ATLAS ElectronGamma Group. *Electron and Photon Calibration for Run2 (energy scale and resolution).* TWiki page. `https://twiki.cern.ch/twiki/bin/view/AtlasProtected/EGammaCalibrationRun2` (Internal documentation). 2016 *Cited on page 73.*

[212] ATLAS JetEtMiss Group. *Uncertainty release for analyses using 2015 and 2016 data in 20.7 (MC15c) releases.* TWiki page. `https://twiki.cern.ch/twiki/bin/viewauth/AtlasProtected/JetUncertainties20152016Data20p7` (Internal documentation). 2018 *Cited on page 73.*

[213] L. A. Harland-Lang et al. "Parton distributions in the LHC era: MMHT 2014 PDFs". In: *Eur. Phys. J.* C75.5 (2015), p. 204. DOI: `10.1140/epjc/s10052-015-3397-6`. arXiv: `1412.3989 [hep-ph]` *Cited on page 74.*

[214] S. Dulat et al. "New parton distribution functions from a global analysis of quantum chromodynamics". In: *Phys. Rev.* D93.3 (2016), p. 033006. DOI: `10.1103/PhysRevD.93.033006`. arXiv: `1506.07443 [hep-ph]` *Cited on page 74.*

[215] ATLAS Collaboration. *Comparison of Monte Carlo generator predictions from Powheg and Sherpa to ATLAS measurements of top pair production at 7 TeV.* Tech. rep. ATL-PHYS-PUB-2015-011. `https://cds.cern.ch/record/2020602`. May 2015 *Cited on page 74.*

[216] ATLAS Top Group. *Run 2 Top PDF Recomendations.* TWiki page. `https://twiki.cern.ch/twiki/bin/viewauth/AtlasProtected/TopMCPDFReccommendations` (Internal documentation). 2017 *Cited on page 75.*

[217] J. Butterworth et al. "PDF4LHC recommendations for LHC Run II". In: *J. Phys.* G43 (2016), p. 023001. DOI: `10.1088/0954-3899/43/2/023001`. arXiv: `1510.03865 [hep-ph]` *Cited on page 75.*

References for Chapter 8: Statistical interpretation

[163] ATLAS Collaboration. "Searches for scalar leptoquarks and differential cross-section measurements in dilepton-dijet events in proton-proton collisions at a centre-of-mass energy of $\sqrt{s}$ = 13 TeV with the ATLAS experiment". In: *Eur. Phys. J.* C79.9 (2019), p. 733. DOI: `10.1140/epjc/s10052-019-7181-x`. arXiv: `1902.00377 [hep-ex]` *Cited on pages 60, 61, 63, 68, 69, 108.*

[168] ATLAS Collaboration. "Search for scalar leptoquarks in pp collisions at $\sqrt{s}$ = 13 TeV with the ATLAS experiment". In: *New J. Phys.* 18.9 (2016), p. 093016. DOI: `10.1088/1367-2630/18/9/093016`. arXiv: `1605.06035 [hep-ex]` *Cited on pages 60, 61, 108.*

[218] G. Cowan. *Statistical Data Analysis.* Oxford University Press Inc., New York, 1998. ISBN: 0-19-850156-0 *Cited on page 97.*

[219] G. Cowan et al. "Asymptotic formulae for likelihood-based tests of new physics". In: *Eur. Phys. J.* C71 (2011). [Erratum: Eur. Phys. J.C73,2501(2013)], p. 1554. DOI: `10.1140/epjc/s10052-011-1554-0,10.1140/epjc/s10052-013-2501-z`. arXiv: `1007.1727 [physics.data-an]` *Cited on page 97.*

[220] J. Fischer. "Study of Higgs boson production in association with $t\bar{t}$ quark pairs at $\sqrt{s}$ = 13 TeV with the ATLAS detector". MA thesis. Johannes Gutenberg-Universität Mainz, Sept. 2018 *Cited on page 97.*

[221] M. Baak et al. “HistFitter software framework for statistical data analysis”. In: *Eur. Phys. J.* C75 (2015), p. 153. DOI: `10.1140/epjc/s10052-015-3327-7`. arXiv: `1410.1280 [hep-ex]` *Cited on page 97.*

[222] A. Wald. “Contributions to the Theory of Statistical Estimation and Testing Hypotheses”. In: *The Annals of Mathematical Statistics* 10.4 (1939), pp. 299–326. ISSN: 00034851 *Cited on page 99.*

[223] CMS Collaboration. “Search for pair production of first-generation scalar leptoquarks at $\sqrt{s} = 13$ TeV”. In: *Phys. Rev.* D99.5 (2019), p. 052002. DOI: `10.1103/PhysRevD.99.052002`. arXiv: `1811.01197 [hep-ex]` *Cited on page 108.*

[224] CMS Collaboration. “Search for pair production of second-generation leptoquarks at $\sqrt{s} = 13$ TeV”. In: *Phys. Rev.* D99.3 (2019), p. 032014. DOI: `10.1103/PhysRevD.99.032014`. arXiv: `1808.05082 [hep-ex]` *Cited on page 108.*

References for Chapter 9: Conclusion and outlook

[86] LHCb Collaboration. “The LHCb Detector at the LHC”. In: *Journal of Instrumentation* 3.08 (Aug. 2008), S08005–S08005. DOI: `10.1088/1748-0221/3/08/s08005` *Cited on pages 31, 111.*

[225] BABAR Collaboration. “The BaBar detector”. In: *Nucl. Instrum. Meth.* A479 (2002), pp. 1–116. DOI: `10.1016/S0168-9002(01)02012-5`. arXiv: `hep-ex/0105044 [hep-ex]` *Cited on page 111.*

[226] Belle Collaboration. “The Belle detector”. In: *Nuclear Instruments and Methods in Physics Research Section A: Accelerators, Spectrometers, Detectors and Associated Equipment* 479.1 (2002). Detectors for Asymmetric B-factories, pp. 117–232. ISSN: 0168-9002. DOI: `doi.org/10.1016/S0168-9002(01)02013-7` *Cited on page 111.*

[227] A. Monteux and A. Rajaraman. “B Anomalies and Leptoquarks at the LHC: Beyond the Lepton-Quark Final State”. In: *Phys. Rev.* D98.11 (2018), p. 115032. DOI: `10.1103/PhysRevD.98.115032`. arXiv: `1803.05962 [hep-ph]` *Cited on page 111.*

References for Chapter 10: Motivation

[228] E. Ertel. “Firmware-Entwicklung für das Reinheitsüberwachungssystem der Flüssig-Argon-Kalorimeter beim ATLAS Experiment”. Diploma thesis. Johannes Gutenberg-Universität Mainz, Apr. 2009 *Cited on pages 115, 117, 133, 136–138.*

References for Chapter 11: Theoretical and system description

[100] *ATLAS liquid-argon calorimeter: Technical Design Report*. Technical Design Report ATLAS. `https://cds.cern.ch/record/331061`. Geneva: CERN, 1996 *Cited on pages 38, 129.*

[228] E. Ertel. “Firmware-Entwicklung für das Reinheitsüberwachungssystem der Flüssig-Argon-Kalorimeter beim ATLAS Experiment”. Diploma thesis. Johannes Gutenberg-Universität Mainz, Apr. 2009 *Cited on pages 115, 117, 133, 136–138.*

[229] W. Walkowiak. "Entwicklung von Flüssig-Argon-Reinheitsmeßgeräten für das ATLAS-Experiment und Messungen zur Energieauflösung eines hadronischen Flüssig-Argon-Kalorimeteres". PhD thesis. Johannes Gutenberg-Universität Mainz, Nov. 1998 *Cited on pages 117, 123, 125, 128, 183.*

[230] W.J. Willis and V. Radeka. "Liquid-argon ionization chambers as total-absorption detectors". In: *Nuclear Instruments and Methods* 120.2 (1974), pp. 221–236. ISSN: 0029-554X. DOI: `10.1016/0029-554X(74)90039-1` *Cited on page 118.*

[231] L. Onsager. "Initial Recombination of Ions". In: *Phys. Rev.* 54 (8 Oct. 1938), pp. 554–557. DOI: `10.1103/PhysRev.54.554` *Cited on page 119.*

[232] J. Thomas and D.A. Imel. "Recombination of electron-ion pairs in liquid argon and liquid xenon". In: *Phys. Rev. A* 36 (2 July 1987), pp. 614–616. DOI: `10.1103/PhysRevA.36.614` *Cited on pages 119, 120.*

[233] G. Jaffé. "Zur Theorie der Ionisation in Kolonnen". In: *Annalen der Physik* 347.12 (1913), pp. 303–344. DOI: `10.1002/andp.19133471205` *Cited on page 119.*

[234] M. Adams et al. "A purity monitoring system for liquid argon calorimeters". In: *Nuclear Instruments and Methods in Physics Research Section A: Accelerators, Spectrometers, Detectors and Associated Equipment* 545.3 (2005), pp. 613–623. ISSN: 0168-9002. DOI: `10.1016/j.nima.2005.03.117` *Cited on pages 121–124, 126, 129, 183.*

[235] W. Hofmann et al. "Production and transport of conduction electrons in a liquid argon ionization chamber". In: *Nuclear Instruments and Methods* 135 (May 1976), pp. 151–156. DOI: `10.1016/0029-554X(76)90839-9` *Cited on pages 122, 127.*

[236] G. Bakale, U. Sowada, and W. Schmidt. "Effect of an electric field on electron attachment to sulfur hexafluoride, nitrous oxide, and molecular oxygen in liquid argon and xenon". In: *The Journal of Physical Chemistry* 80 (Nov. 1976). DOI: `10.1021/j100564a006` *Cited on page 122.*

[237] C.M. Lederer and V.D. Shirley. *Table of isotopes*. 7th ed. John Wiley & Sons, 1978. ISBN: 978-0-471-04180-1 *Cited on pages 124, 125.*

[238] F. Hölldorfer. "Bau und Betrieb einer α/β-Ionisationskammer zur Messung der Reinheit von flüssigem Argon". Diploma thesis. Johannes Gutenberg-Universität Mainz, Mar. 1997 *Cited on pages 124, 130.*

[239] A. Hergesell. "Entwicklung einer CAN-basierten Datenerfassung für die flüssig-Argon-Monitore am ATLAS-Experiment". Diploma thesis. Johannes Gutenberg-Universität Mainz, Apr. 2000 *Cited on page 128.*

[240] R. Othegraven. Private communication. Sept. 2018 *Cited on page 130.*

[241] M. Eppard and C. Zeitnitz. *Internal documentation of the purity monitor probes in the ATLAS LArg calorimeter*. Internal documentation. Sept. 2005 *Cited on page 131.*

[242] C. Zeitnitz. *The Purity Monitor Front-End Board*. Internal documentation. Sept. 2004 *Cited on pages 131, 132.*

[243] M. Becker. *New Liquid argon purity control system (nLAPS)*. Internal documentation. 2016 *Cited on pages 133, 139–141, 154, 188.*

[244] A. Wolf. *LAr purity documentation*. TWiki page. `https://atlasop.cern.ch/twiki/bin/view/LAr/LArPurity` (Internal documentation). 2019 *Cited on pages 139, 154.*

[245] M. Morhac. *Advanced Spectra Processing*. ROOT class documentation. `https://root.cern.ch/root/html530/TSpectrum.html`. 1999 *Cited on page 139.*

References for Chapter 12: Maintenance

[243] M. Becker. *New Liquid argon purity control system (nLAPS)*. Internal documentation. 2016 *Cited on pages 133, 139–141, 154, 188.*

[244] A. Wolf. *LAr purity documentation*. TWiki page. `https://atlasop.cern.ch/twiki/bin/view/LAr/LArPurity` (Internal documentation). 2019 *Cited on pages 139, 154.*

[246] G. van Rossum. *Python tutorial*. Tech. rep. CS-R9526. Amsterdam: Centrum voor Wiskunde en Informatica (CWI), May 1995 *Cited on page 144.*

[247] B. Copy. *WinCC-OA Service*. Web documentation. `https://readthedocs.web.cern.ch/display/ICKB/WinCC-OA+Service/`. Dec. 2018 *Cited on page 144.*

[248] S. Chekulaev. Private communication. Mar. 2019 *Cited on page 150.*

[249] C. Zeitnitz. Private communication. Mar. 2019 *Cited on page 150.*

[250] J. Harder et al. "A low-noise, low stored energy preamplifier for high-voltage radiation detectors". In: *Nuclear Instruments & Methods in Physics Research Section A-accelerators Spectrometers Detectors and Associated Equipment - NUCL INSTRUM METH PHYS RES A* 576 (June 2007), pp. 397–402. DOI: `10.1016/j.nima.2007.03.005` *Cited on page 153.*

References for Chapter 13: Upgrade development

[251] ATLAS Resources Review Board. *ATLAS Upgrade Status Report 2018-2019*. `https://cds.cern.ch/record/2660301/files/CERN-RRB-2019-024.pdf`. Apr. 2019 *Cited on page 157.*

[252] T. Kawamoto et al. *New Small Wheel Technical Design Report*. Tech. rep. CERN-LHCC-2013-006. ATLAS-TDR-020. `https://cds.cern.ch/record/1552862`. June 2013 *Cited on page 157.*

[253] M. Shochet et al. *Fast TracKer (FTK) Technical Design Report*. Tech. rep. CERN-LHCC-2013-007. ATLAS-TDR-021. `https://cds.cern.ch/record/1552953`. June 2013 *Cited on page 157.*

[254] M. Aleksa et al. *ATLAS Liquid Argon Calorimeter Phase-I Upgrade Technical Design Report*. Tech. rep. CERN-LHCC-2013-017. ATLAS-TDR-022. `https://cds.cern.ch/record/1602230`. Sept. 2013 *Cited on page 157.*

[255] ATLAS Collaboration. *Technical Design Report for the Phase-I Upgrade of the ATLAS TDAQ System*. Tech. rep. CERN-LHCC-2013-018. ATLAS-TDR-023. `https://cds.cern.ch/record/1602235`. Sept. 2013 *Cited on page 157.*

[256] L. Adamczyk et al. *Technical Design Report for the ATLAS Forward Proton Detector*. Tech. rep. CERN-LHCC-2015-009. ATLAS-TDR-024. `https://cds.cern.ch/record/2017378`. May 2015 *Cited on page 157.*

[257] ATLAS Collaboration. *Technical Design Report for the ATLAS Inner Tracker Strip Detector*. Tech. rep. CERN-LHCC-2017-005. ATLAS-TDR-025. `https://cds.cern.ch/record/2257755`. Apr. 2017 *Cited on page 158.*

[258] ATLAS Collaboration. *Technical Design Report for the Phase-II Upgrade of the ATLAS Muon Spectrometer*. Tech. rep. CERN-LHCC-2017-017. ATLAS-TDR-026. `https://cds.cern.ch/record/2285580`. Sept. 2017 *Cited on page 158.*

[259] ATLAS Collaboration. *Technical Design Report for the Phase-II Upgrade of the ATLAS LAr Calorimeter*. Tech. rep. CERN-LHCC-2017-018. ATLAS-TDR-027. `https://cds.cern.ch/record/2285582`. Sept. 2017 *Cited on page 158.*

[260] ATLAS Collaboration. *Technical Design Report for the Phase-II Upgrade of the ATLAS Tile Calorimeter*. Tech. rep. CERN-LHCC-2017-019. ATLAS-TDR-028. `https://cds.cern.ch/record/2285583`. Sept. 2017 *Cited on page 158.*

[261] ATLAS Collaboration. *Technical Design Report for the ATLAS Inner Tracker Pixel Detector*. Tech. rep. CERN-LHCC-2017-021. ATLAS-TDR-030. `https://cds.cern.ch/record/2285585`. Sept. 2017 *Cited on page 158.*

[262] ATLAS Collaboration. *Technical Design Report for the Phase-II Upgrade of the ATLAS TDAQ System*. Tech. rep. CERN-LHCC-2017-020. ATLAS-TDR-029. `https://cds.cern.ch/record/2285584`. Sept. 2017 *Cited on page 158.*

[263] ATLAS Upgrade Group. *RadiationBackgroundSimulationsRun2*. TWiki page. `https://twiki.cern.ch/twiki/bin/view/Atlas/RadiationBackgroundSimulationsRun2` (Internal documentation). 2018 *Cited on page 160.*

[264] ATLAS Upgrade Group. *Radiation Maps from Geant4 Simulations*. TWiki page. `https://twiki.cern.ch/twiki/bin/viewauth/Atlas/RadiationMapsGeant4` (Internal documentation). 2018 *Cited on page 160.*

[265] ATLAS Upgrade Group. *Radiation map for proton-proton collisions at* $\sqrt{s} = 14$ *TeV with ATLAS-P2-ITK-21-01-00 normalised to 4000* fb^{-1}. TWiki page. `https://twiki.cern.ch/twiki/pub/Atlas/RadiationMapsGeant4/WebRadMaps_Zoom_ATLAS-P2-ITK-21-01-00-4000ifb-80mb-119994-Pythia8_A2MSTW2008LO_minbias_inelastic_50000_events.html` (Internal documentation). 2018 *Cited on page 160.*

[266] S. Menke. Private communication. Dec. 2018 *Cited on pages 160, 161.*

[267] G. Brooijmans. Private communication. Dec. 2018 *Cited on page 161.*

[268] M. Citterio. *Design of a 48V/12V DC/DC Converter*. Presentation during LAr week. `https://indico.cern.ch/event/759147/contributions/3162144/attachments/1727560/2791083/48to12_DCDC_Converter_LAr_week_Oct2018.pdf` (Internal documentation). Oct. 2018 *Cited on page 162.*

References for Chapter A: Detailed information about MC samples

[269] ATLAS Physics Modelling Group. *CentralMC15ProductionList*. TWiki page. `https://twiki.cern.ch/twiki/bin/view/AtlasProtected/CentralMC15ProductionList` (Internal documentation). 2018 *Cited on page 169.*

References for Chapter B: Details on the purity calculation

[229] W. Walkowiak. “Entwicklung von Flüssig-Argon-Reinheitsmeßgeräten für das ATLAS-Experiment und Messungen zur Energieauflösung eines hadronischen Flüssig-Argon-Kalorimeteres”. PhD thesis. Johannes Gutenberg-Universität Mainz, Nov. 1998 *Cited on pages 117, 123, 125, 128, 183.*

[234] M. Adams et al. “A purity monitoring system for liquid argon calorimeters”. In: *Nuclear Instruments and Methods in Physics Research Section A: Accelerators, Spectrometers, Detectors and Associated Equipment* 545.3 (2005), pp. 613–623. ISSN: 0168-9002. DOI: `10.1016/j.nima.2005.03.117` *Cited on pages 121–124, 126, 129, 183.*

References for Chapter C: More detailed OPC UA server design

[243] M. Becker. *New Liquid argon purity control system (nLAPS).* Internal documentation. 2016 *Cited on pages 133, 139–141, 154, 188.*

ACKNOWLEDGMENTS

> *“I’ve pinned my heart to my sleeve*
> *So that the whole world can see*
> *I have a heart on for you.”*
>
> CELLDWELLER - HEART ON

Personenbezogene Daten sind aus Datenschutzgründen aus der elektronischen Version gelöscht.

Lebenslauf

Personenbezogene Daten sind aus Datenschutzgründen aus der elektronischen Version gelöscht.